Magnetic fields in the intracluster medium

Dissertation

zur Erlangung des Doktorgrades an der Fakultät für Mathematik, Informatik und Naturwissenschaften Fachereich Physik der Universität Hamburg

Vorgelegt von:

PAOLA DOMÍNGUEZ FERNÁNDEZ

Hamburg

2020

Zusammenfassung

Magnetfelder sind von kleinen bis zu großen Skalen allgegenwärtig im Universum. Obwohl es bereits vielfältige Theorien zu ihrer Entstehung gibt, ist ihr Ursprung immer noch nicht gut verstanden. Um uns dieser fundamentalen Frage auf die beste Weise zu nähern, erforschen wir die größten gravitationsgebundenen Systeme, die existieren: Galaxienhaufen. Galaxienhaufen sind ergiebige astrophysische Laboratorien, die uns helfen, Phänomene unseres Universums von den größten kosmologischen Skalen bis hin zu den kleinsten, von Plasmaphysik beherrschten Mikroskalen zu verstehen. Der Raum zwischen den Galaxien in Galaxienhaufen ist mit heißem Plasma gefüllt, dem sogenannten Intracluster-Medium (ICM). Dieses Plasma emittiert in Röntgen- und Radiowellenlängen.

Die Beschleunigung von Elektronen kosmischer Strahlung in Magnetfeldern mit Feldstärken im Mikrogauss-Bereich produziert Mpc-große Strukturen von diffusiver Radioemission, die typischerweise in zwei Kategorien eingeteilt werden: Radiohalos und Radiorelikte. Die Mechanismen zur Teilchenbeschleunigung, die zu diesen großskaligen Quellen führen, sind nicht vollständig verstanden.

In dieser Doktorarbeit habe ich mich darauf fokussiert, die Rolle von Magnetfeldern in Galaxienhaufen zu untersuchen. Meine Motivation war, die folgenden Fragen zu beantworten: 1) Was sind die magnetischen Verstärkungsmechanismen, die zu den heutigen Beobachtungen führen?, 2) Welche Rolle spielen Verschmelzungen (Merger) von Galaxienhaufen bei der Bildung von Magnetfeldern?, 3) Was definiert die Substruktur der Synchrotron- und polarisierten Emissionen in Radiorelikten? Zu diesem Zweck habe ich Ergebnisse des kosmologischen MHD-Code ENZO, des MHD-Code FLASH und des hybriden MHD-Lagrangeschen PLUTO-Code verwendet.

Ich habe ein primordiales Szenario zusammen mit einer kleinskaligen Dynamoverstärkung in simulierten Galaxienhaufen untersucht und damit die Fragen 1) und 2) behandelt. Ich habe herausgefunden, dass ein solches Szenario Magnetfelder in Galaxienhaufen in Größenordnungen von Mikrogauss reproduzieren kann. Große und kleine Verschmelzungen verursachen sowohl Kompression als auch Turbulenz und spielen deshalb eine Schlüsselrolle bei der Verstärkung von Magnetfeldern. Insbesondere leiten sie mehrfache Turbulenz-Kaskaden ein, die das Wachstum eines bereits existierenden kleinskaligen Dynamos beeinflussen können. Ich habe festgestellt, dass große Verschmelzungen die Dynamoverstärkung um einen Zeitraum von 1 Gyr verzögern können.

Im Rahmen von Frage 3) habe ich weiterhin den Mechanismus der diffusiven Stoßwellenbeschleunigung (diffusive shock acceleraction - DSA) untersucht, um Radio- und polarisierte Emissionen zu simulieren, die in Radiorelikten beobachtet werden. Ich habe festgestellt, dass Turbulenz einen signifikanten Einfluss auf die Morphologie von Synchrotron- und polarisierten Emissionen hat. Die beobachtete Diskrepanz zwischen der von Röntgenstrahlung und der von Radiospektren abgeleiteten Mach-Zahl von Schocks wird in diesem Zusammenhang erklärt. Einige beobachtete Radio Relics weisen einen Gradienten der Fraktionspolarisation auf, der entgegen theoretischen Erwartungen an der Schockfront größer und in den abstromigen Regionen niedriger ist. Ich stelle fest, dass dieser Gradient unter Umständen durch Turbulenz erklärt werden kann.

Summary

Magnetic fields are ubiquitous in the Universe from small to large scales. While various theories have been proposed for their generation, their origin is still not well understood. In order to best address this fundamental question, we study the largest gravitationally bound systems that exist: galaxy clusters. Galaxy clusters are rich, astrophysical laboratories that help us understand phenomena in our Universe from the largest cosmological scales down to the micro-scales ruled by plasma physics. The space in between galaxies in galaxy clusters is filled with hot plasma called the intracluster medium (ICM). This plasma emits in X-ray and radio wavelengths.

The acceleration of cosmic-ray electrons in magnetic fields with strengths of microGauss produces Mpc–sized structures of diffuse radio emission in the ICM typically grouped into two categories: radio haloes and radio relics. The particle acceleration mechanisms leading to this large–scale emission is not fully understood.

In this doctoral thesis I have focused on studying the role of magnetic fields in galaxy clusters. My motivation was to answer the following questions: 1) What are the magnetic amplification mechanisms that lead to today's observables?, 2) What is the role of galaxy cluster mergers in shaping magnetic fields?, 3) What defines the substructure in the synchrotron and polarised emission in radio relics?. To this end, I have used results from the cosmological MHD code ENZO, the MHD code FLASH and the hybrid MHD-Lagrangian PLUTO code.

I have studied a primordial scenario along with a small–scale dynamo amplification in simulated galaxy clusters tackling questions 1) and 2). I have found that such scenario can reproduce cluster magnetic fields of the order of microGauss. Major and minor mergers are sources of both compression and turbulence and therefore play a key role in the magnetic amplification. In particular, they introduce multiple turbulence cascades that affect the growth of an existing small-scale dynamo. I found that major mergers can delay the dynamo amplification for a period of 1 Gyr.

I have studied the diffusive shock acceleration (DSA) mechanism to simulate the radio and polarised emission observed in radio relics tackling question 3). I have found that turbulence has a significant impact on the morphology of synchrotron and polarised emission. The observed discrepancy between the Mach number of shocks derived from X-ray and from radio spectra is explained in this framework. Some observed radio relics exhibit a gradient of polarisation fraction which is higher at the shock front and lower at the downstream regions contrary to theoretical expectations. I find that turbulence may be able to explain this gradient.

Eidesstattliche Versicherung

Hiermit versichere ich an Eides statt, die vorliegende Dissertationsschrift selbst verfasst und keine anderen als die angegebenen Hilfsmittel und Quellen benutzt zu haben.

Die eingereichte schriftliche Fassung entspricht der auf dem elektronischen Speichermedium.

Die Dissertation wurde in der vorgelegten oder einer ähnlichen Form nicht schon einmal in einem früheren Promotionsverfahren angenommen oder als ungenügend beurteilt.

Paola Domínguez Fernández
Hamburg, den 09.11.2020

Contents

Chapter 1

Introduction

1.1 Galaxy clusters

Galaxy clusters are the largest gravitationally bound systems in the Universe. They consist of hundreds to thousands of galaxy members with masses ranging from 10^{14}–$10^{15}\,\mathrm{M_\odot}$ within a sphere of typical diameter $\sim$2–5 Mpc. Their composition is dominated by a dark matter component ($\sim$80–85%), followed by a baryonic component consisting of hot diffuse intracluster plasma ($\sim$15–20%) with temperatures in the range of 10^7–10^8 K, and a small fraction of stars, dust, and cold gas (amounting altogether to $\sim 1\%$), mostly located within galaxies. Indeed, the sum of the masses of single galaxies amounts to only $\sim 10^{13}\,\mathrm{M_\odot}$ which is much smaller than the total cluster mass.

In our current vision of structure formation, galaxy clusters are thought to form via a hierarchical sequence of mergers and accretion of smaller systems driven by gravity and Dark Matter that dominates the gravitational field (e.g. Kravtsov & Borgani, 2012). In major cluster mergers, sub-clusters collide at velocities of $\sim$2000 km/s. Such events are the most energetic events in the Universe since the Big Bang, releasing gravitational binding energies of as much as $\gtrsim 10^{64}$ ergs (e.g. Sarazin, 2001). Perhaps the best example of these energetic events to date is the *Bullet cluster* (see Fig. 1.1). The hot gas detected by Chandra in X-rays (pink) in Fig. 1.1 shows most of the baryonic matter in the two clusters, while the dark matter component (blue) was determined by weak gravitational lensing. In particular, the offset of matter distributions proves the existence of Dark Matter. A collisionless type of matter interacting only via gravity explains well why the hot gas in each cluster slows down and lags behind the matter distribution inferred by gravitational lensing. Additionally, these events give us an insight into the formation of clusters of galaxies.

From the largest scales, galaxy clusters are a fundamental part of the so-called
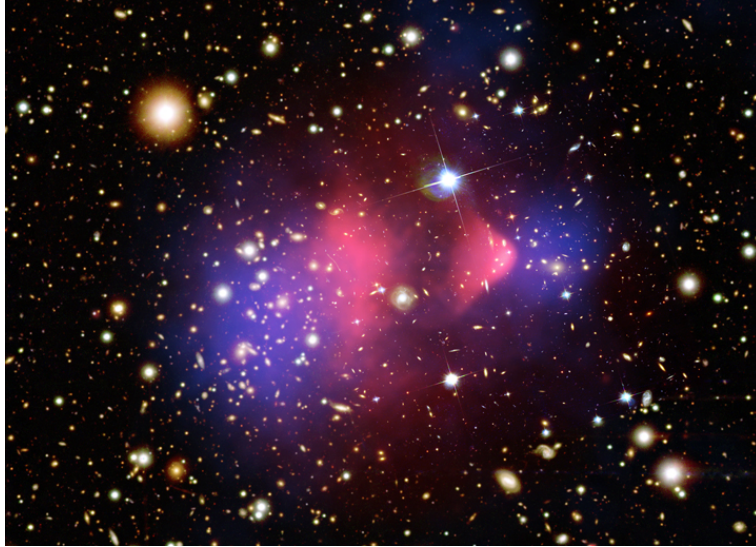
Figure 1.1: Composite image of the galaxy cluster 1E 0657-56, also known as the *Bullet cluster*. Optical (orange and white), X-ray (pink) and lensing map (blue).
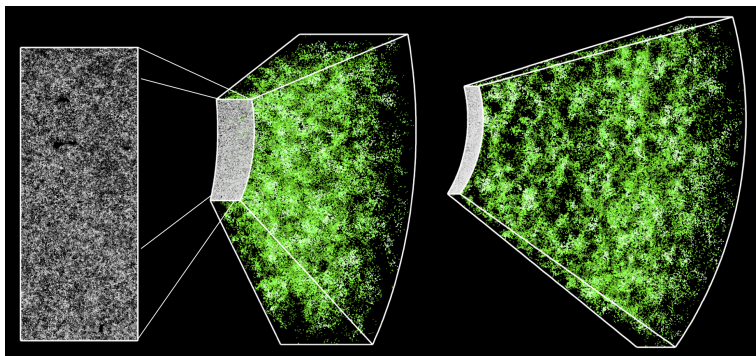
Figure 1.2: Section of the 3D map constructed by BOSS. The rectangle on the left shows a cut-out of 1000 sq. degrees in the sky containing nearly 120,000 galaxies, or roughly 10% of the total survey. The spectroscopic measurements of each galaxy transform the 2D picture into a 3D map.

cosmic web (e.g. Bond et al., 1996; de Lapparent et al., 1986). This web represents the fundamental three-dimensional organization of baryonic (galaxies and intergalactic gas) and dark matter on Mpc scales. The patterns contained here can be classified as dense compact galaxy clusters, long elongated filaments of galaxies, and sheet-like tenuous walls surrounding near-empty void regions, all together resembling a spider web-like structure (see Bond et al., 1996). All these web-like patterns can be observed for example in the spatial distribution of galaxies. In Fig. 1.2 one can observe a 3D reconstruction of a cut-out of 1000 sq. degrees in the sky containing nearly 120,000 galaxies as measured by the SDSS-III's Baryon Oscillation Spectroscopic Survey (BOSS) (e.g. Dawson et al., 2013). The galaxy distribution is not uniform and galaxies are preferentially separated by a characteristic distance defined by acoustic density waves in the primordial plasma of the early universe. These waves that imprinted fluctuations on the distribution of mass and radiation are referred to as baryon acoustic oscillations (BAO) and they give us information on how our Universe has evolved. On the other hand, cosmological N-body simulations (e.g. Bond et al., 1996; Springel et al., 2005; Vogelsberger et al., 2014; Schaye et al., 2015) also predict these web-like patterns and they have been our main theoretical tool to study the cosmic web. In Fig. 1.3, one can observe for example the large-scale structure obtained through the Millennium simulation compared to subregions of the 2-degree Field Galaxy Redshift Survey (2dFGRS) (e.g. Colless et al., 2001), the Sloan Digital Sky Survey (SDSS) (e.g. York et al., 2000), and the Center for Astrophysics (CfA) galaxy redshift survey (e.g. Huchra et al., 1990). The resemblance between simulations and observations illustrates how well our current standard cosmological model, with a Universe dominated by dark matter and dark energy, can fit structure that we observe in the nearby Universe (e.g. Springel et al., 2006).

Some of the main characteristics of the cosmic web components are (see Zhu & Feng (2017) and references therein):

Galaxy clusters: generally located at the intersection of filaments (nodes) as well as found along filaments (knots), typical sizes of $\sim$2–5 Mpc, they become a significant component of the web only at $z < 0.5$ and contain $\sim$12–16 % of the cosmic mass.

Filaments: most prominent structures of the web, sizes in the range of 10–100 Mpc and contain up to 50% of the cosmic mass from $z = 2$. They are hosts of the warm and hot intergalactic medium (WHIM).

Voids: sizes in the range of 20–50 h^{-1} Mpc, they usually have a roundish shape and occupy the greater extent of space in the Universe. They contain 10–15% of the cosmic mass.

3
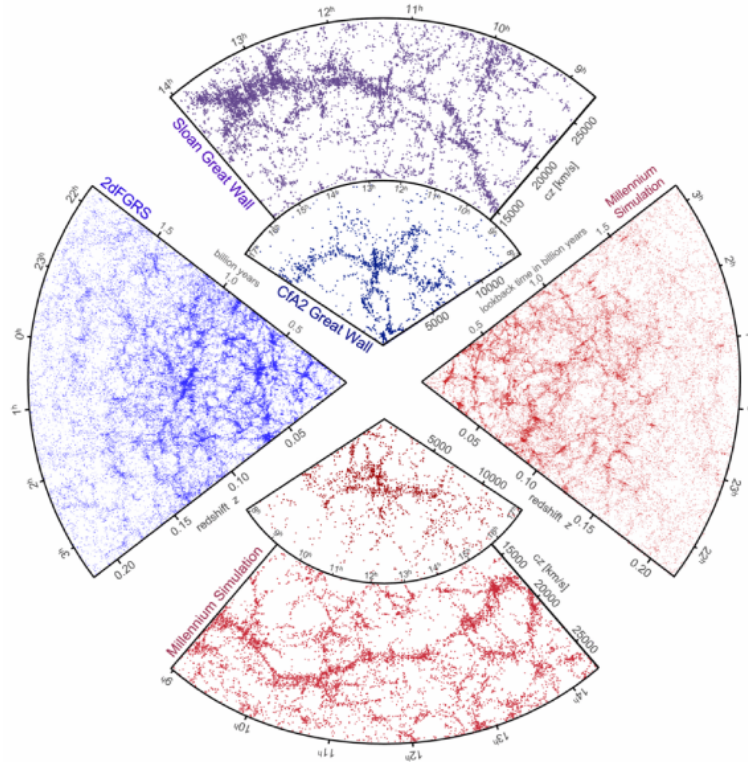
Figure 1.3: The galaxy distribution obtained from spectroscopic redshift surveys and from mock catalogues constructed from cosmological simulations. *Top*: The the CfA2 "Great Wall" and the SDSS "Sloan Great Wall". *Left*: One-half of the 2dFGRS (distances in the southern sky out to a depth of 2 billion light years). *Bottom and right*: Mock galaxy surveys constructed using the "Millennium" simulation and selected with matching survey geometries and magnitude limits.
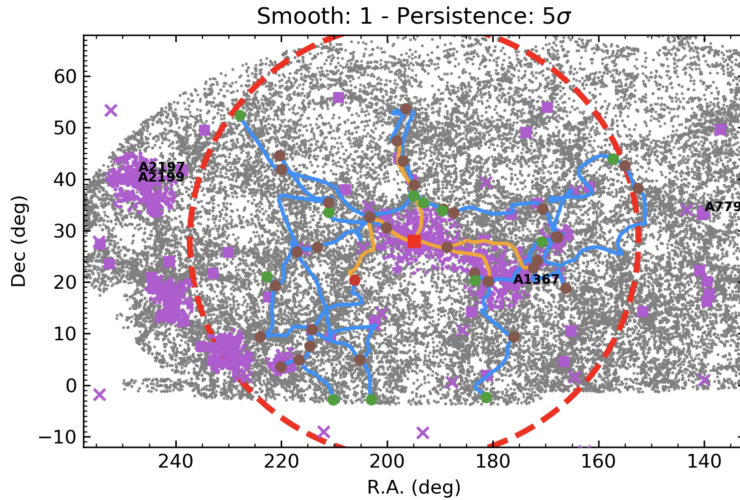
Figure 1.4: Map of the filaments connected directly to the Coma cluster in a ±75 Mpc redshift slice centred on Coma (red square). Small grey points represent the galaxies from the Main Galaxy Sample (MGS). Cyan lines represent filaments connecting critical points as detected by Discrete Persistent Structure Extractor (DisPerSE). Orange lines are first and second generation filaments. Purple crosses are Meta-Catalogue of X-ray detected Clusters of galaxies (MCXC) clusters. IMAGE CREDIT: Malavasi et al. (2020)

In this panorama, galaxy clusters occupy unique places at the intersection of filaments (e.g. Aragón-Calvo et al., 2010; Cautun et al., 2014; Malavasi et al., 2017), and it is due to the latter that matter flows into galaxy clusters and shapes them. For example, the number of filaments connected to galaxy clusters scales with the cluster's mass (e.g. Sarron et al., 2018; Darragh Ford et al., 2019). In Malavasi et al. (2020), the Coma cluster has been studied and all the filaments connected to it up to a ∼ 75 Mpc radius from its position have been identified (see Fig. 1.4). Their results on connectivity seem to be in agreement to those coming from simulations. Indeed, in N-body simulations, clusters are always connected to several filamentary structures and one can measure their connectivity and mass fairly easily (see Aragón-Calvo et al. 2010). Therefore, such measurements are really good tests for theoretical models of large-scale structure (LSS) formation (see e.g. Colombi et al. 2000; Codis et al. 2018 and references therein). Nevertheless, this is certainly not an easy task as several catalogues are needed, in addition of Sunyaev-Zel'dovich (SZ) measurements for the confirmation of filament detection.

Cluster studies also test the current standard cosmological model in a much more powerful way. For example, the measurements of galaxy clusters' masses can

constrain the cosmological parameters associated to it. These studies are consistent with other observations that find that we live in an expanding flat universe dominated by dark energy (73%), with sub-dominant dark matter (23%), and a small amount of baryonic matter (4.6%) (e.g. Komatsu et al., 2011). In a nutshell, astronomers infer cluster masses at different epochs through different techniques and then this information can be used to constrain the evolution of the *cluster mass function*. The cluster mass function, $n_M(M)$, gives the number density of clusters with mass greater than M in a comoving volume element. One can write $n_M(M)$ in terms of the cosmological parameters via a semi-analytical model, where one combines a spherical top-hat collapse with the growth function for linear perturbations (e.g. Press & Schechter, 1974; Bond et al., 1991; Bower, 1991; Lacey & Cole, 1993). This approach is more commonly known as the *Press-Schechter formalism* where the density perturbations are assumed to collapse and virialize once their density contrast $\delta = \delta\rho/\rho$ exceeds a critical threshold δ_c. The cluster mass function on scale M at redshift z is given by,

$$n_M(M, z) = \frac{\Omega_M \rho_{cr0}}{M} \text{erfc} \left[\frac{\delta_c}{\sqrt{2}\sigma(M, z)}, \right] \tag{1.1}$$

where $\rho_{cr0} = 3H_0^2/8\pi G$ is the current critical density, Ω_M is the matter density parameter and $\sigma^2(M, z)$ is the density perturbations variance on a mass scale M as a function of z. It is more common to find the mass function expressed in a differential form,

$$\frac{dn_M}{d\ln \sigma^{-1}} = \sqrt{\frac{2}{\pi}} \frac{\Omega_M \rho_{cr0}}{M} \frac{\delta_c}{\sigma} \exp \left[-\frac{\delta_c^2}{2\sigma^2} \right]. \tag{1.2}$$

Eq. (1.2) is the pioneer result, but one can also work out the mass function when the perturbation collapse is ellipsoidal (e.g. Sheth & Tormen, 1999; Sheth et al., 2001) or use the well-tested fitting formula provided by (e.g. Jenkins et al., 2001), where different cosmologies have been tested. One can observe that Eq. (1.2) is highly sensitive to the cosmological model because the matter density controls the rate at which structure grows. Moreover, if one divides the measurement of the mass function by $\Omega_M \rho_{cr0}$, then one can get an accurate measurement of the primordial power spectrum $\sigma(M)$. Hence, by constraining the cluster mass function one can constrain the cosmological model too. It is clear that the measurement of cluster masses is a crucial point here and as such, the mass function can be a very powerful cosmological probe. On the other hand, the measurement of cluster mass relies on different definitions that can be inconsistent and give rise to systematic errors that directly affect the cluster mass function. Doing this properly requires a consistent definition and a well-calibrated relation linking that mass to some observable. An

extensive review on how clusters of galaxies could be used as powerful cosmological probes is given in Voit (2005) or Allen et al. (2011).

The scientific contribution from LSS and galaxy clusters' evolution studies is in general a two-way process: studies on the LSS help us understand the origin of galaxy clusters and vice-versa, galaxy clusters' studies give us information on the cosmological model. Moreover, this two-way process requires cooperation between observers working with different wavebands, and theoreticians whose extensive numerical work links the cluster observables to the cosmological model of our universe.

But that is not the only relevance of galaxy clusters. A key aspect of their nature is the fact that they offer multiple observable signals across the electromagnetic spectrum (e.g. Sarazin, 1988), which is a direct consequence of the multiple processes happening within them. They offer information from the largest to smallest scales and coming from different wavebands: the *optical* and *near-infrared* band is dominated by the stellar emission coming from galaxies; the *X-ray* band dominated by thermal bremsstrahlung emission and line emission from ionized metals injected into the hot plasma by feedback processes; inverse Compton scattering of Cosmic Microwave Background (CMB) photons by the hot gas in the potential well of galaxy clusters, or what is called the *Sunyaev-Zel'dovich effect*, caused by thermal and bulk velocities of the electrons in the plasma produce two distinct spectral distortions to the CMB that can be separated from one another by multi-frequency observations at *millimeter* wavelengths; *gravitational lensing* offers a unique technique to infer the total matter distributions in clusters; and the *radio* band dominated by synchrotron emission from relativistic electrons spiraling into magnetic fields.

Many of the interesting physical processes and interactions already mentioned can be studied via the hot diluted magnetized plasma permeating galaxy clusters: the *intracluster medium* (ICM). The ICM is a key environment for studying fundamental processes in plasmas such as shocks and magnetic turbulence. Its description involves highly diverse physical phenomena and for this reason, we give an overview of it in the next section.

1.2 The intracluster medium

The ICM is a hot ($\sim 10^7$–10^8 K i.e. particle energies $k_B T \gtrsim 1$ keV), diffuse, ionized, magnetised ($\sim \mu$G), stratified, high-β[1] (~ 100), very weakly collisional plasma that constitutes $\sim 10\%$ of a galaxy cluster's mass.

The ICM was discovered first by early X-ray observations of galaxy clusters (e.g.

---

[1]where $\beta = 8\pi P/B^2$ is the ratio of plasma pressure, P, to the magnetic pressure (usually referred to as *beta plasma*)

Cavaliere et al., 1971; Meekins et al., 1971; Kellogg et al., 1972; Forman et al., 1972).
It has electron densities of $n_e \sim 10^{-4}$–$10^{-2}\,\mathrm{cm}^{-3}$ and it consists of fully ionized hydrogen and helium with a small percentage of highly ionized heavy elements (e.g. Sarazin, 1988; Borgani et al., 2008). Studies on X-ray spectra show that the abundance of heavy elements in the ICM is nearly $\simeq 1/3$ solar (e.g. Edge & Stewart, 1991; Mantz et al., 2017).

The ICM also contains magnetic fields with strengths of $\sim \mu\mathrm{G}$ on kpc-scales. The first attempt to measure cluster magnetic fields was done shortly after the ICM was discovered in X-rays (e.g. Jaffe, 1977). The observed radio emission is due to relativistic cosmic-ray electrons gyrating in magnetic fields and it is exactly due to radio observations, that a new era of study of cosmic magnetic fields started (see e.g. the reviews by Carilli & Taylor 2002; Govoni & Feretti 2004; Ferrari et al. 2008; Feretti et al. 2012; van Weeren et al. 2019).

The ICM is mostly optically-thin, i.e. photons escape once they are emitted without being absorbed. This means that all the ions excited by collisions have sufficient time for radiative de-excitation before a second collision occurs due to the very low density of the plasma (see Boehringer & Werner, 2009). In fact, binary Coulomb collisions between charged particles play a vital role in transport, radiative, relaxation and dissipative processes in the ICM (e.g. Sarazin, 1988). For instance, the existence of thermal electrons undergoing Coulomb collisions in this optically thin medium give rise to thermal bremsstrahlung emission which is observed in the X-ray band with luminosities up to $\sim 10^{45}\,\mathrm{erg\ s}^{-1}$.

Binary collision processes can only be defined for weakly coupled plasmas (see Vogel, 2016). This means that the typical magnitude of the collision frequency is much smaller than the plasma frequency, $\nu_c \ll \omega_p$. Formally speaking, if a particle is electrostatically influenced by all of the other particles within its Debye sphere, but the overall interaction does not cause an abrupt change in the particle's motion, then the plasma is weakly coupled. This is quantified by the plasma parameter defined as:

$$\Lambda = 4\pi n \lambda_D^3 \propto \frac{T^{3/2}}{n^{1/2}}, \tag{1.3}$$

where λ_D is the Debye length. The hot and diffuse ICM satisfies that $\Lambda \gg 1$ and therefore, we define it as a *weakly collisional plasma*. The mean free path of electrons and ions with velocities $v_{th,i} = (k_B T_i/m_i)^{1/2}$ determined by Coulomb collisions in the absence of a magnetic field is estimated to be (e.g. Spitzer, 1956),

$$\lambda_C \sim 0.4\,\mathrm{kpc} \left(\frac{T_e}{10^8\,\mathrm{K}}\right)^2 \left(\frac{n}{0.1\mathrm{cm}^{-3}}\right)^{-1}. \tag{1.4}$$

where this scale can be inferred through X-ray observations. For example, Chandra

X-ray observations of the Virgo cluster have estimated a Coulomb mean free path of the order of ~ 1 kpc (e.g. Werner et al., 2015).

However, the above picture is dramatically changed if magnetic fields are present. Magnetic fields in weakly collisional plasmas are important since they affect transport processes. While they are energetically subdominant in the ICM, they are not a passive component and this makes the ICM one of the most interesting examples of a space plasma. In the presence of a magnetic field, the mean free path is estimated to be (see Riquelme et al. 2016),

$$\langle \lambda_e \rangle \sim 10 \,\mathrm{kpc} \left(\frac{f_M}{2} \right)^{-1} \left(\frac{\beta}{100} \right)^{-0.8} \left(\frac{T_e}{10^8 \,\mathrm{K}} \right)^{1/2} \left(\frac{q^{-1}}{10^8 \,\mathrm{year}} \right), \qquad (1.5)$$

where f_M quantifies the suppression of the thermal conductivity due to mirrors and q^{-1} quantifies the magnetic growth timescale. Comparing the lengths from Eqs. 1.4 and 1.5 to that of the electron ($\rho_e \sim 300$–4×10^4 km) or ion ($\rho_p \sim 10^4$–2×10^6 km) thermal gyroradius, we can see that the mean free path of charged particles can be twelve orders of magnitude larger than the gyroradius (e.g. Narayan & Medvedev, 2001). In such conditions, the electrons predominantly transfer heat along the magnetic field lines (e.g. Braginskii, 1965).

Moreover, the ICM is thought to be turbulent (e.g. Dolag et al., 2005; Vazza et al., 2009; Iapichino & Niemeyer, 2008; Ryu et al., 2008; Lau et al., 2009; Vazza et al., 2011a; Marinacci et al., 2015, and see also Section 1.6.2) and as such, the presence of the magnetic fields can also have a dynamical effect due to the action of the Lorentz force. Thus, the ICM cannot be entirely modelled and studied with hydrodynamics, but it requires magneto-hydrodynamics (e.g Schekochihin & Cowley, 2007).

1.3 Energy budget in the ICM

Galaxy clusters form via gravitational instabilities through mergers and accretion events. These events in turn create flows, shocks and turbulence which dissipates heat into the ICM. The way gravitational energy is transformed into kinetic, thermal, turbulent and magnetic energies remains unclear. Previous works have claimed that there is an energetic ordered hierarchy in which certain energy ratios remain unchanged throughout the cluster's formation (e.g. Miniati & Beresnyak, 2015). However, gravitation is not the only source of heating in the ICM. Supernovae (SNe) and active galactic nuclei (AGN) are another type of energy feedback.

The total *thermal energy* of the ICM amounts to up to 10^{64} erg in massive clusters at present time. Most of this energy content primarily comes from shock heating provided by shocks of cosmological scales travelling through the ICM with

velocities of $\gtrsim 10^3 km/s$ during merger events (see Quilis et al., 1998; Kang et al., 2005). Indeed, these highly energetic events lighten up the large scale structure in galaxy clusters emitting thermal X-ray radiation and diffuse radio emission. Miniati (2002) showed that shock's kinetic energy dissipated into thermal energy amounts to up to $\sim 45\%$ for strong shocks ($4 \lesssim M \lesssim 10$), while Ryu et al. (2003b) showed that it amounts to even $\sim 56\%$ for $M \gtrsim 10$ and that $2 \lesssim M \lesssim 4$ shocks are the most important regarding the shock's energy dissipation. Here the Mach number, M, is defined as the ratio of the shock's speed to the local sound speed (e.g. Landau & Lifshitz, 1987).

On the other hand, AGN feedback can also play a role in heating the ICM in some galaxy clusters. AGN produce strong outflows in the form of jets that inflate cavities or bubbles evacuating regions of the ICM and sometimes also shocks (e.g. Brüggen & Kaiser, 2002). These bubbles of varying diameter (few to hundreds of kpc) can rise out to larger cluster radii due to buoyancy and their lower density in comparison to the ICM. Subsequently, the bubbles are expected to mix and redistribute into the ICM. They have been observed in various clusters as deficits in the X-ray band, while having a radio emission counterpart (e.g. McNamara et al., 2001; Clarke et al., 2005; Wise et al., 2007; Mittal et al., 2009). The turbulence created in response to these events was studied for example in Brüggen et al. (2005a); Heinz et al. (2010), where they estimate that bubbles can generate turbulent velocities as high as ~ 500 km/s in clusters of galaxies. The relevance of the AGN heating mechanism comes from the fact that the energy transferred to the ICM can diminish the amount of cooling (e.g. Gaspari et al., 2012; Wittor & Gaspari, 2020), which could be an explanation for the so-called *cooling problem* (see the end of this Section).

SNe feedback has been also widely considered as a heating mechanism of the ICM. SN driven winds can inject energy into the ICM through SN explosions of type Ia and II (White, 1991; Loewenstein & Mushotzky, 1996). Observational support for this scenario comes from the abundance of heavy elements in the ICM (see Fukazawa et al., 2000; Matsumoto et al., 2000; Simionescu et al., 2019; Mernier et al., 2020b,a). The energy feedback due to SNe explosions is of the order of 10^{51} erg (e.g. Woosley & Weaver, 1986), but there are uncertainties in the exact efficiency of conversion of the SNe explosion energy into thermal energy (see Kravtsov & Yepes, 2000). Additionally, only a small fraction of SNe in galaxy clusters explode at $z \gtrsim 4$ and in general, they fall short of the energy injection required to explain observations. Therefore, this mechanism alone cannot account for all the heating in the ICM, but it can only add to the other heating mechanisms previously mentioned. What makes SNe heating attractive is that it may also influence the initial stages of the formation of cooling flows and therefore, may also help explaining the cooling problem (e.g. Brighenti & Mathews, 2003; Domainko et al., 2004).

All these events are highly important since apart from injecting thermal energy into the ICM, they also inject *non-thermal* energy (especially merger shocks). Therefore, while the X-ray emitting gas provides a greater part of the total pressure support, the rest of the pressure is provided by a component that is invisible in the X-ray band. The non-thermal energy comes in the form of:

i) turbulence,

ii) magnetic fields,

iii) cosmic rays (CRs).

Major mergers between massive subclusters are expected to channel 5–30% of the thermal energy into turbulent energy (see Cassano & Brunetti, 2005). This range percentage has been obtained through various observations (e.g. Churazov et al., 2008, 2012; de Plaa et al., 2012; Sanders & Fabian, 2013) and through numerical simulations (e.g. Dolag et al., 2005; Iapichino et al., 2011; Vazza et al., 2009, 2011a, 2012; Jones et al., 2011; Gaspari & Churazov, 2013) considering relaxed and merging clusters. Both reveal that mergers induce velocity turbulent motions in the ICM of the order of a few 100 km/s on corresponding scales of a few ~ 100 kpc. On the other hand, AGN outflows can also inject some turbulent energy into the innermost region of galaxy clusters. The typical velocity of turbulent motions injected by AGN is $\sim$100–300 km/s, that is, of the same order of the velocities induced by mergers (see Gaspari et al., 2013; Vazza et al., 2012). Once there exists turbulence in the ICM, its energy can be channeled into thermal energy again through turbulent dissipation and into magnetic energy.

The magnetic energy available in the ICM can then increase during these events mainly via adiabatic compression or via the turbulent motions. The magnetic energy in galaxy clusters is believed to amount to only $\sim$1–2% of the thermal energy, nevertheless this is enough to significantly influence the overall properties of the ICM. The existence of magnetic fields is tightly related to the last non-thermal energy component, namely CRs. Indeed, relativistic particles in the presence of magnetic fields give rise to the radio diffuse emission observed in galaxy clusters (e.g. Ferrari et al., 2008; Feretti et al., 2012).

The cosmological shock waves produced by major mergers also accelerate CRs since these shocks are not completely thermalized and therefore, a fraction of the shock's energy can be converted into CRs energy (e.g. Bykov et al., 2008; Dolag et al., 2008). The non-thermal CRs energy amounts to up to $\sim 50\%$ of the kinetic energy of $M \gtrsim 10$ shocks and $\lesssim 10\%$ for weaker shocks (see Ryu et al., 2003b). Nevertheless, the shock acceleration processes are different for protons and electrons and as such,
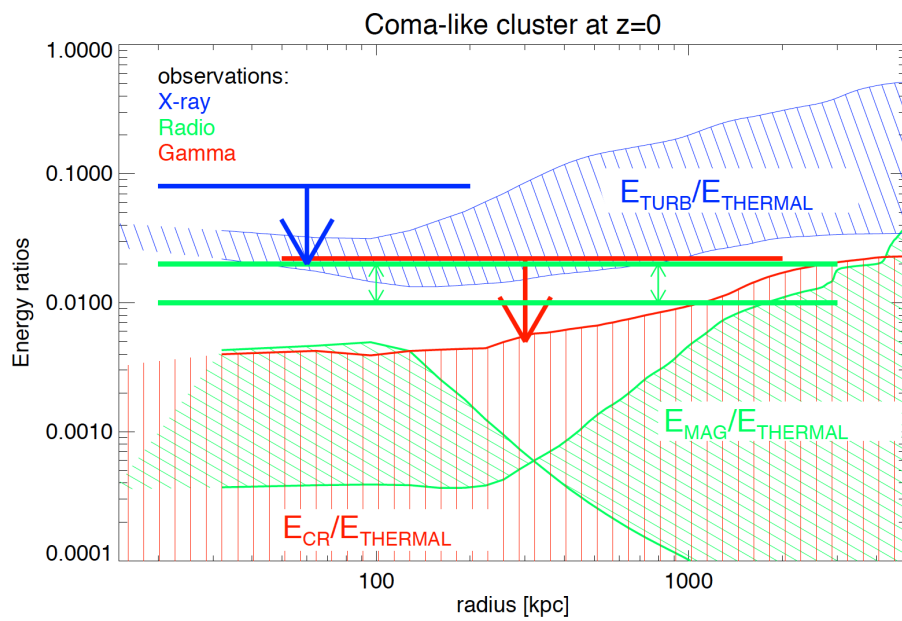
Figure 1.5: Radial profile of the ratios between non-thermal and thermal energies of the ICM for a simulated Coma-like galaxy cluster.

IMAGE CREDIT: Vazza et al. (2016)

their energies differ. The energy budget of CR protons (CRp) is inferred to be of the order of 1–2 % of thermal energy, while that of CR electrons (CRe) may contain less than 1% of thermal energy (e.g. Kang, 2007; Vazza et al., 2016).

Fig. 1.5 summarizes nicely the typical energy budget in the ICM. We can see the ratio of non-thermal to thermal energy in a simulated galaxy cluster as well as limits imposed by observations. We can see the non-thermal contribution coming from turbulence, magnetic fields and CRs that was discussed above. The observational limits (horizontal lines) come from X-ray fluctuations, Faraday rotation and non-detection of hadronic γ–ray emission, respectively (see Vazza et al. 2016 for further details and references therein). What is of relevance is the fact that the non-thermal energy (taking into account the three components), ranges from $\sim$3% of the thermal energy in the cluster's center to $\sim$40% of the thermal energy at the cluster's virial radius.

Another interesting point of CRs is their relation to γ–rays. We would expect CRp to exist and accumulate in galaxy clusters due to their long cooling time in the ICM of the order of a Hubble time (Völk et al., 1996; Ensslin et al., 1997). Additionally, multiple high-energy cluster events such as shocks, AGN outflows and SN-driven galactic winds should be injection sites for both CRe and CRp. Nevertheless, no γ–ray emission associated with the ICM has been detected so far (e.g. Reimer et al., 2003). In fact, there have only been γ–ray detections coming from radio galaxies within clusters (e.g. Strong & Bignami, 1983; Abdo et al., 2009b; Neronov et al., 2010). Up to now, we only count on upper limits of the γ-ray emission from galaxy clusters (Perkins et al., 2006; Aharonian et al., 2009; Ackermann et al., 2010, 2014, 2016) that also sets limits on the CRp to thermal pressure ratio within the virial radius to be below 1.2–1.4%. CRe are directly traced in the ICM through their observed radio synchrotron emission, but it is their origin that remains debatable. On one hand, *re-acceleration models* assume the existence of mildly relativistic seed electrons that may be re-accelerated by turbulence (e.g. Brunetti et al., 2001; Petrosian, 2001). On the other hand, *hadronic models* can explain the observed synchrotron and IC emission as well since elastic collisions of CRp (with energies of $\sim 10^{18}$–10^{19} eV) with other protons or atomic nuclei produce neutral and charged pi mesons (or pions π^0, π^+ and π^-), which decay into gamma rays and electrons/positrons, respectively (e.g. Blasi & Colafrancesco, 1999). Therefore, the potential detection of γ–ray emission in galaxy clusters is highly important and would shed light on the origin of the observed cluster radio emission (e.g. Brunetti et al., 2012).

As it can be seen, the non-thermal energy components are key ingredients for understanding clusters of galaxies. They give rise to a plasma out of equilibrium. In particular, the assumption of hydrostatic equilibrium will be violated and this

is shown for example in the deviation of the so-called cluster *scaling relations* (see Planelles et al. 2015 and references therein):

M-T relation: Under the assumption of spherical symmetry, the mass M of the cluster scales with the ICM temperature as $M \propto T^{3/2}E^{-1}(z)$, where $E(z) = H(z)/H_0$ is the time-dependent Hubble parameter normalized to the Hubble constant[2].

L_X-*T relation*: Using the relation above and the cooling function for the X-ray emission, one can derive that the X-ray luminosity scales with the temperature of the cluster as $L_X \propto T^2 E(z)$ (e.g. Arnaud & Evrard, 1999; Rosati et al., 2002).

σ_V-*T relation*: For a virialised galaxy cluster of total mass M we have $\sigma_v^2 \propto M^{2/3}$. Making use of the first scaling relation above, one can derive that the velocity dispersion scales with temperature as $\sigma_V \propto T^{1/2}$ (e.g. Wu et al., 1999).

Various observations deviate from these predictions mainly because the above scaling relations just take into account gravitational heating, hydrostatic equilibrium and spherical symmetry. The contribution from non-gravitational processes such as those described previously in this section, play a major role in explaining the observed deviations.

The cooling problem

About a third of all galaxy clusters exhibit X-ray emission peaked at their centers. These are regions where the gas loses most of its thermal energy into radiation and therefore, starts forming *cooling flows* (see Fabian 1994 for a review). This can be understood as follows: when the gas cools, the temperature drops and therefore, the gas density within the cooling region needs to increase in order to maintain pressure equilibrium. If these regions continued to cool down, we would expect to then see more star formation, which is at odds with what we observe in these type of clusters, namely, far less cold gas and young stars than predicted (e.g. Johnstone et al., 1987; Heckman et al., 1989; Crawford et al., 1999; McDonald et al., 2010; Hoffer et al., 2012; Molendi et al., 2016). This is the so-called *cooling problem*.

A cooling flow can be formed when the cooling time of the ICM, $t_{cool} \propto T^\delta/n$, is shorter than the lifetime of the galaxy cluster. The ICM density at some galaxy clusters' centers is high enough and the central temperature low enough that the cooling time is of the order of a few billion years, i.e $t_{cool} < H_0^{-1}$. These type of

---

[2]$E^2(z) = \Omega_M(1+z)^3 + \Omega_R(1+z)^4 + (1-\Omega_0)(1+z)^2 + \Omega_\Lambda$, where $\Omega_0 = \Omega_M + \Omega_R + \Omega_\Lambda$

galaxy clusters exhibiting a cool core of about 10% of their virial radius are called *cool clusters* (e.g. White et al., 1997; Hudson et al., 2010; McDonald et al., 2017).

1.4 X-ray emission

Galaxy clusters have deep gravitational potential wells that compress and heat the ICM to X-ray emitting temperatures. The X-ray spectrum gives us information about the ICM temperature, while the emission-line strengths of the same spectrum give us information about the abundance of elements like iron, oxygen, and silicon. It is through this emission, that galaxy clusters are considered the most luminous X-ray sources in the Universe (after quasars), with luminosities of the order of 10^{43}–$10^{45}erg/s$ ($\sim$2–10 keV). The X-ray emission can extend from $\sim$200 to $\sim$3000 kpc (e.g. Sarazin, 1986).

The observed X-ray emission in the ICM is primarily due to three processes depending on the collision (or close encounter) of an electron and an ion (see Kaastra et al., 2008; Boehringer & Werner, 2009):

  i) *Free-free or Bremsstrahlung radiation*: caused by free electrons scattering off ions without being captured.

 ii) *Free-bound or recombination radiation*: when a free electron is captured by an ion (radiative recombination). The energy of the emitted photon is at least the ionisation energy of the recombined ion (for recombination to the ground level) or the ionisation energy that corresponds to the excited state (for recombination to higher levels).

 ii) *Bound-bound or de-excitation radiation*: an electron moves between two bound states in an ion (two-photon decay).

The first two processes give rise to the X-ray continuum emission and the latter to the line emission. For energies $kT \gg 1$ keV, the Bremsstrahlung process dominates the emission, while for $kT \ll 0.1$ keV free-bound emission dominates. Meaning that, at characteristic ICM temperatures, continuum Bremsstrahlung is the dominant radiation process. This is illustrated in Fig. 1.6, where typical X-ray spectra at two different temperatures are shown and where brehmsstrahlung (blue lines) is dominant. The spectral emissivity for the thermal bremsstrahlung spectrum is given by (see Gronenschild & Mewe, 1978; Engel, 1979):

$$\varepsilon(\nu) = \frac{16e^2}{3m_e c^2} \left(\frac{2\pi}{3m_e k_B T_X} \right)^{1/2} n_e n_i Z^2 g_{ff}(Z, T_X, \nu) \exp\left(-\frac{h\nu}{k_B T_X} \right), \qquad (1.6)$$
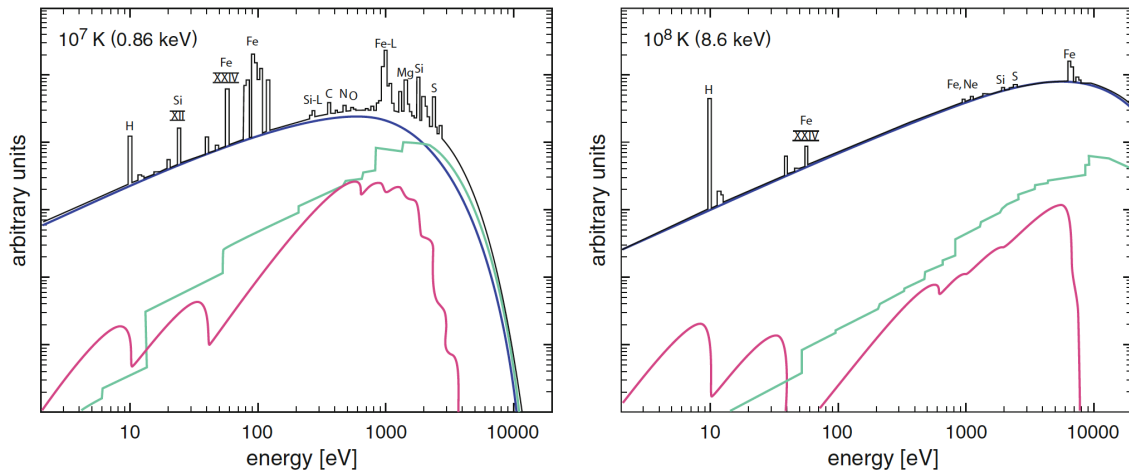
Figure 1.6: X-ray spectra for solar abundance at plasma temperatures of $T = 10^7$ K and $T = 10^8$ K. The continuum contributions from Bremsstrahlung (blue), recombination radiation (green), and de-excitation radiation (red) are indicated.

IMAGE CREDIT: Böhringer & Werner (2010)

where e is the electron charge, Z is the effective charge of the ion and g_{ff} is known as a *Gaunt factor*. One can see from Eq. (1.6), that an X-ray image of a cluster with $E < k_B T_X$ corresponds practically to a map of the gas density squared. The observed X-ray spectrum from a galaxy cluster provides an account of the entire ICM plasma since it has low densities. This means that the cluster X-ray spectrum is straightforward to interpret. Therefore, the main pieces of information extracted from the X-ray emission are the temperature, T_X, gas density and the chemical abundance.

One of the most important aspects of the X-ray emission is that it offers the possibility of indirectly measuring a cluster's mass. The easiest path is using the virial theorem where one finds the self-similar relation between cluster mass and ICM temperature, i.e. the M-T_X scaling relation (see previous Section 1.3). Nevertheless, galaxy clusters are not necessarily virialised and therefore, this method can only give a rough estimate of the mass. A second mass estimate relies on the assumptions of hydrostatic equilibrium and spherical symmetry. In this case, the mass distribution in the cluster is given by (combining the equation of hydrostatic support and mass conservation):

$$M_X(r) = -\frac{G k_B T_X}{\mu m_p} r \left(\frac{d \log n_g}{d \log r} + \frac{d \log T_X}{d \log r} \right), \tag{1.7}$$

16

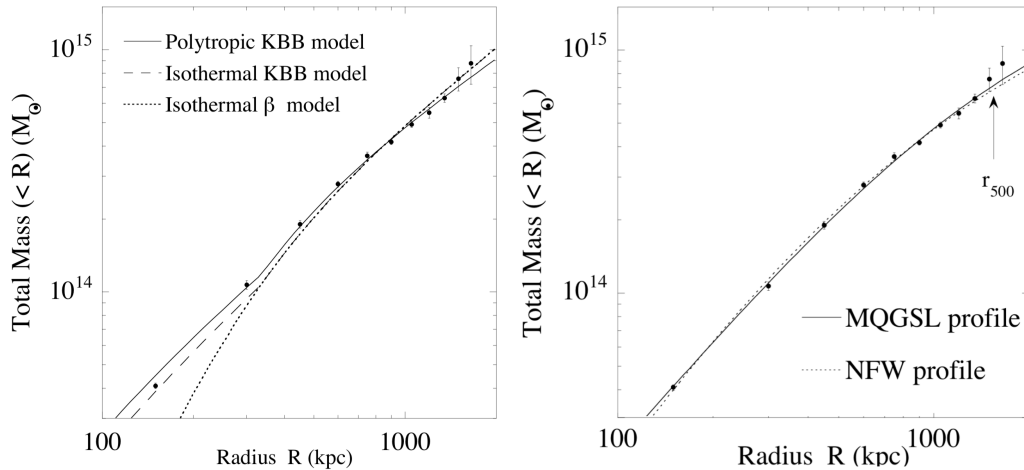Figure 1.7: The mass profile of A1413 derived from XMM- Newton surface brightness and temperature profiles. Left panel: mass profile derived from the hydrodynamic equilibrium equation and alternative modified β–models. Right panel: mass profile fitted with the NFW profile and Moore et al. 1999 profile.

IMAGE CREDIT: Pratt & Arnaud 2002

where G is the gravitational constant, μm_p is the mean molecular weight of the gas (with $\mu \sim 0.6$), m_p the mass of the proton, and n_g the gas density. The gas density can be assumed to be a model depending on the radial coordinate such as the *isothermal β–model*(e.g. Cavaliere & Fusco-Femiano, 1978):

$$ n_g(r) = n_{g,0} \left[1 + \left(\frac{r}{r_c}\right)^2\right]^{-3\beta/2}. \tag{1.8} $$

where $n_{g,0}$ is the central density normalisation, r_c indicates the fitted parameter referred to as the core radius and $\beta = \mu m_p \sigma_v^2 / k_B T_X$ with σ_v is the velocity dispersion. Using Eqs. (1.7) and (1.8) and the T_X measurement obtained from the spectrum, one can calculate the mass profile of a cluster using a Monte Carlo method and finding the best fit values. Nevertheless, the isothermal β–model is simplistic and it has been shown that it leads to a bias in deduced values of the mass of galaxy clusters (e.g. Hallman et al., 2007). Moreover, it is now well-established from XMM and Chandra data that the ICM is not isothermal (e.g. Pratt & Arnaud, 2002; Arnaud, 2009). In Fig. 1.7, we can observe an example of the mass profile obtained using this approach (i.e. considering the $d\log n_g / d\log r$ estimated) for a cluster. The isothermal β–model is compared to other two models and it can be seen that the former underestimates the mass at the center. On the right panel of Fig. 1.7, we can see the same example but considering the famous *NFW density profile* of dark

17
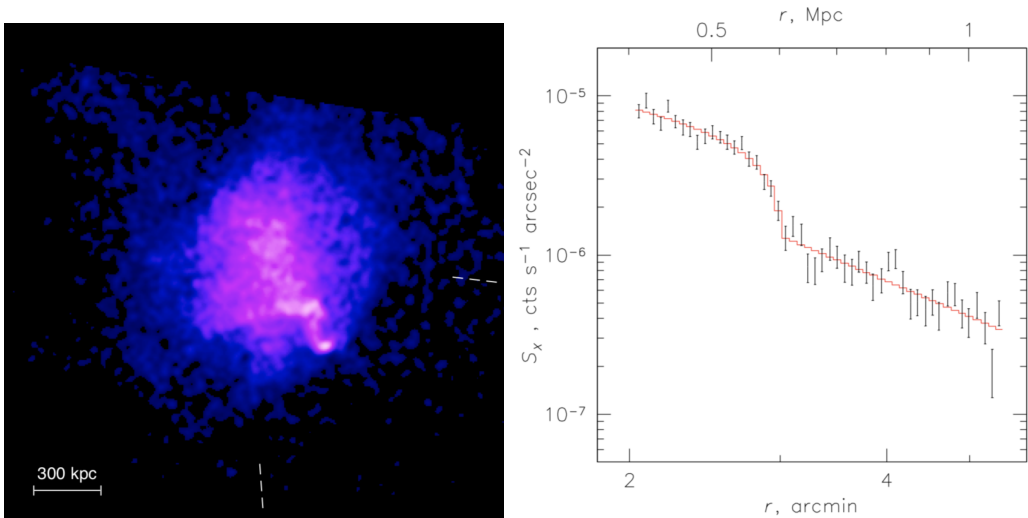
Figure 1.8: Shock front in A520. Left panel: Chandra X-ray image showing a bow shock (faint blue edge southwest). Right panel: X-ray brightness profile across the shock with best-fit model (red line).

matter halos obtained from N-body simulations (e.g. Navarro et al., 1997):

$$\rho(r) = \frac{\rho_c(z)\delta_c}{(r/r_s)(1 + r/r_s)^2}, \tag{1.9}$$

where the critical density at the observed redshift (for a matter dominated Universe $\Omega = 1$, $\Lambda = 0$) is

$$\rho_c(z) = \frac{3H_0^2}{8\pi G}(1 + z)^3, \tag{1.10}$$

and δ_c is a function of a concentration parameter, c:

$$\delta_c = \frac{200c^3}{3\left[\ln(1 + c) - c/(1 + c)\right]}, \tag{1.11}$$

and r_s is a parameter radius such that the radius corresponding to a density contrast of 200 is $r_{200} = cr_s$. The integrated mass of the NFW profile is used for fitting the X-ray data. There has been progress in this direction by introducing new empirical parametric models (e.g. Vikhlinin et al., 2006), as well as new deprojection methods (e.g. Croston et al., 2006).

Gravitational lensing is considered to be a much more powerful tool for the total mass estimates of galaxy clusters, nevertheless some studies comparing X-ray and lensing analyses found that the X-ray mass determination has a smaller

individual uncertainty (e.g. Zhang et al., 2008; Mahdavi et al., 2008). Therefore, the X-ray information of the ICM is highly important for mass estimates and, by extension, for determining the cosmological parameters, as was previously discussed in Chapter 1.1.

The observed X-ray emission is also useful for giving us insights about two non-thermal phenomena in the ICM: shocks and turbulence. An example of a detected shock front in a cluster is given in Fig. 1.8, where one can see a sharp discontinuity in the X-ray brightness profile at the position of the shock. The jump is usually also detected in the temperature profile and with this information observers can estimate the Mach number and velocity of the shock. A common way to determine the Mach number is by fitting the X-ray brightness profile with a model with an abrupt spherical density jump (see red line in right panel of Fig. 1.8) and then making use of the Rankine-Hugoniot jump conditions (e.g. Landau & Lifshitz, 1987). In particular, making use of the density jump condition,

$$\mathcal{M} = \left(\frac{2r}{\gamma_0 + 1 - r(\gamma_0 - 1)} \right)^{1/2}, \tag{1.12}$$

where r is the shock compression ratio defined as the ratio of the upstream (pre-shock) and downstream (post-shock) densities and γ_0 is the adiabatic index of the equation of state (EOS). Independently, $\mathcal{M}$ can be derived using the temperature profile and the corresponding temperature jump condition:

$$\frac{T_2}{T_1} = \frac{5\mathcal{M}^4 + 14\mathcal{M}^2 - 3}{16\mathcal{M}^2}, \tag{1.13}$$

where the subindices 1 and 2 indicate the upstream (pre-shock) and downstream (post-shock) temperatures. Both of these methods are usually consistent in the resulting Mach number (e.g. Markevitch et al., 2005; Markevitch, 2006). As we mentioned in Section 1.3, merger events induce large-scale shocks that can accelerate ultra-relativistic particles. Therefore, it is important to mention that this leads to emission in the radio (see Section 1.5) and also hard X-ray band (see Rephaeli et al. 2008 for a review). Indeed, the same relativistic electrons responsible for the radio emission could also produce hard X-ray emission ($\sim$10–80 keV) by the inverse Compton (IC) scattering of CMB photons (e.g. Blumenthal & Gould, 1970). This already non-thermal emission (energies larger than 10 keV) occurs at the thermal bremsstrahlung exponentially cut-off (see Eq. (1.6)) and has been claimed to be detected only in a few clusters (e.g. Fusco-Femiano et al., 2005; Rephaeli & Gruber, 2002). Nevertheless, neither the X-ray analysis nor a stacking analysis of other cluster samples reveal a non-thermal component (e.g. Nevalainen et al., 2004; Ajello

et al., 2009). Therefore, more data from highly sensitive X-ray satellites is needed to give a solid confirmation of the non-thermal X-ray's component in galaxy clusters.

The X-ray emission is also a powerful tool for studying cold fronts (see a review in Markevitch & Vikhlinin 2007 and references therein) and instabilities such as the *Kelvin-Helmholtz instability* (e.g. Vikhlinin et al., 2001) or the *Rayleigh-Taylor instability* (e.g. Brüggen, 2003; Pizzolato & Soker, 2006).

Finally, the X-ray data has also given us insight into the existence of turbulence in the ICM. The Hitomi X-ray spectrometer was the first instrument to resolve the emission lines of the X-ray spectrum and their Doppler shifts and broadening in the Perseus cluster (see Hitomi Collaboration et al., 2018). By best-fitting the S Lyα, Fe Lyα, Fe Heα and Fe Heβ spectral lines, the Hitomi collaboration found LOS velocity dispersions of the order of $\sigma_v \sim$ 100–200 km/s and bulk velocities of $v_{bulk} \sim$ 50–100 km/s. They also showed that the turbulence in the core of the Perseus cluster is driven primarily on scales smaller than $\sim$100 kpc. Turbulence plays an important role in the non-thermal phenomena of the ICM and it is also relevant for the focus of this thesis. For this reason, we will discuss turbulence in more detail in Section 4.2.1.

1.5 Radio emission

The observed diffuse radio emission from galaxy clusters is synchrotron emission of a population of $\sim$GeV CRe and cluster magnetic fields on μG levels. Therefore, this radio emission provides a clear evidence that relativistic electrons and magnetic fields exist in the ICM (e.g. Giovannini & Feretti, 2002; Feretti et al., 2012). Its study is highly important since we get to know about the role of large scale magnetic fields and the acceleration processes of relativistic particles in the ICM.

One of the features of the synchrotron radiation is that it is beamed in the direction of motion of the electron. The angle between the velocity vector of the electron and the existent magnetic field is called *pitch angle*, θ_{vb}, and it defines the spiral path that the electron will follow as it moves along a magnetic field line. For example, a non-relativistic electron in a uniform magnetic field moves in a spiral path at a constant θ_{vb} and then its gyrofrequency is

$$\nu_g = \frac{eB}{2\pi m_e} = 2.8\,\text{MHz}\left(\frac{B}{G}\right). \tag{1.14}$$

Since the emission is beamed for both non-relativistic and relativistic electrons, not all the radiation is actually emitted at the gyrofrequency. There are Doppler and aberration effects that distort the observed angular distribution of the intensity,

resulting in a spread of emitted frequencies associated with different pitch angles. In fact, the radiation can be decomposed into a sum of equivalent dipoles radiating at Fourier harmonics of ν_g. When it comes to relativistic electrons, the higher harmonics become more important and the final result is that the emission lines become so broad so that the observed synchrotron emission spectrum is a smooth continuum. It can be shown that there is also a special frequency at which this continuum spectrum of a single electron peaks and it is called the *critical frequency*:

$$\nu_c = \frac{3}{2}\nu_g\gamma^2\sin\theta_{vb} \tag{1.15}$$

$$= 4.2\,\mathrm{MHz}\left(\frac{B}{G}\right)\gamma^2\sin\theta_{vb}, \tag{1.16}$$

where γ is the Lorentz factor of the electron[3]. The emission coming from the ICM in the radio band comes from electrons with $\sim$GeV energies ($\gamma \sim 10^4$) spiraling in $\sim \mu$G magnetic fields. The synchrotron power emitted or energy loss rate by a single relativistic electron is (e.g. Engel, 1979):

$$-\frac{dE}{dt} = 2\sigma_T c U_{mag}\gamma^2\sin^2\theta_{vb} \tag{1.17}$$

$$\simeq 1.6\times10^{-27}\left(\frac{B}{\mu G}\right)^2\gamma^2\sin^2\theta_{vb}\,\frac{erg}{s}, \tag{1.18}$$

where $E = \gamma m_e c^2$ and σ_T is the Thomson scattering cross-section. Nevertheless, in order to understand the observed radio emission, one has to take into account a population of relativistic electrons. The energy spectra of CRs can be usually approximated by a power-law. Thus, the number density of electrons in the energy interval E to $E + dE$ is

$$N(E)dE = C_0 E^{-p}dE, \tag{1.19}$$

where C_0 is a constant. In this way, the energy radiated in the frequency range ν to $\nu + \mathrm{d}\nu$ is

$$J(\nu)d\nu = \left(-\frac{dE}{dt}\right)N(E)dE. \tag{1.20}$$

A more detailed derivation of the synchrotron emissivity is given in Rybicki & Lightman (1979) and Ginzburg & Syrovatskii (1965) and we further discuss it in Chapter 4. Here we just mention that after the full analysis of Eq. (1.20), one obtains

---

[3]$\gamma = (1 - v^2/c^2)^{-1/2}$

the emissivity in terms of the magnetic field and frequency,

$$J(\nu) \propto B^{(p+1)/2}\nu^{-(p-1)/2}. \tag{1.21}$$

Therefore, the emitted spectrum can be expressed as a power law, $J(\nu) \propto \nu^{-\alpha}$, where α is called the *spectral index*. Observers usually use different observing frequencies in order to infer the spectral index of the emitted spectrum. This, in turn, gives us information on the type of observed source and on the radiative lifetime of the underlying population of electrons.

When one observes, one would only see a pulse of radiation every time the electron's velocity vector lies within an angle of $\pm 1/\gamma$ to the line of sight, which can be referred to as a *velocity cone*. Having a distribution of pitch angles, the observed intensity has contributions that are elliptically polarised in the opposite directions of the velocity cone. The emissivities of a single electron in the two polarisations are

$$J_\perp = \frac{\sqrt{3}e^3 B \sin\theta_{vb}}{16\pi^2\varepsilon_0 c m_e}\left[F(x) + G(x)\right], \tag{1.22}$$

$$J_\parallel = \frac{\sqrt{3}e^3 B \sin\theta_{vb}}{16\pi^2\varepsilon_0 c m_e}\left[F(x) - G(x)\right]. \tag{1.23}$$

where $F(x)$ and $G(x)$ are Bessel integral functions in term of $x = \nu/\nu_c$ (e.g. Engel, 1979). It is also useful to know the observed degree of polarization:

$$\Pi = \frac{I_\perp + I_\parallel}{I_\perp - I_\parallel}, \tag{1.24}$$

where the corresponding intensities are Eqs. (1.22) and (1.23) integrated over the variable x. In the case of a population of relativistic electrons, one has to consider an energy spectrum of the electrons as in Eq. (1.19) before integrating Eqs. (1.22) and (1.23) over x.

The origin of both non-thermal ingredients for the synchrotron emission in the ICM, namely magnetic fields and CRe, is still uncertain. Yet, diffuse radio emission (not related with galaxies) is observed in more than 80 galaxy clusters at various scales (from 100 kpc to Mpc scales) and at various cluster locations. CRe in the ICM have two main characteristics: 1) they are confined and accumulated inside galaxy clusters for about a Hubble time (e.g. Völk et al., 1996); 2) the estimated lifetime of these radio emitting electrons due to synchrotron and IC energy losses is

$$t_{age} \approx 3.2 \times 10^{10}\frac{B^{1/2}}{B^2 + B_{CMB}^2}\left[(1+z)\nu\right]^{-1/2}\text{yr}, \tag{1.25}$$

where $B_{CMB} \approx 3.5(1 + z)^2 \mu G$ and ν is the observing frequency in MHz. This means that the typical radiative lifetimes of electrons in the ICM are $t_{age} \lesssim 10^8$ yr (e.g. Brunetti & Jones, 2014), which is way shorter than t_{dyn}. Therefore, this population of electrons were either (re-)accelerated or produced *in-situ* (see Jaffe, 1977) in order to produce the observed Mpc-scale diffuse radio emission. The most common classification of the different diffuse sources is: *radio halos*, *radio relics* and *mini halos* (e.g. Feretti & Giovannini, 1996). In Fig. 1.9 we show an example of these three components and in the following Sections we will describe each of them.

As we saw in this Section, the energy spectra of CRe can be usually approximated by a power-law. There exist different models for the injection spectrum, all depending on the parametrisation of the contribution of the synchrotron energy losses. These models differ in the assumed timescales of the particle acceleration and the distribution of pitch-angles: The *Kardashev and Pacholczyk (KP) model* (Kardashev, 1962; Pacholczyk, 1970) describes a synchrotron spectrum from a single burst of acceleration where the pitch angle between the CRe and the magnetic field stays constant over time; the *Jaffe-Perola (JP) model* (see Jaffe & Perola, 1973) is similar to the KP model but it assumes that in a time scale shorter than the radiative, the pitch-angle distribution is rapidly isotropised, with individual electrons sampling all pitch angles. Here the energy losses are independent of the initial electron's pitch angle. More complex models exist where the injection lasts until present, i.e. the *continuous injection (CI) model* (see Pacholczyk, 1970), or where it lasts a finite time, i.e. the *Komissarov-Gubanov (KGJP/KGKP) model* (e.g. Komissarov & Gubanov, 1994).

There are several particle acceleration mechanisms in the ICM that could produce the synchrotron emitting CR electrons. Nevertheless, in the next Section I shall only describe one of them.

1.5.1   DSA mechanism (Fermi I)

The emission coming from the ICM is underlying the physics of this particular high–β plasma and as such, plasma physics also plays a vital role in understanding galaxy clusters. In this Section, I shall discuss the acceleration mechanism related to radio relics as it is what was used in one of my projects (see Chapter 4).

The basic idea behind *diffusive shock acceleration* (DSA) (see Bell, 1978; Drury, 1983; Blandford & Eichler, 1987; Jones & Ellison, 1991; Brunetti & Jones, 2014) is that the number of times a particle interacts with a shock can be considered a stochastic process which leads to an increase of the particle's energy (or acceleration). One of the nice things about DSA theory is that one can derive the key result through probabilistic assumptions (microscopic point of view) and also through solving a
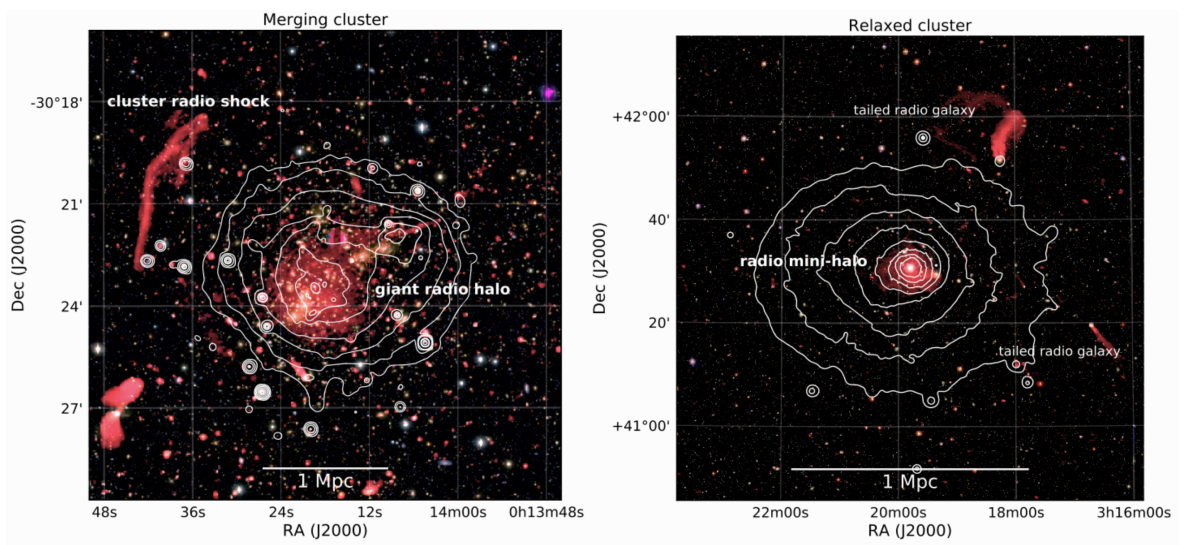
Figure 1.9: Left panel: VLA image of the merging galaxy cluster Abell 2744 with Chandra X-ray contours (white). This cluster hosts a luminous giant radio halo and a cluster radio relic. Right panel: VLA image of the relaxed cool core of Perseus cluster with XMM-Newton X-ray contours (white). This cluster hosts a radio mini-halo and two tailed radio galaxies.

dynamical equation (macroscopic point of view).

From Bell's point of view (Bell, 1978), one starts by taking the average increase in energy of a particle on crossing from the shock's upstream to the downstream. One can work out that the average gain in energy on crossing the shock is

$$\langle \frac{\Delta E}{E} \rangle = \frac{2}{3} \frac{U}{c}. \tag{1.26}$$

This process is classified as a *Fermi-I acceleration process* since the energy gain depends linearly on (U/c) (Fermi, 1954). By scattering in the downstream region, the particle's velocity vector is randomised without energy loss and it is then able to recross the shock, meaning that the particles gain energy from both forward and reverse shock crossings. This cycle can then be repeated k-times and naturally produces a power-law spectrum.

The basic formalism needed to describe the dynamics of CRs is contained in the diffusion-convection equation (also sometimes called CR transport equation):

$$\frac{\partial f}{\partial t} + (\mathbf{U} \cdot \nabla)f - \nabla \cdot \left[\hat{\mathbf{n}} \mathcal{D}_\parallel (\hat{\mathbf{n}} \cdot \nabla)f \right] = \frac{1}{3}(\nabla \cdot \mathbf{U}) p \frac{\partial f}{\partial p}, \tag{1.27}$$

where $f(p, t)$ is the pitch angle averaged distribution function of CR particles, $\mathbf{U}$ is the velocity of the local medium under consideration and $\mathcal{D}_\parallel$ is the particle diffusion coefficient (see Blandford & Eichler, 1987),

$$\mathcal{D}_\parallel = \langle \frac{1}{2}(1 - \mu^2) \frac{v^2}{\nu} \rangle_\mu, \tag{1.28}$$

where $\langle \rangle_\mu$ denotes an average over $\mu = \cos\theta$, θ is the pitch angle and ν is a pitch angle diffusion coefficient.

The solution of Eq. (1.27) for a discontinuous velocity profile (a shock) is called *the test particle approximation*. In particular, for high energy particles, Eq. (1.27) can be reduced to

$$v \frac{\partial f}{\partial x} = \frac{\partial}{\partial p} \mathcal{D} \frac{\partial f}{\partial x}, \tag{1.29}$$

where $\mathcal{D}$ is a spatial diffusion coefficient normal to the shock front. Considering that the flux of particles across the shock front is continuous, one can find that the general solution of Eq. (1.29) simplifies to

$$f_2(p) = \frac{1}{4\pi p^2} \frac{dN}{dp} \propto p^{-3r/(r-1)}, \tag{1.30}$$

where f_2 is the transmitted distribution function (downstream of the shock), $N(x, p) = \int_p^\infty 4\pi p'^2 f(p')dp'$ is the number density of particles and $r = U_1/U_2 = \rho_2/\rho_1$ is the shock compression ratio of the upstream (downstream) to downstream (upstream) densities (velocities)[4]. Therefore, f_2 is the expected distribution function of upstream particles advected into the shock and then accelerated through back and forth scattering. One can see that the power law's shape depends solely on the shock kinematics.

Astrophysical shocks are considered as *collisionless shocks*, i.e., shocks where the energy and momentum conversion is not mediated by inter-particle collisions, but rather by collective electromagnetic processes. The underlying magnetic field topology is likely to define the ability of a shock to accelerate CR particles. The angle of the upstream magnetic field with respect to the normal of the shock, θ_{bn}, classifies collisionless shocks as *quasi-parallel* ($\mathcal{Q}_\parallel$) and *quasi-perpendicular* ($\mathcal{Q}_\perp$) if $\theta_{bn} \leq 45°$ or $\theta_{bn} > 45°$, respectively. The thickness of the shock is of the order of the downstream (post-shock) thermal protons' (ions') gyro-radius, which means that the crossing particles need a momentum greater than a few times the thermal protons' (ions') momentum. Therefore, achieving the necessary energy in order to participate in the DSA process is more challenging for electrons and they firstly need to be pre-accelerated to supra-thermal momenta (e.g. Kang et al., 2002; Caprioli et al., 2015). Thanks to *particle-in-cell (PIC) hybrid simulations* (e.g. Guo et al., 2014; Caprioli & Spitkovsky, 2014a; Park et al., 2015; Caprioli & Spitkovsky, 2014b; Ryu et al., 2019; Kang et al., 2019) along with studies of high–β plasma (such as the ICM) collisionless shocks (e.g. Ha et al., 2018; Kang et al., 2019), the modern picture of the DSA process is that it operates differently in the ICM for CRe and CRp:

  i) *CRe*: accelerated preferentially at $\mathcal{Q}_\perp$ shocks with sonic Mach number $\mathcal{M}_s \gtrsim 2.3$ (e.g. Kang et al., 2019). In order for them to be injected into DSA, they may be initially and mainly accelerated by *shock-drift acceleration* (SDA; Matsukiyo et al. 2011). On the other hand, strong shocks can efficiently accelerate electrons to dowsntream power-law spectra which is consistent with DSA (Xu et al., 2020).

  ii) *CRp*: accelerated preferentially at $\mathcal{Q}_\parallel$ shocks with sonic Mach number $\mathcal{M}_s \gtrsim 2.25$ (e.g. Ha et al., 2018). Before they are injected into DSA, overshoot-undershoot oscillations have to develop in the shock transition, for which the incoming protons (ions) are reflected at the shock.

The appealing part of DSA theory is that it only depends on r and θ_{bn} and it should in principle operate at all types of astrophysical shocks. In particular, it

---

[4]r can be related to the shock's Mach number as described in Chapter 4

is the current interpretation of radio relics (see Section 1.5). Nevertheless, in the case of radio relics, a pure assumption of DSA fails to reproduce the levels of radio emission observed because one would require large electron acceleration efficiencies. As was mentioned in Section 1.5, a pre-existing population of CRe at the position of the relic that will be re-accelerated via DSA has been proposed to solve this problem (see a review in Botteon et al. 2020).

1.5.2 Radio halos

Radio halos are extended diffuse sources ($\sim$0.5–2 Mpc) permeating the central volume of clusters with typical radio powers at 1.4 GHz ranging from $10^{23}\,\mathrm{W\,Hz^{-1}}$ (e.g. Cuciti et al., 2018) to $10^{26}\,\mathrm{W\,Hz^{-1}}$ (e.g. Bonafede et al., 2009a; van Weeren et al., 2009). That is, they have low surface brightness of the order of $\sim \mu$Jy arcsec^{-2} at 1.4 GHz. They typically exhibit a fairly regular morphology that partially follows the distribution of the thermal ICM as detected in the X-ray band (e.g. Govoni et al., 2001; Feretti et al., 2001). This is seen in particular when comparing the radio power of clusters with the X-ray luminosity (e.g. Liang et al., 2000; Enßlin & Röttgering, 2002; Yuan et al., 2015). In the left panel of Fig. 1.10, we show an example of the observed correlation between the radio power at 1.4 GHz, $P_{1.4}$, and X-ray luminosity, L_X, for a sample of radio halo sources. As has been mentioned in Section 1.4, one can obtain an estimate of the cluster's mass through the X-ray luminosity and therefore, we can also study the relation between radio power and masses. An example of this type of study is shown in the right panel of Fig. 1.10.

Radio halos are usually found in massive merging galaxy clusters (e.g. Cassano et al., 2012; Kale et al., 2015; Cuciti et al., 2015). It has been shown (in the redshift range $0.08 < z < 0.33$) that radio halos are hosted in $\sim 60\%$–80% of clusters with masses of $M > 8 \times 10^{14}\,M_\odot$, while this fraction drops to $\sim$20%–30% for $M < 8 \times 10^{14}\,M_\odot$ (a mass limit derived in Cuciti et al. 2015).

Radio halos have integrated spectral indices of $-1.4 < \alpha_{int} < -1.1$[5] (e.g. Giovannini et al., 2009). Since the synchrotron emissivity is close to a power-law, observers use multiple frequencies (most frequently just two different frequencies) and make a fit in order to find out the value of the integrated spectral index α_{int}. However, steepening and deviations of a power-spectrum are interesting, since they give us a hint on the underlying mechanisms for the acceleration of the electrons (see Section 1.5.1 for a more detailed description on these mechanisms). In particular, steepening along with a cut-off in the radio halo spectral shape suggests that an in situ re-acceleration of relativistic electrons (*turbulent re-acceleration* or *primary*

---

[5]Note that there is a relation between the spectral index defined in Eq. (1.21) and the integrated one: $\alpha_{int} = \alpha + 1$. This will be also explained in Chapter 4
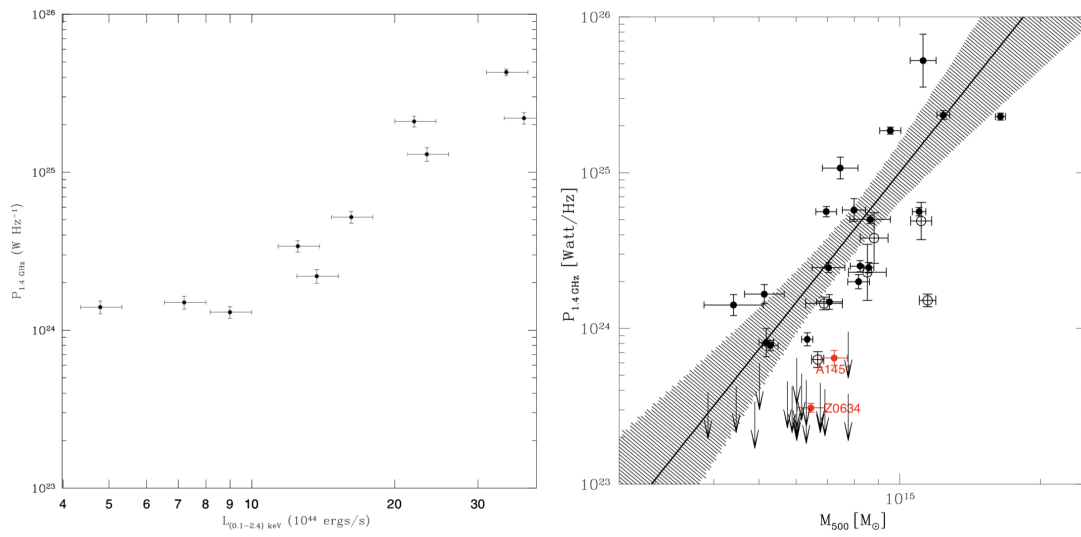
Figure 1.10: Left panel: $P_{1.4\,\mathrm{GHz}} - L_{0.1-2.4\,\mathrm{keV}}$ for various confirmed radio sources. Right panel: The $P_{1.4\,\mathrm{GHz}} - M_{500}$ diagram. The dots indicate giant radio halos (black filled), ultra steep spectrum radio halos (black empty) and underluminous halos (red filled). The black line corresponds to the best fit relation for giant radio halos. IMAGE

model) is a plausible mechanism explaining the radio halo emission (e.g. Brunetti et al., 2001, 2009). The generation of relativistic secondary electrons injected during proton-proton collisions (*hadronic* or *secondary model*) has also been proposed as a mechanism that could explain the radio emission in these sources (Blasi & Colafrancesco, 1999; Blasi et al., 2007; Enßlin et al., 2011). The potential detection of γ–rays would favor the hadronic model; nevertheless, the recent Fermi-LAT observations of the Coma cluster (e.g. Ackermann et al., 2016) and many other clusters rule out this model (e.g. Brunetti et al., 2017).

When radio halos have integrated spectral indices $\alpha_{int} \lesssim -1.6$ they are referred to as *ultra-steep spectrum radio halos* (USSRH) (e.g. Brunetti et al., 2008; Dallacasa et al., 2009; Macario et al., 2010; Wilber et al., 2018). These special type of radio halos are peculiar since they are more easily explained by a turbulent re-acceleration model than with a hadronic model (e.g. Brunetti, 2008). This has been previously concluded in some USSRH due to the very large population and energy budget of CRp necessary to predict the emission in the latter model (e.g. Macario et al., 2010). Further confirmation is needed, in particular coming from sensitive observations at low frequencies (few hundred MHz), since the latter model predicts a cutoff near energies of a few GeV (e.g. Cassano et al., 2006).

Finally, radio halos exhibit little to no polarized emission. However, this could be just a lack of sufficient sensitivity and resolution to solve the characteristic scale of the magnetic field in the radio halos. Indeed, we would expect that turbulence leads to a tangle magnetic field whose characteristic scale can potentially be smaller than the angular resolution of current radio interferometers (see discussion in Govoni et al. (2013) and van Weeren et al. (2019)).

1.5.3 Mini halos

Radio mini halos are diffuse radio sources with typical sizes of $\sim$100–500 kpc found in relaxed cool core clusters. The radio emission surrounds the radio-loud brightest cluster galaxy (BCG) on scales comparable to the cooling region (e.g. Feretti et al., 2012). These objects were originally thought to have their origin in the central AGN, nevertheless the observed radio emission is not connected with the BCG radio bubbles. Contrary to these radio bubbles, where X-ray cavities are found, mini halos exhibit mixed thermal and non-thermal components. This suggests that the radio emission coming from these sources is coming from the ICM (see Gitti 2015 and references therein).

Radio mini-halos have typical radio powers at 1.4 GHz ranging from 10^{23}–10^{25} WHz^{-1} (e.g. Gitti et al., 2006; Doria et al., 2012; Giacintucci et al., 2011, 2014, 2017; Giacintucci et al., 2019). Mini-halos are found in almost all cool cores as was

shown in Giacintucci et al. 2017. By analysing a sample of 58 clusters (using a mass cut of $M_{500} > 6 \times 10^{14} \, M_\odot$), they found that 80% of the massive cool-core clusters exhibit mini-halos, whereas none were found in non-cool-core clusters.

Radio mini halos have integrated spectral indices similar to giant radio halos and thus, their origin could also be explained by either the turbulent re-acceleration model or the hadronic model. The difference with respect to radio halos in the former model is that turbulence is believed to be produced due to sloshing, instead of major cluster merger events (e.g. Fujita et al., 2004; Keshet & Loeb, 2010; ZuHone et al., 2011; Vazza et al., 2012; ZuHone et al., 2013; Brunetti & Jones, 2014). The process of sloshing is a reference for the oscillatory motion produced when a small cluster or group passes by the cluster core leading to cold fronts with a spiral pattern. In this sloshing model, the central AGN could inject relativistic particles producing secondary CRe that then could be advected, streamed or diffused across the cluster core (e.g. Colafrancesco & Marchegiani, 2008). Nevertheless, the energy budget of CRs required to balance the cooling of the gas is larger than the current limits imposed by γ–rays (similar to the radio halos case) (e.g. Huber et al., 2013). This secondary model has also been studied numerically in ZuHone et al. 2015, where they found that secondary CRe in a sloshing cluster core can generate a similar diffuse synchrotron emission as mini halos but being more extended than what has been observed. The current γ-ray upper limits cannot put strong constraints on the origin of these type of radio sources yet. For example, Fermi–LAT does not yet have a good angular resolution at low energies (< 10 GeV) (see Abdo et al., 2009a). For the time being, spectral steepening and a spectral cut–off would help us to distinguish between the two proposed origin scenarios.

1.5.4   Radio relics (shocks)

Radio relic sources have typical sizes of ~ 0.5–2 Mpc and are most commonly located in cluster peripheral regions. Just like radio halos, they do not show an optical counterpart. The diffuse emission is observed as elongated structures (see left panel of Fig. 1.9) and exhibits high levels of polarisation[6] ($\gtrsim 20\%$ at $\gtrsim 1$ GHz frequencies), which suggests highly ordered magnetic fields at their outer edge (e.g. Ensslin et al., 1998). The typical radio powers at 1.4 GHz are in the range of ~ 0.2–17 10^{24} W Hz^{-1}.

The mechanisms responsible for these diffuse radio sources are not fully understood. However, due to the emission's location, shape and polarisation fraction, it seems clear that shocks generated during the assembly of galaxy clusters play a

---

[6]The reader may refer to Table 1 in Wittor et al. 2019 for a recent list of radio relics with available polarization data.
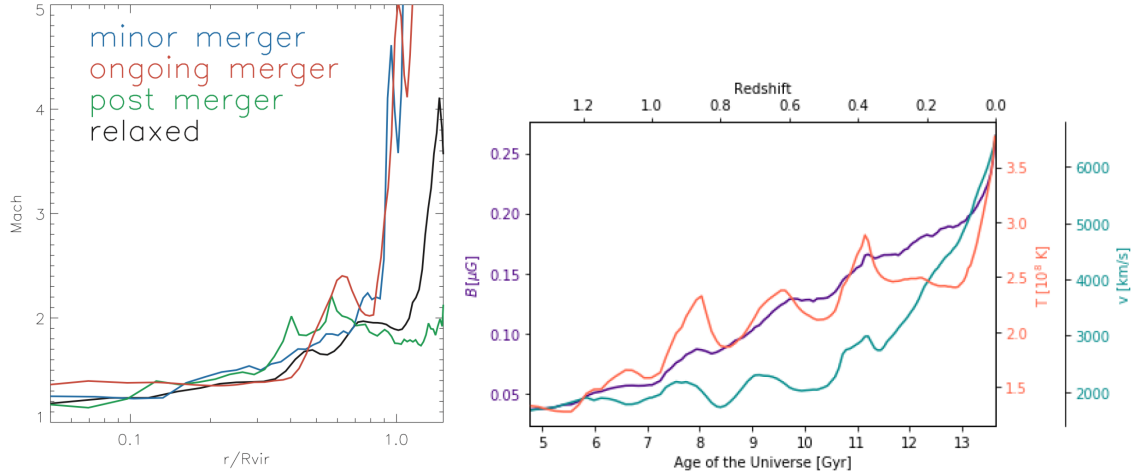
Figure 1.11: Left panel: Radial profile of the mean Mach number (volume averaged) of shocks for simulated galaxy clusters in different dynamical states. Right panel: Evolution of the average magnetic field strength, temperature and velocity for a simulated galaxy cluster classified as ongoing merger. Each peak corresponds to a merger event. IMAGE CREDIT: Vazza et al. 2009; Domínguez-Fernández et al. 2019

key role (see Bykov et al., 2019). The observational confirmation that this radio emission is tracing shocks comes from X-ray observations (e.g. Finoguenov et al., 2010). In this work for example, the authors detected an X-ray surface brightness discontinuity at the outer edge of the radio relic in Abell 3667. But more observations have followed where the location of radio relics coincides with the X-ray surface brightness discontinuity (see Table 2 in van Weeren et al. 2019).

These energetic large-scale shocks have typical Mach numbers $\mathcal{M} \sim$ 1.2–4.5 as inferred from either the X-ray or the radio emission (e.g. Markevitch et al., 1999, 2002; Belsole et al., 2004; Markevitch & Vikhlinin, 2007; Akamatsu et al., 2015; van Weeren et al., 2016; Botteon et al., 2016b; Urdampilleta et al., 2018; Rajpurohit et al., 2018; Botteon et al., 2020), and also have been studied with cosmological simulations (see left panel of Fig. 1.11). A merger timescale is of the same order of the mean lifetime of an ICM shock, i.e. $t_{dyn} \sim 1 \times 10^9$ yr (see right panel of Fig. 1.11[7]), and cosmological simulations show that plentiful shocks are produced as galaxy clusters are forming through various merger events (e.g. Ryu et al., 2003b; Pfrommer et al., 2006; Skillman et al., 2008; Hoeft et al., 2008; Vazza et al., 2009; Hong et al., 2015). There are two main subtle points in a framework where these shocks accelerate electrons (and protons): 1) the observations of radio relics, although

---

[7]Note that this figure shall be discussed in full detail in Chapter 3

now increasing in number ($\sim$60 known to date), are limited; 2) the radio emitting electrons originated at a source would not advect or diffuse in the ICM more than $\sim$100 kpc away from the shock surface before they radiate all their energy (e.g. Kang, 2011) and 3) if CRp are also accelerated at these locations, why do not we observe γ–ray emission?. Therefore, there are various unknowns regarding the particle acceleration mechanisms in the ICM with a rather low sample of observed relics (e.g. Vazza & Brüggen, 2014).

Radio relics may have they origin in fossil radio plasma that has been revived by a shock. Among the physical processes that have been proposed, the DSA theory (see Section 1.5.1) provides a plausible explanation for particles to be accelerated at the location of a merger or accretion shock. Indeed, in most cases cluster radio shocks are associated with DSA processes, yet observations where the X-ray shock front is co-spatially located with a radio relic are in conflict with this theory (e.g. Botteon et al., 2016a; Eckert et al., 2016; Hoang et al., 2017). In particular, if the electrons (and protons) from the thermal pool are accelerated through the DSA mechanism, large acceleration efficiencies are required to reproduce the observed radio emission (see Botteon et al. 2020 and references therein). Hence, it has been proposed that the electrons are pre-accelerated before they enter into the DSA mechanism (e.g. Kang et al., 2012; Pinzke et al., 2013). In particular, a pre-exiting population of electrons with the Lorentz factors of $\gamma_e \sim$ 1–100 (10–10^4) at strong (weak) shocks could be a possible solution.

The general idea behind the DSA mechanism is that particles are scattered several times between the upstream and downstream regions of the shock up until the point that many shock crossing cycles afford significant acceleration (e.g. Blandford & Eichler, 1987; Drury, 1983). In terms of the particle's energy spectrum, this would mean that the CRe would acquire an injection spectrum in the form of power law whose exponent depends on the shock's properties. Without any subsequent acceleration, the CRe will cool down mainly through synchrotron and IC energy losses causing that the spectrum acquires a curvature (it steepens) or what is simply called *spectral ageing* (see an example in Fig. 1.12).

In terms of the observed radio emission, we would then expect that the shock front tracks the freshly (re-)accelerated CRe and that the further we go into the downstream, the older the population of CRe. A common way to see the ageing is by using spectral index maps combining different observing frequencies. In Fig. 1.13, we show an example of these maps for two of the most studied radio relics. The *Sausage relic*, which is located in cluster CIZA J2242.8+5301, and is $\sim$ 2 Mpc long and $\sim$50 kpc wide, shows this steepening where the spectral index values range between $\sim$–0.8 (flat) to $\sim$–1.7 (steep), across its width (e.g. Di Gennaro et al., 2018). The *Toothbrush relic*, located in the merging cluster 1RXS J0603.3+42141RXS, is $\sim$
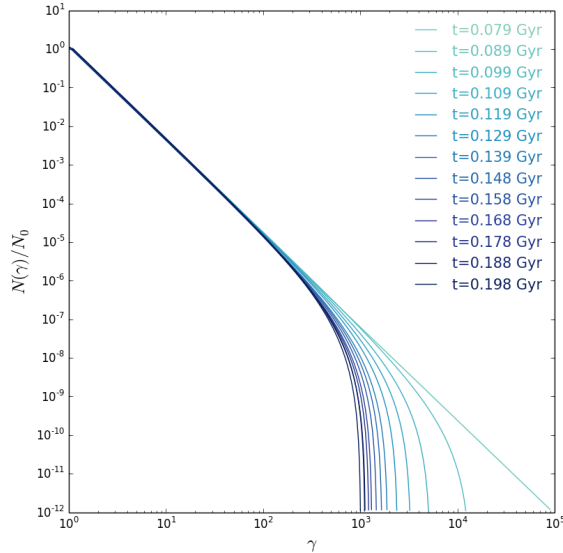
Figure 1.12: Left panel: Spectral ageing (from light to dark colors) of a particle with an initial power law spectrum given by the DSA mechanism. Right panel: Example of different spectral ageing models (see text).

1.9 Mpc long and $\sim$ 530 kpc wide at the region called the "brush" (at 550-750 MHz, see Rajpurohit et al. 2020a) and also shows a spectral steepening in the spectral index maps. Nevertheless, this relic is more complicated as it has more projection effects and the downstream of the "brush" region overlaps with the radio halo. A recent work by de Gasperin et al. (2020) studied the Toothbrush relic at 58 MHz and found that the observed steep spectrum is projected on the radio halo rather than mixed with it. The origin of this relic is puzzling since it is at odds with a simple DSA scenario, so the authors have proposed models based on shock (re-)acceleration of a cloud of fossil electrons and that the electrons are further re-accelerated in the downstream due to turbulence. The radio emission of this relic shows filamentary features like bristles with a width of 3–8 kpc that can be an outcome of turbulence. Other recent high-resolution observations of radio relics have also shown complex small-scale structures (e.g. Rajpurohit et al., 2018, 2020a; Owen et al., 2014; van Weeren et al., 2017; Di Gennaro et al., 2018). In Fig. 1.14, we show the substructures already observed in the Toothbrush relic as this would be the subject of one of the projects presented in this thesis. As we shall see in Chapter 4, turbulence does play a major role even in the simplest acceleration scenarios.

The most important piece of information that the DSA theory can give is the
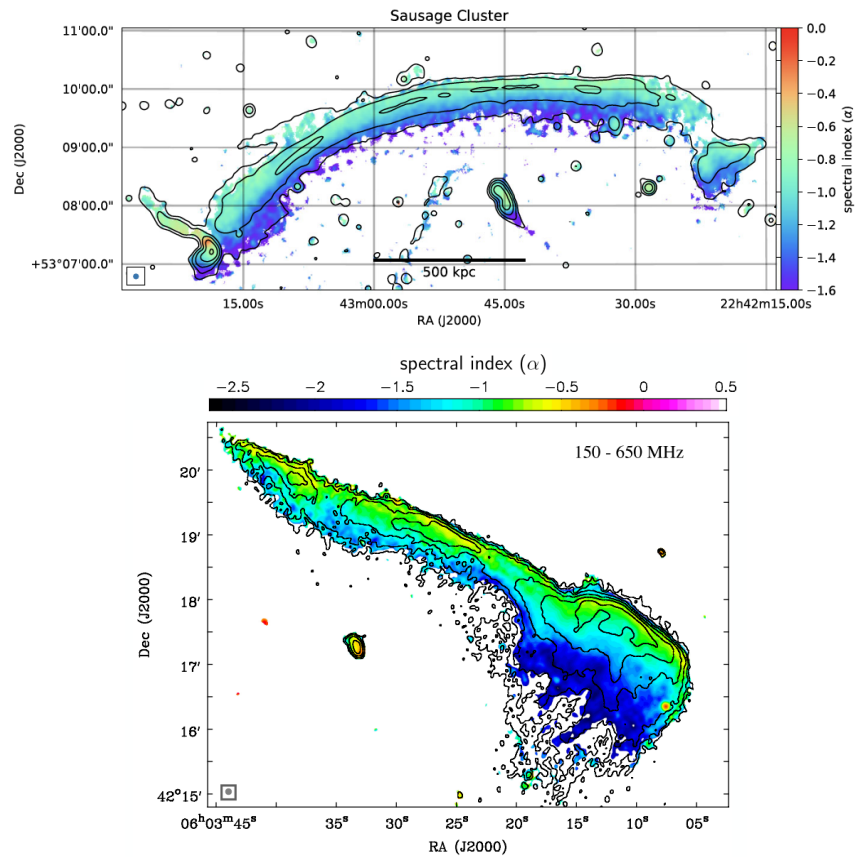
Figure 1.13: Top panel: Spectral index maps of the Sausage relic between 0.15 and 3.0 GHz. Bottom panel: Spectral index maps of the Toothbrush relic between 150 MHz and 650 MHz.

34

Mach number of the observed radio shock since the spectral index depends on that (see Section 1.5.1 and Chapter 4). Nevertheless, the DSA theory can also be used to give us more information about the observed radio relics. For example, when it comes to estimating the magnetic field at the relic's location, one can compute the radio emission in the downstream region as described by Hoeft & Brüggen (2007):

$$\frac{dP(\nu_{obs})}{d\nu} = 6.4 \times 10^{34}\,\mathrm{erg\,s^{-1}Hz^{-1}}\frac{A}{\mathrm{Mpc}^2}\frac{n_e}{10^{-4}\mathrm{cm}^{-3}}\frac{\xi_e}{0.05}\left(\frac{\nu_{obs}}{1.4\,\mathrm{GHz}}\right)^{-s/2}$$
$$\left(\frac{T_d}{7\,\mathrm{keV}}\right)^{3/2}\frac{(B/\mu G)^{1+(s/2)}}{(B_{\mathrm{CMB}}/\mu G)^2 + (B/\mu G)^2}\Psi(\mathcal{M}).$$

(1.31)

where A is the shock surface's area, ξ_e is the fraction of thermal energy injected at the shock front that goes into the acceleration of supra-thermal electrons, T_d is the assumed downstream temperature, $\Psi(\mathcal{M})$ is a function depending on the shock's Mach number and s is the power-law exponent index of the particle's energy[8]. Therefore, this modelling requires the assumption of different parameters such as the downstream temperature, shock's Mach number, projection angle, magnetic field, etc. Therefore, by varying these parameters and comparing with the observed radio emission profiles, one can estimate a value for the magnetic field (e.g. van Weeren et al., 2010; Rajpurohit et al., 2018; Di Gennaro et al., 2018). We show an example of this method in the right panel of Fig. 1.14.

Other methods that rely indirectly on DSA theory have also been used to estimate the strength of the magnetic field at the location of radio relics. One of them relies on comparing the observed width of the emission and the one expected from the characteristic synchrotron and IC energy losses timescale (see Eq. (1.25)). Using the redshift, downstream velocity as inferred from the Mach number, which in turn is inferred from the spectral index (through the DSA theory), one would expect that to a first approximation, the width of the relic is $l_{relic} \sim t_{age}v_d$ (e.g. van Weeren et al., 2010). Another method, although more crude, is to assume that there is equipartition between the magnetic and the relativistic particle's energy following the formulas given in Govoni & Feretti (2004). Examples of this method applied to radio relics can be found in Parekh et al. (2020); Locatelli et al. (2020).

Finally, radio relics help us understand the physics of galaxy cluster mergers. Specifically, the systems of double-relics located on both sides of the center of the cluster (e.g. Bagchi et al., 2006; Bonafede et al., 2009b; van Weeren et al., 2010; Brown et al., 2011; van Weeren et al., 2011b; de Gasperin et al., 2015). The idea is that by simulating the radio emission produced by a binary cluster merger event, one can get an estimate of the merger timescale, masses of the initial clusters or viewing angle (see Fig. 1.15 and Finner et al. 2020 for a recent work). For example,

---

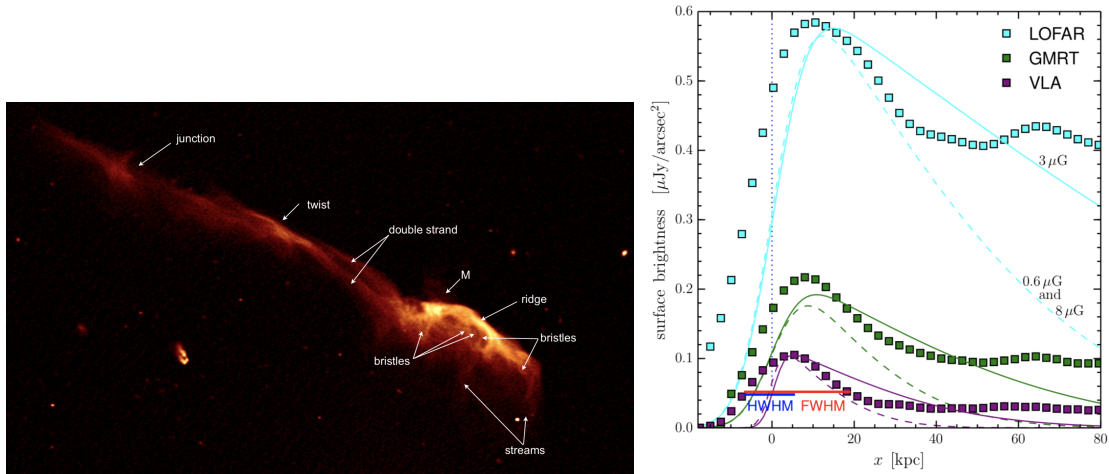[8]This is equivalent to p in the notation of Eq.(1.19) in Section 1.5

Figure 1.14: Left panel: High resolution VLA (1–2 GHz) image of the Toothbrush relic. The complex substructures are pointed out in white. Right panel: Surface brightness profiles measured along the downstream of the brush (squares) and model profiles (lines) according to Hoeft & Brüggen 2007.

a numerical simulation by van Weeren et al. 2011a has shown that the CIZA2242 cluster is a binary cluster merger seen very close to edge-on, while Brüggen et al. 2012b suggested a triple-merger scenario in order to explain the radio emission from the Toothbrush relic. Other numerical studies tailored for studying the simulated emissivity at radio relics have been done by means of cosmological simulations (e.g. Skillman et al., 2013; Hong et al., 2015; Nuza et al., 2017; Wittor et al., 2019).

1.6 Magnetic fields

Magnetic fields are ubiquitous in our Universe on all scales, from planets and stars to galaxies and galaxy clusters (e.g. Stevenson, 2010; Schubert & Soderlund, 2011; Beck, 2001; Beck & Wielebinski, 2013). In galaxy clusters, observations of diffuse synchrotron emission indicate the presence of magnetic fields with strengths of a few μG and coherent scales in the range of $\lambda_B \sim$ 10–50 kpc (e.g. Clarke et al., 2001; Carilli & Taylor, 2002; Govoni & Feretti, 2004; Vogt & Enßlin, 2005).

It is hypothesised that the observed magnetic fields result from the amplification of a weak seed field, whose origin is still debatable to date (e.g. Dolag et al., 1999; Schekochihin et al., 2004). Currently, we have indirect observational indications of their existence in the intergalactic medium (IGM) in voids. Indeed, the lack of sec-
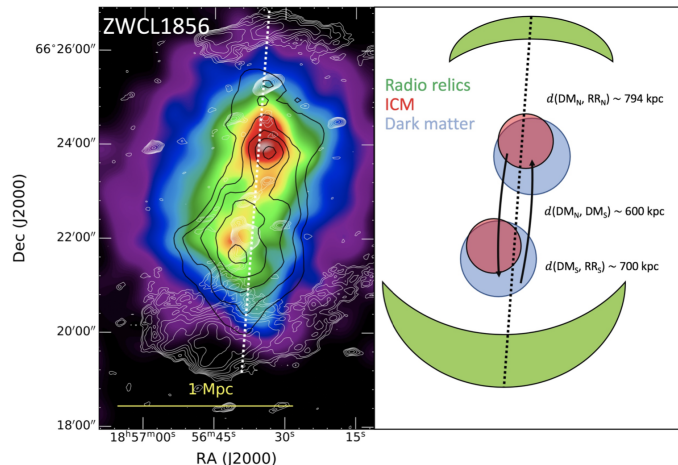
Figure 1.15: Left panel: X-ray emission (XMM-Newton at 0.5-7 keV) and overlapped (white contours) radio emission (LOFAR at 144 MHz) of the ZWCL1856 cluster. Suggested merger axis shown with the white dotted line. Right panel: Schematic of the merger scenario (DM: Dark Matter and RR: Radio Relic).

IMAGE CREDIT: Finner et al. 2020

ondary gamma-rays around blazars in voids puts a lower limit of $B \geq 3 \times 10^{-16}$G (comoving) on intergalactic magnetic fields with coherent Mpc scales (see Neronov & Vovk, 2010). On the other hand, distortions of the spectrum and polarisation properties in the CMB radiation (e.g. Kahniashvili et al., 2009; Seshadri & Subramanian, 2009; Trivedi et al., 2014; Planck Collaboration et al., 2016) infer an upper limit of $B \leq 10^{-9}$ G (comoving). There are three basic magnetogenesis scenarios that have been widely discussed in the literature:

i) *Astrophysical*: Magnetic fields were initially produced from galactic winds (e.g. Völk & Atoyan, 2000; Donnert et al., 2009) or active galactic nuclei (AGN) (e.g. Ensslin et al., 1997; Furlanetto & Loeb, 2001; Xu et al., 2011). These models could explain the observed magnetic fields in galaxy clusters, but they have difficulty in explaining them in voids.

ii) *Primordial*: magnetic fields have been generated in the early Universe possibly during (or after) inflation but prior to galaxy formation (e.g. Turner & Widrow, 1988; Kobayashi, 2014; Grasso & Rubinstein, 2001; Kandus et al., 2011; Subramanian, 2016).

iii) *Cosmic batteries*: magnetic fields could originate from the misalignment between density and temperature gradients in the late Universe. For example,
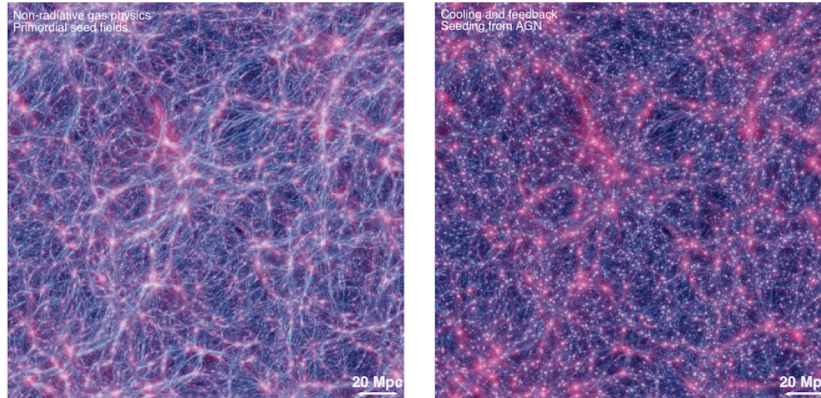
Figure 1.16: Average temperature (red) and average magnetic field strength (green+blue) along the line of sight in the simulated cosmic web. Left panel: Primordial scenario considering an initial uniform magnetic field of $B_0 = 0.1$nG and a non-radiative set-up. Right panel: Astrophysical scenario where magnetic fields have been injected by AGN and the set-up includes cooling and feedback.

during the Epoch of Reionisation (see Gnedin, 2000) and/or in cosmological shocks (see Ryu et al., 1998). This effect is known as the *Biermann battery* (Biermann, 1950).

A sense of the spatial distribution of magnetic fields in the cosmic web considering the first two scenarios can be seen in Fig. 1.16. Primordial magnetic fields permeate voids and filaments more easily than an astrophysical scenario. Vazza et al. 2017 found out that for magnetic fields injected by star formation winds and/or AGN, there is a sharp drop in the magnetisation outside of the virial radius of halos, while this does not happen in the primordial scenario where there is a larger magnetisation in voids and filaments. The above-mentioned observations of blazar spectra favor the primordial scenario. If this is the case, there are also different possibilities for the magnetogenesis (see Subramanian, 2016, for a review):

i) *Inflationary*: quantum vacuum fluctuations of an electromagnetic field give rise to a weak magnetic seed (see Turner & Widrow, 1988). The fast exponential stretching of the produced field can give rise to correlation lengths as large as possible. The inflation-generated magnetic field is usually described by a scale invariant (or a nearly scale invariant) spectrum.

ii) *Phase-transition*: phase transitions (e.g. electroweak or quantum-chromodynamical (QCD)) can give rise to a magnetic seed due to causal processes (see Grasso &

38

Rubinstein, 2001; Kandus et al., 2011; Durrer & Neronov, 2013) This means that the correlation length is restricted to be smaller than the horizon scale at the moment of generation. In this case, the magnetic field is assumed to be stochastic with a power law spectrum.

Regardless of their origin, magnetic fields in galaxy clusters must have been significantly amplified in order to have reached today's values. Adiabatic compression, i.e. $B \propto \rho^{2/3}$, alone is not a solution. Instead, a combined effect of adiabatic compression and the presence of a *small-scale dynamo* would be needed in order for such a magnetic field not to decay. This is naturally provided by minor or major mergers which compress and inject turbulence in the ICM (e.g. Roettiger et al., 1999; Brüggen et al., 2005b; Subramanian, 2016). We refer the reader to Donnert et al. 2018 for a good review on magnetic amplification in galaxy clusters.

1.6.1 Small-scale dynamo

We define a dynamo action as a process where kinetic energy is converted into magnetic energy. In the astrophysical context of galaxy clusters, we know that the magnetised ICM is a turbulent fluid (e.g. Hitomi Collaboration et al. 2018; see Section 1.4). In this case, the small-scale components of the turbulence can have a powerful effect on the magnetic field leading to a dynamo action. The dynamo is referred to as a *small-scale or fluctuation dynamo* when the characteristic scale of the magnetic field is comparable or smaller than the characteristic scale of fluid motions, i.e., the turbulence injection scale (e.g. Batchelor, 1950; Kazantzev, 1967; Zeldovich et al., 1983; Kulsrud & Anderson, 1992).

The essence of this theory lies in the induction equation:

$$\frac{\partial \mathbf{B}}{\partial t} = \nabla \times (\mathbf{V} \times \mathbf{B}) - \eta \nabla^2 \mathbf{B}, \tag{1.32}$$

where $\mathbf{V} = \bar{\mathbf{V}} + \mathbf{v}$ is the velocity field, $\bar{\mathbf{V}}$ are the regular mean, large-scale velocity motions, $\mathbf{v}$ are the turbulent velocity motions and η is the magnetic diffusivity related to the electric conductivity through $\eta = (4\pi\sigma)^{-1}$. The second term on the right-hand-side of Eq. (1.32) defines then the diffusion of the magnetic field. The first term can be rewritten as

$$\nabla \times (\mathbf{V} \times \mathbf{B}) = -\mathbf{B}(\nabla \cdot \mathbf{V}) + (\mathbf{B} \cdot \nabla)\mathbf{V} - (\mathbf{V} \cdot \nabla)\mathbf{B}, \tag{1.33}$$

where the first, second and term describes the compression, stretching and advection of the magnetic field, respectively. In the limit $\mathbf{V} = 0$ in Eq. (1.32), one gets the diffusion timescale $\tau_{diff} = l_0^2/\eta$; and in the other limit $\eta \to 0$, one gets an induction

timescale $\tau_{ind} = l_0/v_0$, where l_0 is the characteristic scale over which the magnetic field varies and v_0 is the characteristic velocity of the fluid at that scale. The comparison of both timescales, i.e., comparing the magnetic induction and diffusion terms, defines the *magnetic Reynolds number*:

$$Re_m = \frac{v_0 l_0}{\eta}, \tag{1.34}$$

where we can estimate a value of $Re_m \sim 10^{29}$ for typical values of $v_0 \sim 100$ km/s, $l_0 \sim 100$ kpc and $\eta \sim 30 \text{cm}^2/\text{s}$[9], corresponding to the ICM (see Table 1 in Schekochihin & Cowley 2006). Note that this is an estimate of the electric conductivity, ν, since this value is unknown. These high values mean that ICM is a highly conductive plasma, for which one can safely assume that there is no magnetic diffusion, i.e. $\eta \sim 0$, and therefore the magnetic field lines can be considered to be frozen into the plasma. Considering this scenario, the weak magnetic field can be efficiently amplified in the presence of turbulence where there is stretching of field lines. The regime in which the magnetic energy is much lower than the kinetic energy of driving eddies at all scales (from injection down to the dissipation scales) and the velocity is homogeneous and isotropic is called the *kinematic or linear regime*. And it is in this regime that the small-scale dynamo has been most studied (e.g. Kazantzev, 1967; Zeldovich et al., 1983; Kraichnan & Nagarajan, 1967; Kulsrud & Anderson, 1992) and the reason behind why it is often also called Kazantsev theory of turbulent dynamo. The most important result of this theory is the magnetic power spectrum. In Fourier space, the magnetic energy per unit mass can be expressed as

$$\varepsilon = \frac{B^2}{8\pi\rho} = \frac{1}{2} \int M(k,t)dk, \tag{1.35}$$

where $M(k,t)$ is the magnetic power spectrum. Following the formalism defined in Kulsrud & Anderson 1992 and taking into account the induction equation, one can arrive to a general dynamical equation for the power spectrum:

$$\frac{\partial M}{\partial t} = \frac{\Gamma}{5} \left(k^2 \frac{\partial^2 M}{\partial k^2} - 2\frac{\partial M}{\partial k} + 6M \right) - 2k^2 \eta M \tag{1.36}$$

where $\Gamma \propto t_{eddy}^{-1}$, and t_{eddy} is the turnover time of the smallest eddies, i.e. k_{max}. The first key outcome is that when one drops the magnetic diffusivity, $\eta = 0$, and integrates Eq. (1.36) over all wavenumbers k, one gets

$$\frac{d\varepsilon}{dt} = 2\Gamma\varepsilon. \tag{1.37}$$

---

[9]where $\eta = 3 \times 10^{13} T^{-3/2}$

This means that in the kinematic regime, the small-scale dynamo grows exponentially at a 2Γ rate and that the fastest magnetic field amplification will come from the smallest turbulent eddies, i.e. $k \sim k_{max}$. The second outcome is the solution of Eq. (1.36):

$$M(k,t) \propto k^{3/2} \exp\left(\frac{3\Gamma}{4}\right) K_0(k), \qquad (1.38)$$

where $K_0(k)$ is a function that can be a Bessel function of the second kind or an error function depending on the range of k considered and if the magnetic diffusivity is taken into account (see Kulsrud & Anderson, 1992, for more details). Therefore, the characteristic magnetic spectrum of a small-scale dynamo varies as $k^{3/2}$.

The kinematic regime breaks down on scales below the equipartition scale of the turbulent and magnetic energies, because the magnetic field starts to back-react (e.g. Schlüter & Biermann, 1950; Brandenburg, 2011). This moment defines the *non-linear regime* of the small-scale dynamo. During this regime, the stretching action is suppressed and since now the magnetic energy is in equipartition with the turbulent kinetic energy over all scales below that equipartition, the hydrodynamic turbulence becomes magneto-hydrodynamic (MHD) turbulence. In this regime, the growth of magnetic energy is linear in time (e.g. Schekochihin & Cowley, 2007; Cho et al., 2009; Ryu et al., 2008; Beresnyak, 2012). Finally, when the magnetic energy is in equipartition with the kinetic energy of the largest turbulent eddy, the small-scale dynamo is in the *saturation state*.

In galaxy clusters, the eddy turnover time is of about 10^6–10^7 yr, while the timescale of the smallest eddies is estimated to be ~ 1000 yr (e.g. Schekochihin et al., 2002; Beresnyak & Miniati, 2016). These timescales are much smaller than the cluster's age. For this reason, the small-scale dynamo is a good candidate for explaining the existence of intracluster magnetic fields. At the same time, this tells us that the linear regime would last a short period and therefore, a dynamo would spend most of its time in the non linear regime in galaxy clusters.

1.6.2 MHD turbulence

As can be seen, the small-scale dynamo depends on a turbulent medium. A fluid becomes turbulent if the *kinematic Reynolds number*, Re, is large enough. The Reynolds number is defined as the ratio of the forcing to the dissipation scale:

$$Re = \frac{v_0}{\nu k_0} = \frac{v_0 l_0}{\nu}, \qquad (1.39)$$

where ν is the kinematic viscosity and k_0 is the injection wavenumber, i.e., the wavenumber correspondent to the injection scale l_0. One way to give an estimate

of the kinematic viscosity is assuming $\nu \sim v_{th,i}\lambda_C$ (e.g. Spitzer, 1956), where $v_{th,i}$ is the ion velocity and λ_C is the Coulomb mean free path (see Eq. 1.4). For the typical values of the ICM, this gives low values of Re. In the most optimistic scenario, one would get $Re \sim 10^2$–10^3 (e.g. Schekochihin & Cowley, 2006; Donnert et al., 2018).

Since in the ICM the turbulent velocities at the outer scales are smaller than $v_{th,i}$, the turbulence is considered to be *subsonic*. In this case, one naturally assumes that the *Kolmogorov theory* is applicable. In this theory, it is assumed that the energy cascades self-similarly and without dissipation from the outer scales down to the dissipative scales. Under the assumption of isotropic, homogeneous and incompressible turbulence, the Kolmogorov kinetic energy spectrum in the inertial range is (Kolmogorov, 1941):

$$E_K(k) \propto \varepsilon_K^{2/3} k^{-5/3}, \tag{1.40}$$

where $\varepsilon_K \sim u_l^3/l$ is the energy rate at a scale l. Since the energy rate should remain constant as it cascades to smaller scales, the viscous scale of the turbulence is $l_\nu \sim l_0 Re^{-3/4}$, which in the ICM would be of the order of ~ 10–30 kpc. Yet this picture is not in agreement with observations. As mentioned in Section 1.4, we have evidence of the existence of turbulence in galaxy clusters where the observed velocity dispersion is of the order of σ_v on scales $\lesssim 100$ kpc (see Hitomi Collaboration et al., 2018). Moreover, Faraday Rotation measures (RM) indicate that magnetic fields with strengths of ~ 1–10 μG in the ICM have a typical reversal scale of the order of 1 kpc (e.g. Taylor et al., 2002; Kuchar & Enßlin, 2011; Vacca et al., 2012; Bonafede et al., 2013; Govoni et al., 2017). The ICM cannot be solely described by Coulomb collisions and furthermore, it is magnetised. Indeed, a magnetised medium with instabilities (e.g. firehose, mirror, etc.) induces other scatterings mediated by the magnetic field. This in turn would lead to a smaller effective mean free path of thermal ions and therefore, also would decrease the effective viscosity (e.g. Schekochihin & Cowley, 2006). In this case, the fluid would behave as collisional on scales less than the Coulomb mean free path, λ_C (e.g. Lazarian & Beresnyak, 2006).

In the presence of magnetic fields, the mean free path of particles is limited to the Larmor gyroradius scale (e.g. Braginskii, 1965):

$$r_g \sim 3 \times 10^{-12} \left(\frac{T}{10\text{keV}}\right) \left(\frac{B}{\mu\text{G}}\right)^{-1} \text{kpc}. \tag{1.41}$$

If one considers this scale for the computation of the Reynolds number, then this results in higher values, i.e. an effective Reynolds number of $Re \sim 10^{19}$. This suggests that the ICM is highly turbulent and therefore, one could describe it as a cascade of turbulence from the largest injection scales down to smaller scales. Yet, magnetic fields are not affecting the largest scales in galaxy clusters, so a common
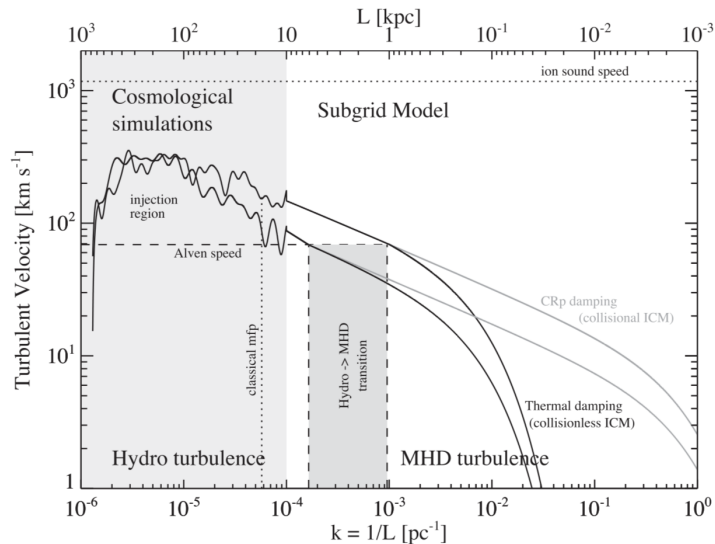
Figure 1.17: Schematic of a simple turbulence cascade model in the ICM. The cascade starts at the largest scales in the form of hydrodynamical turbulence and then it transitions to be MHD turbulence.

framework is to assume that turbulence can be modelled as purely hydrodynamical for the large scales and as magneto-hydrodynamical for smaller scales. Nevertheless, this forces us to define an intermediate scale that describes this transition. An MHD treatment of turbulence involves solving the MHD equations (see Chapter 4). The linearised MHD equations reveal that the perturbations mode can be decomposed into Alfvèn, slow, and fast modes (e.g. Dobrowolny et al., 1980). The Alfvèn mode propagates parallel to the magnetic field and has a solenoidal nature, while the slow and fast modes propagate perpendicular to the magnetic field and have a compressive nature. In this context, the characteristic group velocity at which the Alfvèn wave can travel is called the *Alfvèn velocity*, defined as $v_A = B/\sqrt{4\pi\rho}$. The fast and slow compressible waves then propagate correspondingly with faster and slower than v_A. The plasma beta can then also be written as $\beta = P/(8\pi B^2) = (2c_s^2)/(\gamma_0 v_A^2)$. The ICM is a high-$\beta$ plasma where we have $v_A \sim 70$ km/s. We have also mentioned that the typical velocities are of the order of hundred of km/s in the ICM. Therefore, the definition of sonic and Alfvènic Mach numbers tell us the type of turbulence existing the ICM: *sub-sonic*, with typical $\mathcal{M}_s = v_0/c_s \sim 0.2$–$0.5$ and *super-Alfvènic* $\mathcal{M}_A = v_0/v_A \sim 5$–$10$ (see Brunetti & Lazarian, 2007). In this case, the turbulent hydrodynamic motions can easily bend the magnetic field lines. Therefore, it is

very useful to define the characteristic length where the velocity of turbulent eddies equals the Alfvèn velocity. This scale is called *Alfvèn or MHD scale* (see Brunetti & Lazarian, 2007):

$$l_A \sim 3 \left(\frac{B}{\mu G} \right)^3 \left(\frac{l_0}{1\,\mathrm{Mpc}} \right) \left(\frac{\sigma_{v,0}}{10^3 \mathrm{kms}^{-1}} \right)^{-3} \left(\frac{n}{10^{-3}\mathrm{cm}^{-3}} \right)^{-3/2} \mathrm{kpc}, \qquad (1.42)$$

where l_0 is the reference scale within the Kolmogorov inertial range and $\sigma_{v,0}$ is the corresponding rms velocity. Below this scale, the turbulent eddies are not strong enough to bend the magnetic field lines and therefore, the hydrodynamic turbulence becomes MHD turbulence (hence it is also called the MHD scale). Figure 1.17 shows a good sketch of a model of turbulence in the ICM (see details in Donnert & Brunetti, 2014).

In terms of numerical MHD simulations, this means that there are two important quantities to be taken care of: Re and l_A. The effective Reynolds number can be approximated as (in the ideal case of a uniformly reolved numerical simulation) (Donnert et al., 2018):

$$Re_{min} \sim \left(\frac{L}{\varepsilon \Delta x} \right)^{4/3}, \qquad (1.43)$$

where L is the length of the computational domain, Δx is the resolution and ε is a factor depending on the diffusivity of the numerical method. For example, for second order finite difference/volume codes one can assume $\varepsilon \approx 7$ (e.g. Kritsuk et al., 2011). It can be seen from Eq. (1.43), that the resolution of a simulation defines the Reynolds number, which in turn limits our modelling of turbulence. One of the best improvements in resolution of cosmological MHD simulations is reaching Reynolds number up to 1000 (e.g. Vazza et al., 2018; Domínguez-Fernández et al., 2019). This limitation is relevant as the Reynolds number achieved in simulations directly affects the magnetic field growth in galaxy clusters (see Donnert et al. 2018 and references therein). For example, the growth rate of the small-scale dynamo depends on the eddy turnover time (see Section 1.6.1). This time is the shortest in highly resolved regions, which directly means that the resolution limits the dynamo growth. Since achieving higher resolutions in cosmological simulations is complicated, it is required to at least resolve the Alfvèn scale l_A (see Eq. (1.42)). For example, in Vazza et al. (2018), l_A gets resolved up to $\sim 50\%$ in the highest resolved region of the simulated galaxy clusters. This allowed the authors to resolve the growth of the magnetic field up to observable values.

Finally, it has been suggested that the MHD treatment of the ICM is not valid (e.g. Schekochihin et al., 2005) because the ion mean free path between collisions is of the order of the dynamical scales, which therefore would require a collisionless MHD

treatment. Nevertheless, Santos-Lima et al. (2014) showed that the collisional-MHD approach is applicable in the ICM because the kinetic anisotropies relax much faster than the typical rates of turbulence. Therefore, scales of $\gtrsim$ kpc are reasonably well described by a standard MHD approach.

Chapter 2

Aims and methods

In this thesis I have focused on studying magnetic fields in the ICM, specifically 1) in the central and the 2) outskirts regions of galaxy clusters. In particular, I addressed the following key questions in my projects:

- Project 1 (Chapter 3):

    1) Can primordial magnetic fields lead to today's observables?

    2) What is the role of mergers in the presence of a small-scale dynamo?

- Project 2 (Chapter 4):

    1) What is the role of turbulence in the synchrotron emission?

    2) Can the DSA mechanism still explain radio relics?

- Project 3 (Chapter 5):

    1) What is the role of turbulence in the polarised emission?

In Project 1, I analysed 7 highly resolved simulated galaxy clusters produced with MHD cosmological simulations (ENZO code). My main tool of analysis was the magnetic and kinetic power spectrum.

In project 2, I produced 2 different turbulent media resembling a small region of ICM with turbulent-in-a-box MHD simulations (FLASH code) and studied the synchrotron emission using Lagrangian particles (PLUTO code). This project required the numerical implementation of 1) a shock-finder, in order to keep track of shocks discontinuities in the MHD Eulerian grid, and 2) an activation algorithm, where the Lagrangian particles could detect the shock discontinuity and acquire an energy spectrum as expected from the DSA theory.

In the on-going project 3, I used the same set-up as in project 2. In this case, I focused on studying polarisation by computing the Stokes parameters Q and U.

The numerical implementations in the PLUTO code are explained briefly in Chapter 4. Nevertheless, these were fundamental for the results of projects 2 and 3 and therefore I shall discuss them here.

2.1 Shock finder algorithm

The shock finder tags selected cells in the Eulerian grid according to the following conditions:

1. $\nabla \cdot \mathbf{v} < 0$,

2. $\Delta \log p \geq \log \frac{p_2}{p_1}\Big|_{\mathcal{M}_s = \mathcal{M}_{\min}}$,

where the subscripts 1 and 2 denote the upstream (pre-shock) and downstream (post-shock) regions and where $\Delta Q = Q_{i+1} - Q_{i-1}$ defines central differences of the variable Q. The first condition is a standard criterion for detecting compression zones. Yet, the second condition is the one that filters out spurious and weak shocks (see Ryu et al., 2003a).

The shock discontinuity in a computational domain is usually broadened over a few cells. Thus, in order to compute the pressure jumps $(p_2/p_1)_l$ in each direction $l = x, y, z$, one has to define which is the upstream, p_1, and downstream, p_2. For example, a planar shock discontinuity travelling in the x–axis to the right would mean that $p_1 = p(i+h)$ and $p_2 = p(i-h)$, where $p(i)$ is already tagged as the shock center by the first condition and h is the number of cells away from it. Then the general condition for the x direction is

$$\left(\frac{p_2}{p_1}\right)_x = \frac{max(p(i-h), p(i+h))}{min(p(i+h), p(i-h))}. \tag{2.1}$$

The definition of the other directions is analogous. The second condition is related to the Mach number through the pressure Rankine-Hugoniot jump condition according to Landau & Lifshitz 1987:

$$\frac{p_2}{p_1} = \frac{2\gamma_0 \mathcal{M}_s^2 - (\gamma_0 - 1)}{\gamma_0 + 1}, \tag{2.2}$$

where γ_0 is the adiabatic index of the equation of state (EOS) and $\mathcal{M}_s$ is the sonic Mach number of the shock. Therefore, in order to satisfy the second condition, one

defines a minimum sonic Mach number, $\mathcal{M}_{\min}$, which acts as an external parameter that the user can set in the initial parameter file in the PLUTO code. In our case, we used $\mathcal{M}_{\min} = 1.3$ in order to filter out weaker and spurious shocks. This in turn allows us to study the main shock propagation in the ICM as will be described in Chapter 4. In projects 1 and 2, we studied a shock discontinuity with sonic Mach numbers in the range $\mathcal{M}_s = 2\text{--}3 > \mathcal{M}_{\min}$, which are the typical strengths observed in radio relics.

Having the two conditions fulfilled, one is able to compute the Mach number in each direction, using Eq. (2.2):

$$\mathcal{M}_x^2 = \frac{(\gamma_0 + 1)(p_2/p_1)_x - (\gamma_0 - 1)}{2\gamma_0}, \tag{2.3}$$

$$\mathcal{M}_y^2 = \frac{(\gamma_0 + 1)(p_2/p_1)_y - (\gamma_0 - 1)}{2\gamma_0}, \tag{2.4}$$

$$\mathcal{M}_z^2 = \frac{(\gamma_0 + 1)(p_2/p_1)_z - (\gamma_0 - 1)}{2\gamma_0}. \tag{2.5}$$

Finally, one can obtain that the Mach number of shock is

$$\mathcal{M}_s = (\mathcal{M}_x^2 + \mathcal{M}_y^2 + \mathcal{M}_z^2)^{1/2}, \tag{2.6}$$

where $\mathcal{M}_s = \mathcal{M}_s(i, j, k)$ is an array defined in the whole Eulerian grid.

2.2 Activating Lagrangian particles

Lagrangian particles represent synchrotron emitting electrons in our set-up for projects 1 and 2. Each particle has a unique ID and carries information interpolated from the Eulerian grid at their location: coordinates, speed, density; and also energy information: binned energies and spectral energies. The spectral energy of each particle evolves at each time-step according to the solution of a simplified cosmic-ray transport equation. This part will be explained in Chapter 4 and the reader can also refer to Vaidya et al. (2018) for a complete description of the particle module in the PLUTO code implementation.

Part of project 2 consisted in modifying the PLUTO code to have particles activated in their energy evolution whenever they were located at a shock cell. In order to achieve that, I created a new flag for all the particles. The functionality of this flag is explained in the flow chart in Fig. 2.1. All the particles are passive since the beginning of the simulation, which means that they still move along with the MHD flow, but their energy remains to be zero (flag is equal to 0). The particles
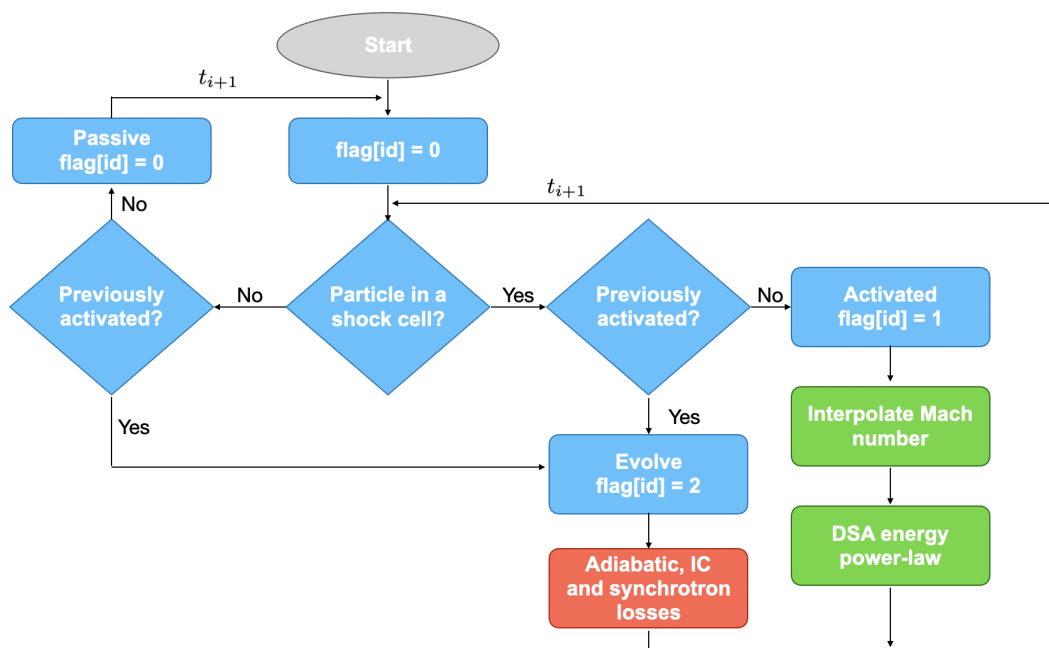
Figure 2.1: Flow chart of the activation flag of a Lagrangian particle in the PLUTO code.

will be activated only when they are at the location of a shock discontinuity which was previously tagged by the shock finder as described in Section 2.1 (flag is equal to 1). At this moment, the Mach number is interpolated to the activated particle and the normalisation and exponent of the DSA power-law can be computed:

$$\chi(E) = \frac{N_0}{n_0} E^{-p}, \tag{2.7}$$

where n_0 is the fluid number density at the position of the particle,

$$p = \frac{4\mathcal{M}^2}{\mathcal{M}^2 - 1} - 2 = \frac{1}{2}\frac{\mathcal{M}^2 + 1}{\mathcal{M}^2 - 1}, \tag{2.8}$$

$$N_0 = \begin{cases} \frac{\eta\, E_{\mathrm{shock}}\,(4-q)}{\left[E_{\mathrm{max}}^{4-q} - E_{\mathrm{min}}^{4-q}\right]}, & \text{if } q \neq 4 \\[2ex] \eta\, E_{\mathrm{shock}} \log\left(\frac{E_{\mathrm{max}}}{E_{\mathrm{min}}}\right), & \text{if } q = 4 \end{cases} \tag{2.9}$$

where $E_{\mathrm{shock}} = \rho_{\mathrm{post}} v_s^2$ and η is the acceleration efficiency, which is a selected constant set by the user. In our case, we selected $\eta = 10^{-3}$ which lies in the range of values required to explain the observed radio relics (see Botteon et al. 2020). The interpolation of the Mach number from the Eulerian grid to the particles was done using the Nearest Grid Point (NGP) method.

At the next time-step, if particles do not encounter another shock discontinuity, their spectral energy will evolve according to the solution of the cosmic-ray equation and it will be subject to adiabatic, IC and synchrotron losses. At this moment they acquire a flag equals to 2.

Finally, if particles encounter another shock they will not be accelerated again through DSA, contrary to what the unmodified PLUTO code does (see Vaidya et al. 2018). This is ensured by keeping the same flag for all particles that have been subject to energy losses (flag equals 2). In this way, we keep a more controlled scenario for analysing the synchrotron emission. Re-acceleration of particles through multiple DSA processes is more complicated as it would require a consistent normalisation. In this case one has to consider not only another DSA power-law for the re-accelerated particles, but also involve the previous energy spectrum that was subject already to energy losses. This problem would be considered for a future work.

Chapter 3

Dynamical evolution of magnetic fields in the intracluster medium

P. Domínguez-Fernández, F. Vazza , M. Brüggen and G. Brunetti

Abstract   We investigate the evolution of magnetic fields in galaxy clusters starting from constant primordial fields using highly resolved ($\approx$ 4 kpc) cosmological MHD simulations. The magnetic fields in our sample exhibit amplification via a small-scale dynamo and compression during structure formation. In particular, we study how the spectral properties of magnetic fields are affected by mergers, and we relate the measured magnetic energy spectra to the dynamical evolution of the intracluster medium. The magnetic energy grows by a factor of $\sim$ 40-50 in a time-span of $\sim$ 9 Gyr and equipartition between kinetic and magnetic energy occurs on a range of scales ($<$ 160 kpc at all epochs) depending on the turbulence state of the system. We also find that, in general, the outer scale of the magnetic field and the MHD scale are not simply correlated in time. The effect of major mergers is to shift the peak magnetic spectra to *smaller scales*, whereas the magnetic amplification only starts after $\lesssim$ 1 Gyr. In contrast, continuous minor mergers promote the steady growth of the magnetic field. We discuss the implications of these findings in the interpretation of future radio observations of galaxy clusters.

3.1 Introduction

Galaxy clusters assemble through mergers and accretion until they reach an approximate virial equilibrium (e.g. Kravtsov & Borgani, 2012; Planelles et al., 2015). These events affect the space between galaxies which is filled with a dilute plasma, known as the intracluster medium (ICM). In particular, radio observations shed light on the non-thermal component of the ICM revealing the existence of cosmic rays and magnetic fields permeating galaxy clusters (e.g. Feretti et al., 2012; Brunetti & Jones, 2014; Donnert et al., 2018). Observations of synchrotron emission indicate magnetic fields with strengths of a few μG (corresponding to an energy density of $\sim 1-2\%$ of the thermal energy of the ICM) and typical coherence scales in the range of $\sim 10-50$ kpc (e.g. Vogt & Enßlin, 2005). Typically, this coherence scale is derived by a Fourier analysis of rotation measure (RM) maps, and inferring the maximum and minimum scales in the magnetic spectrum (often assuming a Kolmogorov-like power spectrum) necessary to reproduce the observed properties within uncertainties (e.g. Murgia et al., 2004; Bonafede et al., 2010, 2013). In order to explain their observed morphology and strength, it has been suggested that magnetic fields get tangled over time by some other process than gas compression (e.g. Dolag et al., 1999; Brüggen et al., 2005b; Xu et al., 2009).

While the origin of magnetic fields in galaxy clusters is still subject to debate, two scenarios have been widely discussed: (i) the *primordial* scenario, in which magnetic fields have been generated in the early Universe possibly during (or after) inflation but prior to the formation of galaxies (e.g. Turner & Widrow, 1988; Kobayashi, 2014; Grasso & Rubinstein, 2001; Kandus et al., 2011; Subramanian, 2016) and (ii) the *astrophysical* scenario, in which magnetic fields were produced from stellar winds (e.g. Donnert et al., 2009) or active galactic nuclei (AGN) (e.g. Xu et al., 2011). A lower bound on the strength of the initial seed field of $B \geq 3 \times 10^{-16}$G (comoving) has been inferred for voids from the non-observation of secondary gamma-rays around blazars (e.g Neronov & Vovk, 2010). On the other extreme, upper limits of the order of $B \leq 10^{-9}$G (comoving), derived from the observed level of cosmic microwave background (CMB) anisotropies (e.g. Planck Collaboration et al., 2016), can be used to limit the strength of any primordial seed field with coherence scales of $\sim$ Mpc or larger.

Regardless of the magnetogenesis scenario, magnetic fields must have been significantly amplified in order to have reached today's values. It is generally assumed that the amplification of the initial magnetic fields occurred via the combined effect of adiabatic compression and the presence of a small-scale dynamo, both of which are driven by minor or major mergers (e.g. Roettiger et al., 1999; Brüggen et al., 2005b; Subramanian, 2016). The presence of a small-scale dynamo requires the existence of

turbulence in the ICM, which is supported by cosmological simulations (e.g. Dolag et al., 2005; Vazza et al., 2009; Iapichino & Niemeyer, 2008; Ryu et al., 2008; Lau et al., 2009; Vazza et al., 2011a; Marinacci et al., 2015, 2018b; Donnert et al., 2018) and more recently, also by observations (e.g. Hitomi Collaboration et al., 2018). A dynamo process converts kinetic energy into magnetic energy over the typical dynamical timescales of the turbulent cascade. It is believed that the amplification of ICM magnetic fields arises from the turbulence developing on scales which are a fraction of cluster virial radius ($\leq 0.5 - 1$ Mpc) (e.g. Donnert et al., 2018, and references therein). Previous simulations have shown that only a few percent of the incompressible turbulent energy needs to be dissipated to account for the observed field strength (e.g Miniati & Beresnyak, 2015, and references therein).

Whenever the characteristic scale of the magnetic field is comparable or smaller than the characteristic scale of fluid motions, the dynamo is referred to as a *small-scale dynamo* (also called fluctuation dynamo) (e.g Zeldovich et al., 1983; Kazantzev, 1967). Conversely, a *large-scale dynamo* refers to magnetic fields that are spatially coherent on scales comparable to the scale of the underlying astrophysical system (e.g Zeldovich et al., 1983; Moffatt, 1978). Since galaxy clusters do not show substantial rotation, it is likely that the turbulent small-scale dynamo winds up magnetic fields on scales smaller than the turbulence injection scale (e.g Subramanian et al., 2006; Brandenburg et al., 2012; Kazantzev, 1967; Kraichnan & Nagarajan, 1967; Kulsrud & Anderson, 1992; Schekochihin & Cowley, 2007; Beresnyak & Lazarian, 2006; Schekochihin et al., 2008).

In previous papers (e.g Beresnyak & Miniati, 2016; Miniati & Beresnyak, 2015), driven turbulence in the ICM has been studied in a cosmological context. Still, it remains a challenge to push the spatial resolution down to the so-called *MHD scale* (l_A) at which the magnetic energy is strong enough to prevent additional bending of the magnetic field lines. It is crucial to resolve l_A in order to fully capture the development of the small-scale dynamo amplification, but l_A can in principle be extremely small ($\ll$ kpc) for arbitrarily small seed magnetic fields. The Reynolds number achieved in simulations is also an important factor that directly affects the magnetic field growth. While the Reynolds number based on the full *Spitzer* viscosity in the ICM is believed to be of the order of $R_e \sim 10^2$ (e.g Brunetti & Lazarian, 2007; Cho, 2014), the reduced proton mean free path in the collisionless ICM can result in much larger Reynolds numbers (Beresnyak & Miniati, 2016; Brunetti & Lazarian, 2011b). This suggests that the fluid approximation provides a suited model for the properties of the ICM (e.g Santos-Lima et al., 2017, 2014).

More recently, it has been shown that initial magnetic field seeds can be amplified via a dynamo up to strengths of $\sim \mu$G in cosmological grid simulations (e.g Vazza et al., 2018) (hereafter Paper I). Here, we present a new sample of galaxy clusters

to study the spectral properties of each galaxy cluster in our sample. Firstly, we study the characteristic spectral features of the magnetic energy in different types of clusters at $z = 0$. Secondly, we follow the spectral evolution of a particular cluster that is merging.

The paper is structured as follows: in Section 3.2 we present the numerical setup and describe the fitting process of the magnetic energy spectra. In Section 3.3 we present our results in two parts, the first one dedicated to the properties of our galaxy cluster sample at $z = 0$, and the second one describing the evolution of a merging cluster. In Section 3.4 we discuss numerical aspects and in Section 3.5, we discuss the implications of our results.

3.2   Methods

3.2.1   The Simulated Dataset

We simulated the formation of massive galaxy clusters in a cosmological framework with the *ENZO* grid code (The Enzo Collaboration et al., 2013). We used the Dedner formulation of MHD equations (Wang & Abel, 2009) and used adaptive mesh refinement (AMR) to increase the dynamical resolution within our clusters, as in Paper I. We assumed a ΛCDM cosmology ($h = 0.72$, $\Omega_{\mathrm{M}} = 0.258$, $\Omega_{\mathrm{b}} = 0.0441$ and $\Omega_{\Lambda} = 0.742$) as in Vazza et al. (2010).

Each cluster was selected in a comoving volume of $(260 \ \mathrm{Mpc})^3$, first simulated at coarse resolution (Vazza et al., 2010), and then resimulated with nested initial conditions (Wise & Abel, 2007). We employed two levels of static uniform grids with 256^3 cells each and using 256^3 particles each to sample the dark matter distribution, with a mass resolution per particle of $m_{\mathrm{DM}} = 1.3 \cdot 10^{10} M_{\odot}$ at the highest level.

Then, we further refined the innermost $\sim (25 \ \mathrm{Mpc})^3$ volume, where each cluster forms, with additional 7 AMR levels (refinement $= 2^7$). The refinement was initiated wherever the gas density was $\geq 1\%$ higher than its surroundings. This gives us a maximum spatial resolution of $\Delta x_{\mathrm{max}} = 3.95$ kpc per cell.

With our setup (see Paper I), for $z \leq 1$ the virial volume of clusters is refined at least up to the 6th AMR level (15.8 kpc) at $z = 0$, and most of the central volume within ≤ 1 Mpc from the cluster centre is simulated with 3.95 kpc/cell.[1]

In this work, we will only discuss *non-radiative* cosmological simulations, meaning that we only included the effect of cosmic expansion, gas, Dark Matter self-gravity and (magneto)hydrodynamics, in order to solely focus on the growth of

---

[1]Each cluster simulation used $\sim 30,000 - 50,000$ core hours running on 64 nodes on JUWELS at Jülich Supercomputing Centre.

magnetic fields by the turbulence induced by structure formation.

In order to seed magnetic fields at the beginning of our runs, we mimic a simple primordial origin of magnetic fields, in which we initialized the field to a uniform value B_0 across the entire computational domain, along each coordinate axis. The initial magnetic seed field of 0.1 nG (comoving) is chosen to be below the upper limits from the analysis of the CMB (e.g. Subramanian, 2016). This particular setup is easy to implement, ensures $\nabla \cdot \vec{B} = 0$ by construction, and has been already tested in our previous work on the subject (Vazza et al., 2014, 2018). Moreover, several studies have shown that the impact on the initial magnetic field topology within galaxy clusters (provided that the simulated dynamical range is large enough to enter the dynamo regime) is negligible (e.g. Marinacci et al., 2015; Vazza et al., 2017; Vazza et al., 2018), hence our results do not strongly depend on this particular setup.

We refer the reader to Appendix 3.7 for a short overview of the key findings of Paper I. There, we showed that our numerical setup provides enough resolution to resolve the MHD scale, l_A, in a large fraction of the cluster volume during its late evolution ($z \leq 1$). Moreover, the simulations show features of small-scale dynamo amplification. However, as we discuss in depth in Section 3.4, some results can be affected by the limited spatial resolution.

3.2.2 Fitting the magnetic power spectrum

The three-dimensional power spectrum is defined as

$$P_{ij}(\mathbf{k}) = \frac{1}{(2\pi)^3} \int \int \int e^{-i\mathbf{k}\cdot\mathbf{x}} R_{ij}(\mathbf{k}) d\mathbf{k}, \tag{3.1}$$

where $R_{ij} = \langle u_i(\mathbf{x_0}) u_j(\mathbf{x_0} + \mathbf{x}) \rangle$ is the two-point correlation function between the velocities u_i and u_j (e.g. Batchelor, 1951). When the corresponding fields do not depend on the position and only depend on the distance between two points, i.e. we consider homogeneous and isotropic fields, the total energy is given by

$$E_{tot} = \frac{1}{2} \left\langle u_i^2 \right\rangle = \frac{1}{2} R_{ii}(\mathbf{0}) = \int_0^\infty E(k) dk, \tag{3.2}$$

where $E(k)$ is thus the scalar energy distribution per unit mass for the mode k related to the diagonal components of the tensor R_{ij}, and therefore, the relation between this spectral energy and the one-dimensional power spectrum is found to be

$$E(k) = 2\pi k^2 P_{ii}(k). \tag{3.3}$$

This approximation works well for the rather chaotic and isotropic velocity field always found in cosmological cluster simulations (e.g. Dolag et al., 2005; Vazza et al., 2011a; Wittor et al., 2017). We computed first the power spectrum by using standard algorithms for the three-dimensional Fast Fourier Transform (FFT) of the velocity and magnetic fields within the simulation box and then by summing up the contributions over spheres within a radius $k = \sqrt{k_x^2 + k_y^2 + k_z^2}$ in Fourier space. Finally, by multiplying by the factor $2\pi k^2$, we obtained the energy spectrum of the magnetic and velocity field.

While the velocity power spectra can be characterized by a power-law and by an injection scale, the magnetic spectra are more complex. We fit the magnetic spectra by the equation:

$$E_M(k) = A\,k^{3/2}\left[1 - \mathrm{erf}\left[B\ln\left(\frac{k}{C}\right)\right]\right], \tag{3.4}$$

where the A parameter gives the normalization of the magnetic spectrum, B is related to the width of the spectra and C is a characteristic wavenumber corresponding to the inverse outer scale of the magnetic field (see Fig. 3.1). Eq. (3.4) is rooted in dynamo theory as a solution for single-scale turbulent flows (Kazantzev (1967), Kraichnan & Nagarajan (1967), Kulsrud & Anderson (1992)). In the remainder of the paper we propose to use Eq. (3.4) as a proxy to characterize our evolving magnetic spectra with a minimal set of parameters (A, B, C as detailed above), even though the equation is not valid for the scales and conditions that we are studying. It should be stressed that the aim of the paper is not to connect directly these parameters with Kazantzev's dynamo model since the generation and evolution of turbulent magnetic fields in the ICM are affected by a hierarchy of complex processes. In particular, we note that:

1) The assumptions under which Eq. (3.4) is derived, such as having a single-scale turbulent flow, a Kolmogorov spectrum for the velocity field, neglecting the resistive scale, etc. (see more details on the assumptions and derivation in Kulsrud & Anderson 1992) are not valid since, in our system, laminar gas motions and advection at many scales may also affect the topology of the magnetic fields in the ICM. Furthermore, the magnetic field is amplified and re-shaped by the turbulence generated every time a merger occurs.

2) The analysis of non-linear effects such as ambipolar diffusion or magnetic reconnection are far beyond the scope of this work. But we can comment that some of these affects have been also studied in Kulsrud & Anderson (1992), where the final magnetic power spectrum exhibits a similar shape, i.e. a power law multiplied by a Macdonald function (or modified Bessel function of second order) of different orders. For small k, they can reduce to Eq. (3.4).

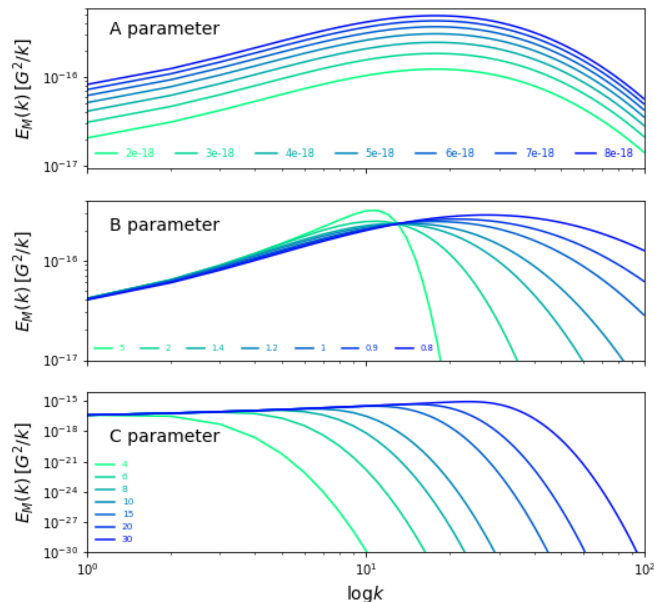3) As long as the velocity scale responsible for the dynamo forcing is larger

Figure 3.1: Variation of A, B and C parameters in Eq. (3.4). *Top panel:* change in the normalization. *Middle panel:* change in the width. *Bottom panel:* change in the position of the outer scale.

than the scales where the magnetic energy spectrum peaks, Eq. (3.4) is valid. This condition is matched during the initial stage of cluster formation, and is later violated after the magnetic field has grown to larger scales. It is our intention to quantify the development of magnetic fields as a function of resolution (as in Paper I) as well as of the cluster evolution. For this reason, it is convenient to apply Eq. (3.4), as the dynamo in our runs is expected to stay in the kinematic regime for long due to the finite numerical resolution (e.g. Beresnyak & Miniati, 2016).

3.3 Results

3.3.1 Magnetic fields in the cluster sample

In this section we analyze a sample of seven clusters in different dynamical states: clusters with ongoing mergers (ME) at $z = 0$, relaxed ones (RE) and post major merger ones (PM). In Fig. 3.2 we show the projected gas density and magnetic field

ID	$M_{100}[\mathrm{M}_\odot]$	R_{100} [Mpc]	Dynamical state	$B_0[\mu\mathrm{G}]$	A (10^{-17} [G²/k])	B ([-])	C (k[1/2 Mpc])
E14	$1.00 \cdot 10^{15}$	2.60	RE	1.726	5.470 ± 0.111	1.090 ± 0.009	6.461 ± 0.096
E5A	$0.66 \cdot 10^{15}$	2.18	ME	1.050	1.985 ± 0.059	1.054 ± 0.012	8.708 ± 0.192
E1	$1.12 \cdot 10^{15}$	2.67	PM ($z_{\mathrm{last}} = 0.1$)	1.308	2.052 ± 0.036	1.118 ± 0.009	10.052 ± 0.131
E3A	$1.38 \cdot 10^{15}$	2.82	PM ($z_{\mathrm{last}} = 0.2$)	1.672	2.372 ± 0.041	1.167 ± 0.009	8.936 ± 0.110
E16B	$1.90 \cdot 10^{15}$	3.14	PM ($z_{\mathrm{last}} = 0.2$)	2.474	9.041 ± 0.164	1.134 ± 0.009	10.437 ± 0.138
E4	$1.36 \cdot 10^{15}$	2.80	PM ($z_{\mathrm{last}} = 0.4$)	1.572	4.521 ± 0.074	1.124 ± 0.008	10.236 ± 0.123
E18B	$1.37 \cdot 10^{15}$	2.80	PM ($z_{\mathrm{last}} = 0.5$)	1.716	3.396 ± 0.049	1.113 ± 0.007	9.974 ± 0.106

Table 3.1: Main parameters at $z = 0$ of the galaxy clusters analyzed in this work. The 4th column lists the tentative dynamical classification of each object (with the approximate redshift of the last major merger, in the case of post-merger clusters). The value of B_0 is the mean magnetic field within 200 kpc from the corresponding radial profiles plotted in Fig. 3.3

strength for all of our clusters, considering the highest resolution of our simulation (3.95 kpc). A list of the main parameters of our simulated clusters is given in Tab. 3.1. The estimate of the total (gas+DM) mass inside R_{100}, as well as the tentative classification of the dynamical state at $z = 0$ of each object follows from Vazza et al. (2010). Our dynamical classification is done in two steps: firstly, clusters with a major merger (based on the total mass accretion history within R_{100}) for $z < 1$ are classified as *post-mergers* (PM). In particular, major mergers in the range $0 \le z \le 1$ are selected considering that the change of the mass increment $\xi = M_2/M_1$ is $\xi > 0.3$, where M_1 is the mass at a time t and M_2 is the mass at time $t + 1$ Gyr (Fakhouri et al., 2010). Secondly, if no major merger is found in this time interval, we additionally compute the ratio between the total kinetic energy of gas motions inside R_{100}, E_K, and the total energy ($E_{\mathrm{tot}} = E_K + E_T$) inside the same volume. This parameter has been shown to characterise the dynamical activity of clusters well (e.g. Tormen et al., 1997). *Relaxed* (RE) clusters typically have $E_K/E_{\mathrm{tot}} < 0.5$ while *merging* (ME) clusters have $E_K/E_{\mathrm{tot}} \ge 0.5$. In Tab. 3.1 we also list the redshift of the last major merger (z_{last}) for post-merger systems, while for relaxed systems we conventionally consider $z_{\mathrm{last}} = 0$ and $z_{\mathrm{last}} = 1$ for merging systems. For a more detailed discussion of the classification scheme we refer the reader to Vazza et al. (2010) and references therein.

For each cluster, we computed the radial profile of the average magnetic field from the peak of gas density at $z = 0$ at the highest resolution, as shown in Fig. 3.3. Within the sample variance, we find that the magnetic field follows gas density as $B(n) \approx B_0 \cdot (n/n_0)^{0.5}$ (where n is the gas density and n_0 is the core gas density) as in Paper I. In fact, the radial profiles in Paper I appear to be consistent with what can be derived by Faraday Rotation analysis of the Coma cluster (Bonafede et al., 2013), despite the fact that the distribution of magnetic field components found in our simulations deviate significantly from a Gaussian distribution. The central
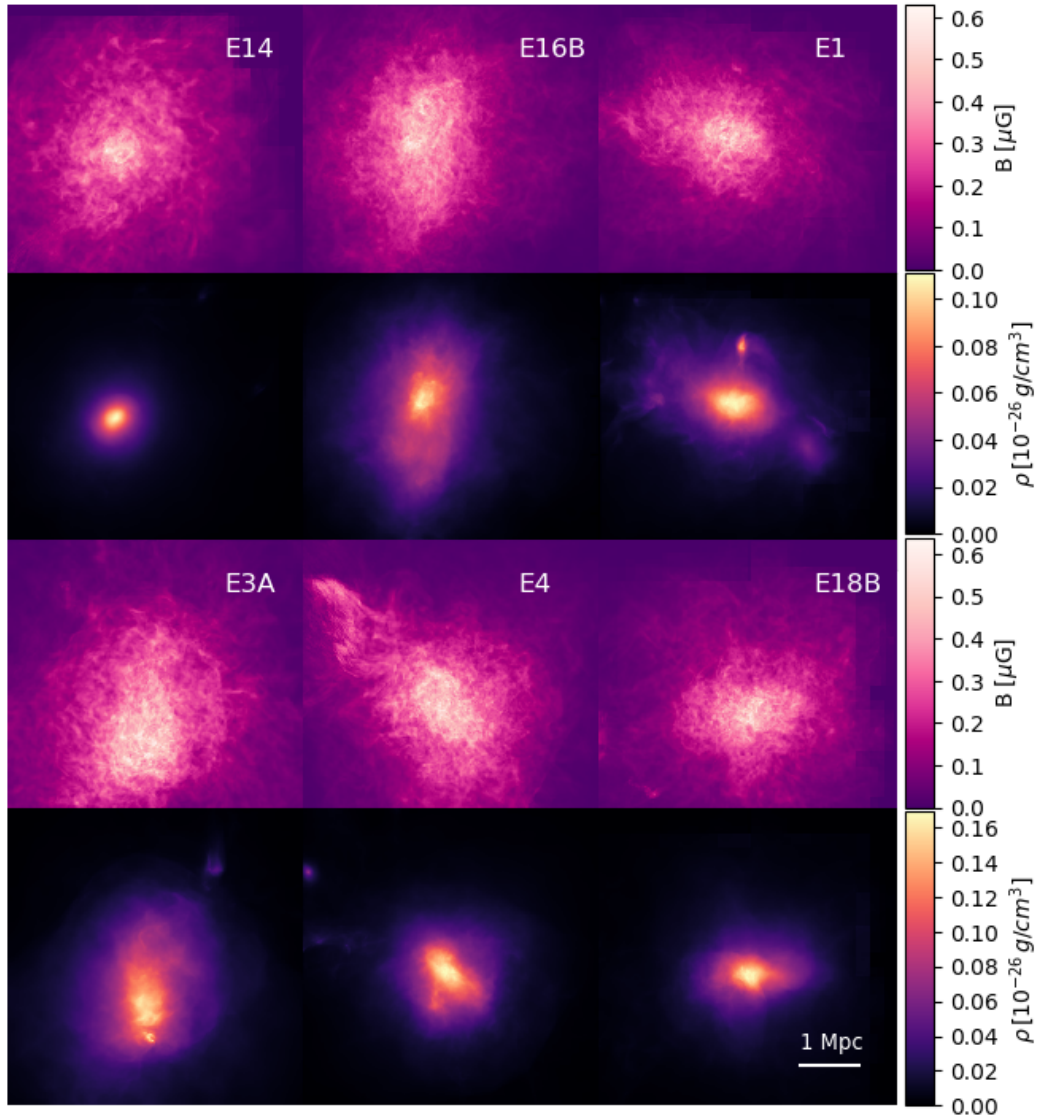
Figure 3.2: Maps of projected gas density and magnetic field strength for all clusters in our sample at $z = 0$ (we omit cluster E5A since this cluster is analyzed in detail in Section 3.3.3 and 3.3.4). The main characteristics of these clusters can be found in Tab. 3.1.
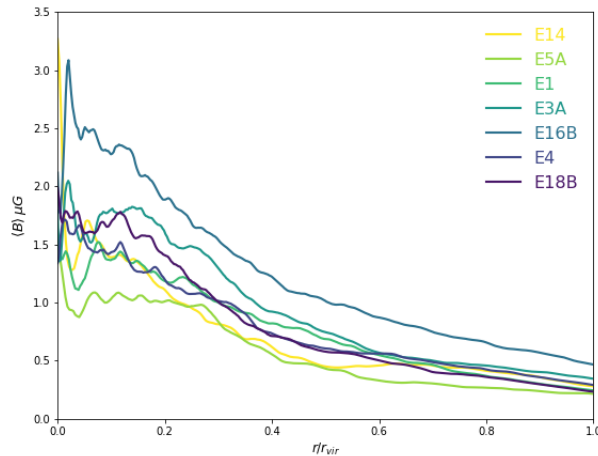
Figure 3.3: Radial profile of the magnetic field for all the clusters in our sample at $z = 0$ computed at our highest resolution run at the 8th AMR level.

magnetic field value of each cluster, B_0, is given for reference in Tab. 3.1. In general, we can see that the most perturbed cluster (E5A) does not show the strongest fields. The central value, B_0 (measured as the average within the innermost ≤ 200 kpc radius from the cluster centre), is strongly correlated with the mass of the cluster. Indeed, in Fig. 3.3 we can see that the higher the mass, the higher the central value of the magnetic field. While observations do not show a clear correlation of the mean magnetic field with the mass of the host cluster (e.g. Govoni et al., 2017), our normalization A, which is the parameter most closely linked to the Faraday Rotation, shows little correlation with mass, and has a large scatter.

3.3.2 Spectral properties in the cluster sample

Next, we proceeded to compute the magnetic energy power spectra for the innermost region of all clusters at $z = 0$ as described in Sec. 3.2.2 . We computed power spectra only for the innermost $\approx 2^3$ Mpc^3 region of each cluster, where the resolution is approximately constant and equal to the 8th and maximum AMR level (corresponding to a 512^3 grid). By doing so, we can neglect the effect of coarse-mesh effects in our FFT analysis as the majority of the central cluster volume is refined up to the highest level for all our clusters (see discussion in Vazza et al., 2018). The corresponding spectra, along with the best-fit curves are plotted in the top panel of Fig. 3.4 and the best-fit parameters are listed in Tab. 3.1. To a good degree of approximation, all spectra are well fitted by Eq. (3.4) regardless of the dynamical state of each cluster. All clusters in the sample show similar spectral shapes, with a peak of magnetic

energy in the range $\sim 200 - 300$ kpc and differences in normalization of a factor ≤ 5. As shown in Vazza et al. (2018), this non-Gaussian distribution of magnetic field strengths may result from the superposition of multiple magnetic field components that have been accreted at different times via mergers. For completeness, we also show the kinetic spectra of all the clusters in the central panel of Fig. 3.4. These kinetic spectra are very similar, i.e. we observe a higher normalization for perturbed clusters as there is more turbulence involved in these systems, and the lowest normalization is observed for the relaxed cluster (E14). Comparing this to the magnetic spectra shown in the top panel of Fig. 3.4, we can clearly see that a higher level of turbulence does not necessarily imply higher values of the magnetic field. This may seem counter-intuitive but it is caused by the fact that the amplification of magnetic fields from small to large spatial scales is a slow process that takes a few eddy turnover times. Therefore, even in the presence of a large input of turbulent kinetic energy, significant magnetic amplification can only be observed with a delay of $\sim$ Gyr. While part of this delay is caused by numerical effects (e.g. our numerical finite growth rate depends on the limited Reynolds number our simulation can resolve), this delay is of the same order as the eddy turnover timescale for ~ 500 kpc turbulent eddies being injected with a $\sigma_v \sim 500$ km/s velocity. This is the necessary time span for turbulence to cascade down to the scales that can drive a dynamo growth.

In the bottom panel of Fig. 3.4 we plot the ratio between kinetic and magnetic energy in order to visualize the scales at which equipartition is reached. RE systems reach equipartition at larger scales compared to PM systems, which is consistent with the general picture of a small-scale dynamo acting according to the amount of turbulence in the system. As expected, we also observe that the ME system is still not in equipartition at larger scales because this is the most perturbed cluster and it is mostly dominated by compressive turbulence.

Parameterization of cluster magnetic spectra

Our analysis in Paper I supports that the magnetic spectra show signs of a dynamo near saturation (see Appendix 3.7). However, as we shall see in Sec. 3.3.3, if a small-scale dynamo is acting, it co-exists with bulk motions on larger scales that are affecting the evolution of the magnetic field during the whole assembly history of the clusters. As a consequence, the magnetic properties in our sample result from the cumulative (and discontinuous) action of dynamo during the entire cluster lifetime. Therefore, there is no immediate connection between the spectral magnetic properties and the turbulent properties of the cluster at a given time.

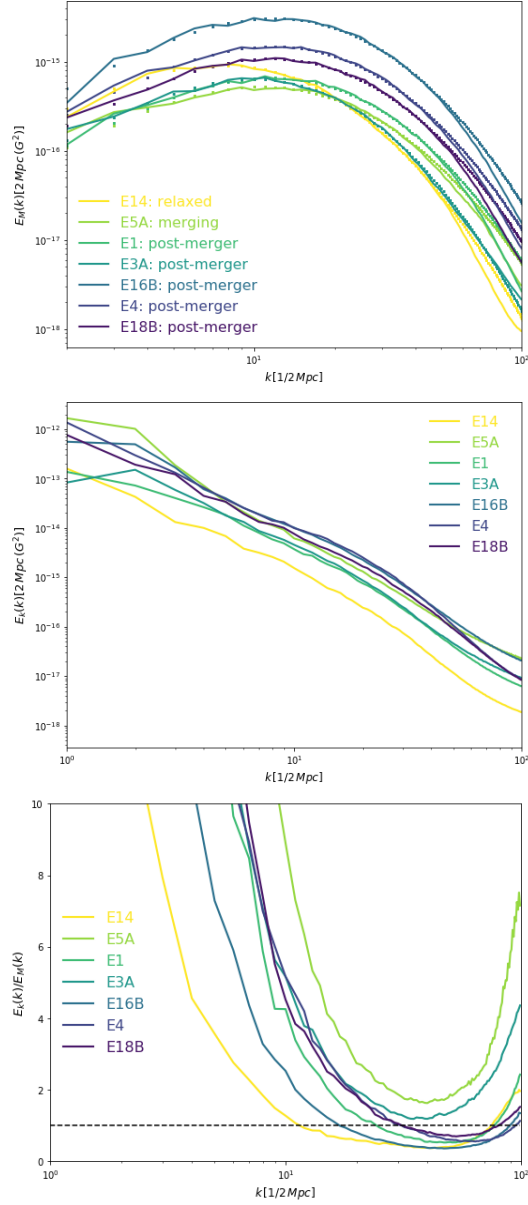In order to study how the best-fit parameters, A, B and C, are related to

Figure 3.4: Magnetic energy (*top panel*) and kinetic energy (*middle panel*) spectra of all of our cluster sample at $z = 0$. The kinetic spectra were multiplied by $\sqrt{n}$, where n is the gas density, in order for the spectra in both panels to have the same units. The solid lines correspond to the data and the scatter plots show the best-fit of the corresponding data using Eq. (3.4). In the *bottom panel* we show the ratio of kinetic to magnetic energy, $E_K/E_M(k)$, the horizontal black dashed line indicates where we have equipartition.
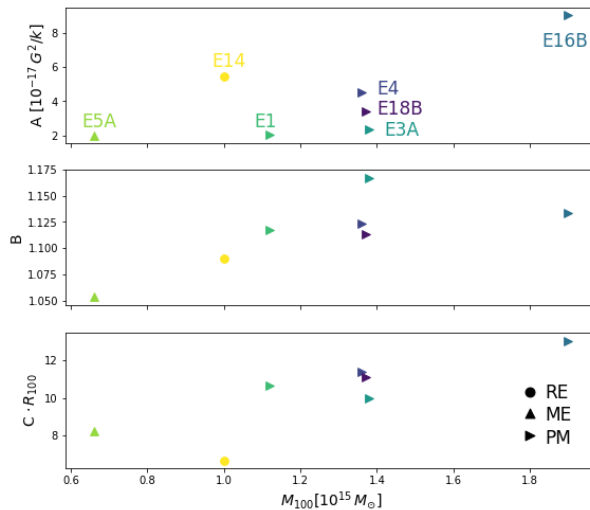
Figure 3.5: Comparison of best-fit parameters of each cluster in our sample at $z = 0$ according to their virial mass.

the mass, dynamical state and redshift since the last major merger, we produced Figs. 3.5, 3.6 and 3.7. For our limited sample, we can conclude:

1) The spectrum normalization (A): We find a dependence of the mass of the host cluster, and also a hint of a dependence on the dynamical state of the cluster. For a given mass bin we find $A_{\mathrm{ME}} < A_{\mathrm{PM}} < A_{\mathrm{RE}}$. On the other hand, we do not find a correlation with the time since the last major merger.

2) The spectrum width (B): This parameter is found to depend on the dynamical state of each cluster, i.e. B is larger in less perturbed systems (PM) and smaller in highly perturbed systems (ME). This presumably means that relaxed systems have had enough time for turbulence to cascade to the small scales and amplify the magnetic field during past mergers resulting in a broader spectrum; whereas the merging systems have a more restricted region of magnetic amplification. As will be mentioned in 3.3.4, mergers shift the spectrum towards smaller scales, thus the combination of this shift and the narrow spectrum means that merging systems contain more small-scale eddies. Therefore perturbed systems have a higher magnetic growth rate than relaxed systems.

3) The inverse of the outer scale of magnetic field (C): we find a hint of a dependence on the mass and the dynamical state of the cluster, $C_{\mathrm{RE}} < C_{\mathrm{ME}} < C_{\mathrm{PM}}$. On the assumption of the existence of a small-scale dynamo, this would suggest that in more relaxed systems the dynamo had more time to grow towards
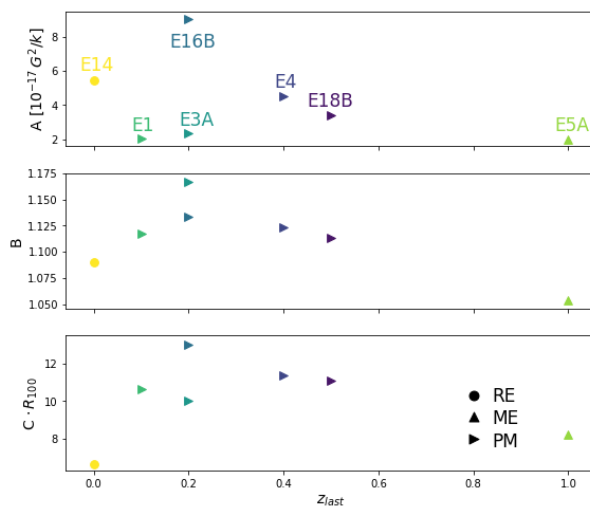
63

Figure 3.6: Comparison of best-fit parameters of each cluster in our sample to their last major merger event.
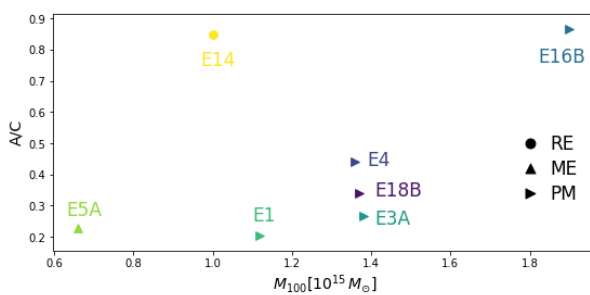

Figure 3.7: Combination of best-fit parameters of each cluster (proportional to the rotation measure (RM)) in our sample compared to their virial mass.

larger scales (i.e. lower values of C). In the case of an on-going merger (as will be discussed in more detail in Sec. 3.3.3), large scale gas motions may also affect the magnetic spectra merely by compression. In principle, it will be possible that advection and buoyancy in a stratified medium such as the ICM also play a role in the outer scale behaviour, but the study of these effects are beyond the scope of this paper.

4) Dependence on the time since the last major merger: We did not find a correlation between the epoch of the last major merger (z_{last}) and the best-fit parameters (A,B and C), which suggests that the magnetic energy spectrum at a given epoch does not retain much information about specific events, as well as that minor mergers are also an important player in setting the spectral properties of the ICM at $z = 0$ (see discussion in 3.3.4). Moreover, given the limited sample size we have here, it is difficult to disentangle effects connected to the mass of the host cluster and the dynamical state.

5) Rotation measure dependence on mass: The rotation measure (RM) of polarised radio emission from background sources scales as $|RM| \propto \int B_{||} \cdot n_e \, dl$, which can be approximated to $|RM| \propto B_\Lambda \cdot \Lambda_B$, where B_Λ is the magnetic field at the autocorrelation scale Λ_B. To a first approximation, the total $|RM|$ from a clusters should scale with the $\propto A/C$.

We find that the RM depends weakly on the mass(because of A and C dependence on mass), but scatters due to a dependence on the dynamical state of each cluster. This causes clusters with a factor ~ 2 difference in mass to show a very similar A/C value (i.e. E14 and E16B, see Fig. 3.7).

In order to link the evolution of magnetic spectra to the dynamical growth of galaxy clusters, in the next section we will analyze the assembly of one particular cluster.

3.3.3 Detailed evolution of cluster E5A

We studied the evolution of the cluster E5A by analysing a total of ≈ 100 snapshots in the range from $z = 1.379$ to $z = 0$. The cluster E5A is an interesting object as it forms via several mergers in the course of nearly 9 Gyr.

We work on uniformly gridded data reconstructed at the 6th AMR level (15.8 kpc resolution). This is done even if the simulation has refined down to the 8th AMR level. In Fig. 3.8 we show snapshots of the density and magnetic fields in a simulation box of 640^3 cells. The maps in Figs. 3.8-3.9 show a volume-weighted projection of the magnetic field strength along the line-of-sight in order to emphasize the diffuse

magnetic field structure on large scales. Hence, the magnetic field values in the map are biased towards lower values than the ones measured in the computational box.

Next, we identified the centre of the main cluster (cyan dot in Fig. 3.8) and then followed the evolution of gas and magnetic fields within a box of 100^3 cells co-moving with the main cluster centre. The trajectory of the centre was obtained by computing the location of the maximum of the thermal energy after smoothing the data over a length of ~ 20 cells at each snapshot, and by applying a cubic spline time interpolation.

The final stage of the merger at $z = 0$ is shown in Fig. 3.9, where the volume distribution of the gas density and the magnetic field strength are plotted in x,y and z directions. The magnetic field distribution is asymmetric, showing a tangled structure and its strength increases towards the centre of the major component. At least two prominent peaks in the magnetic field distribution (at the $\sim \mu G$ level) near the central region are visible in all lines of sight. These peaks correspond to the largest and the second largest components.

In Fig. 3.10 we show the evolution of the magnetic field strength, temperature and velocity within the moving simulation box. Every merger event is found to perturb the system and to increase the thermalization of the ICM, shown as peaks on the temperature evolution in Fig.3.10. While gas velocity and gas temperature show pronounced peaks close each merger event, the evolution of the averaged magnetic field strength is smoother. These smoothed peaks are correlated with the merger events, but show a delay of about ~ 0.5 Gyr with respect to the velocity peaks. In Fig. 3.11 we show the evolution of the total energy budget of the cluster (top panel) and the corresponding evolution of the energy ratios (bottom panel). During the whole period of evolution (~ 9 Gyr), the magnetic energy has grown by a factor $\sim$ 40-50, the kinetic energy by a factor of $\sim$ 90-100, and the thermal energy has grown by a factor $\sim$ 10-20. By the end of the simulation ($z = 0$), the kinetic energy is $\sim$ 10-40% of the thermal energy, while the magnetic energy is $\sim 10^{-3}$ of the thermal energy.

3.3.4   Spectral evolution of cluster E5A

In this section we focus on the spectral features of the magnetic and kinetic energy power spectra, whose entire evolution is given in Fig. 3.12. The spectra are shown using comoving units and are computed within a box of comoving size $L = 1.58$ Mpc, which moves with with the cluster centre identified as described in Section 3.3.3. The first thing to notice is that the shape of both spectra change very little over the period from $z = 1.379$ to $z = 0$, while the normalization increases whenever a minor merger occurs. In the bottom panel of Fig. 3.12, we can observe that the evolution of
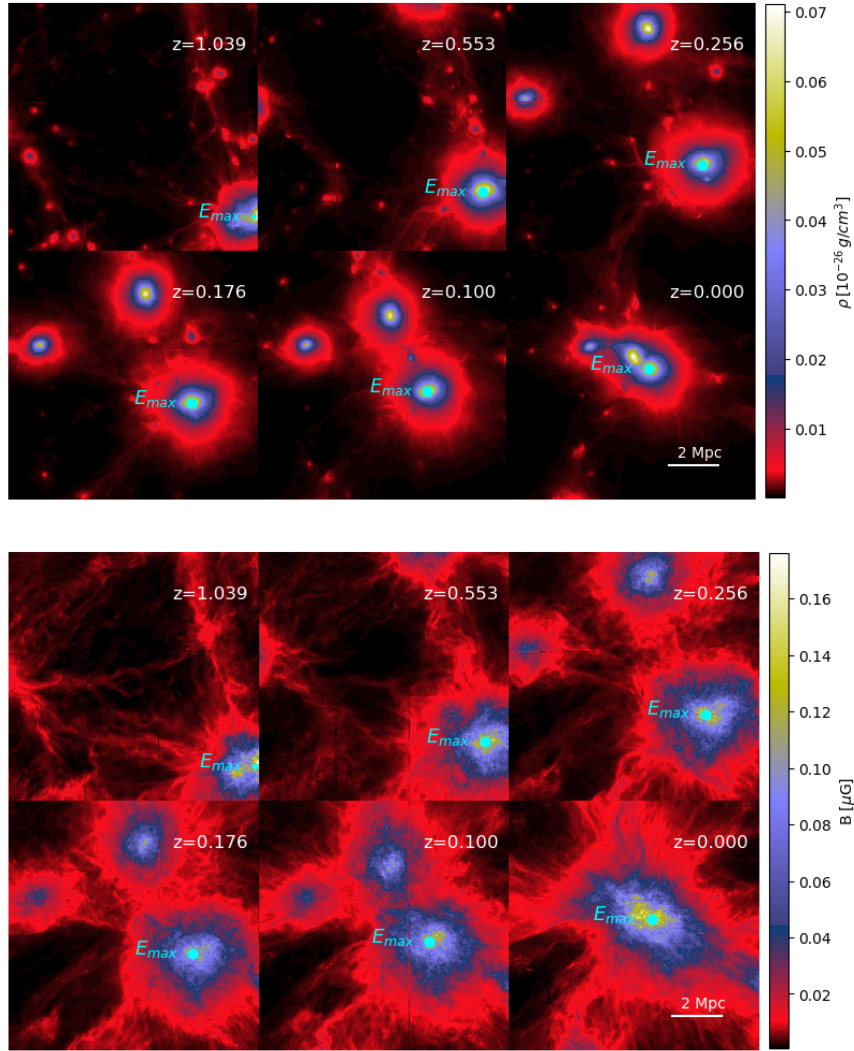
Figure 3.8: *Top panels:* projected z-component density field averaged a long the line-of-sight at various redshifts. *Bottom panels:* projected z-component of the magnetic field strength averaged a long the line-of-sight at the same redshifts as the top panels. The dots indicate the centre of the most massive component at each redshift. The centre position was obtained by taking into account the kinetic energy within a simulation box of 640^3 cells (see text for more details).
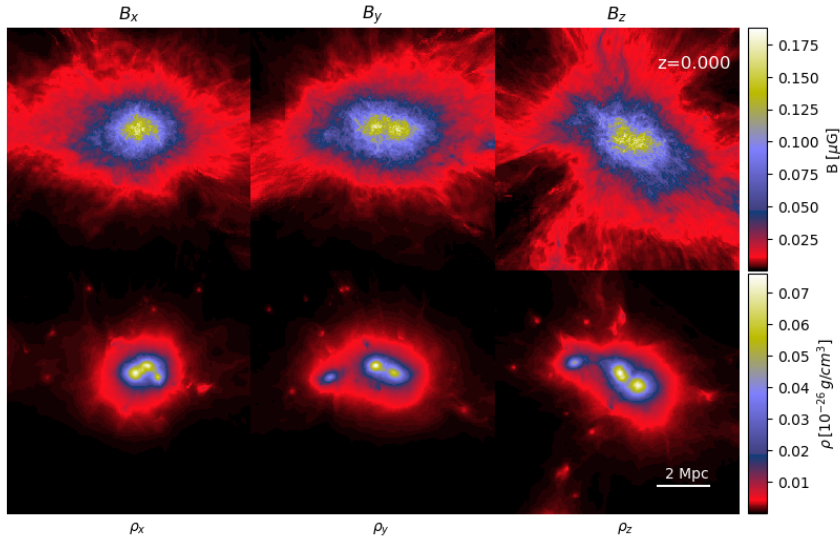
Figure 3.9: Maps averaged along the line-of-sight of the simulation box at z=0. The *top panels* show the projected magnetic field strength and the *bottom panels* show the projected density.
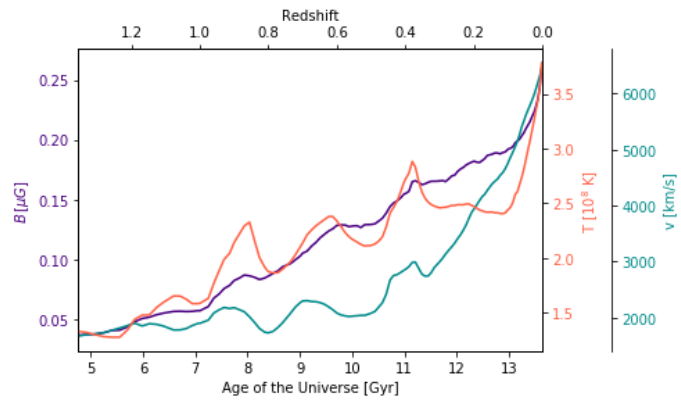

Figure 3.10: Evolution of the average magnetic field strength, temperature and velocity of the 100^3 simulation box
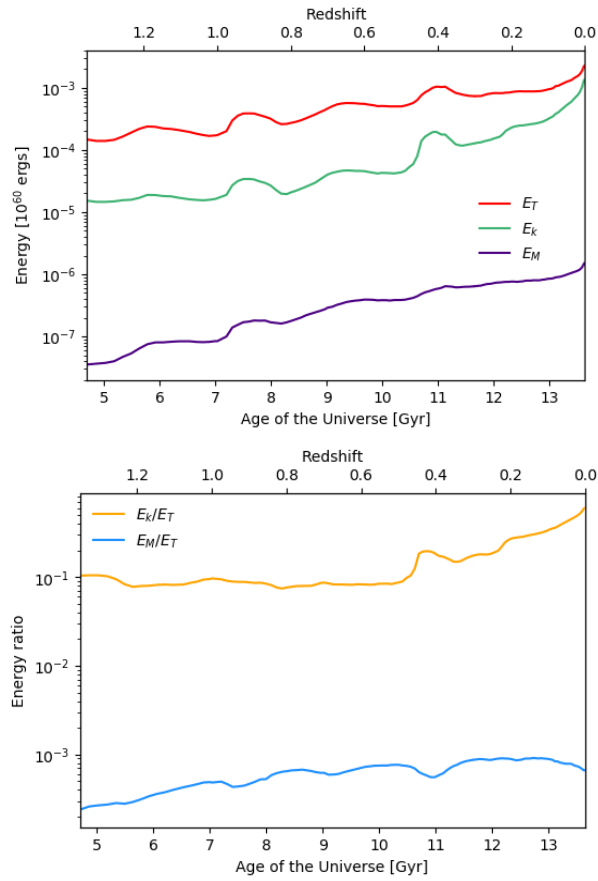
Figure 3.11: Energy evolution of the 100^3 simulation box. The *top panel* shows the evolution of the thermal energy (red), kinetic energy (green) and magnetic energy (purple). The *bottom panel* shows the corresponding energy ratios.

the magnetic energy spectra shows a global increment on the magnetic field strength up to an approximate state of equipartition for $k \sim 20 - 50$ (corresponding to scales $\sim 30 - 80$ kpc). This means that during a significant fraction of the system evolution the magnetic tension is strong enough to prevent the further bending of the magnetic lines, as would be expected from a classic small-scale dynamo. However, the range of scales in which equipartition is reached does not evolve monotonically with time (as expected in a classic dynamo), but it fluctuates in time, with features that are non-trivial to isolate. In particular, the epochs where there is no equipartition coincide with the occurrence of mergers, i.e. when the cluster is more perturbed. The various kinetic injections driving turbulence in this system will continuously change the magnetic field topology on spatial scales larger than the equipartition scale.

In order to examine the evolution of E5A, in Fig. 3.13 we colour coded the amplitude of the magnetic and kinetic spectra as a function of time. This spectral time sequence shows the entire evolution of the ICM as a function of time and spatial scale. As the system evolves, the magnetic power increases and tends to shift towards smaller scales, while the kinetic spectrum is always characterized by a maximum at $k = 1$, which mirrors the fact that the forcing of turbulence always occurs on scales ≥ 1 Mpc. Merger events can be seen as horizontal stripes in the plot, which correspond to the injection of kinetic energy.

The resulting amplification of the magnetic field strength is then a complex interplay between compression and the small-scale dynamo. This is best shown by the appearance of dense gas structures at a similar time, as shown in the power spectra of gas density in Fig. 3.14, which is consistent with the relation between velocity and density fluctuations in the stratified ICM (e.g. Gaspari et al., 2014).

A general trend is that every merger shifts the magnetic spectral power towards *higher* wave numbers, i.e. during most of these events the peak of the magnetic energy spectrum moves towards smaller spatial scales, unlike what is expected from the standard dynamo model, and most likely due to gas compression. As cluster mergers generate shocks and bulk flows that enhance the gas density and compress the magnetic field lines, this can also increase the normalization of the spectrum. Furthermore, it can also move the peak of the spectrum to higher wave numbers because the magnetic field lines get stretched along the merger direction.

Simultaneously, mergers inject turbulence, and only after the latter has decayed to small scales (where the eddy turnover time is the shortest), the peak magnetic spectra shifts towards lower wave numbers and the magnetic field is boosted again. This effect is characteristic of a small-scale dynamo.

Our analysis implies that both, compressive and dynamo amplification, tend to be present at the same time in galaxy clusters. This causes a difficult evolutionary
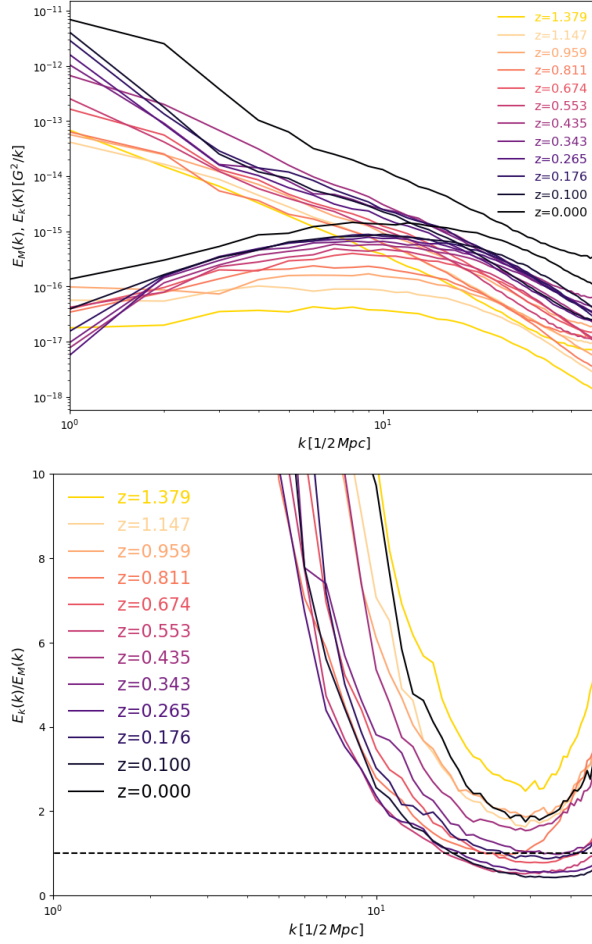
Figure 3.12: *Top panel:* Evolution of the spectral kinetic and magnetic energy in the simulation box of 100^3 cells. The top spectra correspond to the kinetic energy and the bottom spectra correspond to the magnetic energy. The velocity power spectrum was multiplied by $\sqrt{n}$, n being the gas density, in order for the spectra to have the same units. *Bottom panel:* Ratio of kinetic to magnetic energy as function of the wave number. The horizontal dashed line indicates where we have equipartition.
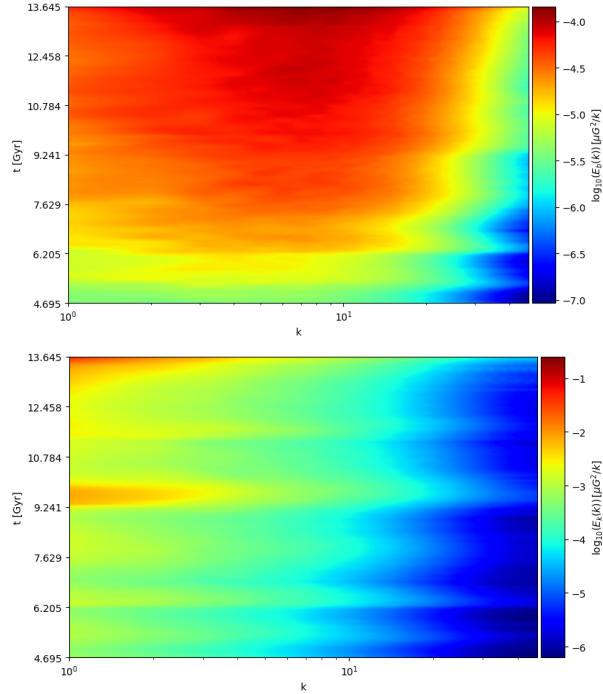
Figure 3.13: Evolution of the spectral energy in the simulation box of 100^3 cells. The *top panel* shows the corresponding evolution of the magnetic energy and the *bottom panel* shows the evolution of the kinetic energy.

pattern in the simulated ICM, adding complexity to what has been previously obtained by more idealized MHD simulations (e.g. Beresnyak & Miniati, 2016; Miniati & Beresnyak, 2015).

For better visualization, Fig. 3.15 shows the residual between magnetic and kinetic spectral energies also as a spectral time sequence plot. At all epochs, the excess magnetic energy is found on wave numbers $k > 10$ (corresponding to scales < 160 kpc), showing that after merger events the magnetic tension gets strong enough to overcome further bending of the magnetic lines only at small scales. The magnetic amplification starts *only* after merger events because the turbulence injected takes a few eddy-turnover times to cascade.

In fact, if the kinetic energy injection is high enough, as we can observe around $t \sim 9.8$ Gyr in Fig. 3.15, the amplification is slowed down.

In order to identify the specific times of kinetic energy injection, we plotted in Fig. 3.16 the difference of the total kinetic energy in the simulation box at timestep t_i with respect to the previous timestep, t_{i-1}. A peak in this plot can account mainly
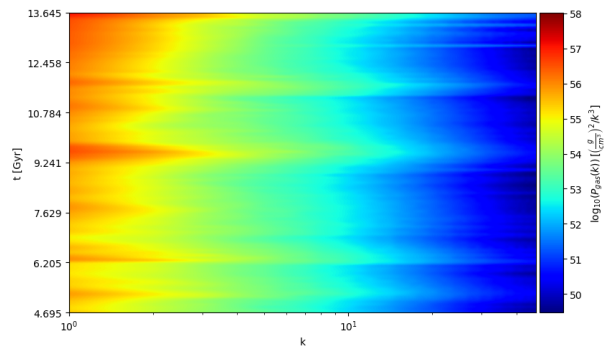
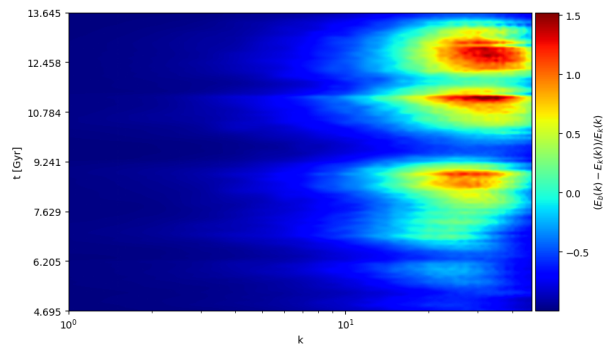Figure 3.14: Density power spectrum as a sequence of time.

Figure 3.15: Energy residual evolution corresponding to the energies in Fig. 3.13. The highest values appear at small scales showing how the amplified magnetic field is able to overcome the kinetic pressure.
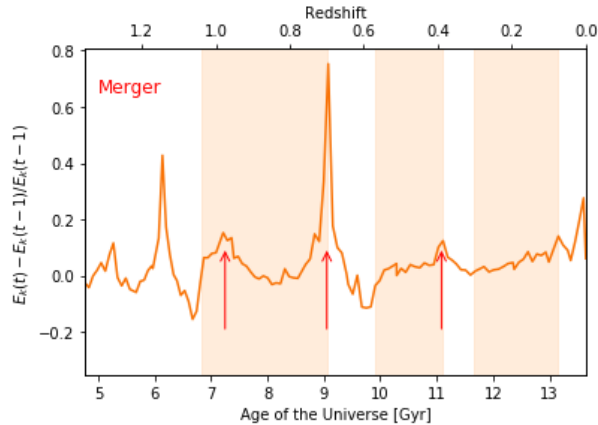
Figure 3.16: Kinetic energy residual as function of time. The red arrows are related to the time when an in-falling gas clump crosses the centre of the cluster. The shaded areas are identified directly with Fig. 3.15, therefore indicating the periods of amplification.

for either the entrance of a clump into the simulation box, a shock traveling across the cluster or a reflected shock. Since we are interested in studying the amplification periods identified in Fig. 3.15, we restrict ourselves to point out only some of these events confirmed by visual inspection with red arrows in Fig. 3.16. The shaded areas in the plot are placed as a reference for the amplification phases found in the spectral time sequence of Fig. 3.15. We noticed that, the maximum kinetic injection appears to happen either when gas substructures cross close to the cluster centre, which typically leads to shock waves ($\mathcal{M} \sim 2$–3 in this case, as we measured with a velocity-based shock finder following Vazza et al. 2017) sweeping through the cluster; or when there is a continuous injection of turbulence by minor mergers (period between $t \sim 12$–13 Gyr). In the first case, the most significant boosts of kinetic energy are followed by the compression of the magnetic field spectra. The injection of large amounts of kinetic energy on large scales impact the magnetic field only after $\lesssim 1$ Gyr (white areas after first and second red arrows in Fig. 3.15), suggesting that a small-scale dynamo is activated only after such amount of time. In the second case, continuous minor mergers contribute to the magnetic amplification at small scales by starting to shift the power towards higher scales (period between $t \sim 12$–13 Gyr). This seems to suggest that minor mergers significantly power the small-scale dynamo amplification.

Finally, we studied the evolution of the MHD scale (l_A) using the result from

Brunetti & Lazarian (2007):

$$l_A \sim 3 \left(\frac{B}{\mu G} \right)^3 \left(\frac{L_0}{1\,\text{Mpc}} \right) \left(\frac{\sigma_v}{10^3 \text{kms}^{-1}} \right)^{-3} \left(\frac{n}{10^{-3} \text{cm}^{-3}} \right)^{-3/2} \text{kpc}, \qquad (3.5)$$

where L_0 is the reference scale within the Kolmogorov inertial range and σ_v is the rms velocity within the scale L_0. In this case, we measure the turbulent velocity by filtering the large motions on ≈ 300 kpc. We obtain a distribution of the MHD scale for all of our snapshots and select the mean at each time. In Fig. 3.17 we show the resulting evolution of the corresponding scale (l_A) and compare it to the evolution of the outer scale of the magnetic spectrum ($1/C$). It has been suggested in former studies (e.g. Beresnyak & Miniati, 2016; Miniati & Beresnyak, 2015) that l_A will follow closely the evolution of the outer scale of the magnetic spectrum. Our analysis suggests that in reality the evolution of magnetic fields during mergers is more complicated than that. The system is significantly affected by compression and large-scale coherent motions, whose energy is larger than the small-scale turbulent energy on ≤ 300 kpc scales. In fact, the injected energy may contribute to advect magnetic field lines on large scales (> 100 kpc). Overall, this means that our galaxy clusters exhibit cumulative turbulence cascades with different injection timescales, able to amplify the existing magnetic fields via a dynamo action. Under these conditions, the evolution of the outer scale is mismatched with respect to that of the MHD scale. This has important implications for the future surveys of magnetic fields in galaxy clusters.

The interpretation of magnetic field spectra inferred by Faraday Rotation will not uniquely constrain the magnetic amplification coming from a small-scale dynamo, but may also be contaminated by compression amplification coming from large-scale gas flows.

Evolution of best-fit parameters for cluster E5A

Following the same approach of Section 3.2.2, we proceeded with the fitting of all magnetic spectra in the evolution of E5A, which yields the evolutionary tracks shown in Fig. 3.18. The top panel shows the normalization of the magnetic energy spectrum, where we can see a clear result: the overall amplification of the magnetic field continues to grow but steepens more where mergers occur. In fact, we observe that the normalization almost increases by one factor on the last ~ 0.5 Gyr where a major merger is about to happen. As a consequence of these events and the other effects previously mentioned, the magnetic growth is not linear. While the total magnetic energy increases by a factor of ~ 40-50 (as mentioned in Section 3.3.3), the normalization of the spectrum only increased by a factor of ~ 5 in nearly 9 Gyr.
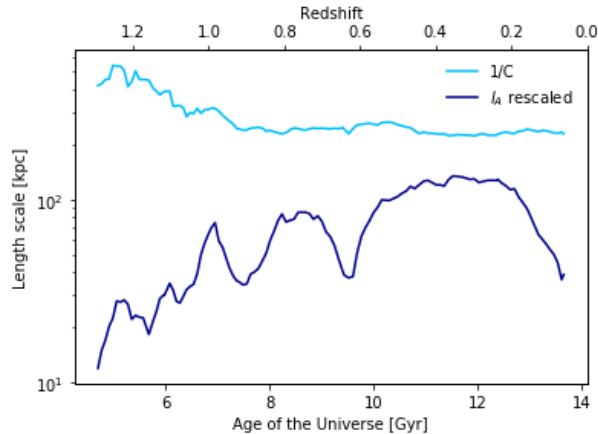
Figure 3.17: Evolution of the MHD scale and the outer scale of the magnetic spectrum (inverse of the C parameter). Note that the MHD scale is rescaled by a factor of 50 for ease of comparison.

In the middle and bottom panels of Fig. 3.18 we show the evolution of the parameters B and C. It is notable that both evolution patterns seem to be correlated. The evolution of C (wave number corresponding to the outer scale of the magnetic spectrum) also shows a correlation with some identified merger events: the red arrows over-plotted corresponding to those in Fig. 3.16. Mergers induce an immediate change of the outer scale of the spectrum by shifting the power towards smaller scales. While this pattern is less obvious in the evolution of the parameter B, we can observe that mergers also induce an immediate broadening of the spectrum. These combined effects can be directly associated with the action of compression. A particular thing to notice is that, the change on B and C at the last (third arrow) merger event is not as large as the previous events. This suggests that at this point, the cluster has had enough turbulence input (at different injection scales and timescales) to amplify the magnetic field at smaller scales, making it harder for the spectrum to broaden or shift its power to even smaller scales.

3.4 Numerical aspects

As in Paper I, we relied on the Dedner cleaning algorithm (Dedner et al., 2002) to get rid of magnetic monopoles. The main limitation of this method is the reduction of the effective dynamical range, compared to Constrained Transport (CT) schemes at the same resolution, due to the intrinsic dissipation of the scheme by $\nabla \cdot \vec{B}$ cleaning
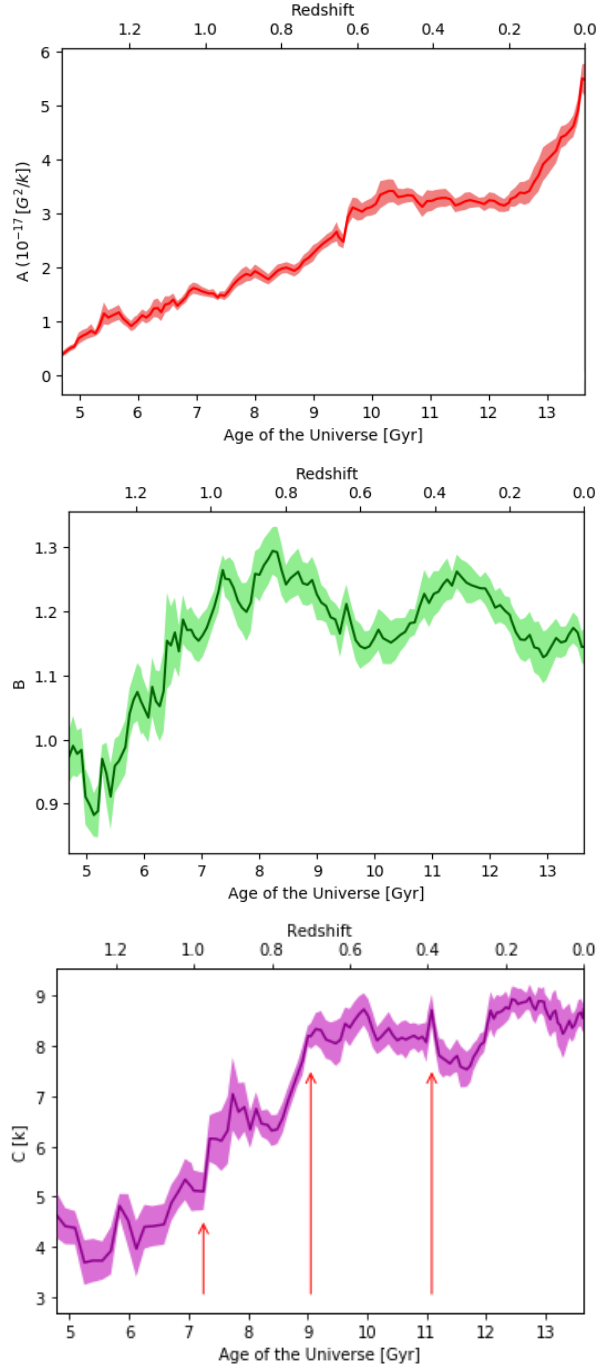
Figure 3.18: Evolution of the best-fit parameters A, B and C obtained by means of Eq. (3.4). The 2σ error envelopes are shown in lighter shades.

77

waves which keep the numerical divergence under control (Kritsuk et al., 2011). Several groups have tested that the Dedner cleaning method is robust and accurate for most idealized test problems, as long as the resolution is opportunely increased (e.g. Wang & Abel, 2009; Wang et al., 2010; Bryan & Enzo Collaboration, 2014). Even in the test of more realistic astrophysical applications, the Dedner method has been shown to quickly converge to the right solution, unlike different approaches to clean $\nabla \cdot \vec{B}$ preserving at run time (Stasyszyn et al., 2013; Hopkins & Raives, 2016; Tricco et al., 2016; Barnes et al., 2018).

Despite the numerical dissipation introduced by the Dedner cleaning, all important features discussed in this paper (e.g. the peak in the power spectrum of magnetic fields, and the equipartition scales) are much larger than the length scales affected by numerical dissipation: e.g. the peak of power spectra are typically on scales $\sim 25 - 50$ larger than the minimum cell size in our the simulation. While the dissipation in the Dedner scheme can considerably slow down the first stage of the dynamo amplification (Beresnyak & Miniati, 2016), once that magnetic structure becomes sufficiently large, they are relatively unaffected by numerical dissipation.

In Paper I we verified that in the largest part of the simulation box, the numerical divergence of B is of order $\sim$ 2-3% of the local magnetic field strength, i.e. $\leq 10^{-4}$ of the magnetic energy on larger scales. We refer the reader to the recent review by Donnert et al. (2018) for a broader discussion of the resolution and accuracy of different MHD schemes in the context of small-scale dynamo processes in galaxy clusters.

Our simulations neglect physical processes other than gravity and magneto–hydrodynamics, such as radiative gas cooling, chemical evolution, star formation and feedback from active galactic nuclei. In this way, we can more easily isolate the effects of compression and dynamo from additional amplification caused by feedback and gas overcooling.[2] Comparisons between the predictions of primordial and astrophysical seeding scenarios of magnetic fields with *ENZO* can be found in Vazza et al. (2017). For recent high-resolution simulation of extragalactic magnetic fields with a moving-mesh algorithm we refer the reader to Marinacci et al. (2018b) and to the recent review by Donnert et al. (2018).

While the initial *topology* of possible seed magnetic fields is unknown, we tested in Paper I that variations of the assumed initial topology of seed fields do not to affect the strength of simulated magnetic fields in the ICM at low redshift. Variations of the assumed initial *strength* of magnetic seed fields are harder to test, as

---

[2]See however Katz et al. (2018), for a possible way of monitoring the growth of different magnetic field components within the same simulation.

for very small seed fields resolving the Alfvènic scale l_A becomes prohibitive and the amplification is stuck in the exponential regime for the entire cluster evolution (Beresnyak & Miniati, 2016). In Paper I, we provided evidence that our simulated magnetic fields are fairly independent on the initial field strength only for ≥ 0.03 nG (comoving) fields. Future re-simulations at even higher resolution, or with less diffusive MHD schemes will be needed to test the scenario for lower seed fields.

Finally, as customary in simulations without explicit viscosity and resistivity, the numerical viscosity and resistivity are of the same order, meaning that the magnetic Prandtl number is $P_M = R_M/R_e = \nu/\eta \approx 1$. This assumption is reasonable enough given the existing uncertainties and the difficulties in the characterization of the magnetised plasma in galaxy clusters (e.g. Schekochihin et al., 2004; Brunetti & Lazarian, 2011a; Beresnyak & Miniati, 2016), and it further allows us to easily compare with the standard literature of small-scale dynamo in a box (e.g. Cho, 2014; Porter et al., 2015). A few groups have explored the role of non-ideal MHD effects in cosmological simulations, such as the presence of a physical resistivity (e.g. Bonafede et al., 2011; Marinacci et al., 2018a), whose usefulness to explain observed ICM magnetic fields has been recently questioned by new simulations (Barnes et al., 2018).

3.5   Summary and conclusions

In this paper, we have presented new high-resolution cosmological MHD simulations of a sample of galaxy clusters, which allow us to study the spectral properties of magnetic amplification with unprecedented spatial and temporal detail.

In agreement with our earlier work, we find that we can reproduce cluster magnetic fields of the order of $\sim 1 - 3$ μG with primordial fields of 10^{-10} G (comoving) at $z = 30$.

We computed the magnetic energy spectra at $z = 0$ for all the clusters in the sample. The spectral shape remains similar across clusters, despite of their different dynamical states. We parameterize the magnetic spectra of all the clusters in our sample at $z = 0$ and as a function of time for the merging cluster E5A by means of Eq. (3.4). The resulting best-fit parameters are used to characterize the magnetic properties of the ICM. In general, we could not find a simple one-to-one relation between the kinetic and magnetic spectra and the dynamical state of the clusters: this indicates that highly perturbed systems, exhibiting more turbulence, do not necessarily imply higher values of the magnetic fields, and that the cycle of amplification of magnetic fields in the realistic ICM is complex.

The normalization of the magnetic spectrum (A), the spectrum width (B) and the inverse of the outer scale of the spectrum (C) show a positive correlation with the virial mass of each cluster. In addition, B is correlated with the dynamical state of clusters. In general, we observe that the magnetic growth rate is larger for merging systems, while it is smaller in the relaxed system in our sample.

Finally, the outer scale of the magnetic spectrum ($\propto 1/C$) also correlates with the dynamical state of the cluster: the relaxed system in our sample reaches higher values of the outer scale (~ 300 kpc) compared to merging (~ 230 kpc) and post-merging (~ 200 kpc) systems, possibly indicating that the dynamo has acted for a longer time in such systems. We caution that the ubiquitous presence of large-scale bulk motions in the ICM may introduce larger correlation scales in the magnetic field, so that our best-fit parameters do not show an evident correlation with the last major merger of each cluster. This suggests that the history of minor mergers matters, but larger statistics of simulated clusters would be necessary to reach firmer conclusions.

Moreover, we studied the co-evolution of magnetic fields and the ICM properties in a merging cluster (E5A), which we could sample with a high time resolution. Our analysis reveals that the peak of the magnetic power spectrum shifts towards smaller spatial scales shortly after mergers, while overall it shifts to larger scales. In the cluster E5A, the peak of the magnetic power spectrum extends to ~ 280 kpc after ~ 9 Gyr of evolution, with equipartition at scales < 160 kpc. Large amounts of kinetic energy are injected by substructures that fall through the cluster which first amplify the magnetic field mainly via compression. These mergers prevent equipartition on the smallest scales, i.e. when the cluster is more perturbed, equipartition is not reached at scales above our current resolution.

In the course of a merger, the spectrum broadens and the outer scale is shifted towards smaller scales. While we observe that the total magnetic energy is continuously growing, the magnetic amplification at smaller scales starts only after the mergers. This behaviour is driven by two mechanisms: 1) strong mergers introduce additional turbulence into the system that raises the kinetic energy above equipartition with the magnetic field. Nevertheless, this new energy will only become available for magnetic amplification after a few eddy-turnover times when the turbulence has already cascaded down to the smaller scales; Consequently, this changes the growth timescales by slowing down the process of amplification soon after a merger event. In particular, when there is a large input of kinetic energy, the magnetic amplification at small scales sets in only after ~ 1 Gyr since the merger.

Finally, our work has important implications for the interpretation of existing or future radio observations of magnetic fields in galaxy clusters. The total rotation

measure $|RM|$ from clusters is expected to scale $\propto A/C$. Therefore, our previous results imply that the RM only weakly depends on the mass of the galaxy cluster. We measure a scatter of up to a ~ 4 difference in RM between clusters of the same mass, while systems with a ~ 2 difference in mass can have the same RM, due to differences in their magnetic field correlation scale. This implies that the RM across the cluster population probably is not universal, but can significantly be affected by the complex sequence of amplification events in the past lifetime of each cluster, with important consequences in the predictions of the RM from galaxy clusters which should be observable by future radio polarisation surveys (e.g. Govoni et al., 2015; Taylor et al., 2015). We defer this analysis to future work.

3.6 Acknowledgements

3.7 Earlier results on dynamo amplification in simulated clusters.

We summarize here the main results of our previous work (Vazza et al., 2018, , Paper I in this work), which motivates the analysis performed in this paper. Using an AMR prescription to refine most of the innermost regions of galaxy clusters with the *ENZO*

code, in Vazza et al. (2018) we simulated the growth of 0.1 nG (comoving) magnetic field seed, assumed of a cosmological origin, from $z = 30$ to $z = 0$. We simulated the field growth as a function of the maximum cell resolution for a Coma-like galaxy cluster ($\sim 10^{15} M_\odot$) an starting from the same initial field, and observed the onset of significant small-scale dynamo for resolutions ≤ 16 kpc, with near-equipartition magnetic fields on ≤ 100 kpc scales. For the best resolved run (≈ 4 kpc/cell), we measured a final magnetic fields strength of $\sim 1 - 2$ μG in the cluster core, with a radial profile that scales as $B(n) \propto n^{0.487}$ (where n is the gas density). For lower resolution, the magnetic field gets increasingly smaller, with a flatter radial profiles and a magnetic power spectrum of a power-law shape. In summary, the following are the key evidences that support that our runs do feature a resolved small-scale dynamo:

- the measured dependence of magnetic field strength and the effective resolution of the simulation: only when the numerical Reynolds number exceeds $R_e \sim 10^2$ the magnetic field reaches values much larger than what gas compression ($\propto n^{2/3}$) can produce;

- the onset of the curved magnetic field power spectrum only when the spatial resolution exceeds a critical value (estimated to be ~ 16 kpc/cell, even if this may vary with the adopted numerical scheme, e.g. Donnert et al. 2018), indicating that only at a large enough Reynolds number and high enough resolution we have enough solenoidal turbulence and we can resolve the l_A scale (Fig.3.19);

- the slope of the power spectra for low wavenumbers is compatible with the Kasantsev model of dynamo $P_B \propto k^{3/2}$ (e.g. Schekochihin et al., 2004), while after the peak the spectrum rapidly steepens from $\propto k^{-5/3}$ to $\propto k^{-2}$ or less, consistent with (e.g. Porter et al., 2015; Rieder & Teyssier, 2017);

- the evolution of magnetic fields in our most resolved simulation, and its relation with the measured dissipation of kinetic turbulent energy, which indicate a $\sim 4\%$ dissipation rate of turbulent into magnetic energy, in line with Miniati & Beresnyak (2015) and Beresnyak & Miniati (2016);

- the measured anti-correlation between the curvature of magnetic field lines in our most resolved simulation and the magnetic field strength, as expected in the dynamo regime (e.g. Schekochihin et al., 2004);

- the measurement that the l_A scale, estimated following in Brunetti & Lazarian (2007), which is well resolved for a good fraction of our cluster volume;
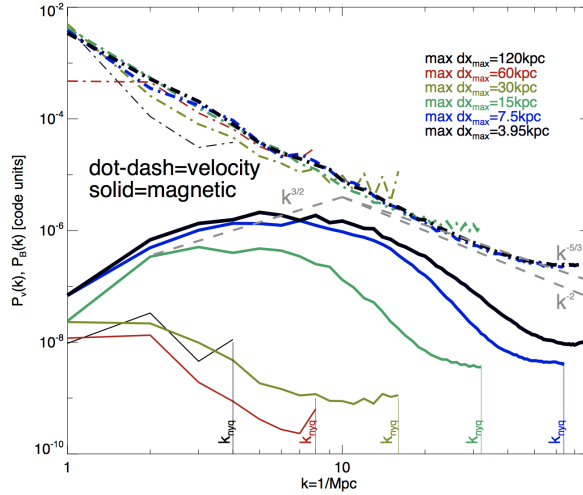
Figure 3.19: Power spectra of velocity (top lines) and magnetic field (lower curved lines) for resimulation of increasing resolution, presented in Paper I. The spectra are measured within the innermost 2^3Mpc^3 of a simulated cluster at $z = 0$, and clearly shows that the increase of resolution leads to an increase of the dynamical range (also marked by the sequence of Nyquist frequencies at the bottom of the panel) and results into a radial change in the magnetic spectrum for ≤ 16 kpc resolutions.

- the independence of the magnetic profile and power spectra at $z = 0$, for ≥ 0.03 nG (comoving), above which our setup ensures to resolve l_A in a large fraction of the cluster volume.

Moreover, the topology of the magnetic fields at $z = 0$ produces profiles of Faraday Rotation of background polarised sources in good agreement with the real observations of the Coma cluster, which are the most stringent to date (Bonafede et al., 2010, 2013). A significant new finding of our first analysis in Paper I is also the detection of a significant non-Gaussian distribution of magnetic field components in the final cluster, which results from the superposition of different amplification patches mixing in the ICM.

All results obtained from this first study are also confirmed with the larger set of cluster simulations which is object of this paper.

3.8   Correlating the best-fit parameters

We computed the cross-correlation matrix of the change in time of the best-fit parameters A, B, C and the kinetic energy E_k and show the result in Fig.3.20.

Where Δ of a variable Q, is defined as $(Q(t) - Q(t\text{-}1))/Q(t\text{-}1)$ as in Fig. 3.16. The Pearson coefficients for all the cross-correlations are shown in the upper part of the diagonal in Fig. 3.20. In this way, we can better quantify the existing correlations and interpret them:

1. $corr(\Delta A, \Delta B)$: a positive change in the normalization implies a negative change in the parameter B. This implies that a sudden increment on the normalization narrows down the spectrum width shortening the magnetic growth timescale. Therefore, the growth rate increases over time.

2. $corr(\Delta A, \Delta C)$: an increment in the normalization implies that $C(t) < C(t\text{-}1)$, i.e the power is shifted towards larger scales. We attribute this feature to the presence of dynamo amplification. This conclusion is supported by Section 3.3.4, where every merger event carrying enough kinetic energy was shown to shift the magnetic spectrum towards smaller scales (i.e. amplifying via compression).

3. $corr(\Delta B, \Delta C)$: a wider spectrum coming along with a shift of the outer scale towards smaller scales is directly related to the action of compression. This matches our previous interpretation of Fig. 3.15, where compression shifts the power to smaller scales (i.e. $C(t\text{-}1) < C(t)$) and the new turbulent cascade does not play a role in the amplification instantaneously, but after an eddy-turnover time.

4. $corr(\Delta C, \Delta E_k)$: a shift of the outer scale towards small scales is weakly correlated with the injection of kinetic energy. In this case, we checked the cross-correlation at each time and identified the times corresponding to some merger events (red arrows in Figs.3.16 and 3.18). The first two arrows corresponding to small clumps falling into the cluster show a higher correlation than the last arrow which corresponds to a larger clump. A plausible explanation is that the first two events generated sufficient turbulence that allowed the magnetic field to grow also at smaller scales (via the small-scale dynamo), so by the time of the third event, the effect of compression is not enough to shift the outer scale towards smaller scales anymore. This can be considered as a momentary state of "balance" between the dynamo and compression effects and it would also explain the period of amplification between $t \sim$ 12-13 Gyr.
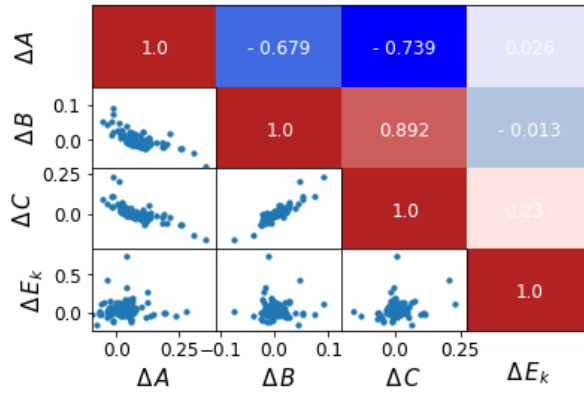
Figure 3.20: Cross-correlation matrix of the best-fit parameters and the kinetic energy changes in the system. The Pearson correlation coefficients are indicated in the upper part of the diagonal and the corresponding scatter plots are shown in the lower part of the diagonal.

Chapter 4

Morphology of radio relics I: What causes the substructure of synchrotron emission?

P. Domínguez-Fernández, M. Brüggen, F. Vazza , W. E. Banda-Barragán, K. Rajpurohit, A. Mignone, D. Mukherjee, B. Vaidya

Abstract   High-resolution radio observations of cluster radio relics often show complex spatial and spectral features. However, it is not clear what these features reveal about the underlying magnetic field properties. We performed three-dimensional magneto-hydrodynamical simulations of merger shock waves propagating through a magnetised, turbulent intracluster medium. Our model includes the diffusive shock acceleration of cosmic-ray electrons, their spatial advection and energy losses at run-time. With this set-up we can investigate the relation between radio substructure and pre-shock plasma conditions in the host cluster. We find that upstream turbulence plays a major role in shaping the properties of radio relics produced downstream. Within the assumption of diffusive shock acceleration, we can reproduce the observed discrepancy between the X-ray derived Mach number of shocks, and the Mach number inferred from radio spectra. Our simulated spectral index maps and profiles across the radio relic also suggest that the standard deviation of the upstream magnetic field must be relatively small ($\sigma_B \leq 1\,\mu\mathrm{G}$) in order to reproduce observations and therefore, radio relics can potentially constrain the distribution of magnetic fields in galaxy clusters outskirts.

4.1 Introduction

Radio observations of galaxy clusters reveal non-thermal processes in the intracluster medium (ICM). The size of diffuse radio sources is of the order of Mpc. Such large-scale emission is typically grouped into two categories: *radio haloes* and *radio relics*. The first category refers to objects located at the cluster center and of a relatively regular and spherical shape, with little to absent polarisation (e.g. Brunetti & Jones, 2014). The second category, refers to objects located at the cluster periphery, with elongated shapes and typically large degrees of polarisation (see Brüggen et al. 2012a and van Weeren et al. 2019 for reviews). Radio relics are the main focus of this work.

The particle acceleration mechanisms causing diffuse radio sources are not fully understood. However, it seems clear that shocks generated during the assembly of galaxy clusters play a key role in accelerating the synchrotron-emitting cosmic-ray electrons (see van Weeren et al. 2011a or Bykov et al. 2019 for a review). The radio emission observed in relics is compatible with synchrotron emission from cosmic-ray (CR) electrons with Lorentz factors of $\gamma_e \sim 10^3$–10^5, which are believed to be accelerated via mild shocks ($\mathcal{M}_{\mathrm{radio}}$[1] $\sim$ 1.7–4.6) crossing the ICM (e.g. Clarke & Ensslin, 2006; van Weeren et al., 2010, 2012).

The first-order Fermi acceleration process, commonly known as diffusive shock acceleration (DSA), explains the acceleration of relativistic particles by the passage of a collisionless shock wave (e.g. Blandford & Eichler, 1987; Drury, 1983). A small fraction ($\ll 10^{-3}$) of thermal particles can cross the shock front multiple times, and receive a boost in their momentum proportional to $\Delta v / c$, where Δv is the velocity jump (difference) across the shock. This acceleration mechanism is observed to be much more efficient than what is expected from theory (see van Weeren et al. 2019; Botteon et al. 2020). Hence, it has been proposed that the electrons are pre-accelerated (e.g. Kang et al., 2012; Pinzke et al., 2013) before they enter the DSA mechanism.

Moreover, the DSA process does not offer a straightforward explanation for the non-detection of γ-rays from clusters (see Ackermann et al. 2010, 2014, 2016 and Vazza & Brüggen 2014). Among the most relevant open challenges in our understanding of radio relics are: (i) the discrepancy between the Mach numbers detected in X-rays and those inferred from radio observations assuming DSA (e.g. Botteon et al., 2020), and (ii) the high electron acceleration efficiency of the order of several percent for the weak shocks commonly associated with radio relics. Up until now, only a few radio relics can readily be explained by the DSA model (e.g. Locatelli et al., 2020).

---

[1]$\mathcal{M}_{\mathrm{radio}}$ is the Mach number inferred from radio observations.

Recent high-resolution radio observations have shown a plethora of complex structures in radio relics (e.g. Rajpurohit et al., 2018, 2020a; Owen et al., 2014; van Weeren et al., 2017; Di Gennaro et al., 2018). Attempts to explain the observed features struggle with the vast range of scales, from cosmological scales ($\gtrsim$ Mpc), down to turbulent scales (~ 10 kpc) (e.g. Egan et al., 2016; Domínguez-Fernández et al., 2019), or even down to plasma scales where particle acceleration occurs ($\sim 10^{-6}$ kpc for the largest gyroradius of relativistic protons). A possible choice is to study particle acceleration from the microphysical point of view using Particle In Cell (PIC) simulations (e.g. Guo et al., 2014; Caprioli & Spitkovsky, 2014a; Park et al., 2015; Caprioli & Spitkovsky, 2014b; Ryu et al., 2019; Kang et al., 2019), or conversely on larger scales using the magneto-hydrodynamical (MHD) approximation, as customarily done with cosmological simulations (the reader may refer to Donnert et al. 2018 for a review).

Radio emission from radio relics has been modelled in previous works on larger scales (e.g. Skillman et al. 2013; Hong et al. 2015; Nuza et al. 2017). Due to the discrepancy in scales, it is not possible for MHD simulations to model the emission produced by single electrons, but rather from an ensemble of *tracer particles*, representing a whole distribution of electrons. Previously, this approach has been applied to cosmological MHD simulations in post-processing (see Wittor et al., 2019).

In this paper, we model the synchrotron emission at run-time in a small fraction of the ICM by means of a new hybrid particle and fluid framework using the MHD code PLUTO (Mignone et al., 2007; Vaidya et al., 2018). Our aim is to study the substructure observed in radio relics (e.g. Rajpurohit et al., 2020a). This method uses *Lagrangian* particles embedded in a large-scale MHD flow, each with its individual energy spectrum. Here we consider a simplified scenario: we set up a shock tube in a turbulent medium that is representative of a small region of the ICM. We then assume that CR electrons are injected instantly at the shock discontinuity and acquire spectral properties according to DSA theory.

The paper is structured as follows: in Section 4.2, we describe our numerical setup and initial conditions. In Section 4.3, we include a description of the particles' initial spectral distribution and evolution. In Section 4.3.3, we explain how we obtain the emission and spectral index maps. Section 4.4 shows our results and we summarize in Section 4.5.

4.2 Numerical set-up

4.2.1 Initial conditions: modelling the turbulent ICM with FLASH

The turbulent ICM initial conditions were produced using the MHD FLASH code version 4.6.1 (Fryxell et al., 2000; Calder et al., 2002), with the goal of generating realistic pre-shock conditions. We used the unsplit staggered mesh (USM) MHD solver which uses a constrained transport (CT) method at cell interfaces for preserving the divergence-free magnetic field property on a staggered grid (e.g. Lee et al., 2009). The simulation domain is chosen to be a cubic box of size $L = L_x = L_y = L_z = 200$ kpc, uniformly spaced over a 256^3 cells grid, with periodic boundary conditions. We assumed an ideal gas equation of state with $\gamma_0 = 5/3$.

Turbulence was created following a spectral forcing method, based on the stochastic Ornstein-Uhlenbeck (OU) process to model the turbulent acceleration $\mathbf{f}$ with a finite autocorrelation time (e.g. Eswaran & Pope, 1988; Schmidt et al., 2006; Federrath et al., 2010). The OU process describes the evolution of the forcing term in Fourier space, $\hat{\mathbf{f}}$, with a stochastic differential equation:

$$d\hat{\mathbf{f}}(\mathbf{k}, t) = f_0(\mathbf{k})\mathcal{P}^\zeta(\mathbf{k})d\mathbf{W}(t) - \hat{\mathbf{f}}(\mathbf{k}, t)\frac{dt}{T}, \tag{4.1}$$

where f_0 is the forcing amplitude, $\mathbf{W}(t)$ is a random Wiener process, $\mathcal{P}^\zeta$ is a projection tensor in Fourier space, ζ is the forcing parameter ($\zeta = 0(1)$ for purely compressive(solenoidal) forcing), and T is the autocorrelation time scale of the forcing (the reader may refer to Federrath et al. 2010 for a detailed explanation on turbulence forcing). In this work, we solely focus on solenoidal subsonic turbulence forcing ($\nabla \cdot \mathbf{f} = 0$), since several authors have shown that the most dominant type of turbulence in the ICM should be subsonic with a large ($\geq 70\%$) predominance of solenoidal modes (e.g. Miniati, 2014; Vazza et al., 2017).

We have run two simulations with two different stirring scales. The forcing amplitude, f_0, was set to be a paraboloid in Fourier space in both simulations only containing power on the largest scales in a small interval of wavenumbers. We chose two different intervals: $1 \leq kL/2\pi \leq 2$ for the first simulation and $1 \leq kL/2\pi \leq 4$ for the second simulation. As the power peaks in $2/3$ and $1/4$ of the box, we will refer to each of them as $2L/3$ and $L/4$, representing injection scales of 133 kpc and 50 kpc, respectively. Furthermore, the maximum k allowed in the box corresponds to the 2L/3 case. Conversely, the $L/4$ case satisfies the minimum condition where its eddy turnover time is smaller than the time needed for our main set-up (where a shock sweeps this turbulent medium).
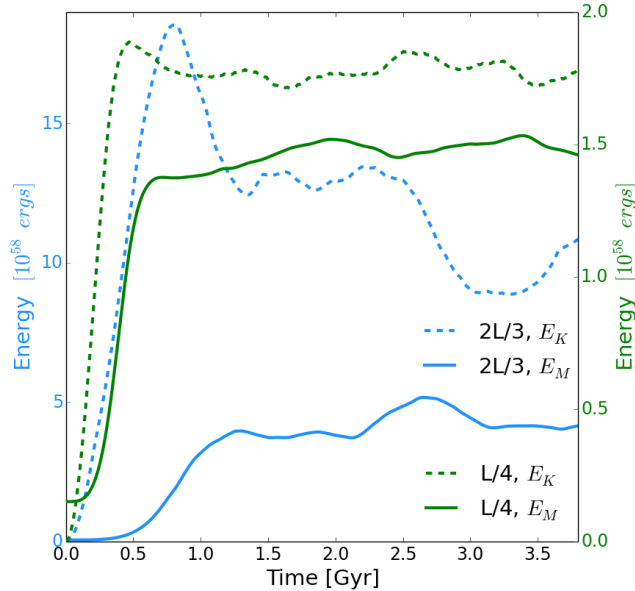
Figure 4.1: Energy evolution for the runs with injection at $2L/3$ (*blue*) and at $L/4$ (*green*). The kinetic energy is shown with *dashed lines* and the magnetic energy with *solid lines*. Saturation is reached at $t = 2t_{2L/3} = 2.1$ Gyr and $t = 2t_{L/4} = 0.78$ Gyr, respectively. After saturation the energy ratio, E_M/E_K, is ~ 0.5 and ~ 0.85 for the $2L/3$ and $L/4$ cases, respectively.

The autocorrelation timescale was set equal to the dynamical timescale (also called eddy turn-over timescale) on the scale of energy injection, $t_{2L/3} = 2L/3\sigma_v$ and $t_{L/4} = L/4\sigma_v$, respectively, where σ_v is the rms velocity to be achieved at saturation. Both simulations were set to have an amplitude of the fluctuations of $\sigma_v = 125$ km/s. The turbulence is fully developed after roughly two dynamical timescales when the magnetic energy, the plasma beta, and the rms Mach number become stable (although some transient fluctuations can still be present depending on the balance between mechanical energy from the forcing term and the dissipation rate). At this point, the magnetic field reaches a saturated state since we start with a relatively strong magnetic field seed of 0.2 μG (for the $2L/3$ case) and 0.4 μG (for the $L/4$ case). This is shown in Fig. 4.1 where we plot the evolution of the total kinetic and magnetic energy and in Fig. 4.2, where we show the evolution of the rms Mach number and the plasma beta, β, for both runs. Even after the magnetic saturation, the thermal pressure fluctuations will continue to increase due to turbulent dissipation and, as a consequence, the rms sonic Mach number decreases.

We selected one snapshot from each of these two runs to represent a small region
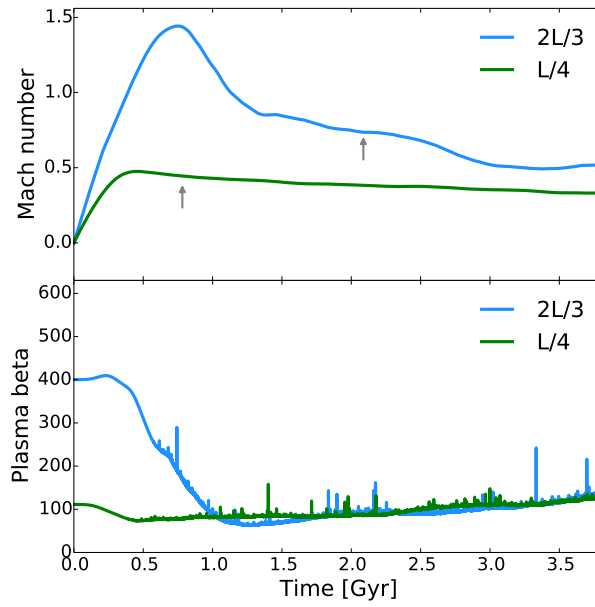
Figure 4.2: Top panel: Evolution of rms Mach number for the runs with injection at $2L/3$ (*blue*) and at $L/4$ (*green*). The arrows point to the selected snapshots to be our initial conditions. Bottom panel: Corresponding evolution of the plasma beta, β. The selected snapshots have an rms Mach number of $\mathcal{M}_s \sim 0.45$-0.7 and a plasma beta of $\beta \sim 110$.
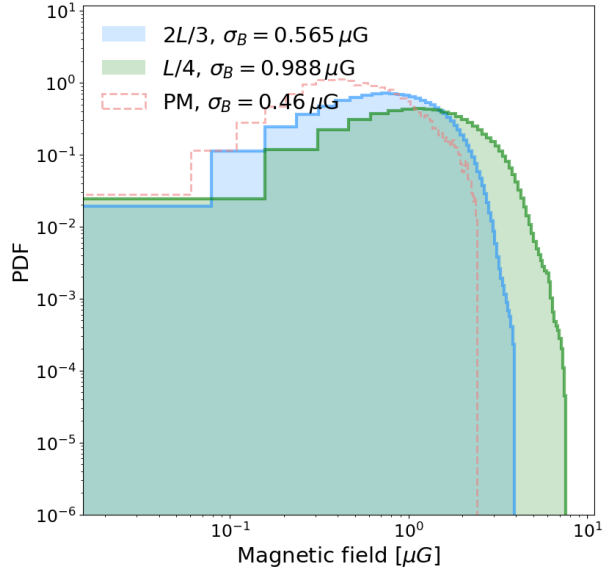
Figure 4.3: PDFs of magnetic field strength at the selected time for the runs with injection at $2L/3$ (*blue*) and at $L/4$ (*green*). Extra dashed line: PDF of a post-merger (PM) galaxy cluster previously analysed in Domínguez-Fernández et al. 2019.

of the ICM and each act as an initial condition (see Sec. 4.2 and Fig. 4.5). The snapshots are taken at the respective saturation times, which is $t = 2.1$ Gyr for the run with injection scale $2L/3$ and $t = 0.78$ Gyr for the run with injection scale $L/4$. In Fig. 4.3, we show the probability distribution function of the magnetic field strength at those times. The two snapshots have a sufficiently different distribution of magnetic fields (due to the difference in the initial magnetic field seed and the interval of wavenumbers of the stirring), yet in terms of the rms sonic Mach number and plasma-β they lie in the range of characteristic values of the ICM (e.g. Ryu et al., 2008). Note that the tail of the $L/4$ distribution extends to ~ 2 times larger magnetic field values. (see Fig. 4.3). For reference we include the PDFs of one galaxy cluster previously produced in a cosmological MHD simulation and analysed in Vazza et al. 2018; Domínguez-Fernández et al. 2019. This cluster is classified as a post-merger (PM) cluster with a mass $M_{200} = 1.9 \times 10^{15} M_\odot$ [2]. We selected a region at a distance of ~ 1 Mpc from the cluster's center with an extent of ~ 250 kpc. As can be seen in Fig. 4.3, the PDF of the magnetic field broadly agrees with previous results from cosmological MHD simulations. The high-magnetic field tail of the distribution is slightly more extended than in cosmological simulations, owing to

---

[2]The reader can find this galaxy cluster in Domínguez-Fernández et al. 2019 with ID E16B

the larger Reynolds number in these new simulations. The magnetic field strength at the outskirts of the clusters is most likely underestimated in the cosmological simulation due to the limited resolution (see Vazza et al., 2018). A more extensive survey of the interaction between merger shocks with a larger range of different initial turbulent conditions for the ICM will be the subject of future work.

4.2.2 Main PLUTO simulations

In order to study the synchrotron emission in an MHD shock tube, we use the code PLUTO (Mignone et al., 2007), which solves the following conservation laws for ideal MHD:

$$\frac{\partial \rho}{\partial t} + \nabla \cdot (\rho \mathbf{v}) = 0, \tag{4.2}$$

$$\frac{\partial \mathbf{m}}{\partial t} + \nabla \cdot \left[\mathbf{m v} - \mathbf{B B} + \mathbf{I} \left(p + \frac{B^2}{2} \right) \right]^T = 0, \tag{4.3}$$

$$\frac{\partial (E_t)}{\partial t} + \nabla \cdot \left[\left(\frac{\rho v^2}{2} + \rho e + p \right) \mathbf{v} - (\mathbf{v} \times \mathbf{B}) \times \mathbf{B} \right] = 0, \tag{4.4}$$

$$\frac{\partial \mathbf{B}}{\partial t} - \nabla \times (\mathbf{v} \times \mathbf{B}) = 0, \tag{4.5}$$

$$\nabla \cdot \mathbf{B} = 0, \tag{4.6}$$

$$\rho e = \frac{p}{\gamma_0 - 1}, \tag{4.7}$$

where ρ is the gas mass density, $\mathbf{m} = \rho \mathbf{v}$ is the momentum density, p is the thermal pressure, $\mathbf{B}$ is the magnetic field (where a factor of $1/\sqrt{4\pi}$ has been absorbed in its definition), E_t is the total energy density, e the specific internal energy and where we assumed an ideal equation of state (EOS), that is $\gamma_0 = 5/3$.

Our computational domain is a rectangular box (400 kpc $\times$ 200 kpc $\times$ 200 kpc with $256 \times 128 \times 128$ cells, respectively), where $x \in$[-200,200] kpc, $y \in$[-100,100] kpc, and $z \in$[-100,100] kpc (see Fig. 4.4). The right-hand half of the domain is filled with a turbulent medium (see Sec. 4.2.1), representing a realistic ICM, while the left-hand half contains a uniform medium in which the shock is launched. We define a shock discontinuity at $x = -100$ kpc (see Fig. 4.4 for the initial configuration of the magnetic field). This defines three regions in our simulation box: a post-shock uniform region (I), a pre-shock uniform region (II) and a pre-shock turbulent region (III).

The turbulent medium is produced externally, with the procedure outlined in Sec. 4.2.1. The turbulent fields are then read into PLUTO and interpolated onto the numerical mesh used to evolve shocks with a bi- or tri-linear interpolation at the desired coordinate location at the initial time.
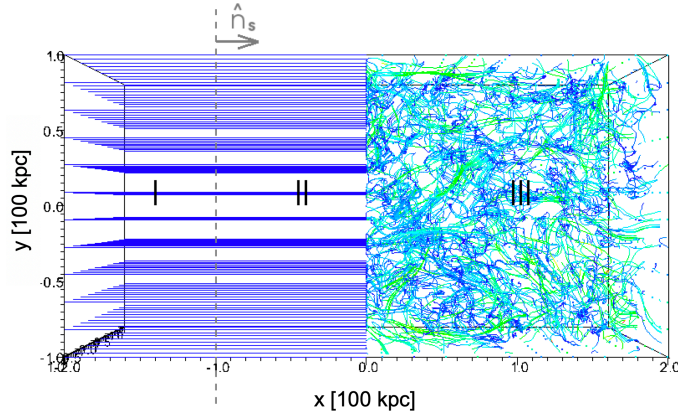
Figure 4.4: Initial magnetic field configuration in the PLUTO code. The streamlines are coloured according to the magnitude of the magnetic field: green, light colours denote higher values, while dark blue colour indicates lower values. I denotes the post-shock region, II denotes the uniform pre-shock region and III the turbulent pre-shock region (see Sec. 4.2.1). The left side is a uniform medium with a B_x component matching the mean value of the B_x of the turbulent medium. We have one Lagrangian particle per cell placed in the whole regions II and III.

The initial boundary conditions of the computational domain are *outflow* in x (zero gradient across the boundary) and *periodic* in y and z. We used a piece-wise parabolic method (PPM) for the spatial integration, whereas a 2nd oder TVD Runge-Kutta method for the time stepping with a Courant-Friedichs-Lewy (CFL) condition of 0.3. The Riemann solver for the flux computation that we used is the Harten-Lax-van Leer-Discontinuities (HLLD) solver (see Miyoshi & Kusano, 2005). We control the $\nabla \cdot \mathbf{B} = 0$ condition with the hyperbolic divergence cleaning technique where the induction equation is coupled to a generalized Lagrange multiplier (GLM) (e.g. Dedner et al., 2002). In Appendix 4.7, we compare how the GLM and constrained transport (CT) methods control the divergence-free condition and find that both methods work reliably in PLUTO.

The initial conditions for the density, pressure and velocity in region II (*pre-shock* uniform region at [-100,0] kpc) are set to the mean value of the corresponding turbulent fields. In the case of the magnetic field in region II, we set it to be the mean value of the B_x component of the turbulent medium. The initial conditions for region I (*post-shock* region) are selected according to the MHD Rankine-Hugoniot conditions (e.g. Landau & Lifshitz, 1987). We performed simulations with two different turbulent media (see Sec. 4.2.1) produced with the code FLASH (e.g. Fryxell et al., 2000; Calder et al., 2002) by varying also the strength of the shock and the angle,

Run ID	Turbulent medium	$\mathcal{M}$	$\theta_{bn}[°]$	$\rho_{\mathrm{II}}\,[10^{-27}\mathrm{g/cm}^3]$	$B_{x,\mathrm{II}}\,[\mu G]$
k1p5_M2_parallel	$2L/3$	2.0	0	1.338	0.4
k1p5_M3_parallel	$2L/3$	3.0	0	1.338	0.4
k4_M2_parallel	$L/4$	2.0	0	1.338	0.4
k4_M3_parallel	$L/4$	3.0	0	1.338	0.4
k1p5_M3_perpendicular	$2L/3$	3.0	90	1.338	1.156×10^{-12}
k4_M3_perpendicular	$L/4$	3.0	90	1.338	1.156×10^{-12}

Table 4.1: Initial conditions: We denote our regions I, II, III where I is the post-shock region ([-2,-1] in box coordinates), II is the uniform pre-shock region ([-1,0] in box coordinates) and III is the turbulent pre-shock region ([0,2]). The initial conditions for the left side of the shock (region I) depend on the pre-shock conditions (region II) and the initial Mach number of the shock $\mathcal{M}$ through the Rankine-Hugoniot jump conditions. L denotes the length of the turbulent region, i.e. 200 kpc (see more details in Sec. 4.2.1). Note that the magnetic field in region II has only an x-component.

θ_{bn}, of the upstream magnetic field[3] with respect to the normal of the shock. Shocks can be classified as quasi-parallel and quasi-perpendicular if $\theta_{bn} \leq 45°$ or $\theta_{bn} > 45°$, respectively. We consider two limits, i.e. $\theta_{bn} = 0°$ and $\theta_{bn} = 90°$. This sums up to a total of six runs for which all the parameters are summarized in Table 4.1. We show the projection maps of the two different initial turbulent media considered for this work in Fig. 4.5 and clarify how these were selected in Sec. 4.2.1.

Finally, we fill the computational domain from the shock discontinuity up to the right side of the box with one *Lagrangian* particle per cell. This gives us a total number of 3,145,728 Lagrangian particles for each run.

4.3   Non-thermal radio emission from shocks

4.3.1   Particle energy spectrum

Each Lagrangian particle represents an ensemble of CR electrons and is characterized by an energy distribution function,

$$\chi(E,\tau) = \frac{N(E,\tau)}{n_0},\qquad(4.8)$$

---

[3]Note that here we define the direction of the upstream magnetic field as the direction of the mean magnetic field of the turbulent medium
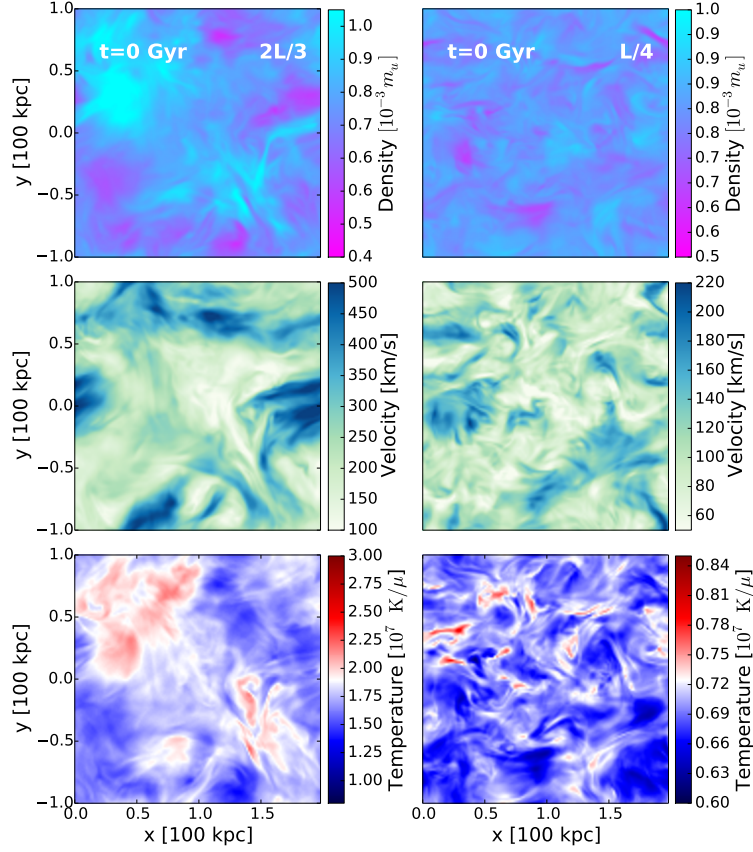
Figure 4.5: Projected maps along the z-axis of the different initial conditions (25 kpc slice), where m_u is the atomic mass unit and μ is the mean molecular weight. Here we show the right-hand half-size of the box containing the turbulent media. From top to bottom the reader can see the average density, velocity and temperature field for the $2L/3$ (*left column*) and $L/4$ (*right column*) cases, where $2L/3$ and $L/4$ refer to the integral scale of each type of turbulence ($L = 200$ kpc).

which gives the number of electrons per fluid number density. These particles evolve according to the cosmic-ray transport equation,

$$\frac{d\chi}{d\tau} + \frac{\partial}{\partial E}\left[\left(-\frac{E}{3}\nabla_\mu u^\mu - c_r E^2\right)\chi\right] = 0, \tag{4.9}$$

where the first term in square brackets accounts for energy losses due to adiabatic expansion, while the second one accounts for the synchrotron and inverse-Compton losses for electrons with isotropically distributed velocity vectors,

$$c_r = \frac{4}{3}\frac{\sigma_T c\beta^2}{m_e^2 c^4}\left[\frac{B^2}{8\pi} + a_{\rm rad}T_{\rm CMB}^4(1+z)^4\right], \tag{4.10}$$

where $\beta = v_e/c$ is the velocity of the electrons, m_e their mass and $a_{\rm rad}$ the radiation constant. For the present work, we assume a constant redshift of $z = 0$. The reader may refer to Vaidya et al. (2018) for a complete description of the numerical implementation and the semi-analytical scheme used for solving Eq. (4.9).

We study a simplified scenario where the non-thermal spectra of the particles are activated instantly at the shock discontinuity. While the particles follow the fluid flow since $t = 0$, the particle's energy distribution starts to evolve only when the particles have passed a shock. We implemented a shock finder based on converging flows and pressure jumps that we describe in Appendix 4.8.

Once the Lagrangian particles are *activated* at the shock discontinuity, they get assigned an initial energy distribution. The corresponding particle momentum distribution function is a power-law distribution, i.e $f(p) \propto p^{-q}$. The power-law index is given by the diffusive shock acceleration (DSA) theory (Drury, 1983).

$$q = \frac{3r}{r - 1}, \tag{4.11}$$

where r is the shock compression ratio defined as the ratio of the upstream and downstream densities. If we consider test particle acceleration at a shock of Mach number $\mathcal{M}$, then it is possible to re-write Eq. (4.11) making use of the Rankine-Hugoniot jump equations (see derivation in Blandford & Eichler 1987):

$$q = \frac{3(\gamma_0 + 1)\mathcal{M}^2}{2(\mathcal{M}^2 - 1)} = \frac{4\mathcal{M}^2}{\mathcal{M}^2 - 1}, \tag{4.12}$$

where for the second equality we have considered an adiabatic index of $\gamma_0 = 5/3$. The corresponding power-law index for the macro-particle distribution function can be also obtained by assuming isotropy, i.e $N(p,\tau) = \int \Omega_\tau p^2 f \approx 4\pi p^2 f$, where $d\Omega_\tau$ is the solid angle around the direction τ. Since the particles are relativistic, we have

that $N(E, \tau)dE = N(p, \tau)dp$. Moreover, from the isotropic condition we also have that $N(E) = 4\pi N(E, \tau)$.

Therefore, the tracer particle energy distribution function at the activation time is given by

$$\chi(E) = \frac{N(E)}{n_0} = \frac{N_0}{n_0} E^{-p}, \tag{4.13}$$

where $p = q - 2$ is what it is usually called the *injection spectral index*, N_0 is the normalisation factor and n_0 is the fluid number density. N_0 is assigned according to the energy contained in the shock. That is, we considered that the total energy per fluid number density is

$$\int \chi(E) \, E \, dE = \frac{E_{tot}}{n_0}, \tag{4.14}$$

where $E_{\text{tot}} = \eta \, E_{\text{shock}} = \eta \, \rho_{\text{post}} \, v_{\text{shock}}^2$ and η is the acceleration efficiency. For which finally one can obtain the normalisation factor:

$$N_0 = \begin{cases} \dfrac{\eta \, E_{\text{shock}} \, (4-q)}{\left[E_{\text{max}}^{4-q} - E_{\text{min}}^{4-q} \right]} & \text{if } q \neq 4 \\[3ex] \eta \, E_{\text{shock}} \log\left(\dfrac{E_{\text{max}}}{E_{\text{min}}} \right) & \text{if } q = 4 \end{cases} \tag{4.15}$$

The PLUTO code allows us to compute the maximum and minimum energy at each time step. The maximum energy E_{max} is imposed considering the maximum allowed Larmor radius for each particle. The minimum energy E_{min} is estimated balancing the synchrotron and acceleration time scales (see full explanation in Vaidya et al. 2018; Böttcher & Dermer 2010; Mimica & Aloy 2012) so it depends on the acceleration efficiency. Moreover, the acceleration efficiency in collisionless relativistic shocks can also depend on the energy of the particles (see Sironi et al., 2013). In this work, for simplicity we assume a fixed acceleration efficiency of $\eta = 10^{-3}$ and fixed energy limits of $\gamma_{\text{min}} = 1$ and $\gamma_{\text{max}} = 10^5$. This acceleration efficiency agrees with the expectations of DSA for strong shocks (e.g. Kang et al., 2012) and lies in the range of values required to explain observations of radio relics (see Botteon et al. 2020). Nevertheless, this means that the final synchrotron emission obtained can be re-scaled to the desired η since in our case the energy limits remain constant.

4.3.2 Synchrotron emission

The synchrotron emission of a tracer particle in a local magnetic field $\mathbf{B}'$ in the direction $\hat{\mathbf{n}}'_{\text{los}}$, per unit solid angle, volume and frequency is given by

$$\mathcal{J}'_{\text{syn}}(\nu'_{\text{obs}}, \hat{\mathbf{n}}'_{\text{los}}, \mathbf{B}') = \int N(E') \mathcal{P}(\nu'_{\text{obs}}, E', \phi') dE' d\Omega', \tag{4.16}$$

where $\mathcal{P}(\nu'_{\rm obs}, E', \phi')$ is the synchrotron power per unit frequency and unit solid angle emitted by a single particle that has energy E' and ϕ' is the angle that the velocity vector of the particle makes with the direction $\hat{\mathbf{n}}'_{\rm los}$. Following Ginzburg & Syrovatskii 1965 we get

$$\mathcal{J}'_{\rm syn}(\nu'_{\rm obs}, \hat{\mathbf{n}}'_{\rm los}, \mathbf{B}') = \frac{\sqrt{3}e^3}{4\pi m_e c^2}|\mathbf{B}' \times \hat{\mathbf{n}}'_{\rm los}| \int N(E')F(\xi)\,dE', \qquad (4.17)$$

where $\hat{\mathbf{n}}'_{\rm los}$ is the unit vector in the direction of the line of sight in the comoving frame and $F(\xi)$ is a Bessel function integral given by

$$F(\xi) = \xi \int_\xi^\infty K_{5/3}(z')\,dz', \qquad (4.18)$$

where

$$\xi = \frac{\nu'_{\rm obs}}{\nu'_c} = \frac{4\pi m_e^3 c^5 \nu'_{\rm obs}}{3eE'^2|\mathbf{B}' \times \hat{\mathbf{n}}'_{\rm los}|}, \qquad (4.19)$$

where ν'_c is defined as the critical frequency at which the emission peaks. Note that only those particles with a pitch angle coinciding with the angle between $\mathbf{B}'$ and $\hat{\mathbf{n}}'_{\rm los}$ contribute to the emission along the line of sight in Eq. (4.17).

The emissivity in Eq. (4.17) is measured in the local comoving frame with the emitting volume. If we want the emissivity in a fixed observer's frame then we have to apply a transformation[4]:

$$\mathcal{J}_{\rm syn}(\nu_{\rm obs}, \hat{\mathbf{n}}_{\rm los}, \mathbf{B}) = \mathcal{D}^2 \mathcal{J}'_{\rm syn}(\nu'_{\rm obs}, \hat{\mathbf{n}}'_{\rm los}, \mathbf{B}'), \qquad (4.20)$$

where $\mathcal{D}$ is a Doppler factor given by

$$\mathcal{D} = \frac{1}{\gamma(1 - \hat{\mathbf{n}}_{\rm los} \cdot \mathbf{v})}, \qquad (4.21)$$

where γ is the Lorentz factor of the tracer particle. The unit vectors on the direction of the line of sight in the comoving and observer's frame are related through

$$\hat{\mathbf{n}}'_{\rm los} = \mathcal{D}\left[\hat{\mathbf{n}}_{\rm los} + \left(\frac{\gamma^2}{\gamma+1}\mathbf{v} \cdot \hat{\mathbf{n}}_{\rm los} - \gamma\right)\mathbf{v}\right]. \qquad (4.22)$$

---

[4]The reader should note that the primed quantities in Eq. (4.20) refer to the comoving frame, whereas standard notation refers to the observer's frame.

4.3.3   Radio emission maps

In the preceding equations, the vector $\hat{\mathbf{n}}_{\mathbf{los}}$ can be selected according to an observing angle θ_{obs} with respect to the line-of-sight. In this work, we only show results considering $\theta_{\mathrm{obs}} = 0°$, that is we consider an observer's reference frame in which z lies along the line of sight $\hat{\mathbf{n}}_{\mathbf{los}}$ and x and y are in the plane of the sky. The specific intensity (or surface brightness) maps can then be obtained by integrating along a line of sight as

$$I_\nu = \int \mathcal{J}_{\mathrm{syn}}(\nu_{\mathrm{obs}}, x, y, z)dz, \tag{4.23}$$

in units of [erg cm^{-2} s^{-1} Hz^{-1} str^{-1}]. This is doable due to the fact that the emissivity information $\mathcal{J}_{\mathrm{syn}}$ of the Lagrangian tracer particles is interpolated back onto the Eulerian grid. It is also possible to obtain spectral index maps by means of

$$-\alpha(x, y) = \frac{\log\left[I_{\nu_2}(x, y)/I_{\nu_1}(x, y)\right]}{\log(\nu_2/\nu_1)}, \tag{4.24}$$

and the integrated spectra (or net flux) can be obtained by integrating the specific intensity I_ν over the area covered by the source in the plane of the sky, that is

$$F_\nu(\nu) = \int I_\nu(\nu, x, y)dxdy, \tag{4.25}$$

in units of [erg s^{-1} Hz^{-1} str^{-1}].

4.4   Results

4.4.1   Fluid properties

In this subsection we describe some of the features of the fluid starting with the evolution of velocity, temperature and magnetic field, for the $2L/3$, $\mathcal{M} = 3$ and $\theta_{bn} = 90°$ case (see Fig. 4.6). In all of our runs, the initial shock sweeps region II maintaining a constant velocity and planar shape due to the fact that this region is initially uniform. Next, the shock enters region III, where the shock will no longer be uniform and be affected by the anisotropies of the fluid. The two first rows in Fig. 4.6 highlight how weak internal shocks and turbulence are generated in the downstream as the main shock travels through the simulation box. The third row shows the streamlines of the magnetic field. The streamlines are coloured according to the magnitude of the y-component of the magnetic field, B_y, to illustrate how the shock compression amplifies the field. The fourth row shows 1D profiles of
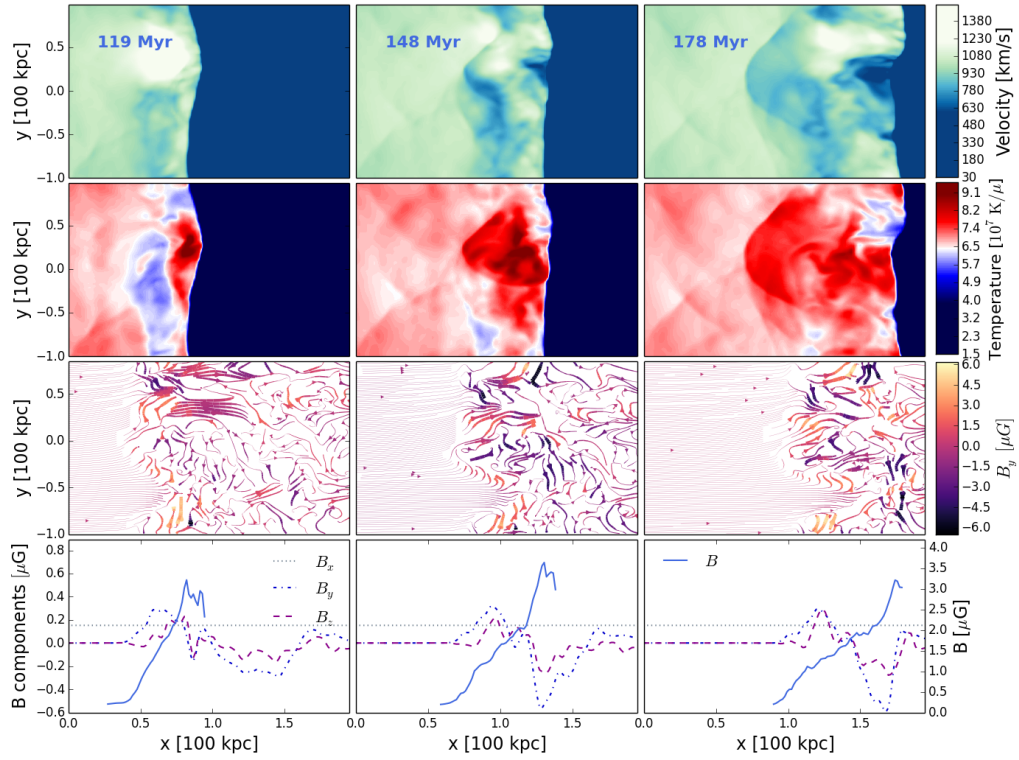
Figure 4.6: Evolution of the $2L/3$, $\mathcal{M} = 3$ and $\theta_{bn} = 90°$ case. *First row*: 20 kpc slice along the z-axis of velocity field. *Second row*: 20 kpc slice along the z-axis of temperature *Third row*: streamlines of total magnetic field (note that the colour-code only denotes the strength of y-component). *Fourth row*: 1D magnetic profiles corresponding. The component's profiles have no weighting, whereas the magnetic field strength, B, is weighted with the 150 MHz synchrotron emissivity.
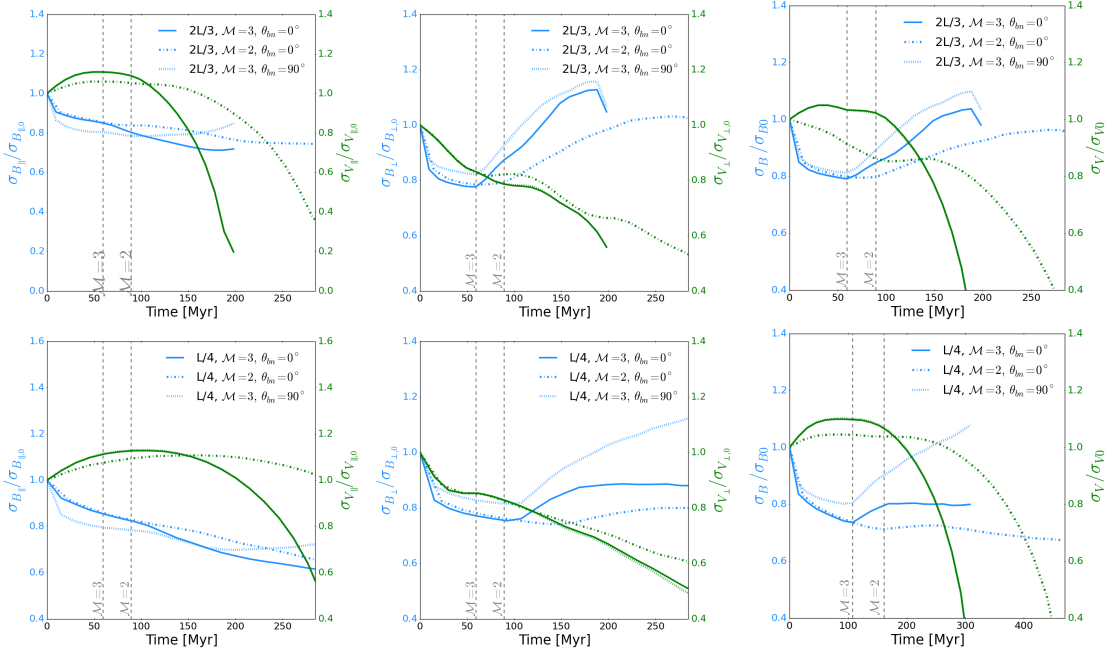
Figure 4.7: Evolution of the standard deviation of the magnetic field (*left axis*) and velocity field (*right axis*). *Top panels*: $2L/3$ case. *Bottom panels*: $L/4$ case. *First column*: Parallel component to the shock, i.e $B_\parallel = B_x$ and $v_\parallel = v_x$. *Second column*: Perpendicular component, i.e $B_\perp = \sqrt{B_y^2 + B_z^2}$ and $v_\perp = \sqrt{v_y^2 + v_z^2}$. *Third column*: Standard deviation of the magnetic and velocity field strengths. σ_B and σ_V are normalised to their value at $t = 0$ for purposes of comparison between different runs (see Table 4.2).

Run ID	σ_{V0}[km/s]	σ_{B0}[μG]	t_{shock}[Myr]
k1p5_M2_parallel	217.7	1.016	282
k1p5_M3_parallel	388.5	1.016	188
k4_M2_parallel	133.1	0.659	439
k4_M3_parallel	246.1	0.513	292
k1p5_M3_perpendicular	388.5	1.099	188
k4_M3_perpendicular	246.1	0.513	293

Table 4.2: Values used in Fig. 4.7 and 4.8. The second and third column are the initial standard deviation of the velocity and magnetic field in the whole simulation box. The fourth column shows the total time needed for the shock to cross the entire simulation box.

the magnetic field obtained by integrating along the LOS. As expected from the MHD Rankine-Hugoniot conditions, the component parallel to the shock normal, B_x, is conserved, while the other components are amplified and stretched as a result of shock compression. We show also the magnetic field profile weighted with the synchrotron emission at 150 MHz (blue solid lines).

In Fig. 4.7 we show how the standard deviation (volumetric value) of the magnetic and velocity field evolve for all runs listed in Tab. 4.1. The evolution is characterized by two phases: 1) a first phase in which the shock is crossing region II (lasting 50–150 Myr depending on the type of run), and we have a purely decaying turbulence system on the right-hand side of the box ([0,200] kpc, see Fig. 4.4), and 2) a second phase in which the shock has already entered region III and is compressing the turbulent medium. The dashed gray vertical lines in Fig. 4.7 define the beginning of this second phase (the time differs according to the initial Mach number of each run).

The evolution of the standard deviation of the velocity and magnetic field are in general not correlated (see third column of Fig. 4.7). We also analysed the standard deviation of the parallel and perpendicular components of both fields with respect to the shock normal. In general, we find that the evolution of the parallel component dominates the evolution of σ_V, whereas the perpendicular component dominates the evolution of σ_B. The standard deviation of the parallel component (see first column of Fig. 4.7) decreases with time for both fields. The standard deviations of the perpendicular components (see second column of Fig. 4.7) show a different evolution: the perpendicular component, $\sigma_{V_\perp}$, follows the same behaviour of σ_V, while the perpendicular σ_B always increases right after the shock crossing in all runs. This trend is persistent and gets stronger with higher resolution (see Fig. 4.23 in Appendix 4.9).

The reason for this is that most velocity fluctuations are driven in the direction parallel to the shock normal, while magnetic field fluctuations are initially driven perpendicular to the shock normal due to compression. With time, the dynamics gets more complicated due to the shock compression and possibly also stretching of the magnetic field. The increase in σ_B induces a delay in the velocity field dissipation. The plateau observed in σ_V in the second phase (evolution to the right of the dashed gray lines in Fig. 4.7) indicates that the shock-induced turbulence could be maintained only for some time before σ_V decreases due to turbulent dissipation.

For all our runs, we verified that the density and also the temperature evolve in the same fashion as the velocity field in Fig. 4.7 and it is only the standard deviation of the magnetic field that has a characteristic evolution in both phases.

In the following, we summarize the observed effects for this second phase:

i) *The role of different turbulent injection scales*: We find that σ_B decreases faster in a system with smaller magnetic fluctuations ($L/4$) than in one with larger fluctuations ($2L/3$). This is expected as the turbulence injection scale is smaller in the $L/4$ case and therefore the eddy-turnover time is shorter. In fact, in the $L/4$ case, the shock-induced turbulence seems to only have an increasing effect on σ_B whenever the shock is perpendicular, i.e. $\theta_{bn} = 90°$.

ii) *The role of the main shock's Mach number*: The largest impact on increasing σ_B is due to a larger Mach number. For example, the $\mathcal{M} = 3$ and $\theta_{bn} = 0°$ case shows an increase of $\sim 31\%$ for the $2L/3$ turbulence and $\sim 7\%$ for the $L/4$ turbulence. Conversely, the $\mathcal{M} = 2$ and $\theta_{bn} = 0°$ case shows an increase of $\sim 25\%$ for the $2L/3$ turbulence and a decrease of $\sim 4\%$ for the $L/4$ turbulence. This suggests that weak shocks ($\mathcal{M} = 2$) are less likely to modify the initial distribution of magnetic fields for smaller turbulent scales.

iii) *The role of obliquity*: A perpendicular shock has the strongest effect on broadening the downstream magnetic field distribution. This is expected as the perpendicular components of the magnetic field are the only ones affected by the shock compression. The largest increase in both runs is $\sim 38\%$ (with respect to the corresponding dashed gray vertical line in Fig. 4.7).

Finally, we show in Fig. 4.8 the profiles of the total magnetic field strength for all runs for two snapshots. These 1D profiles are obtained integrating along the LOS and then taking an average. Each profile is again normalised to the pre-shock magnetic field of each run, B_{pre}. The two times shown in Fig. 4.8 correspond to when the shock is starting to compress the turbulent medium (left panel of Fig. 4.8), and when the shock has crossed the whole simulation box (right panel of Fig. 4.8). The
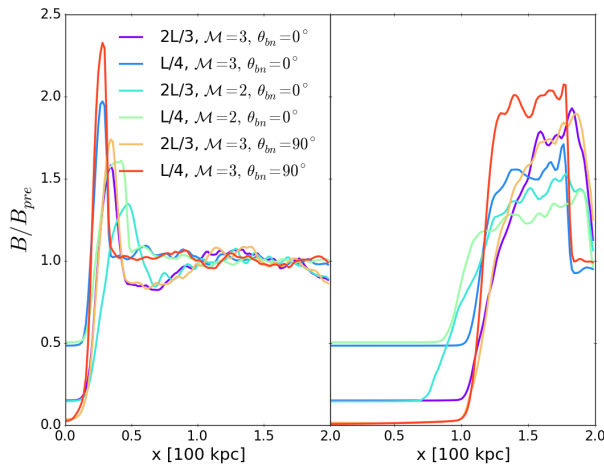
Figure 4.8: 1D magnetic field profile of all runs. *Left panel*: Shock front just entering the turbulent medium at $t_{\mathrm{shock}}/9$. *Right panel*: Shock front is almost at the right end of the x-axis at $t_{\mathrm{shock}}/19$. Refer to Tab. 4.2 for the value of t_{shock} of each run.

overall magnetic amplification in the downstream region differs in each run. The discrepancies observed in Fig. 4.8 can be explained by the different distribution of incidence angles between the upstream magnetic field and the shock normal along the shock front in the different runs. The downstream region in the $\mathcal{M} = 3$ case develops very similar profiles for both types of turbulence. In particular, the $L/4$ case leads to higher magnetic amplification (compare blue and red lines), whereas the $2L/3$ case leads to comparable downstream magnetic profiles (compare purple and orange lines). We observe that a lower Mach number, such as $\mathcal{M} = 2$, leads to less magnetic amplification, owing to the lower shock compression factor. In this case, the final extent of the region where a magnetic field amplification occurs in the downstream is ~ 25 kpc larger than in the case with a $\mathcal{M} = 3$ shock. This means that the strength of this shock is insufficient to further compress the turbulent medium, thus producing a more extended turbulent magnetic region which will be also reflected in the synchrotron emission.

4.4.2 Emission

We present a few three-dimensional renderings of the synchrotron emission produced by our modelling in Fig. 4.9, as seen along different lines of sight. Although the radio emission seems fairly uniform when observed edge-on (see following Fig. 4.10), the emission is not spatially uniform, but concentrated into threads and filaments in the shock plane. The combination of shock compression and turbulence introduces
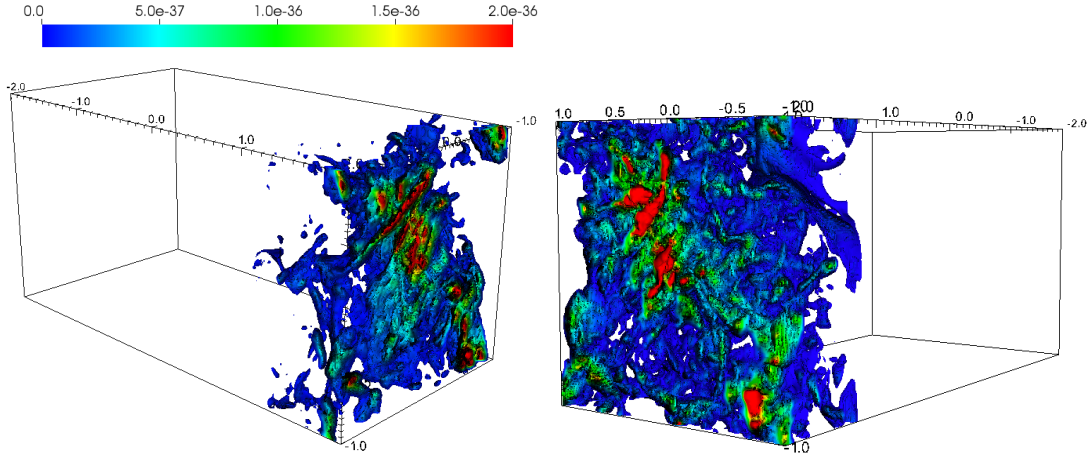
105

Figure 4.9: Visualization of synchrotron emissivity $\mathcal{J}_{\mathrm{syn}}$ isocurves for the $2L/3$, $\mathcal{M} = 3$ and $\theta_{bn} = 0°$ run at $t = 178$ Myr. The emissivity is shown in units of [erg cm^{-3} s^{-1} Hz^{-1} str^{-1}]. The axis are shown in units of [100 kpc].

anisotropies and fluctuations in the flow. This, in turn, directly affects the advection properties and energy evolution of the CR particles.

We show the surface brightness maps at 150 MHz for all runs at a time when the shock front has reached almost the right end of the simulation box in Fig. 4.10 (the different times are specified in the upper left corner of each panel)[5]. Note that we only applied Gaussian smoothing for the surface brightness maps in Fig. 4.10 (meant to mimic the finite spatial resolution of a typical LOFAR-HBA observation), while all of our following analysis was done without any smoothing. In the 3D view presented in Fig. 4.9, we can distinguish the complex substructure of the emission in the form of filaments, bristles, ribbons or other structures that cannot be classified in a single group. Nevertheless, since the emissivity is not volume-filling and the strength of the emission varies from region to region, some of this structure vanishes in projection.

The morphology observed in Figs. 4.9 and 4.10 depends on three factors: the strength of the shock, the obliquity of the shock, and the type of turbulence. A higher Mach number leads to stronger emission and elongated patterns due to a stronger compression of the magnetic field. On the other hand, the role of the upstream turbulence is more complex.

One can observe the effect of more elongated patterns for the cases with a shock

---

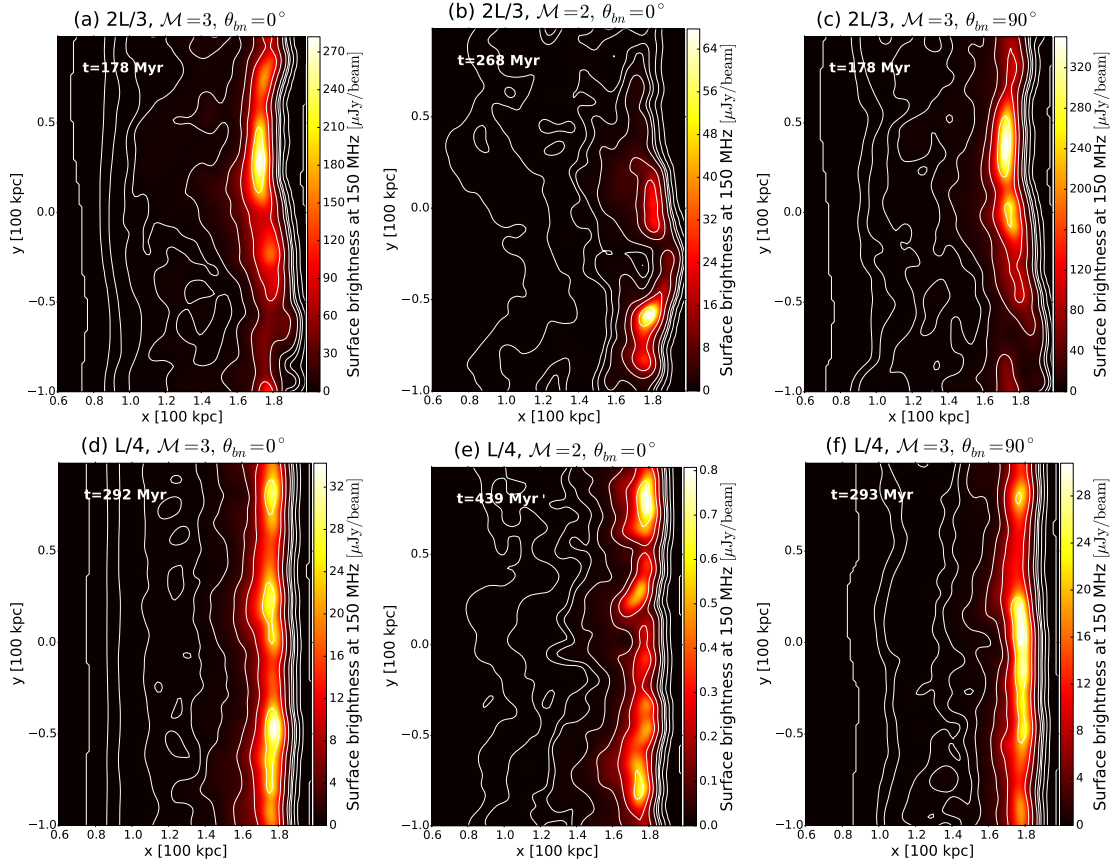[5]We have included the surface brightness maps along the x-axis in Appendix 4.10 for completeness.

Figure 4.10: Surface brightness at 150 MHz for all runs in Tab. 4.1 (see Equation 4.23). We considered a beam of $\theta^2 = 15" \times 15"$ to get the surface brightness $(\theta^2 I_\nu)$ in units of μJy/beam. We smoothed the maps with a Gaussian kernel with FWHM = 7.24 kpc (assuming $z = 0.023$).

of $\mathcal{M} = 3$ (comparing panels (a), (c), (d) and (f) of Fig. 4.10) due to the increased stretching of the eddies.

On the other hand, a shock of strength $\mathcal{M} = 2$ can produce disrupted patterns in our simulated emission. The shock front is less likely to look totally disrupted in the $L/4$ case (see panel (e)), while this effect is particularly noticeable in the $2L/3$ case (see panel (b)). We notice that this is a direct consequence of the sound speed in the media. For example, the $2L/3$ turbulence easily leads to regions with Mach numbers lower than our threshold ($\mathcal{M}_{\mathrm{min}} = 1.3$, see Appendix 4.8). This happens then because the initial sound speed of the $2L/3$ turbulence is slightly higher than that of the $L/4$ case (see Sec. 4.2.1). Subsequently, turbulent dissipation leads to an increase in sound speed and therefore, lowering the Mach number. Such low Mach numbers are not expected to accelerate electrons via the DSA process and therefore, they are excluded from our modelling. In fact, Kang et al. 2019 found that quasi-perpendicular shocks with $\mathcal{M} \lesssim 2.3$ may not efficiently accelerate electrons through DSA. Assessing the impact of different turbulent injection scales in $\mathcal{M} = 2$ shocks, would then require a tailored set-up which we leave for future work.

Finally, obliquity produces more elongated emission because shock compression only amplifies the component parallel to the shock front (i.e. the B_y and B_z components in this study).

In Fig. 4.11, we show 1D profiles of the emission presented in Fig. 4.10, at two more observing frequencies: 1.5 GHz and 650 MHz. The most extended emission is found in the runs with $\mathcal{M} = 2$ (see bottom panel of Fig. 4.11) in agreement with the 1D magnetic profiles previously shown in Fig. 4.8. These low Mach number runs also show the lowest values of surface brightness along the downstream due to the initial normalisation depending on the Mach number. This suggests that, in our survey of merger shocks, only those with $\mathcal{M} \sim 2$ would require a higher acceleration efficiency to reach observable values as it has been pointed out in previous works (e.g. Botteon et al., 2020). Finally, the steepness of the emission profile depends on the magnetic morphology. Comparing all the $\mathcal{M} = 3$ runs, the $2L/3$ turbulence case shows a shallower decline compared to the $L/4$ case. This is a direct consequence of the initial distribution of the magnetic field strength. In Fig. 4.3 of Sec. 4.2.1, we showed that initially the $L/4$ run reaches higher magnetic field values in the tail of its PDF, which leads to larger synchrotron losses.

Spectral index

In Fig. 4.12, we show the spectral index maps for the two different turbulent media with the $\mathcal{M} = 3$ shock using Eq. (4.24). We can observe the expected spectral index gradient starting from the shock front (red) to the end of the downstream
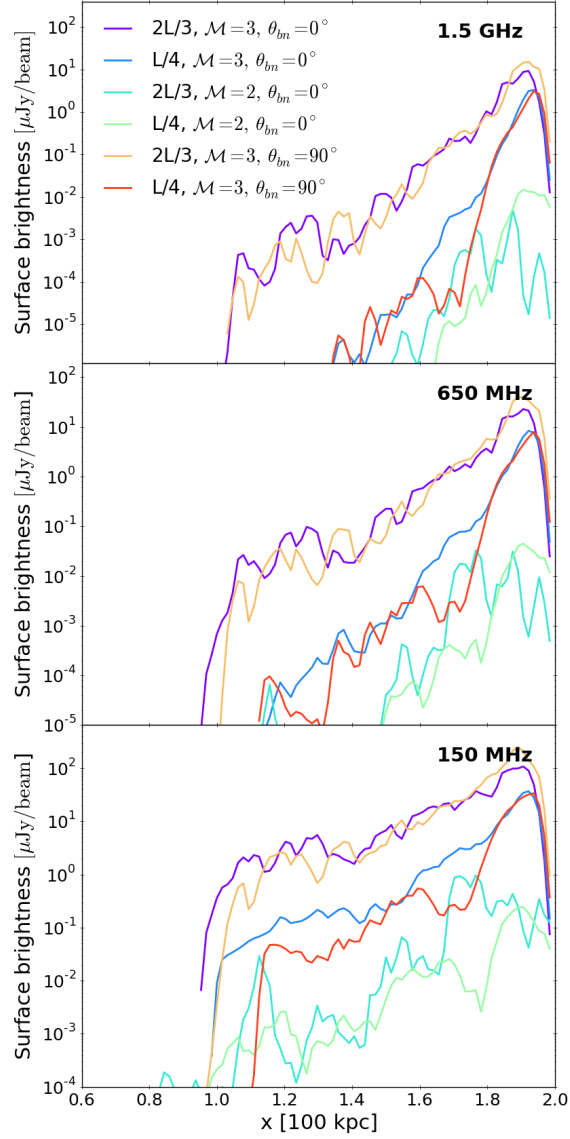
Figure 4.11: 1D surface brightness profiles obtained from the emission maps at 1.5 GHz (*top panel*), 650 MHz (*middle panel*) and 150 MHz (*bottom panel*) for all runs.
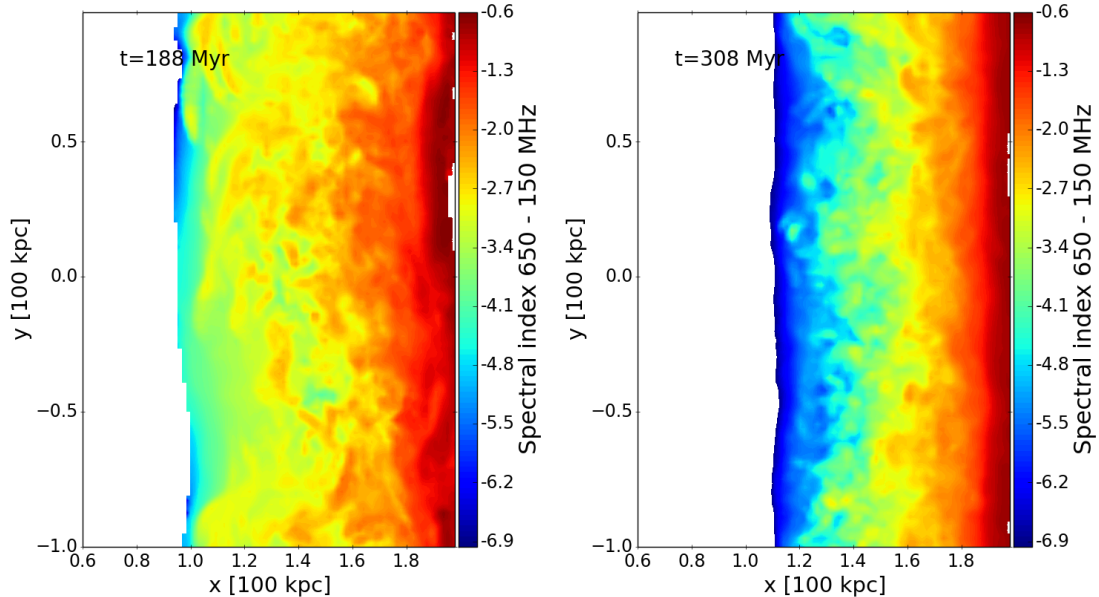
Figure 4.12: Spectral index maps obtained between 150 MHz and 650 MHz at t_{shock} using Equation (4.24). *Left panel:* $2L/3$, $\mathcal{M} = 3$, $\theta_{bn} = 0°$ run. *Right panel:* $L/4$, $\mathcal{M} = 3$, $\theta_{bn} = 0°$.

region (blue). In the $2L/3$ case, the spectral index values range between $\alpha = -0.6$ and $\alpha = -4.9$, while it goes from $\alpha = -0.6$ to $\alpha = -6.9$ in the $L/4$ case. This agrees with the previous subsection, where we discussed the emission profiles. In the same way, the turbulent medium with smaller initial fluctuations $L/4$ is more likely to produce a steeper gradient because the initial magnetic field distribution has a larger tail (see Fig. 4.3).

In Fig. 4.13, we show the corresponding spectral index profiles along the downstream region for completeness. In the top panel of Fig. 4.13 we show how the profile changes when taking into account different frequencies for one specific run: $2L/3$, $\mathcal{M} = 3$, $\theta_{bn} = 0°$. The profiles start to differ beyond ~ 20 kpc from the shock front where the emission at lower frequencies decreases more slowly. In the lower panel, we show the spectral index profiles for all of our runs between 650 and 150 MHz. The selected snapshots correspond to those in Fig. 4.10. For the higher Mach number (i.e. $\mathcal{M} = 3$), the $2L/3$ profiles agree more with observations than the $L/4$ profiles. In the $L/4$ case, the spectral index profiles are steeper than observed. For example, the relic in the cluster MACS J0717.5+3745 (see van Weeren et al., 2017; Bonafede et al., 2018) with a Mach number of $\mathcal{M} = 2.7$ (inferred from the injection spectral index α), shows a spectral index steepening up to values of ~ -2.5 over a region of

110

$\lesssim 170$ kpc. Another example is the "Toothbrush" relic (see Rajpurohit et al., 2018, 2020a) which steepens also up to values of ~ -2.5 over a region of ~ 500 kpc. This suggests that the initial turbulent magnetic field distribution before a shock crossing is rather narrow. For the forced turbulence used in this work, this means that the standard deviation must be smaller than $\sigma_B \sim 1 \, \mu G$ (see Fig. 4.3 in Sec. 4.2.1 for the initial magnetic field distribution). On the other hand, this also suggests that the injection scale (and also the magnetic coherence scale) of the turbulence in galaxy clusters outskirts could be $2L/3$ (~ 133 kpc) or even larger.

It is fairly common in observations of radio relics, that only the integrated spectral index can be computed. This is done by fitting the total observed flux (see Eq. 4.25) against different available frequencies. We computed the integrated spectral index in this fashion using 1.5 GHz, 650 MHz and 150 MHz frequencies. In Fig. 4.14 we show how the integrated spectral index evolves as the shock sweeps across the simulation box. In the first ~ 60 Myr the integrated spectral indices differ quite significantly, whereas after ~ 140 Myr the value of the integrated spectra seems to converge to the same value for all runs. The relation between the real spectral index α and the integrated one is often assumed to be (e.g. Kardashev, 1962; Heavens & Meisenheimer, 1987):

$$\alpha_{\text{int}} = \alpha + \frac{1}{2} = \frac{\mathcal{M}^2 + 1}{\mathcal{M}^2 - 1}, \tag{4.26}$$

and therefore we also plot the expected α_{int} for different Mach numbers as a reference in Fig. 4.14 with gray dashed horizontal lines. The integrated spectral index from our runs does not follow a characteristic pattern and it does not remain strictly constant through a time span of roughly 200–300 Myr. In addition, we include the corresponding evolution of the integrated spectral index for two extra runs with a completely uniform medium (density, velocity, pressure and magnetic field) with shocks of strength $\mathcal{M} = 2$ and $\mathcal{M} = 3$. In the uniform media, Eq. (4.26) holds after ~ 50 Myr when the energy spectrum reaches a steady state at the shock (see Kang et al. 2017 for a one-dimensional uniform media study), however this is not the case for all the turbulent media. In particular, the effect of turbulence on the 3D distribution of the synchrotron emissivity is that it makes it patchy and not volume-filling (as can be observed in Fig. 4.9). This in turn has an effect on the integrated flux and therefore, the integrated spectral index.

Hence, it can be difficult to recover the real spectral index and Mach number through this method, even if recent high-resolution observations of radio relics show consistent integrated and injection spectra (e.g. Rajpurohit et al., 2020a). The fact that Eq. (4.26) only holds for a planar shock where all the fields are uniform, suggests that one should be careful when making use of it. One good way to confirm if it is applicable or not is by cross-checking with the result from high-resolution spectral

index maps.

This has also been found in previous studies. For example, Kang 2015 showed that the relation in Eq. (4.26) only holds for planar shocks, but not for spherical shocks. In the presence of a turbulent medium, the geometry of the shock is more complicated leading to the evolution observed in Fig. 4.14.

We find that the integrated spectral index in Fig. 4.14 is biased towards higher Mach numbers for all runs. The main reason for this is that the brightest radio emitting regions correspond to the strongest shock compression regions, which in average gives a bias towards higher Mach numbers. In Sec. 4.4.4. we will show an analysis of the Mach number distribution and compare it to the one inferred from the thermal fluid.

In Fig. 4.15 we show how the emission at the shock front correlates with the magnetic field strength in 3D and 2D. We show the evolution for the $2L/3$ case with $\mathcal{M} = 3$ and $\theta_{bn} = 0°$ run. The emissivity computed from Eq. (4.20) scales with the magnetic field and frequency as

$$\mathcal{J}_{\mathrm{syn}} \propto B^{(p+1)/2} \nu^{-(p-1)/2}, \tag{4.27}$$

(see Engel, 1979) where $\alpha = (p-1)/2$ is the spectral index and p is related to the Mach number through Eqs. (4.13) and (4.12),

$$\alpha = \frac{(p-1)}{2} = \frac{(q-3)}{2} = \frac{\mathcal{M}^2 + 3}{2(\mathcal{M}^2 - 1)}. \tag{4.28}$$

In the top panel of Fig. 4.15, we show this relation for different Mach numbers with coloured lines and we add an additional black dashed line corresponding to a fit of all the data points. Overall, we find that there is always a systematic mismatch with the initial real Mach number of the shock. During the first ~ 20 Myr, the 3D distribution shows a sharper relation coinciding with what is expected from Eq. (4.28). Nevertheless, shortly after that there will be a spread in the Mach number and magnetic field distribution along the shock front. This spread will keep changing as a consequence of all the turbulent motions in the medium. The black dashed line shows that the relation is biased towards larger Mach numbers. For the 2D case shown in the bottom panel of Fig. 4.15, we considered a magnetic field weighted with the radio emissivity:

$$B_w = \frac{\int B \, \mathcal{J}_{\mathrm{syn}} dZ}{\int \mathcal{J}_{\mathrm{syn}} dZ}. \tag{4.29}$$

We show the same relation pointed out in the upper panel as a reference. The dashed black line in this case corresponds to the fit of all data points in the 2D map.
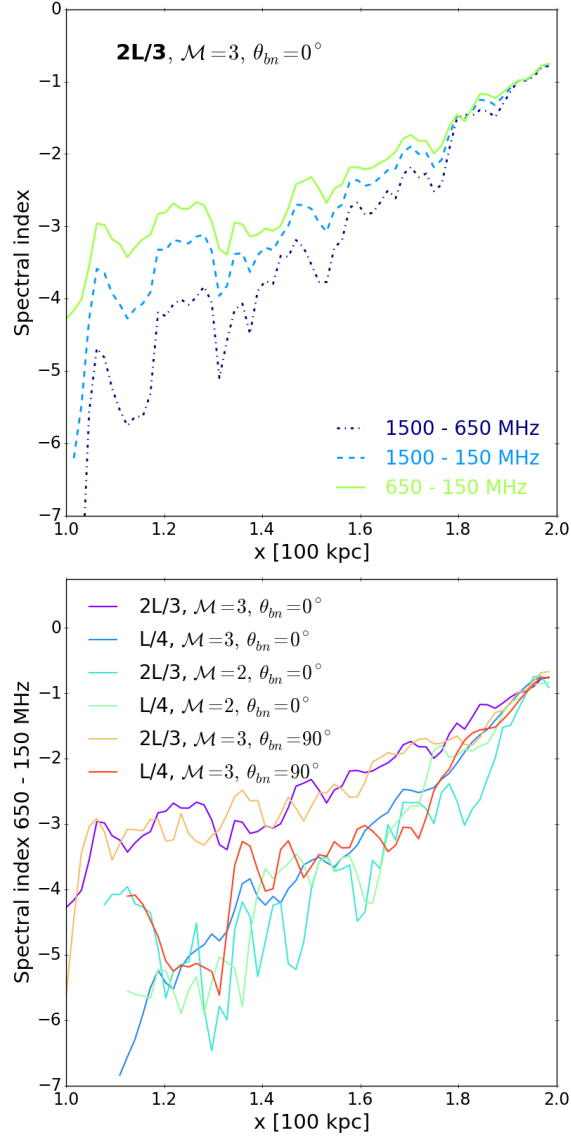
Figure 4.13: *Top panel*: Spectral index profile for the $2L/3$, $\mathcal{M} = 3$, $\theta_{bn} = 0°$ case at $t = 178$ Myr. *Bottom panel*: Spectral index profiles between 150 MHz and 650 MHz for all the cases. The profiles are computed at the same times as in Fig. 4.10.
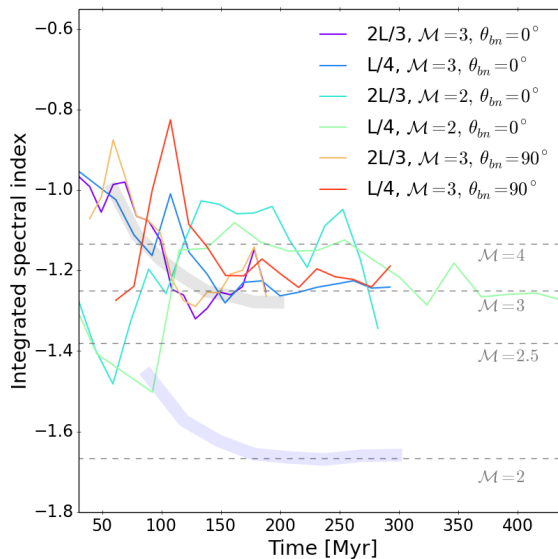
Figure 4.14: Integrated spectral index evolution computed from fitting the total flux. The gray horizontal dashed lines show the expected integrated spectral index assuming that $\alpha_{\text{int}} = \alpha + 1/2$ for different Mach numbers (see Eq. 4.26). The shaded areas correspond to the uniform runs with $\mathcal{M} = 2$ (*blue*) and $\mathcal{M} = 3$ (*gray*) shocks.

While in this case we have less data points due to the integral along the LOS, it is interesting to see that the bias towards higher Mach numbers is still there. This suggests that the bias is not due to projection effects. We will further discuss the reason behind this bias in Sec. 4.4.4.

4.4.3 Spectral properties

Magnetic field

One important feature that characterizes the magnetic field is its *power spectrum*:

$$P_{ij}(\mathbf{k}) = \frac{1}{(2\pi)^3} \int \int \int e^{-i\mathbf{k}\cdot\mathbf{x}} R_{ij}(\mathbf{k}) d\mathbf{k}, \tag{4.30}$$

where $R_{ij} = \langle b_i(\mathbf{x_0}) b_j(\mathbf{x_0} + \mathbf{x}) \rangle$ is the two-point correlation function between the magnetic fields b_i and b_j (e.g. Batchelor, 1951). In the case of homogeneous and isotropic fields the relation between the spectral energy and the 1D power spectrum is found to be

$$E(k) = 2\pi k^2 P_{ii}(k). \tag{4.31}$$

114
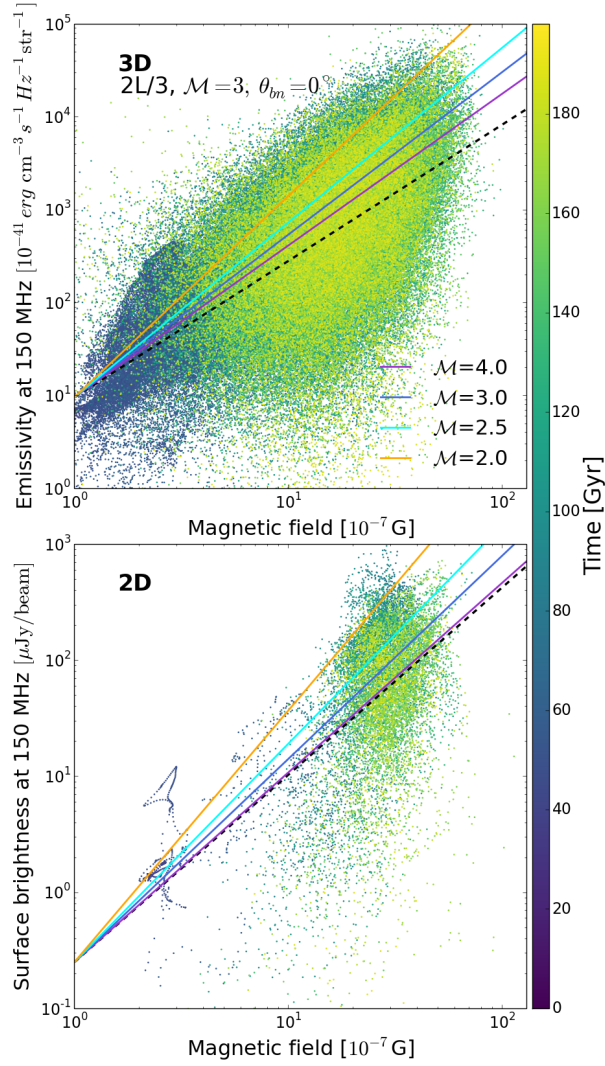
Figure 4.15: Phase-plots of the magnetic field versus the radio emission at 150 MHz at the cells where the shock front is located for the $2L/3$, $\mathcal{M} = 3$, $\theta_{bn} = 0°$ run. *Top panel*: values extracted out of the 3D distributions, i.e. the emissivity $\mathcal{J}_{\mathrm{syn}}$. The coloured lines show the expected fit for different Mach numbers and the black dashed line shows a fit of the data at $t = 188$ Myr. *Bottom panel*: values extracted out of the 2D maps, i.e here we have the surface brightness and the values of the magnetic field weighted with the emission (see Eq. 4.29).

We will refer to the 1D power spectrum $P_{ii}(k)$ simply as $P(k)$. In order to obtain the 1D power spectrum we averaged the 3D power spectrum of the magnetic field over spherical shells:

$$P(k) = \frac{1}{N_k} \sum_{k-\frac{1}{2} < |\mathbf{k}| \leq k+\frac{1}{2}} P(\mathbf{k}). \tag{4.32}$$

We computed the energy power spectrum in the right half part of the simulation (region III, [0,200] kpc) (see Fig. 4.4). In the top panel of Fig. 4.16 we show the final magnetic energy spectra for all our runs and in the bottom panel we show the final power spectra computed for the emissivity at 150 MHz. In Fig. 4.17, we present the whole evolution of the magnetic energy spectrum $E_B(k)$ condensed in the form maps. Each of these maps contains the following information: the y-axis shows the evolution and the x-axis shows the wavenumber k coloured with the amplitude of the magnetic energy spectrum at that k. In this way, the darker colours denote the regions where the power is peaking (see Fig. 4.16 as a reference). The dashed gray line is a reference for the reader to know when the shock enters this turbulent region, i.e. region III. We are interested in understanding the effect of shocks in the magnetic energy spectrum, in presence of an ICM with decaying turbulence. We can see in Fig. 4.17 two important features: i) the wavenumbers $k \gtrsim 10$ (corresponding to scales $\lesssim 10$ kpc) are largely unaffected by shocks with strength $\mathcal{M} =$2–3. The resolution may play a role in this case. For example, when a shock enters a turbulent medium, Richtmyer–Meshkov instabilities peaking at small scales can arise. Nevertheless, such instability would take a long time to grow considering weak shocks and therefore, we do not expect those to have a major effect in the context of radio relics; ii) the shock compression has a notable effect only in the $\theta_{bn} = 90°$ cases (see the two bottom panels of Fig. 4.17) at $k \lesssim 2$ (corresponding to scales $\gtrsim 50$ kpc). In these cases, power shifts towards smaller wavenumbers (larger scales) due to the new turbulence introduced after the shock passage. This agrees with previous results from cosmological MHD simulations. In Domínguez-Fernández et al. 2019, we observed the same effect when analysing the evolution of a merging galaxy cluster over a time span of almost 10 Gyr. After every merger, shock waves are created and after every shock crossing, the magnetic power shifts to smaller wavenumbers (or larger scales).

Emission

In this subsection we make the same analysis as in subsection 4.4.3, but for the radio emission and we compare it to the results from the magnetic field. We compute the power spectrum of the 3D distributions and also of the 2D maps (computed by integrating along the LOS). The 1D power spectrum is obtained by averaging the
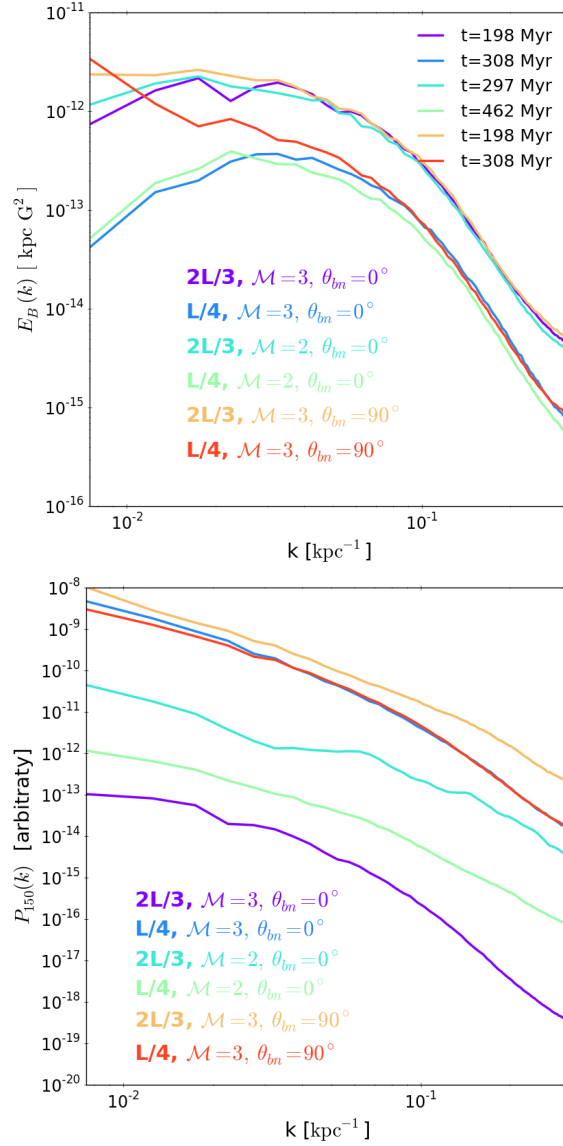
Figure 4.16: *Top panel*: Final magnetic energy spectrum for all our runs. The spectra are computed in a $(200 \text{ kpc})^3$ volume through Eqs. (4.31) and (4.32). The final time step differs for each run and it is specified in the legend. *Bottom panel*: Final power spectrum of the synchrotron emissivity at 150 MHz for all our runs (same times as in the top panel).
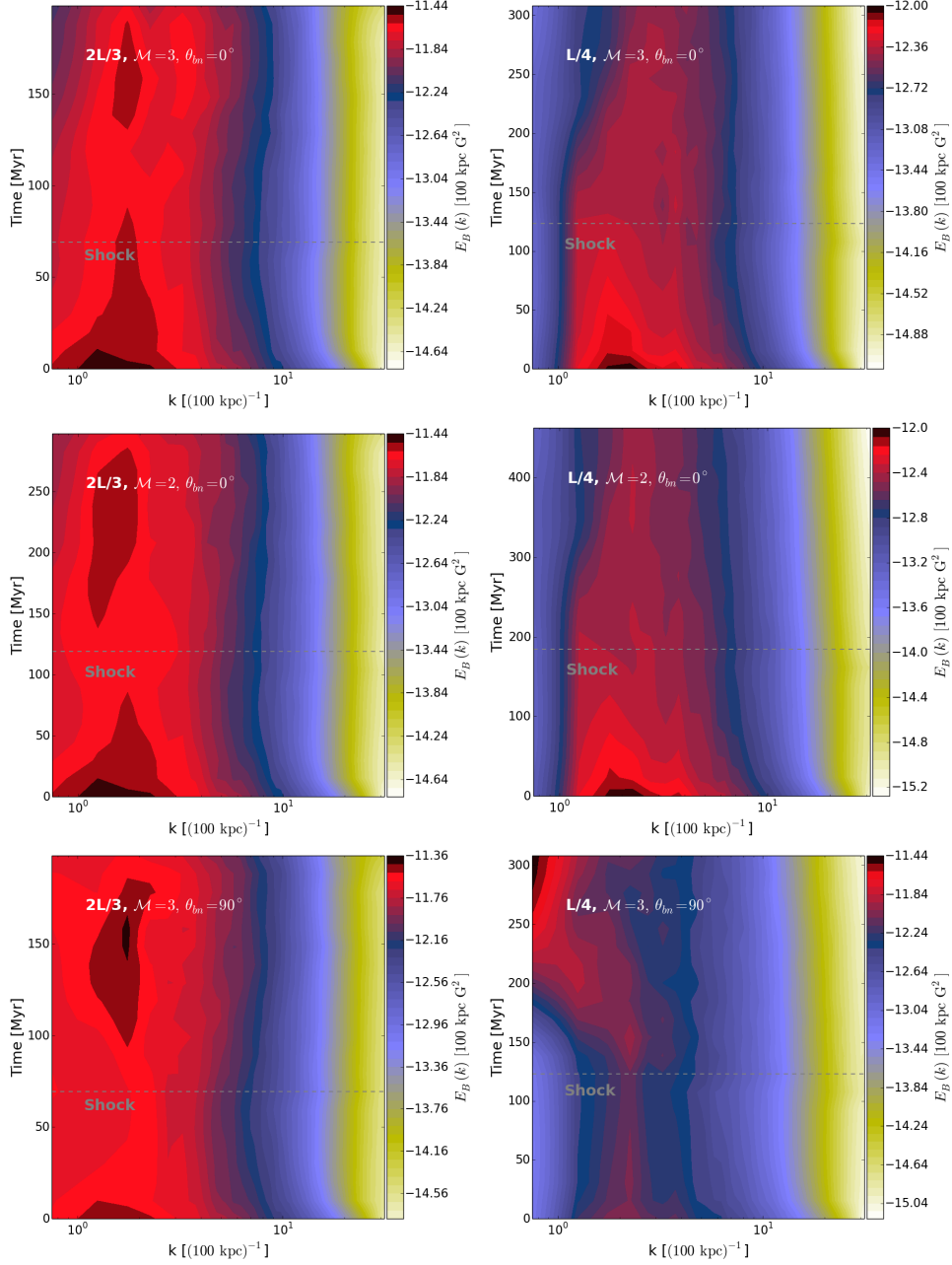
117

Figure 4.17: Evolution of the magnetic energy spectrum in the turbulent part of the box (region III [0,2] in Fig. 4.4 corresponding to a (200 kpc)³ cube). At each time-step (y-axis), we show the magnetic power spectrum by colouring the x-axis with its amplitude (see colourbar in logarithmic scale).

3D spectrum over spherical shells (see Eq. (4.32)) as mentioned above; while for the 2D maps, we averaged the 2D spectrum over annuli. Afterwards we can compute the characteristic length of the power spectrum for the emission as

$$\lambda_c = \frac{\int k^{-1} P(k) \, dk}{\int P(k) \, dk}, \tag{4.33}$$

and for the magnetic field as,

$$\lambda_B = \frac{\int k^{-1} P_B(k) \, dk}{\int P_B(k) \, dk}, \tag{4.34}$$

where $P(k)$ and $P_B(k)$ correspond to the power spectrum of the synchrotron emission (see Eq. (4.20)) and the power spectrum of the magnetic field, respectively.

In the first two columns of Fig. 4.18 we show the results for the 3D case for all of the runs including also the characteristic scale of the magnetic field λ_B. The characteristic scale of the radio emission is in general of the same order of the characteristic scale of the magnetic field, that is of the order of $\lesssim 100$ kpc. There are some specifics regarding 1) the Mach number: higher Mach numbers lead to larger emission scales, for example a $\mathcal{M} = 3$ leads to a maximum scale of ~ 100 kpc, whereas a $\mathcal{M} = 2$ leads to a maximum of ~ 80 kpc; and 2) the injection scale of the turbulence in the $\theta_{bn} = 0°$ case: the characteristic scale of the emission seems not to be affected by the injection scale, but it cannot be directly correlated with the magnetic field's scale. For example, the top panels of the first two columns in Fig. 4.18 show how λ_c is of the same order for both cases while the underlying turbulence is different. In contrast, λ_B is directly affected by the underlying turbulence and therefore, it is of a different order. The type of injection scale of the turbulence in the $\theta_{bn} = 90°$ case plays a big role for the evolution of λ_B, but this is not reflected in the evolution of λ_c. This happens only due to the fact that the acceleration efficiency, η, does not depend on θ_{bn} in our modelling. The role of a varying η will be subject of future work.

The characteristic scales of the integrated LOS variables are also shown in Fig. 4.18 (last two columns). In this case, λ_B can be smaller than in reality is by roughly 17–23% in some cases, while λ_c is only smaller by $\sim$10-15 %. Therefore, we do not observe strong changes in these results due to projection effects.

In summary, we find that the characteristic scales that can be derived from the radio emission could serve as a good proxy for knowing the order of magnitude of the magnetic field's characteristic scale. However, we also find a rather complicated evolution that cannot give us a one-to-one correlation between these two scales and therefore, this exercise alone will not give us much information regarding the type of turbulence existing in the outskirts of ICM. In practice, also the resolution of the radio telescopes plays an important role and will definitely affect these results.
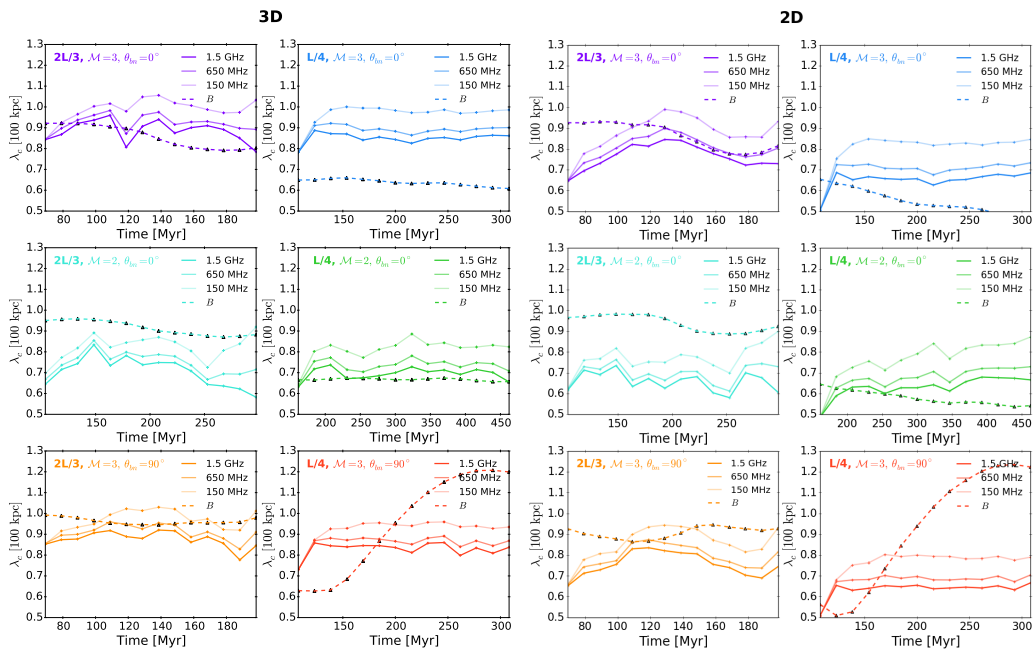
Figure 4.18: *First two columns*: Characteristic scale of the 3D distributions according to Eq. (4.33). *Last two columns*: Characteristic scale of the 2D distributions. Each panel shows the evolution of λ_c for 1.5 GHz, 650 MHz and 150 MHz and also the evolution of the magnetic field's characteristic scale λ_B.

4.4.4 Mach number distributions

3D distribution

While the shock front's Mach number distribution peaks at its initial Mach number for almost the whole evolution, it develops a tail towards higher Mach numbers owing to turbulent motions[6]. In order to study its impact on the emission, we obtain the emissivity, $\mathcal{J}_{\mathrm{syn}}$, corresponding to the cells tracking the shock front at each time step and correlated it with its Mach number. We can do this because the particles are being activated whenever they detect the shock front. In Fig. 4.19, we show the binned statistics for the two quantities obtained considering 16 time steps.

In order to generate an X-ray alike estimate of the Mach number, we computed the X-ray emissivity

$$\mathcal{J}_{\mathrm{X-ray}} = 1.2 \times 10^{-28} T^{1/2} \left(\frac{\rho}{m_p} \right)^2, \qquad (4.35)$$

in units of [erg cm^{-3} s^{-1} Hz^{-1} str^{-1}], where m_p is the proton's mass and T and ρ are in cgs units. Thus, we selected the emission $\mathcal{J}_{\mathrm{syn}}$ and $\mathcal{J}_{\mathrm{X-ray}}$ only at the shocked cells at each time step in order to compute the binned statistics. We show the distributions at different times with dashed coloured lines and that of the whole evolution with the solid blue lines in Fig. 4.19. The top panels show the binned statistics considering the radio emissivity and the bottom panels show that of the X-ray emissivity.

The discrepancy between the two statistical distributions is evident. While the radio emissivity is always biased towards larger Mach numbers, the X-ray emissivity is biased towards smaller Mach numbers. In fact, the peak of the binned distribution of the radio emissivity (temporal envelope) is similar to the values in the tail of the real 3D Mach number distribution (i.e. see an example in Fig. 4.22 in Appendix 4.8). Out of the six cases analysed, only the $L/4$, $\mathcal{M} = 2$, $\theta_{bn} = 0°$ case shows a partial match between both distributions. We also observe that the radio-Mach number statistics fluctuates with time such that the peak Mach number can vary a fair bit.

In addition, we analysed two runs with uniform media (all fields) but the same Mach numbers (i.e. $\mathcal{M} = 2$ and $\mathcal{M} = 3$). We verified that in this case the distributions of both emissivities and Mach numbers are the same. Hence, our results suggest that the difference in Mach numbers in radio and in X-ray is a result of turbulence.

---

[6]see an example for the case $2L/3$, $\mathcal{M} = 3$, $\theta_{bn} = 0°$ in Fig. 4.22 of the Appendix 4.8
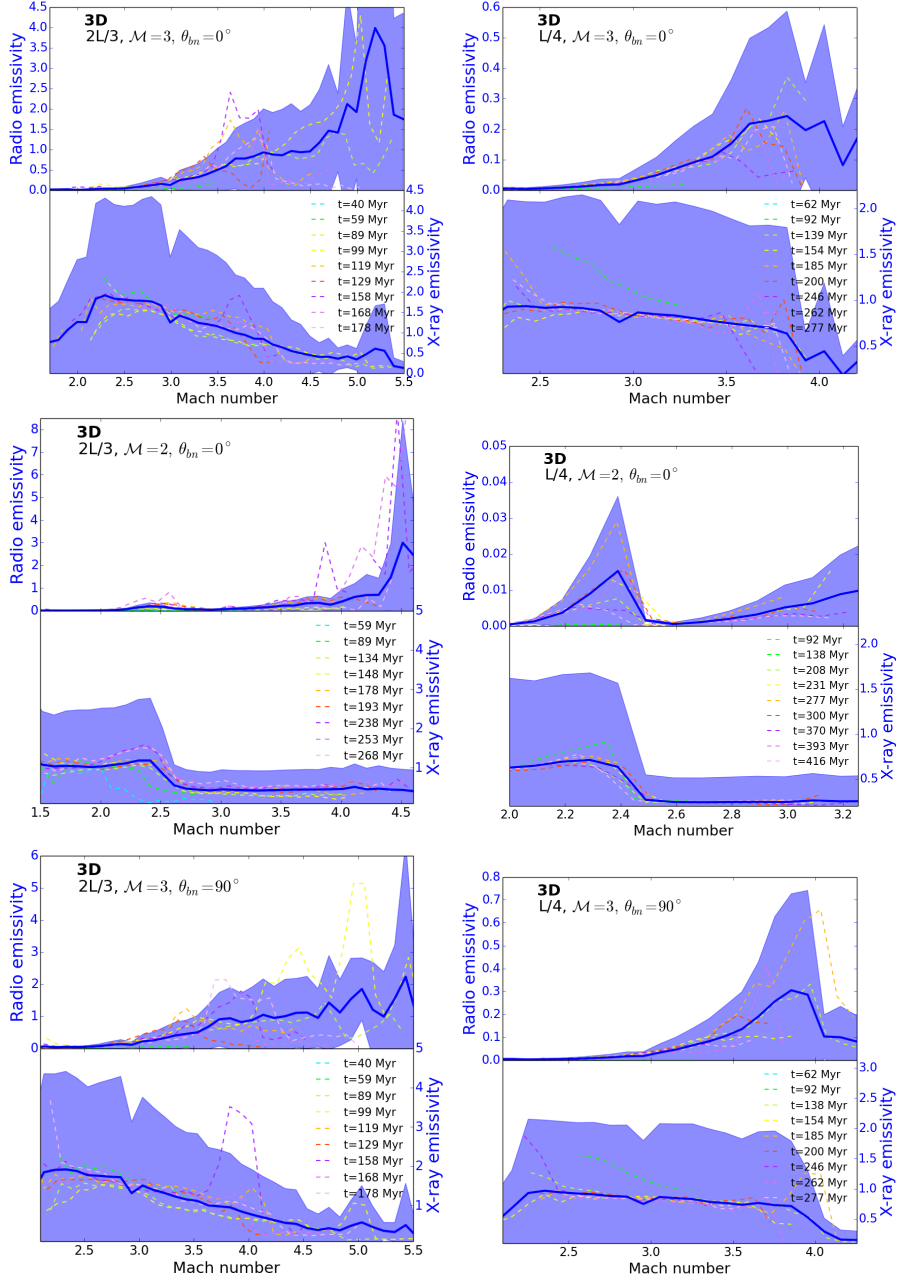
Figure 4.19: Binned statistics of radio emissivity at 1.5 GHz (*left axis*) and X-ray emissivity (*right axis*) with the Mach number of the shock front for different time steps (dashed coloured lines). The dark blue line shows the statistics taken into account the whole evolution and the shadowed areas denote the corresponding 75-th percentile of the distribution. The emissivity is shown in units of $[10^{-38}\mathrm{erg\,cm^{-3}}s^{-1}\mathrm{Hz^{-1}str^{-1}}]$.

In the presence of turbulence, the radio emissivity is not volume-filling, while the X-ray emissivity comes from the whole shock front. The fact that compression is different from region to region leads to a patchier radio emissivity that can probe a limited part of the shock front (see Fig. 4.9). Apart from that, the radio emission is biased towards higher Mach numbers because the initial CR energy is $\propto \mathcal{M}^3$ (which in our work corresponds to the normalisation N_0 defined in Eq. (4.15)). Finally, the magnetic field fluctuations created after the shock-crossing play an important role. As discussed in Sec. 4.4.1, the amplitude of the magnetic field fluctuations (which directly affects the radio emission) decreases more slowly than the velocity, density and temperature fluctuations. This adds to the discrepancy because the X-ray emissivity depends only on the temperature and density fields.

4.5 Summary and conclusions

We have presented a hybrid framework to compute the synchrotron emission from a shock wave propagating through a medium with decaying turbulence representing a small fraction of the ICM. In our framework, the MHD grid represents a thermal fluid, whereas Lagrangian particles represent CR electrons. We injected CR electrons at the shock discontinuity assuming diffusive shock acceleration. Each CR electron evolves according to the cosmic-ray transport equation in the diffusion approximation.

Our simulations explored shocks with Mach numbers characteristic of radio relics, i.e. $\mathcal{M} = 2$ and $\mathcal{M} = 3$. Moreover, we varied the downstream turbulence using turbulence-in-a-box simulations: a solenoidal subsonic turbulence with power peaking at 2/3 of the box (case $2L/3$) and a solenoidal subsonic turbulence with power peaking at 1/4 of the box (case $L/4$). One snapshot of each simulation was selected as an initial condition for our shock-tube simulation. Our results can be summarized as follows:

i) *Impact of a shock on decaying turbulence*: We find that mild shocks produce magnetic fluctuations in the downstream region that do not correlate with fluctuations in velocity, density and temperature. In fact, we find that magnetic fluctuations can increase even when velocity fluctuations decrease. This, in turn, can affect the final extent of the magnetic downstream. We find the strongest effect in perpendicular shocks, as expected from theory. Shocks with $\mathcal{M} = 2$ travelling in a medium with smaller fluctuations, such as our $L/4$ case, cause the least effect and seem to hardly modify the initial magnetic field distribution.

ii) *Radio emission*: The existence of substructure in the synchrotron emission is a direct consequence of a turbulent medium. We found that $\mathcal{M} = 2$ shocks in our set-up are unlikely to reproduce observable radio relics. The physical reason behind this is that $\mathcal{M} = 2$ shocks are not strong enough to modify the initial pre-shock magnetic field. For example, the relic at Abell 2744 (e.g. Govoni et al., 2001; Eckert et al., 2016; Pearce et al., 2017; Paul et al., 2020) reaches a surface brightness of the order of tens of mJy/beam at 1.4 GHz, which would require an acceleration efficiency of $\eta \sim 1$ in our $L/4$ turbulence.

iii) *Discrepancies in the spectral index*: Our spectral index profiles suggest that in the case of $\mathcal{M} = 3$ shocks, a turbulent injection scale of $2L/3$ or even larger reproduces observations better than the $L/4$ case. The $L/4$ initial magnetic field distribution allows for higher values of the magnetic field strength reflected in the tail of the PDF which steepens the spectral index profiles more than in the $2L/3$ case. We conclude that an initial turbulent, magnetic field distribution in the ICM must have a standard deviation smaller than $\sigma_B = 1\,\mu$G. We compare our results of the integrated spectral index to the relation $\alpha_{\mathrm{int}} = \alpha + 1/2$ and find that this relation does not seem to hold in the presence of a turbulent medium. The reason for this is the distribution of Mach numbers within a shock front in a turbulent medium. As a consequence, the injected electrons will have different initial energy spectra.

iv) *Discrepancies in Mach numbers*: We find that the synchrotron emission is biased towards larger Mach numbers when comparing to the X-ray emission. This agrees with previous numerical work (e.g. Hong et al., 2015) and a number of observations of radio relics. For example, X-ray observations of the Toothbrush relic in the cluster 1RXS J0603.3+4214 infer a Mach number of $\mathcal{M} \sim 1.5$ (e.g. Ogrean et al., 2013; van Weeren et al., 2016), while radio observations infer a higher Mach number of $\mathcal{M} \sim 3.7$ (e.g. Rajpurohit et al., 2018, 2020a). The source of this discrepancy lies in 1) the stronger dependence of the synchrotron emission on the compression in the shock and 2) the fact that the amplitude of the magnetic field fluctuations (which affect the radio emission) decreases more slowly than the density and temperature fluctuations. Hence, higher Mach numbers in the tail of the Mach number distribution bias the overall Mach number.

v) *Magnetic energy spectrum*: We find that scales $\lesssim 10$ kpc are largely unaffected

by shocks with $\mathcal{M} = 2$–3, independent of the type of turbulence. We find that the power shifts towards smaller wave numbers (larger scales) after shock passage which is more pronounced in perpendicular shocks.

vi) *Characteristic length of the radio emission*: The characteristic lengths derived from the power spectrum of the emission, λ_c, and magnetic field, λ_B, are of the same order. We find that λ_c is in general of the order of $\lesssim 100$ kpc. Analysing the LOS variables, we do not observe strong projection effects and λ_B and λ_c are only 17–23% and 10–15% smaller than in 3D.

In summary, we could identify the most important features that link the observable properties of radio relics with the dynamical properties of the upstream ICM. Our work confirms that the Mach numbers inferred from the radio emission are likely to be overestimates of the real Mach number of the thermal fluid in the presence of turbulence. This has been previously pointed out as a possible solution that can alleviate the problem of acceleration efficiencies and as a possible explanation for the non-detection of γ-rays from galaxy clusters (see Ackermann et al. 2010, 2014, 2016 and Vazza & Brüggen 2014). While CRe and CRp are expected to be accelerated at the same places, their acceleration mechanisms and efficiencies will differ (e.g. Caprioli & Spitkovsky, 2014a). CRe are accelerated preferentially at quasi-perpendicular shocks and CRp at quasi-parallel shocks. Recent works by Wittor et al. 2020 and Banfi et al. 2020 used cosmological MHD simulations to show that indeed the predominance of quasi-perpendicular shocks in merger and accretion shocks might be enough to explain the absence of CRp. Therefore, in future work we will include the obliquity dependence in our acceleration efficiency, η. Moreover, we intend to survey a larger range of possible parameters, both, for the ICM conditions and for the shock properties. This will help us to assess whether the large variety of relic sources can be explained by the model adopted here. We will also present a detailed study considering polarisation (Q and U Stokes parameters, as well as Rotation Measure), different lines-of-sight, projection and beam effects.

4.6 Acknowledgements

4.7 Appendix A: Numerical divergence of the magnetic field

The $\nabla \cdot \mathbf{B} = 0$ condition in the particle module of the PLUTO code is maintained with the hyperbolic divergence cleaning technique where the induction equation is coupled to a generalized Lagrange multiplier (GLM) (e.g. Dedner et al., 2002). In Kritsuk et al. 2011, it has been argued that the best results for the divergence-free evolution of the magnetic field are achieved using the constrained transport (CT) method. Keeping this in mind, we tested the differences of the $\nabla \cdot \mathbf{B} = 0$ condition with the GLM and CT techniques. In Fig. 4.20, we show the evolution of the magnetic field divergence using the same set-up as our $2L/3$, $\mathcal{M} = 3$ and $\theta_{bn} = 90°$ run (see Table 4.1) for the whole simulation box. Both methods are comparable and keep the numerical magnetic field divergence under $\sim 0.001\%$ of the local magnetic field value. This demonstrates that the use of the GLM divergence cleaning technique is robust against CT for our particular set-up. Thus, we do not expect our numerical scheme to have an impact in our final synchrotron emission maps. Additionally, we show how the divergence condition behaves for the interface between regions II and III in our setup in Fig. 4.20. The effects of the initial interpolation of the external input get diminished after a few steps and the numerical magnetic field divergence drops again below $\sim 0.001\%$ before the shock enters the region of interest (i.e. region III); see an additional discussion about this in Appendix D of Banda-Barragán et al. 2018.

4.8 Appendix B: Shock finder

The algorithm to find shocks is already implemented in the PLUTO code (see Vaidya et al., 2018). In the first step, shock cells are tagged through the $\nabla \cdot \mathbf{v} < 0$ condition. Then we implemented an extra condition for the activation time of the tracer particles in order to compute the initial Mach number and compression ratio. This
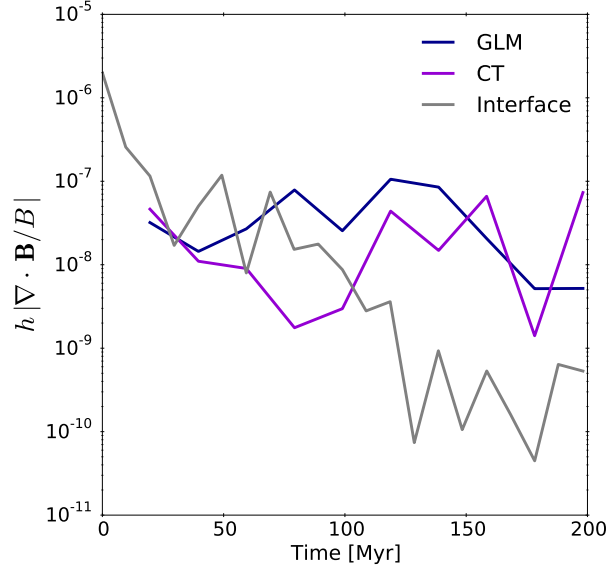
Figure 4.20: Test on the numerical conservation of the $\nabla \cdot \mathbf{B} = 0$ condition (where $h = \Delta x$). We compare two runs only differing in their divergence cleaning method: GLM (*blue*) and CT (*purple*). The gray line shows the corresponding evolution for the interface between regions II and III using the GLM method. We performed this test using the set-up $2L/3$, $\mathcal{M} = 3$ and $\theta_{bn} = 90°$.

Figure 4.21: Numerical test on the shock's directionality. We show a 2D parallel shock propagating with an angle of $60°$.

Figure 4.22: Evolution of Mach number distribution at the shock front for the case $2L/3$, $\mathcal{M} = 3$, $\theta_{bn} = 0°$.

in turn is needed for assigning the initial energy spectra with an spectral index q (see Eq. (4.12)) to each tracer particle. The Mach number at the shock center is computed from the Rankine-Hugoniot pressure jump condition:

$$\Delta \log p \geq \log \frac{p_2}{p_1}\bigg|_{\mathcal{M}=\mathcal{M}_{\min}}, \qquad (4.36)$$

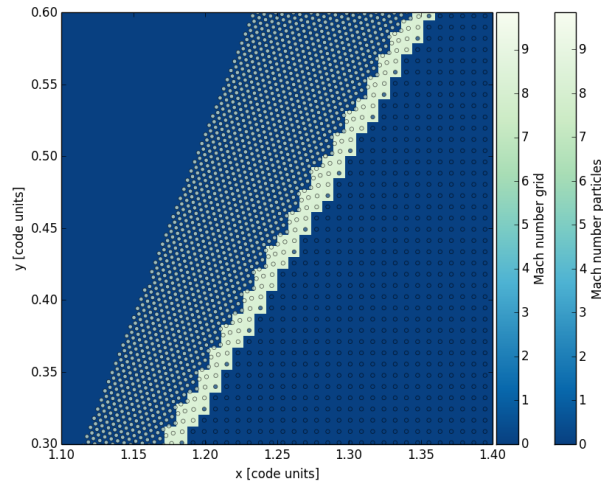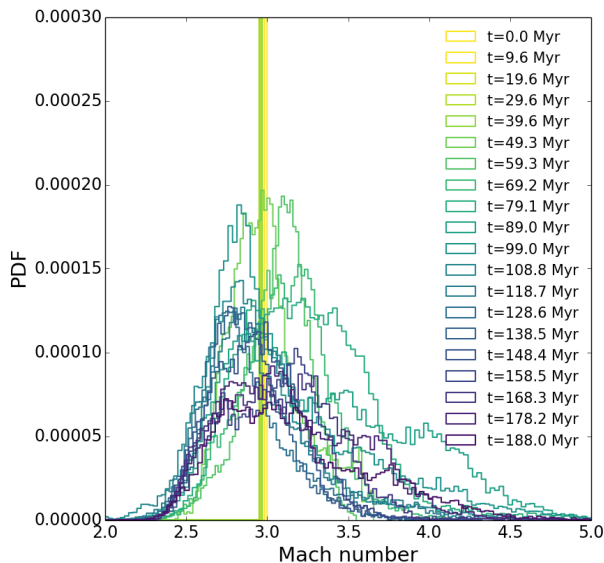where the subscripts 1 and 2 denote the pre-shock and post-shock regions, respectively. The minimum Mach number is set to $\mathcal{M}_{\min} = 1.3$ and it acts as a threshold to filter out weaker shocks. The pressure jump is computed with the neighbouring cells along the three directions for which a Mach number distribution is finally obtained: $\mathcal{M}^2 = \mathcal{M}_x^2 + \mathcal{M}_y^2 + \mathcal{M}_z^2$ (see Ryu et al. 2003a, Vazza et al. 2011b, Schaal & Springel 2015).

The PLUTO code is able to compute the compression ratio for the update of the spectra once the particle has crossed a shock, nevertheless we implemented this extra condition as it was necessary for computing the compression ratio at the time of activation and not a time step afterwards as in Vaidya et al. 2018. In this fashion, the tracer particles have an initial spectrum consistent with DSA theory at the time of activation and after a time step their spectra will evolve subject to radiative losses.

We tested the directionality of the shock finder by setting up a 2D parallel shock
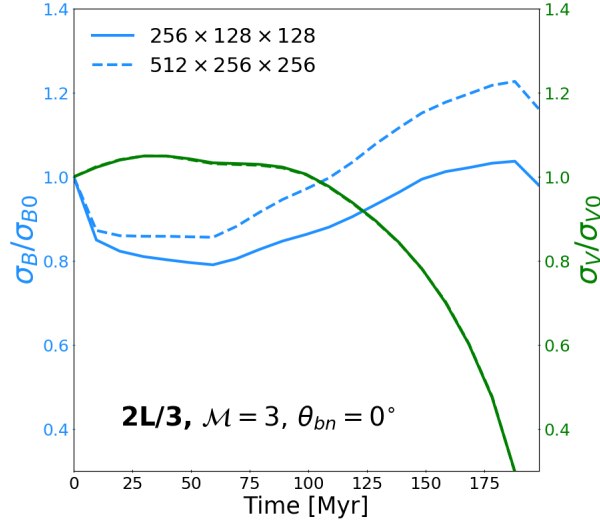
Figure 4.23: Evolution of the standard deviation of the magnetic field (*left green axis*) and velocity field (*right blue axis*). The solid lines correspond to the lower resolution run ($256 \times 128 \times 128$ cells) and the dashed lines correspond to the higher resolution run ($512 \times 256 \times 256$ cells).

propagating with an angle of $60°$ with respect to the x-axis and placing one particle per cell on a quarter of the domain. The shock propagates with a Mach number of $\mathcal{M} = 10$ and the interpolation of the grid quantity at the particle position in PLUTO is done with standard techniques used for Particle-In-Cell (PIC) codes (see Birdsall et al., 2004). We used the Nearest Grid Point (NGP) method for the implementation of this test. In Fig. 4.21, we show the Mach grid distribution as well as the particle's interpolated Mach number for a snapshot of this set-up. We also show the evolution of the shock's Mach number in our final set-up for one of our studied cases in Fig. 4.22.

4.9 Appendix C: Resolution

We tested our set-up doubling the resolution to $512 \times 256 \times 256$ cells and number of Lagrangian particles to 25,165,824. Here we will limit ourselves to show the run $2L/3$, $\mathcal{M} = 3$ and $\theta_{bn} = 90°$. In Fig. 4.23 we show the evolution of the standard deviation of the magnetic and velocity field for the resolution used in this work, i.e. $256 \times 128 \times 128$ cells, and for the higher resolution. This result was shown and explained in detail in Sec. 4.4.1. This figure confirms that the velocity field
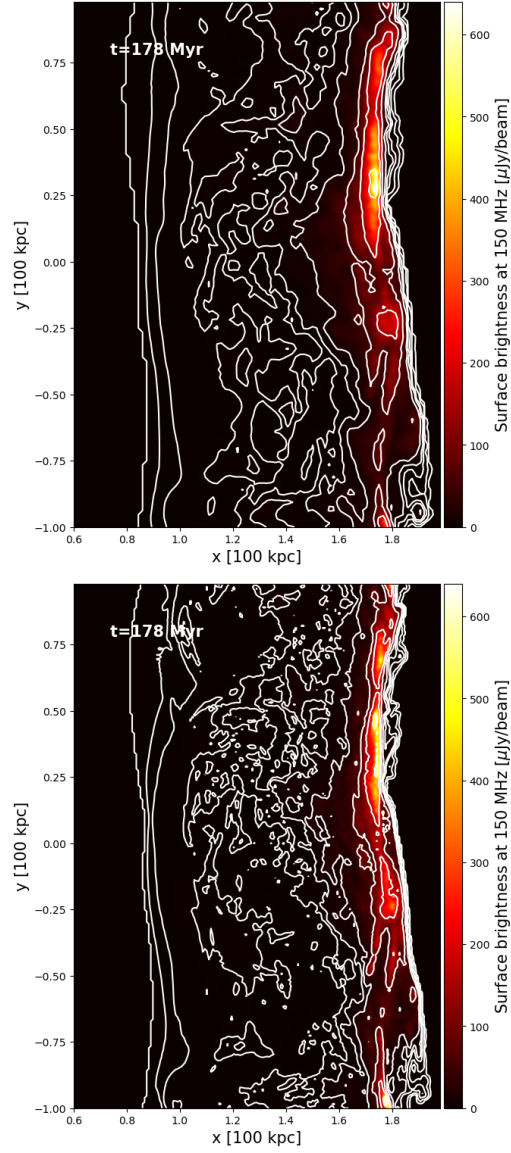
Figure 4.24: Surface brightness at 150 MHz for the run $2L/3$, $\mathcal{M} = 3$ and $\theta_{bn} = 90°$. We considered a beam of $\theta^2 = 15" \times 15"$ to get the surface brightness ($\theta^2 I_\nu$) in units of μJy/beam. No smoothing is considered here. *Left panel*: $256 \times 128 \times 128$ cells simulation. *Right panel*: $512 \times 256 \times 256$ cells simulation.

(and also the density and temperature field) dynamics is largely unaffected by a higher resolution. In fact, it is only the magnetic field fluctuations that are $\sim 20\%$ enhanced. This means that our result on the non-correlation between magnetic and velocity fluctuations is even more accentuated at higher resolution. This is expected as we are increasing the effective Reynolds number of the simulation. An upper limit of the Reynolds number is given by:

$$\mathrm{Re_{max}} \approx \left(\frac{l}{\Delta x}\right)^{4/3}, \tag{4.37}$$

where l is the maximum correlation scale in the flow and Δx is the resolution. In this case, $l = 2L/3 \approx 133.3$ kpc, $\Delta x_{256} = 1.56$ kpc and $\Delta x_{512} = 0.78$ kpc would lead to an upper limit of the effective Reynolds number of ~ 377 and ~ 950 for the low and high resolution runs, respectively. A lower limit is given in contrast by:

$$\mathrm{Re_{min}} \approx \left(\frac{l}{\varepsilon \Delta x}\right)^{4/3}, \tag{4.38}$$

where ε is a factor depending on the diffusivity of the numerical method. For second order finite difference/volume codes such as our case with the PLUTO code, one can assume $\varepsilon \approx 7$ (e.g. Kritsuk et al., 2011). This leads to a lower limit of the effective Reynolds number of ~ 28 and ~ 71 for the low and high resolution runs, respectively. Finally, we show in Fig. 4.24 a comparison between surface brightness maps at 150 MHz with both resolutions. As it can be observed, the broader features as well as the extent of the downstream are consistent in both resolutions, while the higher resolution run highlights smaller features (~ 1 kpc).

4.10 Appendix D: Surface brightness along the x-axis

We present the surface brightness maps at 150 MHz for all our runs as viewed from the x-axis in Fig. 4.25. We want to point out that these maps were obtained by projecting the emissivity already used for this work along the z-axis. In order to compute self-consistently the surface brightness maps changing the LOS, one has to change the observing angle, θ_{obs}, (see Sec. 4.3.3) and the vector $\hat{\mathbf{n}}_{\mathbf{los}}$. This is turn shall be used for computing the integral and Doppler factor in the emissivity equation (see Sec. 4.3.2). The maximum value of surface brightness in each panel of Fig. 4.25, is lower than its correspondent panel in Fig. 4.10. This is because in this case, we end up summing up the contribution of the emissivity for a smaller region (~ 100 kpc).
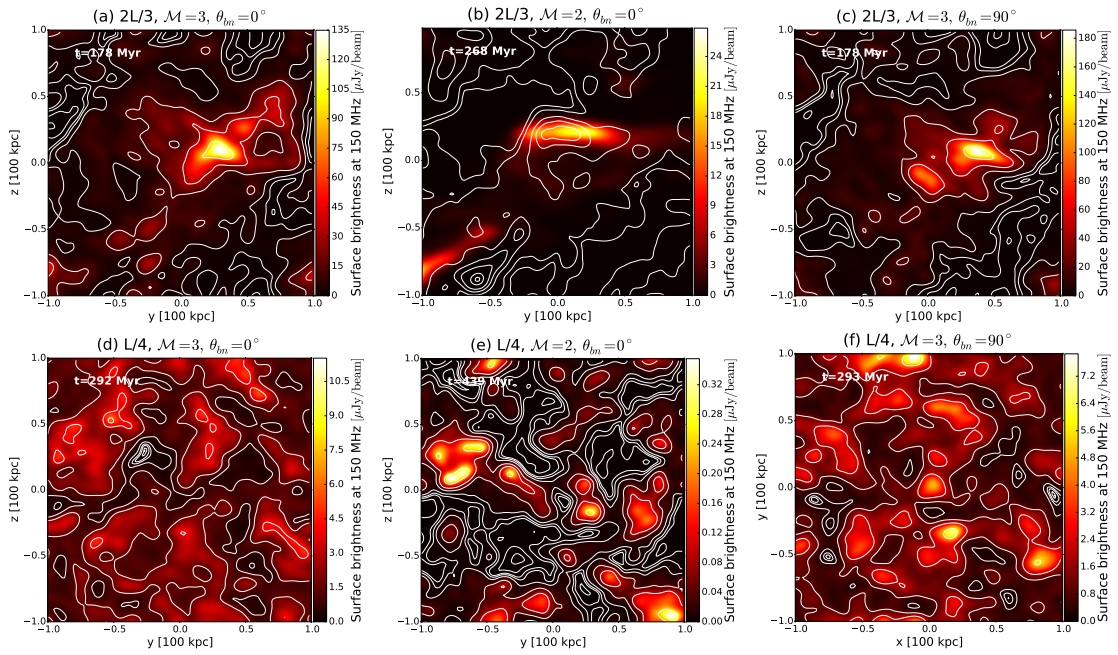
Figure 4.25: Surface brightness at 150 MHz integrated along the x-axis (in correspondence to Fig. 4.10). We considered a beam of $\theta^2 = 15" \times 15"$ to get the surface brightness $(\theta^2 I_\nu)$ in units of μJy/beam. We smoothed the maps with a Gaussian kernel with FWHM = 7.24 kpc (assuming $z = 0.023$).

Chapter 5

Morphology of radio relics II: Polarisation

P. Domínguez-Fernández, M. Brüggen, F. Vazza , W. E. Banda-Barragán, K. Rajpurohit, M. Hoeft, A. Mignone, D. Mukherjee, B. Vaidya

This project is an on-going study of the polarised counterpart of the already published paper described in Chapter 4. The format presented in this Chapter forms part of the draft Domínguez-Fernández et al. in prep. I will discuss here the algorithm for computing the polarisation along with the preliminary results.

5.1 Introduction

Radio observations of galaxy clusters reveal Mpc scale diffuse emission in the intracluster medium (ICM). *Radio relics* are particular objects located at the cluster periphery, with elongated shapes and typically large degrees of polarisation (see Brüggen et al. 2012a and van Weeren et al. 2019 for reviews). Recent high-resolution radio observations have shown that radio relics have substructure and a complex morphology (e.g. Rajpurohit et al., 2018, 2020a; Owen et al., 2014; van Weeren et al., 2017; Di Gennaro et al., 2018).

Radio relics trace shocks generated during merger events of galaxy clusters (see van Weeren et al. 2011a or Bykov et al. 2019 for a review). One plausible mechanism that accelerates synchrotron-emitting cosmic-ray electrons in shocks is the *diffusive shock acceleration* (DSA) (e.g. Blandford & Eichler, 1987; Drury, 1983). Neverthe-

less, only a few radio relics can be explained by the DSA model (e.g. Locatelli et al., 2020) and the for the others, the DSA mechanism results to be much more efficient than what is expected from theory (see van Weeren et al. 2019; Botteon et al. 2020). An alternative model is that a pre-existing population of mildly relativistic cosmic-ray electrons exists (e.g. Kang et al., 2012; Pinzke et al., 2013) before they enter the DSA mechanism.

The observed polarisation fraction in several radio relics is inferred to be $\lesssim 65\%$ (e.g. van Weeren et al., 2010, 2012; Owen et al., 2014; Kierdorf et al., 2017; Loi et al., 2020; Rajpurohit et al., 2020b). Nevertheless, the mechanism producing this large fraction of polarisation is not fully understood. In particular, it is often observed that the electric field vector (E-vector) is aligned with the shock normal, i.e. the magnetic field vector (B-vector) is aligned with the shock front (e.g. van Weeren et al., 2010; Pearce et al., 2017; Golovich et al., 2017). Other observations show a varying alignment along the length of the relics (e.g. Bonafede et al. 2009a; Kale et al. 2012; de Gasperin et al. 2014, 2015, Rajpurohit et al. submitted). Therefore, the alignment could be either produced by a large-scale uniform or a randomly oriented magnetic field (e.g. Laing, 1980). It is also not clear if the typically observed mild shocks of strengths ($\mathcal{M}_{\mathrm{radio}}$[1] $\sim$ 1.7–4.6 would be enough to explain this alignment (e.g. Clarke & Ensslin, 2006; van Weeren et al., 2010, 2012). A compilation of the observed radio relics in polarisation can be found in Table 1 of Wittor et al. (2019).

The high polarisation fraction in radio relics makes them ideal objects for studying magnetic field properties at high radio frequencies. Indeed, the effect of Faraday depolarisation is small at higher frequencies and also at low density regions such as the periphery of galaxy clusters, where radio relics are located. These characteristics make it easier to analyse polarisation properties.

Modelling the observed features of radio relics is challenging from the numerical point of view. On one hand, cosmological simulations lack the resolution to solve the cosmic-ray electron's scales (e.g. Skillman et al. 2013; Hong et al. 2015; Nuza et al. 2017 and more recently Wittor et al. 2019). On the other hand, Particle In Cell (PIC) simulations can only tell us about the dynamics at microphysical scales (e.g. Guo et al., 2014; Caprioli & Spitkovsky, 2014a; Park et al., 2015; Caprioli & Spitkovsky, 2014b; Ryu et al., 2019; Kang et al., 2019). In Domínguez-Fernández et al. (2020) (hereafter paper I) we modelled the synchrotron emission at run-time in a small fraction of the ICM by means of a new hybrid particle and fluid framework using the MHD code PLUTO (Mignone et al., 2007; Vaidya et al., 2018). This method uses *Lagrangian* particles embedded in a large-scale MHD flow, each with

---

[1]$\mathcal{M}_{\mathrm{radio}}$ is the Mach number inferred from radio observations.

its individual energy spectrum. In this new work, we extend our study by including the modelling of polarised emission. Our aim is to study the substructure in the observed polarisation fraction in radio relics (e.g. Rajpurohit et al. submitted). We consider the same set-up as in Paper I: we propagate a shock in a turbulent medium that is representative of a small region of the ICM. We then assume that CR electrons are injected instantly at the shock discontinuity and acquire spectral properties according to DSA theory.

The paper is structured as follows: in Section 5.2, we describe our numerical set-up and initial conditions. In Section 5.3, we include a description of the polarisation emissivity and explain how we obtain the U and Q Stokes parameters maps. Section 5.4 shows our preliminary results and we summarize in Section 5.5.

5.2 Numerical set-up

Our set-up is the same is in Domínguez-Fernández et al. 2020 (hereafter paper I)[2]. Our computational domain is a rectangular box (400 kpc × 200 kpc × 200 kpc with 256 × 128 × 128 cells, respectively), where $x \in$ [-200,200] kpc, $y \in$ [-100,100] kpc, and $z \in$ [-100,100] kpc. The right-hand half of the domain is filled with a turbulent medium, representing a realistic ICM, while the left-hand half contains a uniform medium in which the shock is launched. We define a shock discontinuity at $x = -100$ kpc (see Fig. 4.4 of Paper I for the initial configuration of the magnetic field). This defines three regions in our simulation box: a post-shock uniform region (I), a pre-shock uniform region (II) and a pre-shock turbulent region (III).

The turbulent ICM initial conditions for region (III) were previously produced using the MHD FLASH code version 4.6.1 (Fryxell et al., 2000; Calder et al., 2002). For all specifics regarding these simulations we refer the reader to Paper I. In order to study the polarised emission, we used the code PLUTO (Mignone et al., 2007), which solves the conservation laws for ideal MHD. We assumed an ideal equation of state (EOS), that is $\gamma_0 = 5/3$. The initial boundary conditions of the computational domain are *outflow* in x (zero gradient across the boundary) and *periodic* in y and z. We used a piecewise parabolic method (PPM) for the spatial integration, whereas a 2nd oder TVD Runge-Kutta method for the time stepping with a Courant-Friedichs-Lewy (CFL) condition of 0.3. The Riemann solver for the flux computation that we used is the Harten-Lax-van Leer-Discontinuities (HLLD) solver (see Miyoshi & Kusano, 2005). We control the $\nabla \cdot \mathbf{B} = 0$ condition with the hyperbolic divergence cleaning technique where the induction equation is coupled to a generalized Lagrange multiplier (GLM) (e.g. Dedner et al., 2002).

---

[2]See also Section 4

Turbulent medium	$\mathcal{M}$	$\theta_{bn}[^\circ]$	$\rho_{\mathrm{II}}\,[10^{-27}\mathrm{g/cm}^3]$	$B_{x,\mathrm{II}}\,[\mu G]$
$2L/3$	3.0	0	1.338	0.4
$L/4$	3.0	0	1.338	0.4

Table 5.1: Initial conditions: We denote our regions I, II, III where I is the post-shock region ([-2,-1] in box coordinates), II is the uniform pre-shock region ([-1,0] in box coordinates) and III is the turbulent pre-shock region ([0,2]). The initial conditions for the left side of the shock (region I) depend on the pre-shock conditions (region II) and the initial Mach number of the shock $\mathcal{M}$ through the Rankine-Hugoniot jump conditions. L denotes the length of the turbulent region, i.e. 200 kpc. Note that the magnetic field in region II has only an x-component.

We performed simulations with both turbulent media from paper I, namely the $2L/3$ and $L/4$ cases. These media have its power peaking at $2L/3(L/4)$ of the box, representing an injection scale of 133 kpc(50 kpc). The initial conditions for the density, pressure and velocity in region II (*pre-shock* uniform region at [-100,0] kpc) are set to the mean value of the corresponding turbulent fields. In the case of the magnetic field in region II, we set it to be the mean value of the B_x component of the turbulent medium. The initial conditions for region I (*post-shock* region) are selected according to the MHD Rankine-Hugoniot conditions (e.g. Landau & Lifshitz, 1987). We set-up an initial shock with sonic Mach number $\mathcal{M}$ and study the polarisation as observed from different lines of sight. Finally, we fill the computational domain from the shock discontinuity up to the right side of the box with one *Lagrangian* particle per cell. This gives us a total number of 3,145,728 Lagrangian particles for each run.

All the parameters of the used runs are summarized in Table 5.1. For each of configuration in the Table, we produced polarisation maps at three high frequencies: 1.5 GHz, 3 GHz and 6.5 GHz; and at three different lines of sight defined by the observing angle, θ_{obs}: 0°, 45°, 60° (see Section 5.3). This sums up to a total of 18 different combinations. In addition, we produced maps at 150 MHz for the testing of our modelling as will be described in Sections 5.4.1 and 5.4.2.

We selected these configurations (see Table 5.1) because in Paper I we found that $\mathcal{M} = 2$ shocks in our set-up are unlikely to reproduce observable radio relics. In Paper I, we also found differences in the synchrotron emission computed with the two different turbulent media. In this spirit, we want to study the correspondent differences produced in the polarised emission. We leave the cases with $\theta_{bn} = 90°$ out of this work as the study of the shock's obliquity will be our subject of study in the third edition of these series of papers.

136

5.3 Methods

5.3.1 Polarisation

The linearly polarized emission can be computed in a similar fashion as the synchrotron emission, for which we have (see Ginzburg & Syrovatskii, 1965):

$$\mathcal{J}'_{pol}(\nu'_{obs}, \hat{\mathbf{n}}'_{\mathbf{los}}, \mathbf{B}') = \frac{\sqrt{3}e^3}{4\pi m_e c^2} |\mathbf{B}' \times \hat{\mathbf{n}}'_{\mathbf{los}}| \int N(E')G(\xi)\, dE', \tag{5.1}$$

where $\mathbf{B}'$ is the local magnetic field, $\hat{\mathbf{n}}'_{\mathbf{los}}$ is the unit vector in the direction of the line of sight in the comoving frame, $N(E)$ is defined as in Paper I, i.e. as the tracer particle energy distribution function at the activation time

$$\chi(E) = \frac{N(E)}{n_0} = \frac{N_0}{n_0}\, E^{-p}, \tag{5.2}$$

where $p = q - 2$ is the *injection spectral index*, q is the power–law index of the corresponding particle momentum distribution and related to the shock's Mach number $\mathcal{M}$ via the DSA theory, N_0 is the normalisation factor and n_0 is the fluid number density (see Section 3.1 of Paper I). Finally, $G(\xi) = \xi K_{2/3}(\xi)$, with $K_{2/3}(\xi)$ is a modified Bessel function and

$$\xi = \frac{\nu'_{\mathrm{obs}}}{\nu'_c} = \frac{4\pi m_e^3 c^5 \nu'_{\mathrm{obs}}}{3e E'^2 |\mathbf{B}' \times \hat{\mathbf{n}}'_{\mathbf{los}}|}, \tag{5.3}$$

where ν'_{obs} and ν'_c are the observing and critical frequencies, respectively. The reader should note that here the primed quantities refer to the comoving frame, whereas standard notation refers to the observer's frame. Note also that only those particles with pitch angle coinciding with the angle between $\mathbf{B}'$ and $\hat{\mathbf{n}}'_{\mathbf{los}}$ contribute to the emission along the line of sight in Eqs. (4.17) and (5.1).

The emissivities in Eq. (4.17) and Eq. (5.1) are measured in the local comoving frame with the emitting volume. Nevertheless, if we want the emissivity in a fixed observer's frame then we have to apply a transformation:

$$\mathcal{J}_{pol}(\nu_{obs}, \hat{\mathbf{n}}_{\mathbf{los}}, \mathbf{B}) = \mathcal{D}^2 \mathcal{J}'_{pol}(\nu'_{obs}, \hat{\mathbf{n}}'_{\mathbf{los}}, \mathbf{B}'), \tag{5.4}$$

where $\mathcal{D}$ is a Doppler factor given by Eq. (4.21) in Paper I.

5.3.2 Polarisation maps

In this work, we consider again an observer's reference frame in which z lies along the line of sight $\hat{\mathbf{n}}_{\mathbf{los}}$ and x and y are in the plane of the sky. That is, we choose the
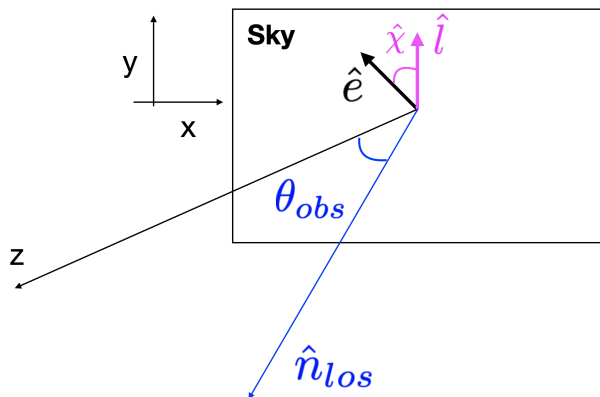
Figure 5.1: Schematic of the plane of the sky. The two polarisations in the plane of the sky are defined with respect the vector $\hat{\mathbf{l}}$.

vector $\hat{\mathbf{n}}_{\mathbf{los}}$ according an observing angle θ_{obs} with respect of the z-axis (see Fig. 5.1). The Stokes parameters Q and U maps can be obtained in the same fashion as the specific intensity (or surface brightness) maps by integrating along a line of sight as

$$Q_\nu = \int \mathcal{J}_{pol}(\nu_{obs}, x, y, z) \cos 2\hat{\chi} \, dz, \qquad (5.5)$$

$$U_\nu = \int \mathcal{J}_{pol}(\nu_{obs}, x, y, z) \sin 2\hat{\chi} \, dz, \qquad (5.6)$$

where $\hat{\chi}$ is the local *polarisation angle*, that is, the angle of the electric field vector in the plane of the sky measured from the z-axis. This can be computed as we have the polarisation emissivity as a grid distribution, this means that we assign the information given by the macro-particles back onto the grid. Eqs. (4.23),(5.5) and (5.6) allow us then to get the degree of (linear) polarization, or also referred as the *polarisation fraction*:

$$\Pi_\nu = \frac{\sqrt{Q_\nu^2 + U_\nu^2}}{I_\nu}. \qquad (5.7)$$

5.3.3 The polarisation angle

The PLUTO code computes the polarisation angle at each Lagrangian particle following the method described in Lyutikov et al. (2003). The unitary electric field vector of a linearly polarized electromagnetic wave in the comoving frame is normal to the unitary local magnetic field vector, $\hat{\mathbf{B}}'$, and to the LOS, $\hat{\mathbf{n}}'_{\mathbf{los}}$, i.e., directed along the unit vector $\hat{\mathbf{e}}' = \hat{\mathbf{n}}'_{\mathbf{los}} \times \hat{\mathbf{B}}'$. In this way, the radiated magnetic field is

therefore $\hat{\mathbf{b}}' = \hat{\mathbf{n}}'_{\mathbf{los}} \times \hat{\mathbf{e}}'$. The electric field in the observer's frame obtained with Lorentz transformations is

$$\mathbf{e} = \gamma \left[\hat{\mathbf{e}}' - \frac{\gamma}{\gamma + 1} (\hat{\mathbf{e}}' \cdot \mathbf{v})\mathbf{v} - \mathbf{v} \times \hat{\mathbf{b}}' \right]. \tag{5.8}$$

On the other hand, the Lorentz transformation of Maxwell's equations in the ideal MHD case $\mathbf{E} + \mathbf{v} \times \mathbf{B} = 0$ allows us to express the comoving frame unit vector $\hat{\mathbf{B}}'$ in terms of the observer's frame unit vector $\hat{\mathbf{B}}$:

$$\hat{\mathbf{B}} = \frac{1}{\sqrt{1 - (\hat{\mathbf{B}}' \cdot \mathbf{v})^2}} \left[\hat{\mathbf{B}}' - \frac{\gamma}{\gamma + 1} (\hat{\mathbf{B}}' \cdot \mathbf{v})\mathbf{v} \right]. \tag{5.9}$$

Using Eqs. (4.22) and (5.9), one arrives to a general expression giving the polarization vector in terms of the observed quantities:

$$\hat{\mathbf{e}} = \frac{\hat{\mathbf{n}}_{\mathbf{los}} \times \mathbf{q}}{\sqrt{q^2 - (\hat{\mathbf{n}}_{\mathbf{los}} \cdot \mathbf{q})^2}}, \tag{5.10}$$

where

$$\mathbf{q} = \hat{\mathbf{B}} + \hat{\mathbf{n}}_{\mathbf{los}} \times (\mathbf{v} \times \hat{\mathbf{B}}). \tag{5.11}$$

One can then introduce a unit vector $\hat{\mathbf{l}}$ normal to the plane containing $\hat{\mathbf{n}}_{\mathbf{los}}$ (in our case it is defined in the y–axis of plane of the sky), one can obtain the components of the $\mathbf{q}$ vector in the plane of the sky:

$$\cos \hat{\chi} = \hat{\mathbf{e}} \cdot (\hat{\mathbf{n}}_{\mathbf{los}} \times \hat{\mathbf{l}}) \tag{5.12}$$

$$\sin \hat{\chi} = \hat{\mathbf{e}} \cdot \hat{\mathbf{l}}. \tag{5.13}$$

Eqs. (5.12) and (5.13) can be then rewritten in terms of $2\hat{\chi}$ using simple trigonometric relations and finally substituting in Eqs. (5.5) and (5.6).

5.4 Preliminary results

5.4.1 Uniform medium

We started testing our polarisation modelling using the first set-up in Table 5.1 in an uniform medium. This means that the initial conditions for the pre-shock region (III) are equal to those in region (II). Such configuration where we have a magnetic field with only an x–component in the plane of the sky introduces simplifications
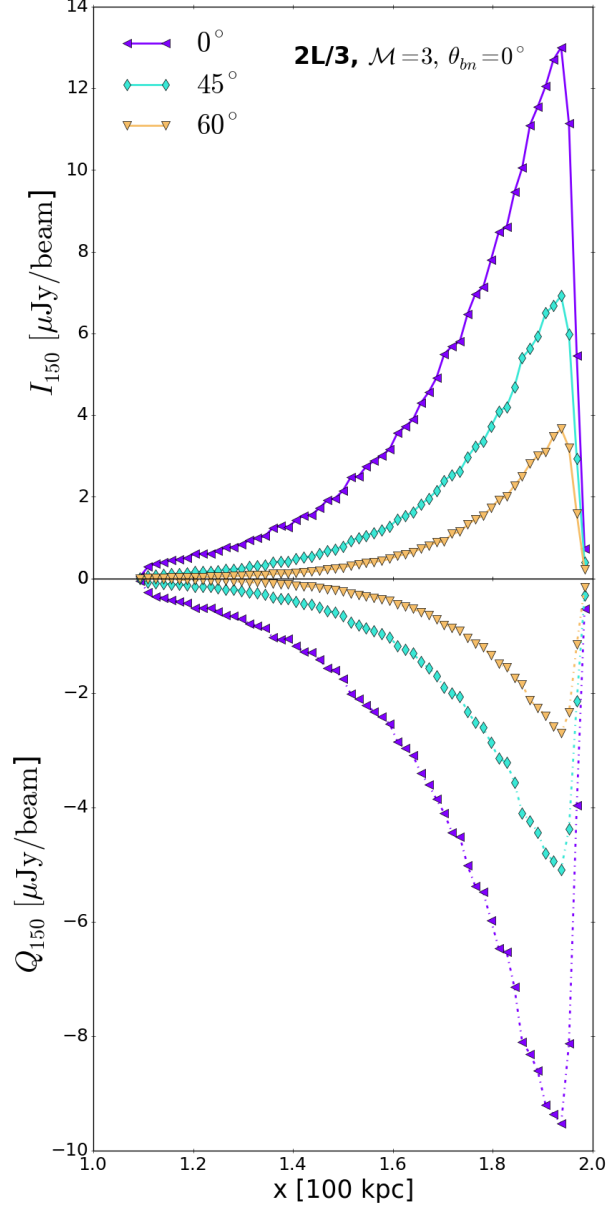
Figure 5.2: *I* Stokes parameter (or surface brightness) at 150 MHz (*top panel*) and *Q* Stokes parameter at 150 MHz(*bottom panel*) integrated along the *z*-axis. We show the observing angles $\theta_{obs} = 0°,45°$ and $60°$ in purple, cyan and yellow colours, respectively. We considered a beam of $\theta^2 = 15" \times 15"$ to get units of μJy/beam but no smoothing is used.
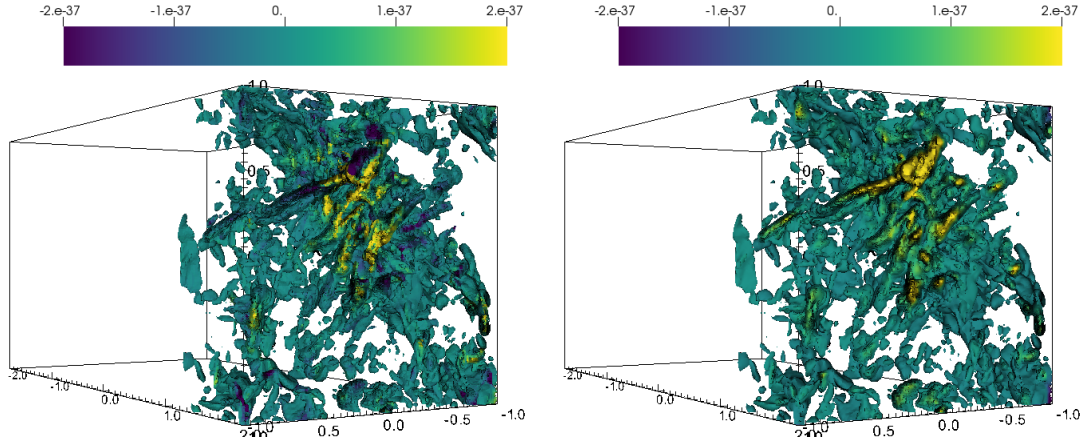
Figure 5.3: Visualization of the polarisation emissivity $\mathcal{J}_{\mathrm{pol}}$ isocurves for the $2L/3$, $\mathcal{M} = 3$ and $\theta_{bn} = 0°$ run at $t = 178$ Myr and at $\theta_{obs} = 60°$. The left panel shows the polarisation correspondent to the Q Stokes parameter (i.e. $\mathcal{J}_{pol} \cos 2\hat{\chi}$), while the right panel shows its correspondent U Stokes parameter (i.e. $\mathcal{J}_{pol} \sin 2\hat{\chi}$) The emissivity is shown in units of [erg cm^{-3} s^{-1} Hz^{-1} str^{-1}]. The axis are shown in units of [100 kpc].

such as $|\mathbf{B}' \times \hat{\mathbf{n}}'_{\mathbf{los}}| \propto \cos(\theta_{obs})$ and $\cos\hat{\chi} = 0$ [3]. This also implies that the U_ν Stokes parameter is zero in Eq. (5.7) and that we can get estimates of the resulting U_ν parameter and polarisation degree Π_ν in terms of the values at $\theta_{obs} = 0°$:

$$Q_\nu(\theta_{obs}) \sim Q_\nu(0°)\cos^2(\theta_{obs}), \tag{5.14}$$

and therefore, $\Pi_\nu(\theta_{obs}) \sim Q_\nu(0°)/I_\nu(0°)$. In Fig.5.2, we show the I_{150} (top panel) and Q_{150} (bottom panel) profiles at an observing frequency of 150 MHz at a time when the shock front has reached almost the right end of the simulation box (corresponding to 178 Myr). We show the observing angles $0°,45°$ and $60°$, respectively. The Q Stokes parameter should be then smaller than $Q(0°$, by a factor of $\sim 1/2$ for the $45°$ observing angle and $\sim 1/4$ for the $60°$ observing angle (see Eq. (5.14)). This is verified and shown in Fig.5.2. Note that Eqs. (5.5) and (5.6) are integrated along the z-axis, while the different LOS are defined through the observing angle between the LOS and the z-axis.

5.4.2 Turbulent medium

We present three-dimensional renderings of the polarisation emission produced by our modelling for the $2L/3$, $\mathcal{M} = 3$ and $\theta_{bn} = 0°$ run in Fig. 5.3, as seen along the line of sight defined by $\theta_{obs} = 60°$ at 150 MHz. The polarisation emission is not spatially uniform coinciding with the synchrotron emissivity studied in Paper I. We see that the combination of the shock compression and turbulence produces fluctuations in the flow that are translated into threads and filaments in the synchrotron and polarisation emissivities.

One of the major unknowns in observed radio relics, is the physical mechanisms of the high degree of alignment of the magnetic field with the shock plane or shock front. We started to investigate this by computing the polarisation fraction with Eq. (5.7). We first considered the same run as the three-dimensional renderings of Fig. 5.3, namely, the $2L/3$, $\mathcal{M} = 3$ and $\theta_{bn} = 0°$ run and compare it with the corresponding uniform medium run (see Section 5.4.1). In the lower panels of Fig. 5.4, we show the polarisation fraction computed considering $\theta_{obs} = 0°$ (i.e. when the LOS is aligned to the z–axis) and a frequency of 150 MHz. We overplot the polarisation angle as computed with[4]

$$\psi = \frac{1}{2} \arctan\left(\frac{U_\nu}{Q_\nu}\right). \tag{5.15}$$

We additionally plot the projected magnetic field,

$$B_{proj} = \frac{\int B dz}{\int dz}, \tag{5.16}$$

for the uniform and turbulent medium in the upper panels of Fig. 5.4. We also overplot the magnetic field vectors as a reference. A turbulent medium will naturally produce fluctuations in the polarisation fraction, and also in the polarisation E–vectors and B–vectors. In the uniform medium, we see a polarisation fraction gradient steepening towards the downstream of the shock, spanning from ~ 0.7 to ~ 0.8. This is expected as the freshly activated particles at the shock front age the further they are from the downstream which causes a steepening in their energy spectrum. The polarisation fraction for an injection power-law E^{-p} is: (e.g. Engel, 1979; Rybicki & Lightman, 1979)

$$\Pi = \frac{p+1}{p+7/3}. \tag{5.17}$$

---

[3]Note that here the xy plane is the plane of the sky.

[4]The computation of $\arctan(\theta)$ needs to consider the four quadrants, i.e. $\theta \in [-\pi, \pi]$

In our uniform run, we have $p = 2.5$ (corresponding to $\mathcal{M} = 3$) corresponding to $\Pi = 0.724$ (see shock front value at left–lower panel in Fig. 5.4). After the activation the energy power-law index, p, increases due to synchrotron and IC losses. One can easily check that if p increases, Π increases as well, as shown in Eq. (5.17). In this case, the polarisation E-vector is aligned with the shock's surface (or B–vector is aligned with the shock's normal vector) in agreement with the corresponding upper panel in Fig. 5.4. The situation gets different when one considers a turbulent medium. We do not observe a clean gradient towards the downstream in the polarisation fraction, instead the low polarisation fraction underlines the turbulent substructure. The shock's front exhibits regions of high polarisation fraction of the order of $\sim 70\%$. Note that at the very end of the downstream, i.e. ~ 100 kpc away from the shock front, the polarisation fraction is higher because this denotes the region where the magnetic field is uniform (region II in the initial set-up) as can be seen in the corresponding upper panel. The more uniform the magnetic field is, the higher the polarisation fraction is. In this case, the polarisation E-vectors are more randomly oriented. Nevertheless, we see that there are large regions of the order of ~ 50 kpc where the alignment is maintained. This is roughly of the same order of the characteristic length of the magnetic field (see Paper I).

5.4.3   High frequencies

Having tested our numerical framework as described in Sections 5.4.1 and 5.4.2, we proceed to do the analysis of the runs in Table 5.1 at higher frequencies. Here we applied Gaussian smoothing for the surface brightness and the Stokes parameters maps. We considered a beam of $\theta^2 = 2" \times 2"$ to get the maps $(\theta^2 I_\nu)$ in units of μJy/beam. We smoothed the maps with a Gaussian kernel with FWHM = 5.5 kpc (assuming $z = 0.22$). These characteristics are chosen to mimic the finite spatial resolution of a typical VLA observation. The selected redshift corresponds to that of the merging galaxy cluster 1RXS J0603.3+4214 which hosts one of the largest and brightest radio relics known to date, namely the "Toothbrush relic".
 In Fig. 5.5, we show the polarisation fraction maps for the two turbulent media at three frequencies. The first thing we can see is that in both media there are regions of the shock front that are highly polarised, i.e. up to $\lesssim 65\%$. Going further towards the downstream region, the polarisation fraction decreases. Note that at the very end of the downstream, i.e. $\sim$80–100 kpc away from the shock front, the polarisation fraction is higher again because the CRes have been already subject to energetic losses for which their spectra is steeper. Note that due to this cooling, the region where the uniform magnetic field (region II in the initial set-up) is interacting with the turbulent medium at this high frequency is not visible (see
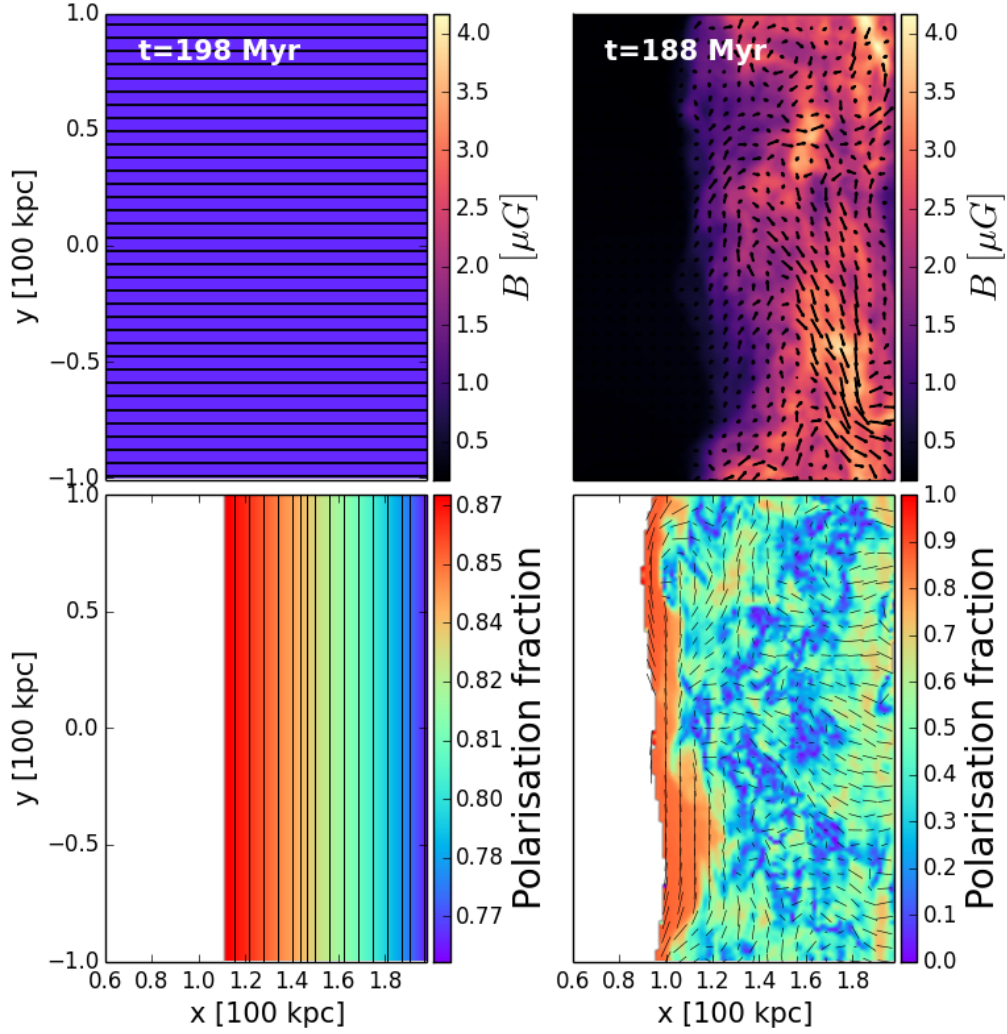
Figure 5.4: Comparison of magnetic field and polarisation fraction for a uniform (left column) and a turbulent (right column) medium. *Upper panels*: Projected magnetic field with magnetic field vectors. *Lower panels*: Colormap of the polarisation fraction computed with Eq. (5.7). We overplot the polarisation E–vector computed with Eq. (5.15).
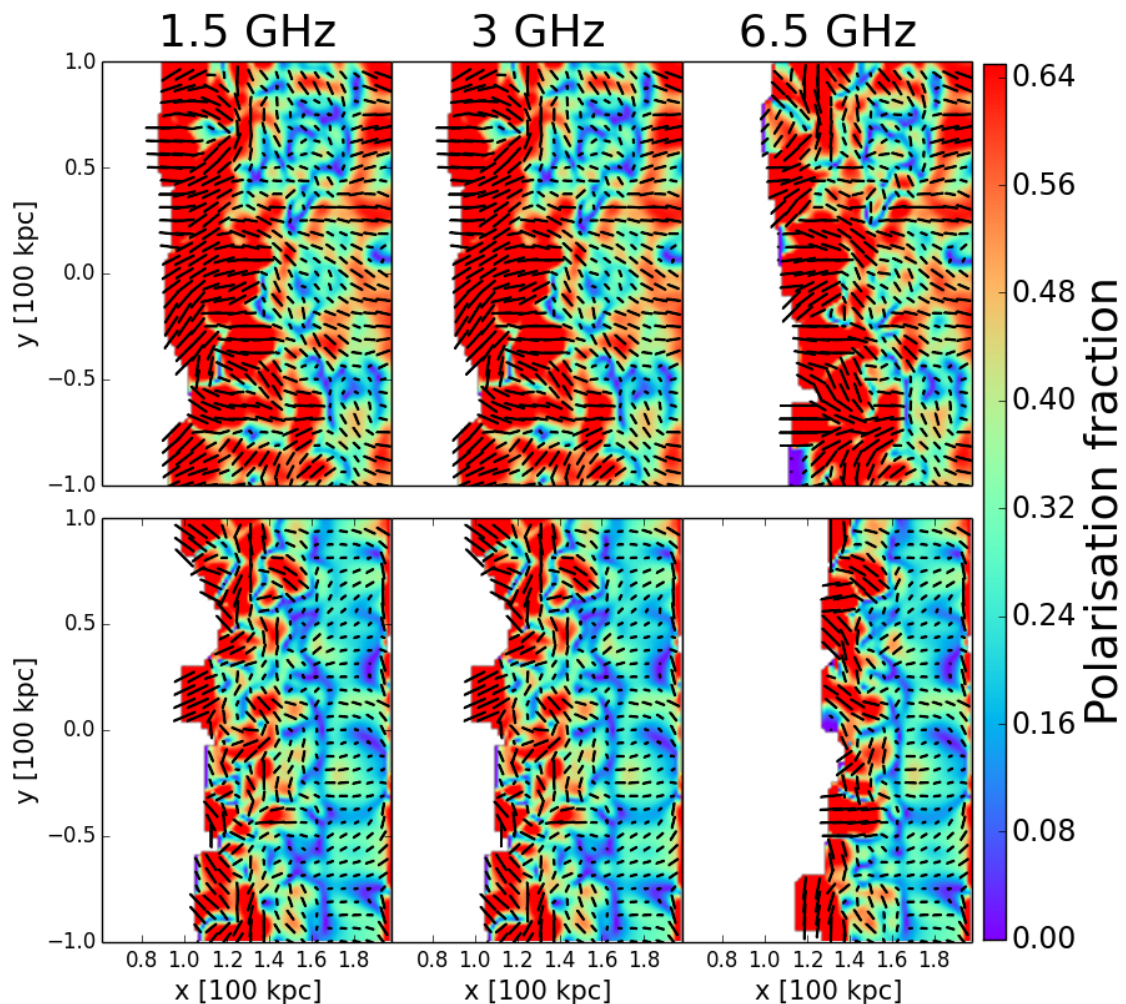
Figure 5.5: Polarisation fraction maps of the $2L/3$ (*upper panels*) and $L/4$ (*lower panels*) runs with $\mathcal{M} = 3$ and $\theta_{bn} = 0°$. The observing angle is $0°$ and each column from left to right corresponds to an observing frequency of 1.5, 3 and 6.5 GHz, respectively. The selected snapshots correspond to $t = 178$ Myr and $t = 277$ Myr for the $2L/3$ and $L/4$ cases, respectively. We overplot the polarisation E–vectors computed with Eq. (5.15)
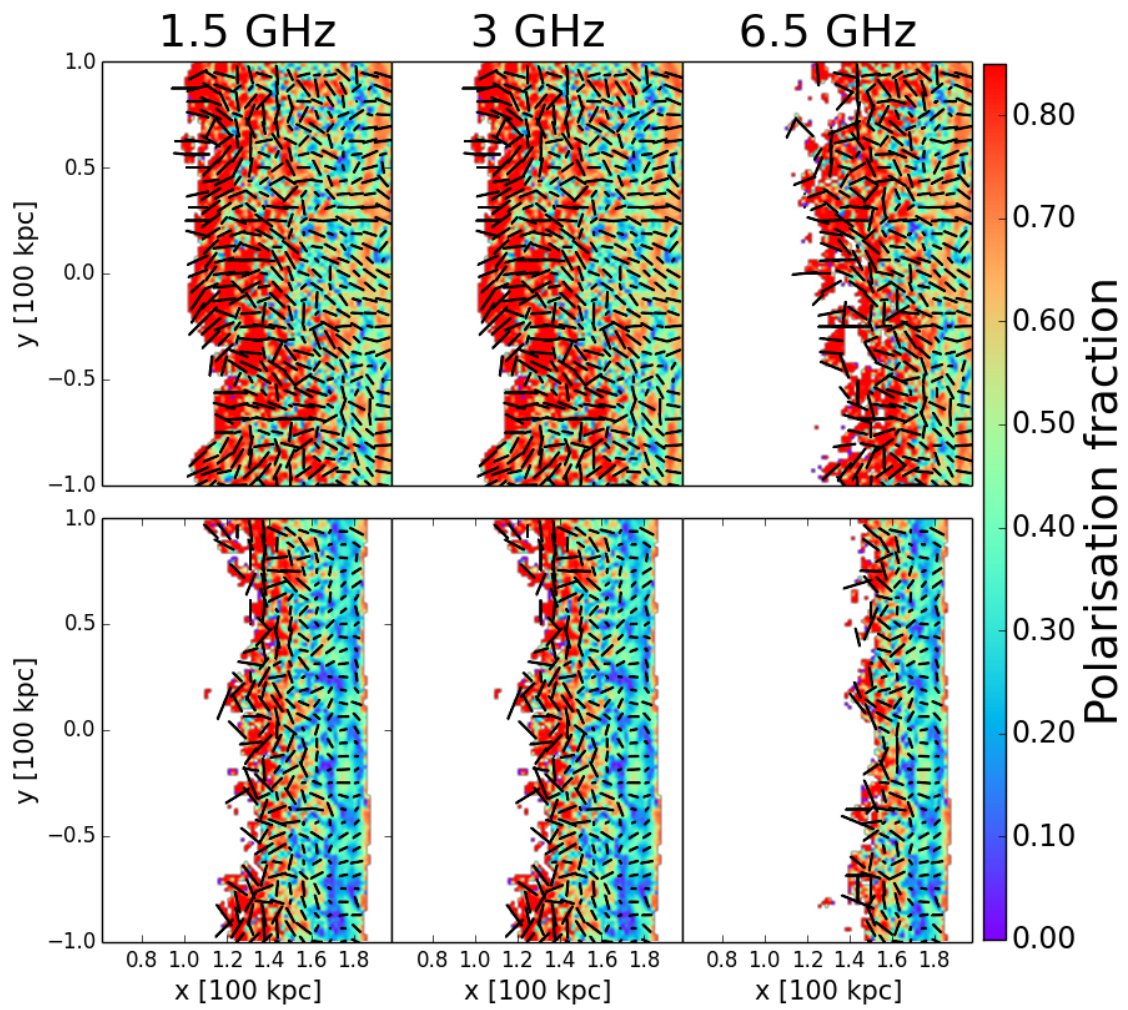
Figure 5.6: Same description as Fig. 5.6 but where no convolution mimicking a beam was applied.

also Section 5.4.2). A similar trend with high polarisation at the shock front has been observed in particular in two radio relics, namely the Toothbrush relic (e.g. Rajpurohit et al., 2020b) and the MACSJ0717.5+3745 relic (e.g. Rajpurohit et al. submitted). Secondly, we do not observe that the polarisation fraction depends on the observing frequency in the region from the shock front down to ∼60 kpc away from the shock front. Nevertheless, at the very end of the downstream the polarisation fraction at 6.5 GHz is different from that at 1.5 and 3 GHz. Again, this is due to the narrower area of the downstream tracked by the emission maps at 6.5 GHz in combination of the beam smoothing. Thirdly, we observe that a turbulent medium with larger magnetic fluctuations such as our $2L/3$ case, results in a higher alignment of the E–vector with the shock's normal than our $L/4$ medium containing smaller magnetic fluctuations.

This last point results to be dependent of the beam size selected. Beam smoothing can change the orientation of the polarisation E- and B-vectors. This effect is known as *beam depolarisation* and could be stronger when the magnetic fluctuations' scale is small in comparison to the beam size. This is shown in Fig. 5.6, where we plot the same polarisation fraction maps as in Fig. 5.5, but where there is no smoothing considered. In order to better study this, we plot profiles of the polarisation intensity, $P_\nu = \sqrt{Q_\nu^2 + U_\nu^2}$, in Fig. 5.7 considering different beam sizes. We selected the 1.5 GHz frequency and show beam sizes of 2"×2", 5"×5" and 12.5"×12.5". The $2L/3$ case exhibits maximum values of the polarisation intensity of ∼ 0.12 mJy/beam, while for the $L/4$ case the maximum value is ∼ 0.06 mJy/beam. When smoothing the images these values correspond to the ∼15–40% of the non-smoothed values. When no smoothing is taken into account, both turbulent media along with the strength of the shock, i.e. $\mathcal{M} = 3$, show polarisation intensities of the order expected by observations of radio relics. Yet, when taking into account the different beam sizes, the polarisation values of the $L/4$ turbulent medium are lower with respect of those of the $2L/3$ turbulent medium. For example, the MACSJ0717.5+3745 relic (see van Weeren et al., 2017; Bonafede et al., 2018) with a Mach number of $\mathcal{M} = 2.7$ (inferred from the injection spectral index α_{int}), exhibits polarisation intensity values in the VLA L-band at 1–2 GHz of 0.01–0.06 mJy/beam with a resolution of 5" (e.g. Rajpurohit et al. submitted). Comparing our results to this particular work, where the authors also observe that the polarisation fraction increases with increasing the resolution, would suggest that the best candidate from our models to represent this relic is the $2L/3$ turbulent medium.

Finally, the beam depolarisation effect on the polarisation angle as obtained from the polarisation maps, i.e. using Eq. (5.15), can be observed in Fig.5.8. We show the PDF of the polarisation angle considering the cells in which the polarisation intensity is greater than zero. On the right panel of Fig.5.8, we show the $2L/3$ type
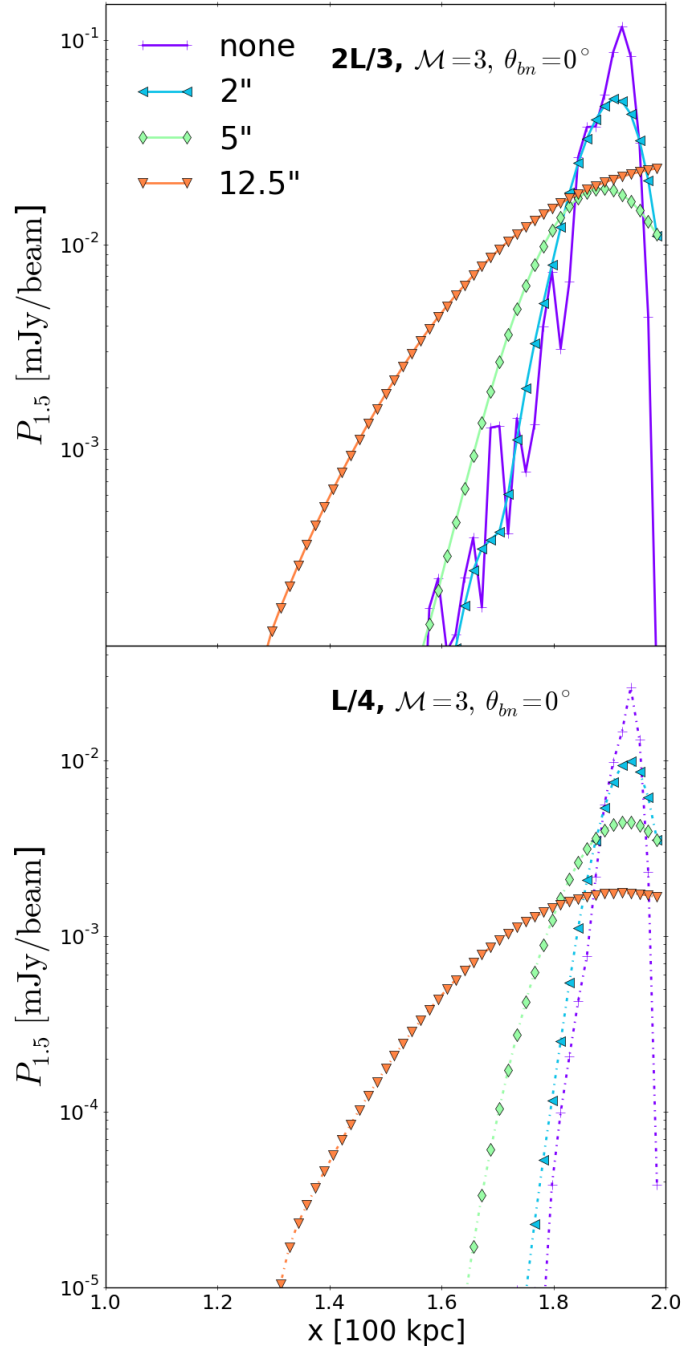
Figure 5.7: 1D polarisation intensity profiles obtained from the $P_\nu = \sqrt{Q_\nu^2 + U_\nu^2}$ maps at 1.5 GHz for the $2L/3$ case (*upper panel*) and $L/4$ case (*lower panel*). The observing angle is 0°.
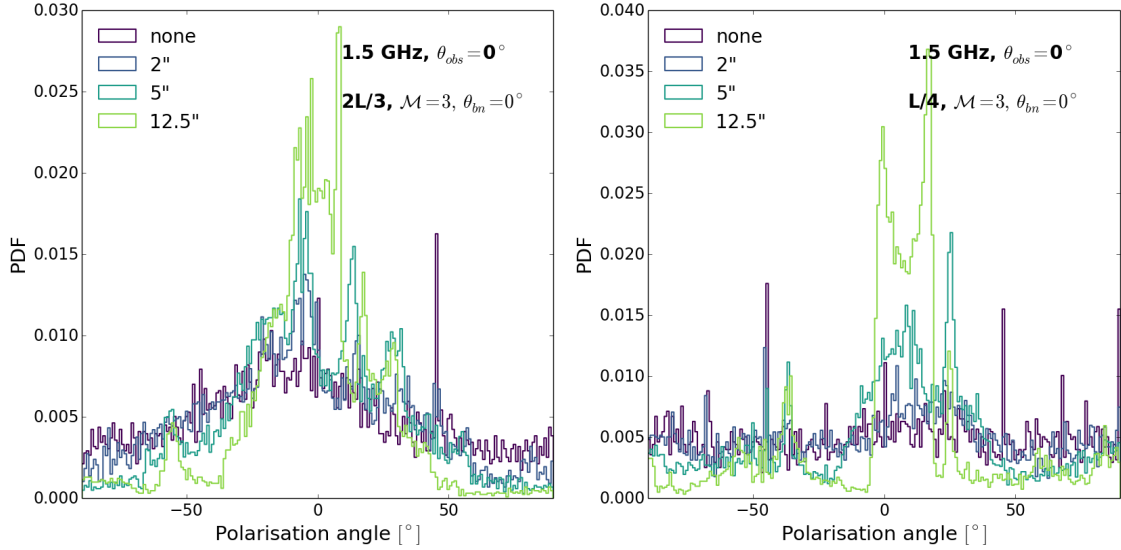
Figure 5.8: PDF distribution of the polarisation angle as computed from Eq. (5.15) for the $2L/3$ case (*left panel*) and $L/4$ case (*right panel*) for different beam sizes.

of turbulence, while on the left panel we show the $L/4$ case. Confirming what we mentioned above, the $2L/3$ case shows a stronger alignment. This can be seen in the shape of PDF, whereas the PDF of the $L/4$ case is flatter than the PDF for the $2L/3$ case, confirming the more random degree of orientation of polarisation vectors. Note that here we are considering the whole downstream region of the emission, and that thus we are not restricting ourselves to the shock front. We notice that a resolution of 2" keeps the shape of the PDF roughly unchanged and thereafter a lower resolution changes more the orientation of the polarisation angle. In particular, the 12.5" resolution tends to align more the E–vectors at smaller angles (defined with respect of our x–axis), i.e $\mid \psi \mid \leq 50°$ for the $2L/3$ case and $\mid \psi \mid \leq 25°$ for the $L/4$ case. This happens because when we apply a larger beam size, the resulting smoothed maps highlight the brightest cells. These brightest cells correspond to those regions at the shock front where the E-vector is mainly aligned with the shock normal, i.e $\psi \sim 0°$.

5.5   Discussion

Radio relics have a high polarization fraction up to 65% (e.g. van Weeren et al., 2010, 2012; Owen et al., 2014; Kierdorf et al., 2017; Loi et al., 2020; Rajpurohit et al., 2020b). The polarisation vector determined by the electric field vector is

often found to be aligned with the shock normal (e.g. van Weeren et al., 2010; Pearce et al., 2017; Golovich et al., 2017). The physical origin behind the high polarisation fraction and alignment remain to be unclear. One explanation relies on the compression of either a uniform large-scale or a randomly oriented magnetic field (e.g. Laing, 1980). However, some radio relics show more complex polarisation patterns that require more understanding. In particular, some relics exhibit a high polarisation fraction at the shock front region contrary to theoretical expectations (e.g. Rajpurohit et al. 2020b,Rajpurohit et al. submitted).

In this work, we have studied the intrinsic polarisation emission from a shock wave propagating through a medium with decaying turbulence representing a small fraction of the ICM. In our hybrid framework, the MHD grid represents a thermal fluid, whereas Lagrangian particles represent CR electrons. We injected CR electrons at the shock discontinuity assuming diffusive shock acceleration. Each CR electron evolves according to a simplified cosmic-ray transport equation.

Our simulations explored a scenario with a shock with $\mathcal{M} = 3$. We varied the downstream turbulence using turbulence-in-a-box simulations as previously considered in the first edition of this series (see Paper I): a solenoidal subsonic turbulence with power peaking at $2/3$ of the box (case $2L/3$) and a solenoidal subsonic turbulence with power peaking at $1/4$ of the box (case $L/4$). One snapshot of each simulation was selected as an initial condition for our shock-tube simulation. Moreover, in this work, we varied the observing angles, beam sizes and analysed also higher frequencies. We have considered typical observing characteristics of observed radio relics in polarisation.

Our preliminary results can be summarized as follows:

i) *Polarisation fraction*: Our polarisation fraction maps show that the polarised emission follows the signatures of an underlying turbulent ICM. In particular, we observe a high polarisation fraction at the shock front which then decreases towards the downstream in line with observations. This result is contrary to a uniform medium where the polarisation fraction only increases towards the downstream.

ii) *Alignment*: We found that a high degree of alignment at the shock front is also reproducible considering a turbulent medium. In particular, a type of turbulence such as the $2L/3$ produces a stronger alignment of the E-vectors with the shock normal compared to our $L/4$ model. Such high degree of alignment, together with variations in the polarisation fraction in the downstream regions, are observed for example in the radio relic located in the MACSJ0717.5+3745 galaxy cluster (e.g. Rajpurohit et al. submitted). In this case, our $2L/3$ model appears to be a good representation of this relic. Other observed relics at high

frequencies such as the Sausage relic, the relic in ZwCl0008+52, and Abell 1612 (see Kierdorf et al., 2017; Govoni et al., 2017) exhibit a much stronger alignment. This in turn could be explained either by a) a uniform magnetic field (see Section 5.4.1), b) beam depolarisation (see following point) or c) Faraday depolarisation (still not included in our analysis) or a combination.

iii) *Beam depolarisation*: Our polarisation intensity profiles show that beam depolarisation results in a $\sim$15–40% decrease with respect of the real values. In addition, we find that beam depolarisation affects on the orientation of the E–vectors mainly at the downstream of the shock. We find that the distribution of polarisation angles gets the most affected at a 12.5" resolution, as expected. In particular, the distribution function of the polarisation angles gets narrowed to $\mid \psi \mid \leq 50°$ for the $2L/3$ case and $\mid \psi \mid \leq 25°$ for the $L/4$ case (where ψ is defined with respect of the x–axis).

In summary, we have so far identified key features of the polarisation emission produced by a turbulent upstream ICM that can be linked to the observable polarisation properties of radio relics. Our work confirms that a turbulent ICM can in principle reproduce the observed polarisation fraction at the shock's surface, in contrast to a uniform ICM. We find that the degree of alignment of the E-vectors with the shock normal also depends on the underlying turbulence. Our work also confirms that a high alignment at the very shock front, as observed in most of the radio relics, is reproducible with a turbulent medium. Nevertheless, there is a vast diversity regarding the alignment of the polarisation vectors in the observed radio relics (e.g. Wittor et al., 2019) which are susceptible to other effects such as Faraday Rotation. Our results do not include still the effect of Faraday Rotation Measures. Faraday depolarisation has been detected for example in the MACSJ0717.5+3745 relic (e.g. Rajpurohit et al. submitted). Therefore, this work will be completed by including this effect in post-processing so we can compare the outcome with the already computed intrinsic polarisation. We will also produce extra runs with an extended turbulent region that encompasses a doubled-sized region III. This will serve us to double-check our results at the end of the shock's downstream.

The data underlying this Chapter will be used as it is here and/or modified and adapted finally for publication in Domínguez-Fernández et al. in prep.

Chapter 6

Conclusions

6.1 Context

Radio observations with higher resolution and sensitivity can unveil the properties of cluster magnetic fields. At the same time, highly resolved images give us a better understanding in the particle acceleration mechanisms in high–β plasmas. Some of the latest radio observations challenge our current theoretical models. It is therefore necessary to add complexity to our existing simulations, which also means coming up with innovative frameworks.

The main focus of the present thesis was to study magnetic fields in the ICM using a variety of numerical simulations. We studied magnetic fields at the center and at the periphery of galaxy clusters. The whole project was planned in two phases, starting from a large-scale (Mpc) perspective and then finishing with a small-scale (kpc) perspective:

Phase 1:

- *Aim*: Studying the amplification of magnetic fields in simulated galaxy clusters produced by cosmological simulations.
- *Assumed scenario*: Primordial magnetogenesis scenario in combination with a small-scale turbulent dynamo.
- *Application*: magnetic power spectra model that can be used for Faraday RM.
- *Uniqueness/novelty*: The use of the first cosmological MHD simulations able to resolve the growth of a small-scale dynamo in galaxy clusters.
- *Publications*: "Dynamical evolution of magnetic fields in the intracluster medium" (Domínguez-Fernández et al. 2019; Chapter 3).

Phase 2:

- *Aim*: Studying the synchrotron and polarisation emission produced by magnetic turbulent media representing the outskirts of the ICM.

- *Assumed scenario*: CRe injected directly at shock discontinuity and accelerated via DSA.

- *Application*: Observed total intensity and polarisation in radio relics.

- *Uniqueness/novelty*: First study combining Eulerian and Lagrangian particles including spatial advection and energy losses at run–time tailored for radio relics.

- *Publications*: "Morphology of radio relics I: What causes the substructure of synchrotron emission?" (Domínguez-Fernández et al. 2020; Chapter 4) and "Morphology of radio relics II: Polarisation" (Domínguez-Fernández et al. in prep; Chapter 5)

One of the additional main purposes of the PhD project was also to create a link between large-scales and those scales that are out of reach for cosmological simulations. It is for this reason that we simulated a small region of the turbulent ICM using turbulence-in-a-box simulations for the publications described in the second phase. Therefore, all the projects within this PhD thesis have the study of turbulent magnetic fields and shock dynamics in the ICM as a common ground.

While the origin of magnetic fields in the ICM is still under debate, we know that turbulence and merger events play an important role in their amplification (e.g. Subramanian, 2016). At the center of galaxy clusters, turbulence is most likely to explain radio halos. In particular, a turbulent small-scale dynamo action is the favorite explanation for the observed μG levels. Nevertheless, there are still things to be understood such as: if there is dynamo amplification, when does it start? for how long can a small-scale dynamo be active taking into account merger and accretion events? how efficient is the magnetic amplification? how come we observe the same levels of radio luminosities at high and low redshifts, i.e. $z \gtrsim 0.6$ and $z \sim 0.2$ (e.g. Di Gennaro et al., 2020)? There have been lots of studies on the growth of the small-scale dynamo in idealised set-ups (e.g. Schekochihin et al., 2004; Porter et al., 2015). Yet, it is important to take into account that galaxy clusters assemble through merger and accretion events that change the evolution of turbulence while the system grows in size. Therefore, one cannot longer consider an idealised set-up. The relevance of studying the small-scale dynamo with cosmological simulations is that it brings us a perspective that is closer to the real dynamics of cluster magnetic fields. Thus, the first project presented in this PhD thesis has its relevance in the

characterisation of the magnetic amplification in galaxy clusters with evidence of a small-scale dynamo in the presence of merger events.

On the other hand, magnetic amplification at the periphery of galaxy clusters due to merger events is most likely to explain radio relics. Nevertheless, there are still puzzling questions: what are the particle acceleration mechanisms behind the observed radio emission? are the outskirts of galaxy clusters turbulent?; if so, which type of turbulence exists in these regions?; what are the efficiencies of CRe and CRp at ICM shocks?; if CRp are accelerated at the same locations as CRe, why does the observed radio emission not match the constraints imposed by the γ–ray emission (e.g. Vazza & Brüggen, 2014; Brunetti & Jones, 2014; Vazza et al., 2015)?; is the DSA mechanism still able to explain some observed features of radio relics?. Radio emission from radio relics has been modelled in previous works on larger scales in post-processing (e.g. Skillman et al. 2013; Hong et al. 2015; Nuza et al. 2017; Wittor et al. 2019). The relevance of the second and third projects presented in this PhD thesis lies in the development of a numerical tool where one does not lose track of the spatial and temporal dynamics of simulated CRe.

6.2   Summary of results

The results in this doctoral thesis can be summarised as follows:

First publication: In Domínguez-Fernández et al. (2019), we have studied magnetic fields at the center of galaxy clusters with cosmological MHD simulations. We have studied the possible scenario in which the origin of magnetic fields in the Universe is primordial scenario (initially 0.1 nG comoving), i.e. magnetic fields have been generated in the early Universe. We studied in detail the magnetic field evolution of a sample of 7 highly resolved simulated galaxy clusters produced with the MHD cosmological ENZO code (see Vazza et al., 2018). Each of these clusters shows clear signatures of magnetic field amplification via a small-scale dynamo. The main results of this work can be summarised as follows:

- A primordial scenario with the aid of a small-scale dynamo action can reproduce cluster magnetic fields of the order of μG.

- Mergers play the main role in the magnetic amplification as they are sources of both compression and turbulence.

- The magnetic power spectral shape is similar across the clusters in our sample, despite their different dynamical states.

- The effect of major mergers in the magnetic power spectra is to shift its power peak towards larger wavenumbers (smaller scales).

- Major mergers introduce new turbulent cascades that can delay the dynamo amplification for a period of 1 Gyr. In contrast, minor mergers promote the steady growth of the small-scale dynamo.

The main outcome of this first part of my PhD project is the characterisation of the magnetic power spectra in several galaxy clusters. This work allowed me to collaborate with members of my own group in Hamburg and Bologna. The first collaboration lead to the publication Locatelli et al. (2018), in which I analysed the magnetic power spectrum of intracluster simulated filaments. The aim of this work was to compare the RM of this intracluster filaments and assessing how probable is their detection. The second collaboration lead to the publication Wittor et al. (2019) where I used the outcome of the magnetic power spectrum in Domínguez-Fernández et al. (2019) in order to find the correlation length of the magnetic field at the position of a radio relic. The aim of this study was to study the polarisation emission in a simulated radio relic. A third collaboration has lead to Stuardi et al. to be submitted, where a direct application of one of our best-fit models has been used in analysing the RM in the cluster Abell 2345. In this work, mock RM maps are compared to RM derived from the RM-synthesis computed from JVLA polarised observations.

Second publication: In Domínguez-Fernández et al. (2020), we have studied the synchrotron emission of CRe accelerated through DSA in a turbulent medium. We aimed to study the recent results of high resolution radio observations revealing that radio relics have a complex substructure (e.g. Owen et al., 2014; Rajpurohit et al., 2020a). We computed the synchrotron emission during run time making use of a state-of-art hybrid framework offered by the code PLUTO where a MHD Eulerian grid is combined with a module of Lagrangian particles that model the non-thermal emission by solving a simplified version of the cosmic ray transport equation. The most important results in this work are:

- Turbulence has an impact on the morphology of synchrotron emission.

- The synchrotron emission is biased towards larger Mach numbers when comparing to the X-ray emission. This is in agreement with observations.

- We found that $\mathcal{M} = 2$ shocks in our set-up not strong enough to modify the initial pre-shock magnetic field. Within our framework, this makes these shocks unlikely to reproduce observable radio relics.

- Shocks propagating in a turbulent ICM affect the magnetic power spectrum. First, the magnetic power shifts towards larger wave numbers (smaller scales) as the shock compresses the medium. Next, turbulence is generated after the shock passage which leads to a shift of the peak spectra towards smaller wave numbers (larger scales). This is in agreement with our previous work (see Domínguez-Fernández et al., 2019).

Third publication: In Domínguez-Fernández et al. in prep, we have studied the intrinsic polarisation emission of CRe accelerated through DSA in a turbulent medium. This work is a follow up of the work in Domínguez-Fernández et al. (2020). While this is an ongoing work, I have already presented in this thesis the main preliminary results:

- The polarised emission follows the signatures of an underlying turbulent ICM.

- We found that a turbulent medium produces a high polarisation fraction at the shock front which then decreases towards the downstream in line with observations. In contrast, we found that in an uniform medium the polarisation fraction only increases towards the downstream, as expected from theory.

- A high degree of alignment of the polarisation E-vectors with the shock's normal at the shock front is reproducible in a turbulent medium.

- Beam depolarisation affects the intrinsic polarisation fraction and alignment of the polarisation vectors.

In summary, simulating the impact of turbulent magnetic fields on radio observables is fundamental for understanding the non-thermal emission in galaxy clusters. Moreover, identifying the processes responsible for the amplification of magnetic fields in galaxy clusters gives us a better hint on their origin in the Universe. The results found in the first phase of this doctoral thesis revealed that primordial magnetic fields may indeed be a viable scenario explaining the origin of magnetic fields. Yet, we still need a decisive observational signature in order to discriminate between magnetogenesis scenarios. On the numerical side, there are still things to address such as: exploring different initial configuration of magnetic fields; implementing the imprint of a magnetic seed in the initial matter perturbations; assessing the growth of the small-scale dynamo with higher resolution. The results found in the second phase of this doctoral thesis confirm and strengthen the idea that the DSA mechanism can in principle reproduce some of the observed features in radio relics. Nevertheless, there are some unanswered aspects such as: the acceleration efficiency necessary to reproduce the low $\mathcal{M} = 2$ shocks and the role of obliquity, as well as particle re-acceleration in weak shocks.

6.3 Future work

Recent and upcoming radio observations are already revealing more substructure of the diffuse emission in galaxy clusters. This opens a new window for studying the morphology of magnetic fields in galaxy clusters. In particular, each new observation will provide us with a unique scenario to test our theoretical models of magnetic fields and acceleration of cosmic rays.

Numerical simulations are our main tool to model observations and more fundamentally, the physics of galaxy clusters. Nevertheless, it is numerically impossible to resolve all relevant scales in these systems, namely from cosmological down to turbulent scales or plasma scales. Therefore, we study them from either the microphysical or the cosmological large-scale point of view. The modelling of cosmic rays acceleration for example, requires a creative solution where we can link all the relevant scales. Hybrid simulations where one combines Eulerian and Lagrangian descriptions provide a good deal for this type of modelling. The results from this thesis open up avenues for further research on cluster's magnetic fields and cosmic rays on both, large scales and also small scales.

On the side of cosmological simulations, I have analysed highly resolved galaxy clusters considering a primordial scenario with a uniform magnetic field seed in combination with a small-scale dynamo action. Primordial magnetic seeds coming from scenarios such as inflation or phase-transitions are nonetheless predicted to have characteristic distributions. Therefore, the study of such magnetic field seeds using the same cosmological MHD simulations as described in Chapter 3 of this thesis is a certain future project for me (i.e. Mtchedlidze et al. in prep).

On the side of hybrid simulations, I have studied the synchrotron emission in radio relics considering the DSA mechanism. Within this framework, I have also studied more observational aspects such as polarisation, as described in Chapter 5. This project has the advantage of working during run time without losing any temporal information of the grid and as such, it opens new possible parameters to explore. In future work, I will study the impact of the shock's obliquity and the dynamical change of the energy limits of the CRe at each time and location. The re-acceleration of pre-existing CR electrons has been suggested as a possible solution for the efficiency argument. Therefore, a logical next step of this hybrid set-up is to implement a re-acceleration model. This project also opens new opportunities for studying different injection models or a more systematic study of synchrotron emission in turbulent media.

Acknowledgements

I would like first to deeply thank my two supervisors Prof. Dr. Franco Vazza and Prof. Dr. Marcus Brüggen. Without their support the completion of this thesis would not have been possible. I can say I have had the fortune to be guided by the perfect combination. Franco, I want to thank you because you have always been there to help me in this long way. Even though you are in Bologna, it felt almost like you were here in Hamburg. Marcus, you have been encouraging me all the way and you have always made sure I kept on track. Spending these last three years in Hamburg have been one of the best experiences of my life and what is more important, you both Franco and Marcus have inspired me to continue to pursue my career as a scientist.

I want to thank my life partner and partner in crime: Malte. Without all your support I would have gone crazy. You are a pillar in my life and I am so grateful I am walking this road by your side and more happy that we will continue to live new adventures together.

I dedicate this thesis to my parents and my brother. I would not have made it all the way here if it was not for you. My heart is and always will be in México. You are with me in every single step of my life.

I want to thank my friends that live in Germany. Liza, my crazy Russian who I have shared so many unique and unrepeatable adventures. Thanks for being there. David, my archi-compa with whom I cannot spend one second without laughing and has been always been there for me. I would like also to thank all of the amazing people that I have met in Hamburg: the first colleagues that I had at the Observatory and then became my good friends: Federica and Amanda; the Italian crew that joined the Observatory afterwards and with whom I have spend many cool weekends: Virginia and Francesco; Toño, for keeping the Mexican in me alive; Alex, for being one of the nicest office-mates ever.

To my friends in México who are practically my family: Sharon, Alicia, Ada, Adrián, Claudia, Tania and I include also here my favorite Spanish person, Fer who is now part of this family. Thanks for always being proud of me and for thinking that I am crazy to study Astrophysics. I am! and I love it!

Bibliography

Abdo A. A. et al., 2009a, ApJ, 699, 31

Abdo A. A. et al., 2009b, ApJ, 707, 55

Ackermann M. et al., 2014, ApJ, 787, 18

Ackermann M. et al., 2016, ApJ, 819, 149

Ackermann M. et al., 2010, ApJL, 717, L71

Aharonian F. et al., 2009, A & A, 495, 27

Ajello M. et al., 2009, ApJ, 690, 367

Akamatsu H. et al., 2015, A & A, 582, A87

Allen S. W., Evrard A. E., Mantz A. B., 2011, ARAA, 49, 409

Aragón-Calvo M. A., van de Weygaert R., Jones B. J. T., 2010, MNRAS, 408, 2163

Arnaud M., 2009, A & A, 500, 103

Arnaud M., Evrard A. E., 1999, MNRAS, 305, 631

Bagchi J., Durret F., Neto G. B. L., Paul S., 2006, Science, 314, 791

Banda-Barragán W. E., Federrath C., Crocker R. M., Bicknell G. V., 2018, MNRAS, 473, 3454

Banfi S., Vazza F., Wittor D., 2020, MNRAS, 496, 3648

Barnes D. J., On A. Y. L., Wu K., Kawata D., 2018, MNRAS, 476, 2890

Batchelor G. K., 1950, Proceedings of the Royal Society of London Series A, 201, 405

Batchelor G. K., 1951, Mathematical Proceedings of the Cambridge Philosophical Society, 47, 359–374

Beck R., 2001, Science & Space Review, 99, 243

Beck R., Wielebinski R., 2013, Magnetic Fields in Galaxies, Oswalt T. D., Gilmore G., eds., Vol. 5, p. 641

Bell A. R., 1978, MNRAS, 182, 147

Belsole E., Pratt G. W., Sauvageot J. L., Bourdin H., 2004, A & A, 415, 821

Beresnyak A., 2012, Physical Review Letters, 108, 035002

Beresnyak A., Lazarian A., 2006, The Astrophysical Journal, 640, L175

Beresnyak A., Miniati F., 2016, ApJ, 817, 127

Biermann L., 1950, Zeitschrift Naturforschung Teil A, 5, 65

Birdsall C. K. N., Estacio E. T., Plasma Theory, Simulation Group (PTSG), 2004, Computer Physics Communications, 164, 189

Blandford R., Eichler D., 1987, Physical Reports, 154, 1

Blasi P., Colafrancesco S., 1999, Astroparticle Physics, 12, 169

Blasi P., Gabici S., Brunetti G., 2007, International Journal of Modern Physics A, 22, 681

Blumenthal G. R., Gould R. J., 1970, Reviews of Modern Physics, 42, 237

Boehringer H., Werner N., 2009, arXiv e-prints, arXiv:0907.4277

Böhringer H., Werner N., 2010, The Astronomy and Astrophysics Review, 18, 127

Bonafede A. et al., 2018, MNRAS, 478, 2927

Bonafede A., Dolag K., Stasyszyn F., Murante G., Borgani S., 2011, ArXiv e-prints

Bonafede A. et al., 2009a, A & A, 503, 707

Bonafede A., Feretti L., Murgia M., Govoni F., Giovannini G., Dallacasa D., Dolag K., Taylor G. B., 2010, A & A, 513, A30+

Bonafede A., Giovannini G., Feretti L., Govoni F., Murgia M., 2009b, A & A, 494, 429

Bonafede A., Vazza F., Brüggen M., Murgia M., Govoni F., Feretti L., Giovannini G., Ogrean G., 2013, MNRAS, 433, 3208

Bond J. R., Cole S., Efstathiou G., Kaiser N., 1991, ApJ, 379, 440

Bond J. R., Kofman L., Pogosyan D., 1996, Nature, 380, 603

Borgani S., Fabjan D., Tornatore L., Schindler S., Dolag K., Diaferio A., 2008, Science & Space Review, 134, 379

Böttcher M., Dermer C. D., 2010, ApJ, 711, 445

Botteon A., Brunetti G., Ryu D., Roh S., 2020, A & A, 634, A64

Botteon A., Gastaldello F., Brunetti G., Dallacasa D., 2016a, MNRAS, 460, L84

Botteon A., Gastaldello F., Brunetti G., Kale R., 2016b, MNRAS, 463, 1534

Bower R. G., 1991, MNRAS, 248, 332

Braginskii S. I., 1965, Reviews of Plasma Physics, 1, 205

Brandenburg A., 2011, ApJ, 741, 92

Brandenburg A., Sokoloff D., Subramanian K., 2012, Science & Space Review, 169, 123

Brighenti F., Mathews W. G., 2003, ApJ, 587, 580

Brown S., Duesterhoeft J., Rudnick L., 2011, ApJL, 727, L25

Brüggen M., 2003, ApJ, 592, 839

Brüggen M., Bykov A., Ryu D., Röttgering H., 2012a, Science & Space Review, 166, 187

Brüggen M., Kaiser C. R., 2002, Nature, 418, 301

Brüggen M., Ruszkowski M., Hallman E., 2005a, ApJ, 630, 740

Brüggen M., Ruszkowski M., Simionescu A., Hoeft M., Dalla Vecchia C., 2005b, ApJ, 631, L21

Brüggen M., van Weeren R. J., Röttgering H. J. A., 2012b, MNRAS, 425, L76

Brunetti G., 2008, Non-thermal emission from galaxy clusters and future observations with the fermi gamma-ray telescope and lofar

Brunetti G., Blasi P., Reimer O., Rudnick L., Bonafede A., Brown S., 2012, MNRAS, 426, 956

Brunetti G., Cassano R., Dolag K., Setti G., 2009, A & A, 507, 661

Brunetti G. et al., 2008, Nature, 455, 944

Brunetti G., Jones T. W., 2014, International Journal of Modern Physics D, 23, 1430007

Brunetti G., Lazarian A., 2007, Monthly Notices of the Royal Astronomical Society, 378, 245

Brunetti G., Lazarian A., 2011a, MNRAS, 410, 127

Brunetti G., Lazarian A., 2011b, MNRAS, 412, 817

Brunetti G., Setti G., Feretti L., Giovannini G., 2001, MNRAS, 320, 365

Brunetti G., Zimmer S., Zandanel F., 2017, MNRAS, 472, 1506

Bryan G. L. e. a., Enzo Collaboration, 2014, The Astrophysical Journal Supplement, 211, 19

Bykov A. M., Dolag K., Durret F., 2008, Science & Space Review, 134, 119

Bykov A. M., Kaastra J. S., Brüggen M., Markevitch M., Falanga M., Paerels F. B. S., 2019, Science & Space Review, 215, 27

Calder A. C. et al., 2002, ApJS, 143, 201

Caprioli D., Pop A.-R., Spitkovsky A., 2015, ApJL, 798, L28

Caprioli D., Spitkovsky A., 2014a, ApJ, 783, 91

Caprioli D., Spitkovsky A., 2014b, ApJ, 794, 46

Carilli C. L., Taylor G. B., 2002, ARAA, 40, 319

Cassano R., Brunetti G., 2005, MNRAS, 357, 1313

Cassano R., Brunetti G., Norris R. P., Röttgering H. J. A., Johnston-Hollitt M., Trasatti M., 2012, A & A, 548, A100

Cassano R., Brunetti G., Setti G., 2006, MNRAS, 369, 1577

Cautun M., van de Weygaert R., Jones B. J. T., Frenk C. S., 2014, MNRAS, 441, 2923

Cavaliere A., Fusco-Femiano R., 1978, A & A, 70, 677

Cavaliere A. G., Gursky H., Tucker W. H., 1971, Nature, 231, 437

Childs H. et al., 2012, in High Performance Visualization–Enabling Extreme-Scale Scientific Insight, pp. 357–372

Cho J., 2014, ApJ, 797, 133

Cho J., Vishniac E. T., Beresnyak A., Lazarian A., Ryu D., 2009, ApJ, 693, 1449

Churazov E., Forman W., Vikhlinin A., Tremaine S., Gerhard O., Jones C., 2008, MNRAS, 388, 1062

Churazov E. et al., 2012, MNRAS, 421, 1123

Clarke T. E., Ensslin T. A., 2006, ApJ, 131, 2900

Clarke T. E., Kronberg P. P., Böhringer H., 2001, ApJL, 547, L111

Clarke T. E., Sarazin C. L., Blanton E. L., Neumann D. M., Kassim N. E., 2005, ApJ, 625, 748

Clowe D., Bradač M., Gonzalez A. H., Markevitch M., Randall S. W., Jones C., Zaritsky D., 2006a, ApJL, 648, L109

Clowe D., Gonzalez A., Markevitch M., 2004, ApJ, 604, 596

Clowe D. et al., 2006b, A & A, 451, 395

Codis S., Pogosyan D., Pichon C., 2018, MNRAS, 479, 973

Colafrancesco S., Marchegiani P., 2008, A & A, 484, 51

Colless M. et al., 2001, MNRAS, 328, 1039

Colombi S., Pogosyan D., Souradeep T., 2000, Physical Review Letters, 85, 5515

163

Crawford C. S., Allen S. W., Ebeling H., Edge A. C., Fabian A. C., 1999, MNRAS, 306, 857

Croston J. H., Arnaud M., Pointecouteau E., Pratt G. W., 2006, A & A, 459, 1007

Cuciti V., Brunetti G., van Weeren R., Bonafede A., Dallacasa D., Cassano R., Venturi T., Kale R., 2018, A & A, 609, A61

Cuciti V., Cassano R., Brunetti G., Dallacasa D., Kale R., Ettori S., Venturi T., 2015, A & A, 580, A97

Dallacasa D. et al., 2009, ApJ, 699, 1288

Darragh Ford E. et al., 2019, MNRAS, 489, 5695

Dawson K. S. et al., 2013, ApJ, 145, 10

de Gasperin F. et al., 2020, arXiv e-prints, arXiv:2007.16043

de Gasperin F., Intema H. T., van Weeren R. J., Dawson W. A., Golovich N., Wittman D., Bonafede A., Brüggen M., 2015, MNRAS, 453, 3483

de Gasperin F., van Weeren R. J., Brüggen M., Vazza F., Bonafede A., Intema H. T., 2014, MNRAS, 444, 3130

de Lapparent V., Geller M. J., Huchra J. P., 1986, ApJL, 302, L1

de Plaa J., Zhuravleva I., Werner N., Kaastra J. S., Churazov E., Smith R. K., Raassen A. J. J., Grange Y. G., 2012, A & A, 539, A34

Dedner A., Kemm F., Kröner D., Munz C. D., Schnitzer T., Wesenberg M., 2002, Journal of Computational Physics, 175, 645

Di Gennaro G. et al., 2020, Nature Astronomy

Di Gennaro G. et al., 2018, ApJ, 865, 24

Dobrowolny M., Mangeney A., Veltri P., 1980, A & A, 83, 26

Dolag K., Bartelmann M., Lesch H., 1999, A & A, 348, 351

Dolag K., Bykov A. M., Diaferio A., 2008, Science & Space Review, 134, 311

Dolag K., Vazza F., Brunetti G., Tormen G., 2005, MNRAS, 364, 753

Domainko W., Gitti M., Schindler S., Kapferer W., 2004, A & A, 425, L21

Domínguez-Fernández P., Vazza F., Brüggen M., Brunetti G., 2019, MNRAS, 486, 623

Domínguez-Fernández P., Brüggen M., Vazza F., Banda-Barragán W. E., Rajpurohit K., Mignone A., Mukherjee D., Vaidya B., 2020, MNRAS

Donnert J., Brunetti G., 2014, MNRAS, 443, 3564

Donnert J., Dolag K., Lesch H., Müller E., 2009, MNRAS, 392, 1008

Donnert J., Vazza F., Brüggen M., ZuHone J., 2018, ArXiv e-prints

Doria A., Gitti M., Ettori S., Brighenti F., Nulsen P. E. J., McNamara B. R., 2012, ApJ, 753, 47

Drury L. O., 1983, Reports on Progress in Physics, 46, 973

Durrer R., Neronov A., 2013, The Astronomy and Astrophysics Review, 21, 62

Eckert D., Jauzac M., Vazza F., Owers M., Kneib J.-P., Tchernin C., Intema H., Knowles K., 2016, Mon. Not. Roy. Astron. Soc., 461, 1302

Edge A. C., Stewart G. C., 1991, MNRAS, 252, 414

Egan H., O'Shea B. W., Hallman E., Burns J., Xu H., Collins D., Li H., Norman M. L., 2016, arXiv e-prints, arXiv:1601.05083

Engel A. R., 1979, Physics Bulletin, 30, 158

Enßlin T., Pfrommer C., Miniati F., Subramanian K., 2011, A & A, 527, A99

Ensslin T. A., Biermann P. L., Klein U., Kohle S., 1998, ArXiv Astrophysics e-prints

Ensslin T. A., Biermann P. L., Kronberg P. P., Wu X.-P., 1997, ApJ, 477, 560

Enßlin T. A., Röttgering H., 2002, A & A, 396, 83

Eswaran V., Pope S. B., 1988, Physics of Fluids, 31, 506

Fabian A. C., 1994, ARAA, 32, 277

Fakhouri O., Ma C.-P., Boylan-Kolchin M., 2010, MNRAS, 406, 2267

Federrath C., Roman-Duval J., Klessen R. S., Schmidt W., Mac Low M. M., 2010, A & A, 512, A81

Feretti L., Fusco-Femiano R., Giovannini G., Govoni F., 2001, A & A, 373, 106

Feretti L., Giovannini G., 1996, in IAU Symposium, Vol. 175, Extragalactic Radio Sources, Ekers R. D., Fanti C., Padrielli L., eds., p. 333

Feretti L., Giovannini G., Govoni F., Murgia M., 2012, The Astronomy and Astrophysics Review, 20, 54

Fermi E., 1954, ApJ, 119, 1

Ferrari C., Govoni F., Schindler S., Bykov A. M., Rephaeli Y., 2008, Space Science Reviews, 134, 93

Finner K. et al., 2020, arXiv e-prints, arXiv:2010.02226

Finoguenov A., Sarazin C. L., Nakazawa K., Wik D. R., Clarke T. E., 2010, ApJ, 715, 1143

Forman W., Kellogg E., Gursky H., Tananbaum H., Giacconi R., 1972, ApJ, 178, 309

Fryxell B. et al., 2000, ApJS, 131, 273

Fujita Y., Matsumoto T., Wada K., 2004, ApJL, 612, L9

Fukazawa Y., Makishima K., Tamura T., Nakazawa K., Ezawa H., Ikebe Y., Kikuchi K., Ohashi T., 2000, MNRAS, 313, 21

Furlanetto S. R., Loeb A., 2001, ApJ, 556, 619

Fusco-Femiano R., Landi R., Orlandini M., 2005, ApJL, 624, L69

Gaspari M., Brighenti F., Ruszkowski M., 2013, Astronomische Nachrichten, 334, 394

Gaspari M., Brighenti F., Temi P., 2012, MNRAS, 424, 190

Gaspari M., Churazov E., 2013, A & A, 559, A78

Gaspari M., Churazov E., Nagai D., Lau E. T., Zhuravleva I., 2014, A & A, 569, A67

Giacintucci S., Markevitch M., Brunetti G., Cassano R., Venturi T., 2011, A & A, 525, L10

Giacintucci S., Markevitch M., Cassano R., Venturi T., Clarke T. E., Brunetti G., 2017, ApJ, 841, 71

Giacintucci S., Markevitch M., Cassano R., Venturi T., Clarke T. E., Kale R., Cuciti V., 2019, The Astrophysical Journal, 880, 70

Giacintucci S., Markevitch M., Venturi T., Clarke T. E., Cassano R., Mazzotta P., 2014, ApJ, 781, 9

Ginzburg V. L., Syrovatskii S. I., 1965, ARAA, 3, 297

Giovannini G., Bonafede A., Feretti L., Govoni F., Murgia M., Ferrari F., Monti G., 2009, A & A, 507, 1257

Giovannini G., Feretti L., 2002, 272, 197

Gitti M., 2015, in Proceedings of "The many facets of extragalactic radio surveys: towards new scientific challenges", p. 43

Gitti M., Feretti L., Schindler S., 2006, A & A, 448, 853

Gnedin N. Y., 2000, ApJ, 542, 535

Golovich N., van Weeren R. J., Dawson W. A., Jee M. J., Wittman D., 2017, ApJ, 838, 110

Govoni F., Enßlin T. A., Feretti L., Giovannini G., 2001, A & A, 369, 441

Govoni F., Feretti L., 2004, International Journal of Modern Physics D, 13, 1549

Govoni F., Feretti L., Giovannini G., Böhringer H., Reiprich T. H., Murgia M., 2001, Astronomy Astrophysics, 376, 803–819

Govoni F. et al., 2017, A & A, 603, A122

Govoni F. et al., 2015, Advancing Astrophysics with the Square Kilometre Array (AASKA14), 105

Govoni F., Murgia M., Xu H., Li H., Norman M. L., Feretti L., Giovannini G., Vacca V., 2013, A & A, 554, A102

Grasso D., Rubinstein H. R., 2001, Physics Reports, 348, 163

Gronenschild E. H. B. M., Mewe R., 1978, A & A, 32, 283

Guo X., Sironi L., Narayan R., 2014, ApJ, 797, 47

Ha J.-H., Ryu D., Kang H., van Marle A. J., 2018, ApJ, 864, 105

Hallman E. J., Burns J. O., Motl P. M., Norman M. L., 2007, Astrophys.J., 665, 911

Heavens A. F., Meisenheimer K., 1987, MNRAS, 225, 335

Heckman T. M., Baum S. A., van Breugel W. J. M., McCarthy P., 1989, ApJ, 338, 48

Heinz S., Brüggen M., Morsony B., 2010, ApJ, 708, 462

Hitomi Collaboration et al., 2018, Publications of the Astronomical Society of Japan, 70, 9

Hoang D. N. et al., 2017, MNRAS, 471, 1107

Hoeft M., Brüggen M., 2007, MNRAS, 375, 77

Hoeft M., Brüggen M., Yepes G., Gottlöber S., Schwope A., 2008, MNRAS, 391, 1511

Hoffer A. S., Donahue M., Hicks A., Barthelemy R. S., 2012, ApJS, 199, 23

Hong S. E., Kang H., Ryu D., 2015, ApJ, 812, 49

Hopkins P. F., Raives M. J., 2016, MNRAS, 455, 51

Huber B., Tchernin C., Eckert D., Farnier C., Manalaysay A., Straumann U., Walter R., 2013, A & A, 560, A64

Huchra J. P., Geller M. J., de Lapparent V., Corwin, Harold G. J., 1990, ApJS, 72, 433

Hudson D. S., Mittal R., Reiprich T. H., Nulsen P. E. J., Andernach H., Sarazin C. L., 2010, A & A, 513, A37

Iapichino L., Niemeyer J. C., 2008, MNRAS, 388, 1089

Iapichino L., Schmidt W., Niemeyer J. C., Merklein J., 2011, MNRAS, 414, 2297

Jaffe W. J., 1977, ApJ, 212, 1

Jaffe W. J., Perola G. C., 1973, A & A, 26, 423

Jenkins A., Frenk C. S., White S. D. M., Colberg J. M., Cole S., Evrard A. E., Couchman H. M. P., Yoshida N., 2001, MNRAS, 321, 372

Johnstone R. M., Fabian A. C., Nulsen P. E. J., 1987, MNRAS, 224, 75

Jones F. C., Ellison D. C., 1991, Science & Space Review, 58, 259

Jones T. W., Porter D. H., Ryu D., Cho J., 2011, Memorie della Societá Astronomica Italiana, 82, 588

Kaastra J. S., Paerels F. B. S., Durret F., Schindler S., Richter P., 2008, Space Science Reviews, 134, 155–190

Kahniashvili T., Maravin Y., Kosowsky A., 2009, , 80, 023009

Kale R., Dwarakanath K. S., Bagchi J., Paul S., 2012, MNRAS, 426, 1204

Kale R. et al., 2015, A & A, 579, A92

Kandus A., Kunze K. E., Tsagas C. G., 2011, Physics reports, 505, 1

Kang H., 2007, in Energy Budget in the High Energy Universe, Sato K., Hisano J., eds., pp. 28–38

Kang H., 2011, Journal of Korean Astronomical Society, 44, 49

Kang H., 2015, Journal of Korean Astronomical Society, 48, 9

Kang H., Jones T. W., Gieseler U. D. J., 2002, ApJ, 579, 337

Kang H., Ryu D., Cen R., Song D., 2005, ApJ, 620, 21

Kang H., Ryu D., Ha J.-H., 2019, ApJ, 876, 79

Kang H., Ryu D., Jones T. W., 2012, ApJ, 756, 97

Kang H., Ryu D., Jones T. W., 2017, ApJ, 840, 42

Kardashev N. S., 1962, , 6, 317

Katz H., Martin-Alvarez S., Devriendt J., Slyz A., Kimm T., 2018, ArXiv e-prints

Kazantzev A. P., 1967, Journal of Experimental and Theoretical Physics, 53, 1806

Kellogg E., Gursky H., Tananbaum H., Giacconi R., Pounds K., 1972, ApJL, 174, L65

Keshet U., Loeb A., 2010, ApJ, 722, 737

Kierdorf M., Beck R., Hoeft M., Klein U., van Weeren R. J., Forman W. R., Jones C., 2017, A & A, 600, A18

Kobayashi T., 2014, Journal of Cosmology and Astroparticle Physics, 2014, 040

Kolmogorov A. N., 1941, Akademiia Nauk SSSR Doklady, 32, 16

Komatsu E. et al., 2011, ApJS, 192, 18

Komissarov S. S., Gubanov A. G., 1994, A & A, 285, 27

Kraichnan R. H., Nagarajan S., 1967, Physics of Fluids, 10, 859

Kravtsov A. V., Borgani S., 2012, ARAA, 50, 353

Kravtsov A. V., Yepes G., 2000, Monthly Notices of the Royal Astronomical Society, 318, 227–238

Kritsuk A. G. et al., 2011, ApJ, 737, 13

Kuchar P., Enßlin T. A., 2011, A & A, 529, A13

Kulsrud R. M., Anderson S. W., 1992, Astrophysical Journal, 396, 606

Lacey C., Cole S., 1993, MNRAS, 262, 627

Laing R. A., 1980, MNRAS, 193, 439

Landau L. D., Lifshitz E. M., 1987, Fluid Mechanics, Second Edition: Volume 6, 2nd edn., Vol. 6. Butterworth-Heinemann

Lau E. T., Kravtsov A. V., Nagai D., 2009, ApJ, 705, 1129

Lazarian A., Beresnyak A., 2006, MNRAS, 373, 1195

Lee D., Deane A. E., Federrath C., 2009, Astronomical Society of the Pacific Conference Series, Vol. 406, A New Multidimensional Unsplit MHD Solver in FLASH3, Pogorelov N. V., Audit E., Colella P., Zank G. P., eds., p. 243

Liang H., Hunstead R. W., Birkinshaw M., Andreani P., 2000, ApJ, 544, 686

Locatelli N., Vazza F., Domínguez-Fernández P., 2018, Galaxies, 6, 128

Locatelli N. T. et al., 2020, MNRAS

Loewenstein M., Mushotzky R. F., 1996, ApJ, 466, 695

Loi F. et al., 2020, MNRAS, 498, 1628

Lyutikov M., Pariev V. I., Blandford R. D., 2003, ApJ, 597, 998

Macario G., Venturi T., Brunetti G., Dallacasa D., Giacintucci S., Cassano R., Bardelli S., Athreya R., 2010, A & A, 517, A43

Mahdavi A., Hoekstra H., Babul A., Henry J. P., 2008, MNRAS, 384, 1567

Malavasi N., Aghanim N., Tanimura H., Bonjean V., Douspis M., 2020, Astronomy Astrophysics, 634, A30

Malavasi N. et al., 2017, MNRAS, 465, 3817

Mantz A. B., Allen S. W., Morris R. G., Simionescu A., Urban O., Werner N., Zhuravleva I., 2017, Monthly Notices of the Royal Astronomical Society, 472, 2877–2888

Marinacci F., Vogelsberger M., Kannan R., Mocz P., Pakmor R., Springel V., 2018a, MNRAS, 476, 2476

Marinacci F., Vogelsberger M., Mocz P., Pakmor R., 2015, MNRAS, 453, 3999

Marinacci F. et al., 2018b, MNRAS, 480, 5113

Markevitch M., 2006, in ESA Special Publication, Vol. 604, The X-ray Universe 2005, Wilson A., ed., p. 723

Markevitch M., Gonzalez A. H., Clowe D., Vikhlinin A., Forman W., Jones C., Murray S., Tucker W., 2004, ApJ, 606, 819

Markevitch M., Gonzalez A. H., David L., Vikhlinin A., Murray S., Forman W., Jones C., Tucker W., 2002, ApJL, 567, L27

Markevitch M., Govoni F., Brunetti G., Jerius D., 2005, ApJ, 627, 733

Markevitch M., Sarazin C. L., Vikhlinin A., 1999, ApJ, 521, 526

171

Markevitch M., Vikhlinin A., 2007, Physical Reports, 443, 1

Matsukiyo S., Ohira Y., Yamazaki R., Umeda T., 2011, ApJ, 742, 47

Matsumoto H., Tsuru T. G., Fukazawa Y., Hattori M., Davis D. S., 2000, Publications of the Astronomical Society of Japan, 52, 153

McDonald M. et al., 2017, ApJ, 843, 28

McDonald M., Veilleux S., Rupke D. S. N., Mushotzky R., 2010, ApJ, 721, 1262

McNamara B. R. et al., 2001, ApJL, 562, L149

Meekins J. F., Fritz G., Chubb T. A., Friedman H., 1971, Nature, 231, 107

Mernier F. et al., 2020a, A & A, 642, A90

Mernier F. et al., 2020b, Astronomische Nachrichten, 341, 203

Mignone A., Bodo G., Massaglia S., Matsakos T., Tesileanu O., Zanni C., Ferrari A., 2007, ApJS, 170, 228

Mimica P., Aloy M. A., 2012, MNRAS, 421, 2635

Miniati F., 2002, MNRAS, 337, 199

Miniati F., 2014, ApJ, 782, 21

Miniati F., Beresnyak A., 2015, Nature, 523, 59

Mittal R., Hudson D. S., Reiprich T. H., Clarke T., 2009, A & A, 501, 835

Miyoshi T., Kusano K., 2005, Journal of Computational Physics, 208, 315

Moffatt H. K., 1978, Magnetic field generation in electrically conducting fluids

Molendi S., Tozzi P., Gaspari M., De Grandi S., Gastaldello F., Ghizzardi S., Rossetti M., 2016, A & A, 595, A123

Moore B., Quinn T., Governato F., Stadel J., Lake G., 1999, MNRAS, 310, 1147

Murgia M., Govoni F., Feretti L., Giovannini G., Dallacasa D., Fanti R., Taylor G. B., Dolag K., 2004, A & A, 424, 429

Narayan R., Medvedev M. V., 2001, ApJL, 562, L129

Navarro J. F., Frenk C. S., White S. D. M., 1997, ApJ, 490, 493

Neronov A., Semikoz D., Vovk I., 2010, A & A, 519, L6

Neronov A., Vovk I., 2010, Science, 328, 73

Nevalainen J., Oosterbroek T., Bonamente M., Colafrancesco S., 2004, ApJ, 608, 166

Nuza S. E., Gelszinnis J., Hoeft M., Yepes G., 2017, MNRAS, 470, 240

Ogrean G. A., Brüggen M., van Weeren R. J., Röttgering H., Croston J. H., Hoeft M., 2013, Monthly Notices of the Royal Astronomical Society, 433, 812–824

Owen F. N., Rudnick L., Eilek J., Rau U., Bhatnagar S., Kogan L., 2014, ApJ, 794, 24

Pacholczyk A. G., 1970, Radio astrophysics. Nonthermal processes in galactic and extragalactic sources

Parekh V. et al., 2020, Monthly Notices of the Royal Astronomical Society, 499, 404–414

Park J., Caprioli D., Spitkovsky A., 2015, Physical Review Letters, 114, 085003

Paul S., Salunkhe S., Sonkamble S., Gupta P., Mroczkowski T., Raychaudhury S., 2020, Astronomy Astrophysics, 633, A59

Pearce C. J. J. et al., 2017, ApJ, 845, 81

Perkins J. S. et al., 2006, ApJ, 644, 148

Petrosian V., 2001, ApJ, 557, 560

Pfrommer C., Springel V., Enßlin T. A., Jubelgas M., 2006, MNRAS, 367, 113

Pinzke A., Oh S. P., Pfrommer C., 2013, MNRAS, 435, 1061

Pizzolato F., Soker N., 2006, MNRAS, 371, 1835

Planck Collaboration et al., 2016, Astronomy and Astrophysics, 594, A19

Planelles S., Schleicher D. R. G., Bykov A. M., 2015, Science & Space Review, 188, 93

Porter D. H., Jones T. W., Ryu D., 2015, ApJ, 810, 93

Pratt G. W., Arnaud M., 2002, A & A, 394, 375

Press W. H., Schechter P., 1974, ApJ, 187, 425

Quilis V., M J., Ibáñez ., Sáez D., 1998, ApJ, 502, 518

Rajpurohit K. et al., 2018, ApJ, 852, 65

Rajpurohit K. et al., 2020a, A & A, 636, A30

Rajpurohit K. et al., 2020b, A & A, 642, L13

Reimer O., Pohl M., Sreekumar P., Mattox J. R., 2003, ApJ, 588, 155

Rephaeli Y., Gruber D., 2002, ApJ, 579, 587

Rephaeli Y., Nevalainen J., Ohashi T., Bykov A. M., 2008, Space Science Reviews, 134, 71

Rieder M., Teyssier R., 2017, ArXiv e-prints

Riquelme M. A., Quataert E., Verscharen D., 2016, ApJ, 824, 123

Roettiger K., Stone J. M., Burns J. O., 1999, ApJ, 518, 594

Rosati P., Borgani S., Norman C., 2002, ARAA, 40, 539

Rybicki G. B., Lightman A. P., 1979, Radiative processes in astrophysics

Ryu D., Kang H., Biermann P. L., 1998, A & A, 335, 19

Ryu D., Kang H., Cho J., Das S., 2008, Science, 320, 909

Ryu D., Kang H., Ha J.-H., 2019, ApJ, 883, 60

Ryu D., Kang H., Hallman E., Jones T. W., 2003a, ApJ, 593, 599

Ryu D., Kang H., Hallman E., Jones T. W., 2003b, ApJ, 593, 599

Sanders J. S., Fabian A. C., 2013, Monthly Notices of the Royal Astronomical Society, 429, 2727–2738

Santos-Lima R., de Gouveia Dal Pino E. M., Falceta-Gonçalves D. A., Nakwacki M. S., Kowal G., 2017, MNRAS, 465, 4866

Santos-Lima R., de Gouveia Dal Pino E. M., Kowal G., Falceta-Gonçalves D., Lazarian A., Nakwacki M. S., 2014, ApJ, 781, 84

Sarazin C. L., 1986, Rev. Mod. Phys., 58, 1

Sarazin C. L., 1988, X-ray emission from clusters of galaxies

Sarazin C. L., 2001, in Clusters of Galaxies and the High Redshift Universe Observed in X-rays, Neumann D. M., Tran J. T. V., eds., p. 61

Sarron F., Martinet N., Durret F., Adami C., 2018, A & A, 613, A67

Schaal K., Springel V., 2015, MNRAS, 446, 3992

Schaye J. et al., 2015, MNRAS, 446, 521

Schekochihin A. A., Boldyrev S. A., Kulsrud R. M., 2002, Astrophysical Journal, 567, 828

Schekochihin A. A., Cowley S. C., 2006, Physics of Plasmas, 13, 056501

Schekochihin A. A., Cowley S. C., 2007, Turbulence and Magnetic Fields in Astrophysical Plasmas, Molokov S., Moreau R., Moffatt H. K., eds., Springer, p. 85

Schekochihin A. A., Cowley S. C., Kulsrud R. M., Hammett G. W., Sharma P., 2005, ApJ, 629, 139

Schekochihin A. A., Cowley S. C., Kulsrud R. M., Rosin M. S., Heinemann T., 2008, Physical Review Letters, 100, 081301

Schekochihin A. A., Cowley S. C., Taylor S. F., Maron J. L., McWilliams J. C., 2004, Astrophysical Journal, 612, 276

Schlüter A., Biermann L., 1950, Zeitschrift Naturforschung Teil A, 5, 237

Schmidt W., Niemeyer J. C., Hillebrandt W., 2006, A & A, 450, 265

Schubert G., Soderlund K. M., 2011, Physics of the Earth and Planetary Interiors, 187, 92

Seshadri T. R., Subramanian K., 2009, Physical Review Letters, 103, 081303

Sheth R. K., Mo H. J., Tormen G., 2001, MNRAS, 323, 1

Sheth R. K., Tormen G., 1999, MNRAS, 308, 119

175

Simionescu A. et al., 2019, MNRAS, 483, 1701

Sironi L., Spitkovsky A., Arons J., 2013, ApJ, 771, 54

Skillman S. W., O'Shea B. W., Hallman E. J., Burns J. O., Norman M. L., 2008, ApJ, 689, 1063

Skillman S. W., Xu H., Hallman E. J., O'Shea B. W., Burns J. O., Li H., Collins D. C., Norman M. L., 2013, ApJ, 765, 21

Spitzer L., 1956, Physics of Fully Ionized Gases

Springel V., Frenk C. S., White S. D. M., 2006, Nature, 440, 1137

Springel V. et al., 2005, Nature, 435, 629

Stasyszyn F. A., Dolag K., Beck A. M., 2013, MNRAS, 428, 13

Stevenson D. J., 2010, Science & Space Review, 152, 651

Strong A. W., Bignami G. F., 1983, ApJ, 274, 549

Subramanian K., 2016, Reports on Progress in Physics, 79, 076901

Subramanian K., Shukurov A., Haugen N. E. L., 2006, MNRAS, 366, 1437

Taylor A. R. et al., 2015, ArXiv e-prints

Taylor G. B., Fabian A. C., Allen S. W., 2002, MNRAS, 334, 769

The Enzo Collaboration et al., 2013, ArXiv e-prints

Tormen G., Bouchet F., White S., 1997, MNRAS, 286, 865

Tricco T. S., Price D. J., Federrath C., 2016, MNRAS, 461, 1260

Trivedi P., Subramanian K., Seshadri T. R., 2014, , 89, 043523

Turner M. S., Widrow L. M., 1988, Phys. Rev. D, 37, 2743

Urdampilleta I., Akamatsu H., Mernier F., Kaastra J. S., de Plaa J., Ohashi T., Ishisaki Y., Kawahara H., 2018, A & A, 618, A74

Vacca V., Murgia M., Govoni F., Feretti L., Giovannini G., Perley R. A., Taylor G. B., 2012, A & A, 540, A38

Vaidya B., Mignone A., Bodo G., Rossi P., Massaglia S., 2018, ApJ, 865, 144

van Weeren R. J., Brüggen M., Röttgering H. J. A., Hoeft M., 2011a, Journal of Astrophysics and Astronomy, 32, 505

van Weeren R. J. et al., 2016, ApJ, 818, 204

van Weeren R. J. et al., 2016, The Astrophysical Journal, 818, 204

van Weeren R. J., de Gasperin F., Akamatsu H., Brüggen M., Feretti L., Kang H., Stroe A., Zandanel F., 2019, Science & Space Review, 215, 16

van Weeren R. J., Hoeft M., Röttgering H. J. A., Brüggen M., Intema H. T., van Velzen S., 2011b, A & A, 528, A38

van Weeren R. J. et al., 2017, ApJ, 835, 197

van Weeren R. J. et al., 2017, The Astrophysical Journal, 835, 197

van Weeren R. J., Röttgering H. J. A., Brüggen M., Cohen A., 2009, A & A, 505, 991

van Weeren R. J., Röttgering H. J. A., Brüggen M., Hoeft M., 2010, Science, 330, 347

van Weeren R. J., Röttgering H. J. A., Intema H. T., Rudnick L., Brüggen M., Hoeft M., Oonk J. B. R., 2012, A & A, 546, A124

Vazza F., Brueggen M., Gheller C., Hackstein S., Wittor D., Hinz P. M., 2017, Classical and Quantum Gravity

Vazza F., Brüggen M., 2014, MNRAS, 437, 2291

Vazza F., Brüggen M., Gheller C., Wang P., 2014, MNRAS, 445, 3706

Vazza F., Brunetti G., Brüggen M., Bonafede A., 2018, MNRAS, 474, 1672

Vazza F., Brunetti G., Gheller C., Brunino R., 2010, New Astronomy, 15, 695

Vazza F., Brunetti G., Gheller C., Brunino R., Brüggen M., 2011a, A & A, 529, A17

Vazza F., Brunetti G., Kritsuk A., Wagner R., Gheller C., Norman M., 2009, A & A, 504, 33

Vazza F., Dolag K., Ryu D., Brunetti G., Gheller C., Kang H., Pfrommer C., 2011b, MNRAS, 418, 960

Vazza F., Eckert D., Brüggen M., Huber B., 2015, MNRAS, 451, 2198

Vazza F., Jones T. W., Brüggen M., Brunetti G., Gheller C., Porter D., Ryu D., 2017, MNRAS, 464, 210

Vazza F., Roediger E., Brüggen M., 2012, A & A, 544, A103

Vazza F., Wittor D., Brüggen M., Gheller C., 2016, Galaxies, 4, 60

Vikhlinin A., Kravtsov A., Forman W., Jones C., Markevitch M., Murray S. S., Van Speybroeck L., 2006, ApJ, 640, 691

Vikhlinin A., Markevitch M., Murray S. S., 2001, ApJ, 551, 160

Vogel M., 2016, Contemporary Physics, 57, 606

Vogelsberger M. et al., 2014, MNRAS, 444, 1518

Vogt C., Enßlin T. A., 2005, A & A, 434, 67

Voit G. M., 2005, Reviews of Modern Physics, 77, 207

Völk H. J., Aharonian F. A., Breitschwerdt D., 1996, Science & Space Review, 75, 279

Völk H. J., Atoyan A. M., 2000, ApJ, 541, 88

Wang P., Abel T., 2009, ApJ, 696, 96

Wang P., Abel T., Kaehler R., 2010, New Astronomy, 15, 581

Werner N. et al., 2015, Monthly Notices of the Royal Astronomical Society, 455, 846–858

White D. A., Jones C., Forman W., 1997, MNRAS, 292, 419

White, Raymond E. I., 1991, ApJ, 367, 69

Wilber A. et al., 2018, MNRAS, 473, 3536

Wise J. H., Abel T., 2007, ApJ, 665, 899

Wise M. W., McNamara B. R., Nulsen P. E. J., Houck J. C., David L. P., 2007, ApJ, 659, 1153

Wittor D., Gaspari M., 2020, MNRAS, 498, 4983

Wittor D., Hoeft M., Vazza F., Brüggen M., Domínguez-Fernández P., 2019, MNRAS, 490, 3987

Wittor D., Vazza F., Brüggen M., 2017, MNRAS, 464, 4448

Wittor D., Vazza F., Ryu D., Kang H., 2020, MNRAS, 495, L112

Woosley S. E., Weaver T. A., 1986, The Physics of Supernovae, Mihalas D., Winkler K.-H. A., eds., Vol. 255, p. 91

Wu X.-P., Xue Y.-J., Fang L.-Z., 1999, ApJ, 524, 22

Xu H., Li H., Collins D. C., Li S., Norman M. L., 2009, ApJL, 698, L14

Xu H., Li H., Collins D. C., Li S., Norman M. L., 2011, ApJ, 739, 77

Xu R., Spitkovsky A., Caprioli D., 2020, ApJL, 897, L41

York D. G. et al., 2000, ApJ, 120, 1579

Yuan Z. S., Han J. L., Wen Z. L., 2015, ApJ, 813, 77

Zeldovich I. B., Ruzmaikin A. A., Sokolov D. D., eds., 1983, Magnetic fields in astrophysics, Vol. 3

Zhang Y. Y., Finoguenov A., Böhringer H., Kneib J. P., Smith G. P., Kneissl R., Okabe N., Dahle H., 2008, A & A, 482, 451

Zhu W., Feng L.-L., 2017, ApJ, 838, 21

ZuHone J. A., Brunetti G., Giacintucci S., Markevitch M., 2015, ApJ, 801, 146

ZuHone J. A., Markevitch M., Brunetti G., Giacintucci S., 2013, ApJ, 762, 78

ZuHone J. A., Markevitch M., Lee D., 2011, ApJ, 743, 16